FABRICATION AND OPTICAL PROPERTIES OF (I) ERBIUM-DOPED NANOWIRES CONTAINING GERMANIUM AND/OR ZINC OXIDE AND (II) POROUS GERMANIUM NANOWIRES

by

XUEZHEN HUANG

Master of Engineering, July 2002
Nanjing University of Chemistry
Nanjing, Jiangsu, China

Submitted to the Graduate Faculty of the
College of Science and Engineering
Texas Christian University
in partial fulfillment of the requirements
for the degree of

Doctor of Philosophy

May, 2010

ACKNOWLEDGEMENTS

First, I would like to express my sincere gratitude to my most respected graduate advisor, Dr. Jeffery L. Coffer. The thanks to him are not only for his effective instruction, broad knowledge, free discussion, and encouragement during my study for Ph.D. degree, which lead me to nanoscience with rapid knowledge expansion in the related field, but also for his help in the American culture learning and English language practice. These experiences definitely have the most important impact on my career development in the future.

I would also like to thank the members of the Coffer research group for their help, and suggestions in our lab. Ji Wu helped me to use SEM and TEM. Dr. Ernest F. Couch of the Department of Biology also gave me help to understand more about TEM. Dr. Yuri M. Strzhemechny of the TCU Physics Department and his graduate student J. Antonio Paramo helped me with ZnO UV/visible photoluminescence measurement.

Thirdly, I really appreciate other people who ever assisted me in doing research in the past five years. Dr. Neilson, Dr. Hanna, Dr. Annunziata and Dr. Richards helped me in revising my degree proposal.

Financial support from Robert A. Welch Foundation and National Science Foundation is also much appreciated by the author.

TABLE OF CONTENTS

LIST OF FIGURES

LIST OF TABLES

LIST OF ABBREVIATIONS

1-D	one-dimensional
ALD	atomic layer deposition
AM	air mass
ASTM	American Society for Testing and Materials
C-AFM	conductive atomic force microscopy
CL	cathodoluminescence
CMOS	complementary metal oxide semiconductor
DMSO	dimethylsulfoxide
EDX	energy dispersive X-ray analysis
FET	field effect transistor
FFT	fast Fourier transform
GC	graphite cloth
HBP	high boiling point
IEC	International Electrotechnical Commission
IR	infrared
LED	light emitting diode
MBE	molecular beam epitaxy
NBE	near band edge
NW	nanowire

PCL	polycaprolactone
PEO	poly(ethylene oxide)
PG	porous germanium
PL	photoluminescence
PLD	pulsed laser deposition
PPV	poly(phenylene vinylene)
PS	porous silicon
PVD	physical vapor deposition
PVP	poly(vinyl pyrrolidone)
SBF	simulated body fluid
SCCM	standard-state cubic centimeter
SCR	space charge region
SEM	scanning electron microscopy
SFLS	supercritical fluid-liquid-solid
SLS	solution-liquid-solid
STC	standard test condition
TEG	tetraethylgermane
HRTEM	high resolution transmission electron microscopy
TEOG	tetraethyl orthogermane
TEOS	tetraethyl orthosilicate
TMHD	2,2,6,6-tetramethyl-3,5-heptanedionato

TOA	trioctylamine
TOP	trioctylphosphine
TP	tetrapod
TVD	thermal vapor deposition
UV	ultraviolet
VLS	vapor-liquid-solid
VOC	open-circuit voltage
VS	vapor-solid
XPS	X-ray photoelectron spectroscopy
XRD	X-ray diffraction

Chapter I

Literature Review

1.0 Introduction

1.0.1 Nanotechnology and nanomaterials

The term nanotechnology is used to describe the creation and exploitation of materials with structural features in between those of atoms and bulk materials, with at least one dimension in the nanometer range.[1] Scientists have intensive interest in nanotechnology not only because it can be used to make very small structures, but also because nanostructured materials exhibit superior mechanical, thermal, chemical, electrical and optical properties than those with larger dimensions.[2] The nano dimension mainly contributes to these differences due to a large surface-to-volume ratio, high surface energy, spatial confinement and reduced imperfections. For example, the large surface area to volume ratio causes a large fraction of atoms of the materials to be on the surface or at the interface, resulting in more "surface" dependent material properties.[3]

Going back to the early 1980s, nano became a buzzword for a new type of electronic device. For example, strained–layer superlattices were created by single atomic layer deposition precisely via molecular beam epitaxy and metalorganic chemical vapor deposition (CVD) technology, which made it possible to build quantum well structures with electronic and optical properties entirely different from those of the constituent bulk materials.[4-7] During the same period of time, material scientists viewed microorganisms as potential ecofriendly nanofactories, such as exploring the nature of the metal deposit onto native *Bacillus subtilis* walls.[8,9] In 1985, the fullerene C_{60} was discovered spectroscopically by Kroto *et al*., which stimulated considerable interest in the structures

accessible by graphitic carbon sheets, and eventually resulted in the discovery of carbon nanotubes by Iijima in 1991, a milestone in the development of nanoscience and nanotechnology.[10-12]

One of the most important contributions of carbon nanotubes is having initiated scientists' enthusiasm in one-dimensional nanostructures. Various techniques have been practiced in order to invent a variety of quasi-one-dimensional nanostructures, the geometrical shapes of which include tubes,[12,13] cages,[14,15] wires,[16,17] rods,[18,19] nails,[20] ribbons or belts[21,22] and more.

1.0.2 The fabrication of nanostructures

The importance of nanotechnology has been associated with the name of miniaturization by Feynman as early as 1959 in his famous lecture entitled ''There is Plenty of Room at the Bottom.''[23] Suitable control of the properties of nanometer-scale structures can lead to new science as well as new products, devices, and technologies. In recent years, the most effective industry methods to fabricate nanostructures are top-down strategies. Based on photolithography, the top-down technology challenges the physical limits of microelectronics miniaturization with the requirement of smaller devices.[24] With the development and significant assistance of the electron microscope, there has been explosive growth of nanoscience and technology in the last two decades due to the availability of new methods of synthesizing nanomaterials based on so-called

"bottom-up" technology. Nanoscience and technology has entered a commercial exploration period recently.[25]

The synthesis of nanomaterials spans inorganic, organic and biological systems, all with control of size, shape and structure. A large number of approaches have been devised to synthesize nanomaterials with different dimensions in solution or the gas phase.[1,2,26] Size and shape control can be achieved with a template, which can be employed in quite a few different synthetic routes. Assembling the nanostructures into ordered arrays is often necessary to render them functional and operational. For example, biological self-assembly was used to fabricate 3D DNA nanotubules through integration of Au particles, as shown in Fig. 1.[27] In another work, 10 layers of Ge/Si nanowire field effect transistors (NW FET) were used to build 3D multifunctional electronics by the layer-by-layer assembly of NWs. This represents the highest number of functional device layers reported vertically stacked with any single-crystalline channel material (Fig. 2).[28]

With both "top-down" and "bottom-up" technology development, ultimately, nanotechnology–based products will require a convergence of the two approaches for practical use, both to engineer the nanoscale device and to interface with the outside world. The bottom-up approach permits control of the chemical and structural architecture; however, manual assembly of individual nanometer-sized components is clearly prohibitive in time and cost. Top-down technologies provide a gradual scalable bridge between the meter, millimeter, micron and nano-size regime.[25]

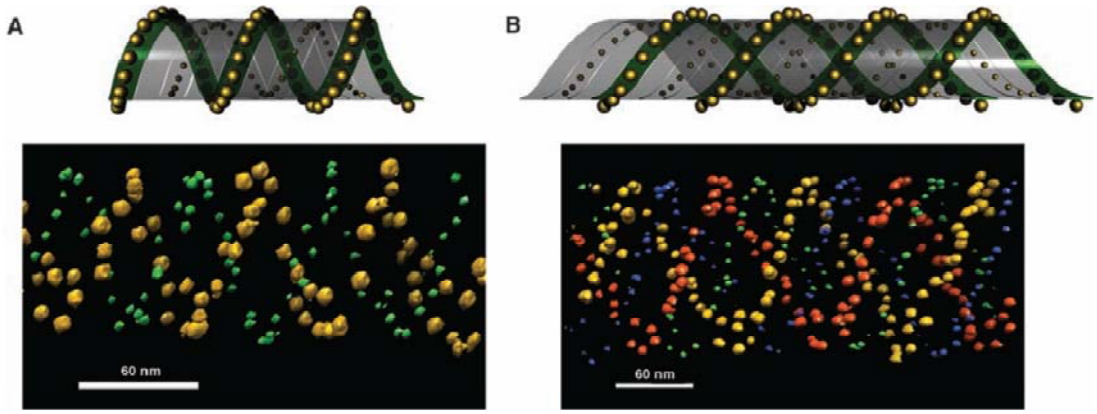

Figure 1. Representative 3D structures of nanoparticle tubes formed with 5 and 10 nm Au NPs placed on opposite surfaces of the DNA tile array. (A and B) The top panels are schematic side and top views of the binary particle tube architectures; the bottom panels are corresponding representative electron tomographic images showing the 3D architectures. (adapted from ref. 27.)

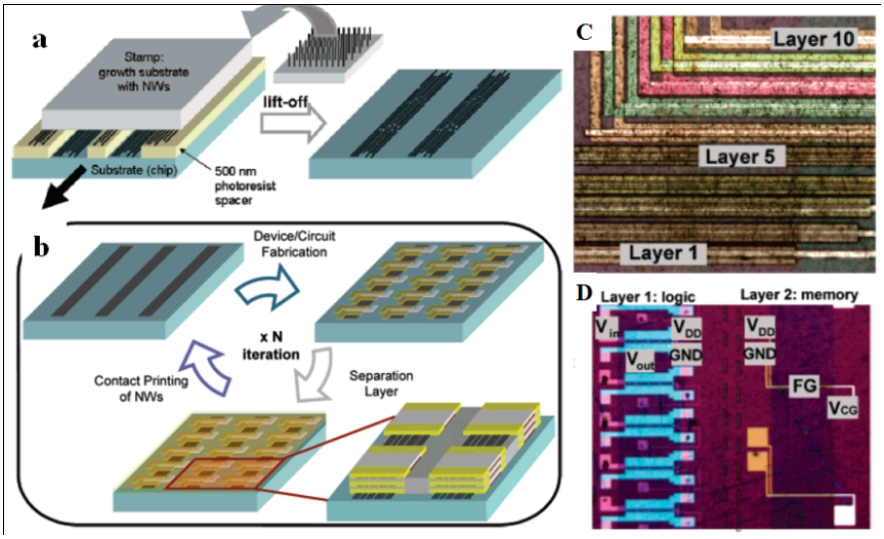

Figure 2. (a)(b) Overview of 3D NW circuit integration. (c) Optical microscope image of 10 layers of Ge/Si NW FETs. (d) Optical image of inverters (layer 1) and floating gate memory (layer 2) on Kapton. (adapted from ref. 28.)

1.0.3 The potential applications of nanomaterials

Nanotechnology is looked upon as a new revolution in science and engineering in the human world in the 21 century.[29,30] A variety of potential applications of nanomaterials have been intensively investigated, from nanophase ceramic materials in textiles and plastics to non-linear optics and optoelectronics applications.[31-33] The most important and far-reaching applications of nanomaterials will be in nanodevices and nanoelectronics applications, including FETs, LEDs, anode materials in Li batteries, single electron memory devices, spin polarized electronics, quantum computing, sensors, photonic crystals/devices, magnetic and electrical applications, solar cells etc.[34-49]

In addition to electronics, nanotechnology will be extremely useful to biology. The potential linkage between nanotechnology and biological science is enormous because physiological functions depend greatly on nano-sized units.[50,51] Living organisms are built of cells that are typically 10 μm across. However, the cell parts are much smaller and are in the sub-micron size domain. Even smaller are the proteins with a typical size of just 5 nm, which is comparable with the dimensions of smallest synthetic nanoparticles. This simple size comparison gives an idea of using nanoparticles as very small probes that could be used to spy at the cellular machinery without introducing too much interference.[52] Fig. 3 shows some of the applications of nanomaterials to biology or medicine. For example, for a prosthesis, one could reduce the chances of rejection as well as stimulate osteogenic integration of the artificial material with the biological system by creating nano-sized features on the surface of the hip or knee.[53]

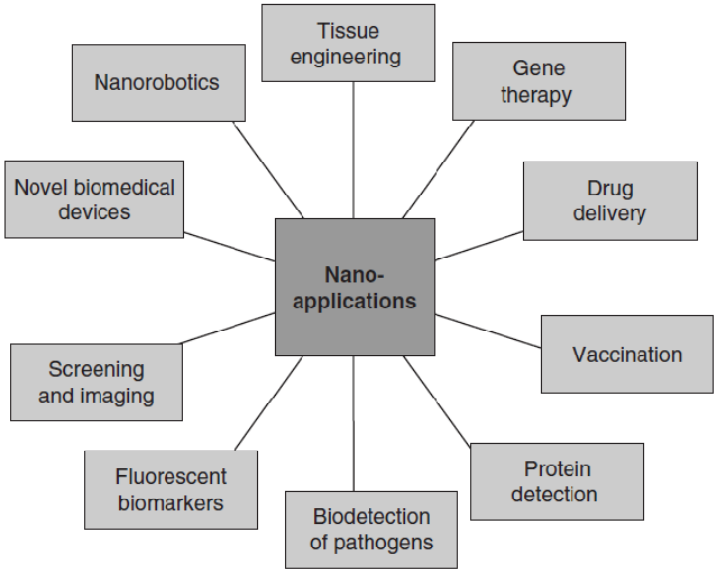

Figure 3. Various applications of nanotechnology in biology and medicine. (adapted from ref. 50.)

Recently, companies are developing pharmaceutical applications based on nanoscale platforms, mainly for drug delivery.[51] Several companies exploit quantum size effects in semiconductor nanocrystals for tagging biomolecules, or use bio-conjugated gold nanoparticles for labeling various cellular parts. A number of companies are applying nano-ceramic materials to tissue engineering and orthopaedics.[51] Most major and established pharmaceutical companies have internal research programs on drug delivery that are on formulations or dispersions containing components down to nano sizes.[51] However, these applications are still at the concept level, requiring much more basic research before they can be incorporated in to viable products. In brief, although

nanotechnology has been emphasized by many countries in the world, its commercialization has a long way to go. Different from traditional industry, it will not reach the commercialized achievement until compelling applications are found and adapted in the future.[25]

1.1 1D nanowires of Germanium (Ge)

1.1.0 Fabrication of Ge nanowires (GeNWs)

1.1.0. 1 GeNW growth via Au-catalyzed vapor-liquid-solid (VLS) process

Electronic nanodevices based on two-dimensional (2D) quantum wells, one dimensional (1D) quantum wires, and zero-dimensional (0D) quantum dots are rapidly approaching systems where carrier transport is entirely controlled by quantum effects.[54] Semiconductor nanowires produced by the VLS method exhibit unique electrical and optical properties in connection with the quantum confinement effect.[54] Such a method was first proposed by Wagner and Ellis in the fabrication of Si whiskers with diameters ranging from 100 nm to 0.2 mm.[55]

Germanium is an important semiconductor material. As a congener of Si, Ge has a smaller indirect band gap of 0.74 eV, a higher carrier mobility (3900 and 1500 $cm^2 V^{-1}s^{-1}$ for electrons and holes in Ge, 1500 and 450 $cm^2 V^{-1}s^{-1}$ in Si, respectively), a larger dielectric constant, and a larger excitonic Bohr radius (24.3 and 4.9 nm for Ge and Si, respectively).[56-58] This not only means that Ge has various potential applications in

electronics and photonics, but also that more prominent quantum confinement effects can probably be achieved in Ge nanostructures with a relatively bigger size than those of Si.

The past decade has witnessed tremendous progress toward the synthesis of GeNWs using various approaches like laser ablation,[59] solvothermal/hydrothermal synthesis,[60-62] chemical vapor deposition (CVD),[63-65] vapor transport,[66-68] vapor phase epitaxy,[69,70] electrochemical etching,[71] templating,[72-74] and supercritical fluid-liquid-solid synthesis.[75] Among them, the VLS approach is most preferred because of the high quality of single

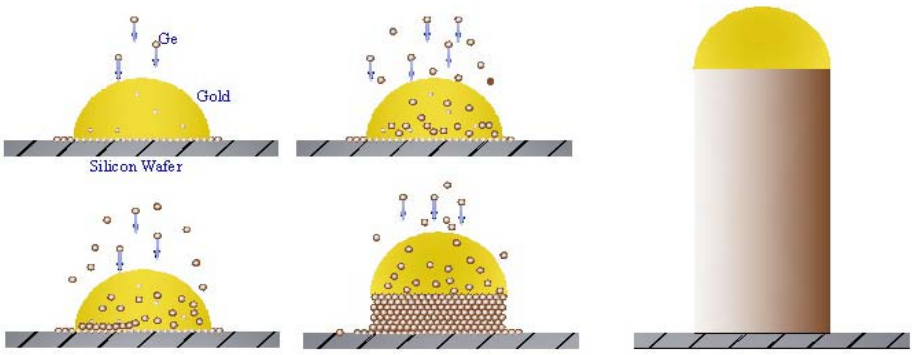

Figure 4. The scheme of GeNWs growth mechanism (VLS).

crystalline products and a relatively high yield. In the VLS process, the semiconductor material (gas or thermal evaporation) is absorbed by liquid nanodroplets of an appropriate catalytic material such as gold (as shown in Fig. 4). These nanodroplets, located at the nanowire tips, serve as seeds for nanowire growth and also determine the nanowire diameters. When the alloy is supersaturated, the semiconductor material

nucleates at the interface between the droplet and the nanowire, thereby extending the length of the nanowire.[76]

The VLS mechanism returned to serious scientific attention after Morales and Lieber combined it with laser ablation to fabricate Si and Ge nanowires successfully in 1998, which triggered a worldwide avalanche of research activities into nanowire synthesis.[59] In the case of Ge, Morales selected 820 °C as a reaction temperature, because the phases above 838 °C are $FeGe_x$ (l) and Ge(s) in the Ge-rich region of the Ge-Fe diagram, and below this temperature they are β-$FeGe_2$(s) and Ge(s). The latter were expected due to the stability of $FeGe_2$ composition in liquid in the Ge-rich region of the phase diagram. Laser ablation of a $Ge_{0.9}Fe_{0.1}$ target produced a good yield of GeNWs in a low temperature area (<400 °C) of the reactor with diameters between 3 and 9 nm, and TEM images show that these nanowires are crystalline, have uniform diameters without an amorphous coating, and terminate in nanoclusters.[59]

Another interesting story correlating GeNWs to VLS mechanism involves a controversy concerning whether, below a certain temperature, the growth of semiconductor nanowires involves a liquid droplet or a solid particle of the catalytic material.[76, 77] In VLS growth, the liquid droplet consists of both catalytic material (like Au) and semiconductor material. The lowest possible melting temperature for a specific composition is the eutectic temperature, T_E. Above the eutectic temperature, semiconductor nanowires grow via the VLS mechanism. However, nanowire growth has also been reported to occur at temperatures below the eutectic temperature.[78,79]

Kodambaka et al. used in situ TEM microscopy to observe GeNWs growth with Au catalyst and Ge_2H_6 source.[77] The experimental results showed that nanowire growth can occur below the eutectic temperature with either liquid or solid catalysts at the same temperature as shown in Fig. 5.

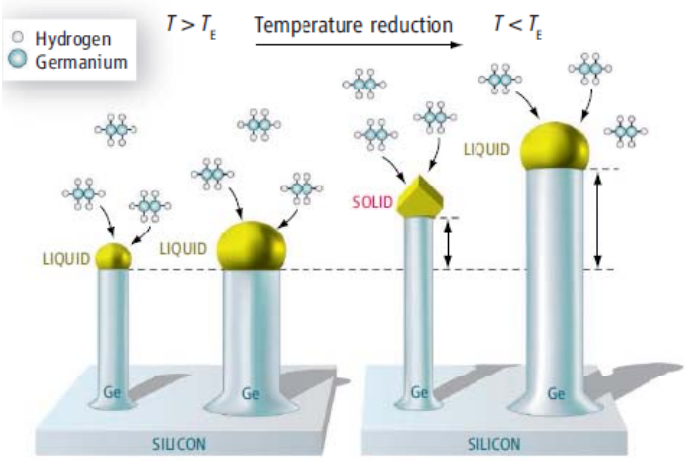

Figure 5. The mechanism by which Ge nanowires grow may depend not only on the temperature but also on the diameter of the nanowire, as shown by Kodambaka *et al.* Above T_E (left), the nanowires have a liquid gold cap and grow via VLS growth. Below T_E (right), the cap of relatively thick nanowires is liquid, whereas the cap of relatively thin nanowires becomes a crystalline solid. The latter nanowires grow via a different mechanism that is slower than VLS growth. (adapted from ref. 76.)

To answer the question why the liquid phase persists below T_E, they suggested that solidification requires some undercooling to overcome the nucleation barrier for a new phase. Therefore, the key step for solidification is nucleation of a solid Au particle, and this step controls the degree of undercooling. Once Au nucleates, the liquid solidifies abruptly, with Ge coming out of solution and incorporating into the wire. Unexpectedly, they found that the catalyst state depends on the growth pressure in the reactor and

thermal history.[77] These results may help to devise methods for controlling the growth of nanowires.

VLS growth mechanisms are often employed in the context of vapor deposition, in which reactive gases are selectively absorbed by a metal seed particle. The seed particle is typically deposited in a separate step. The most representative method is CVD, which has been used intensively to grow semiconductor nanowires recently. Wang and Dai first used this method to fabricate GeNWs in 2002.[80] GeH_4 (10 sccm, 10% in He) was decomposed at 275 °C in H_2 (100 sccm) for 15 min and then deposited onto Au-coated Si substrate to form GeNWs. The average diameter of GeNWs was ~23 nm. This CVD method has the advantages of low temperature, high yield and uniform size distribution, but GeH_4 is flammable, toxic and expensive.

The Coffer group first reported a GeNW fabrication approach by physical vapor deposition (PVD) in 2004.[66] GeNWs were grown on Au coated Si wafers with high quality and yield by heating Ge powder to ~1000 °C for 1.5 h in He carrier gas (300 sccm). Prior to Ge exposure, a preannealing process is necessary to form Au islands of the proper dimension. The average size of GeNWs ranged from 40~130 nm and could be controlled by carrier gas flow rate and/or duration. This method is one of the simplest for GeNW fabrication in terms of precursor handling and cost.

In comparison, solution-liquid-solid (SLS)[62,81] and supercritical fluid-liquid-solid[61] (SFLS) nanowire growth methods provide straightforward means to synthesize both seed particles and nanowires sequentially in the same reactor. However, this advantage is

sometimes mitigated by the challenge of controlling the incorporation of intentional impurities, such as dopants, as well as unintentional impurities from the precursors.[82] In the supercritical fluid-liquid-solid route, Hanrath and Korgel used tetraethylgermane (TEG) and diphenylgermane (DPG) as precursors to grow GeNWs with alkanethiol-coated Au nanocrystal catalysts (2.5 or 6.5 nm) in anhydrous deoxygenated cyclohexane (in supercritical states).[61] GeNWs formed at growth temperatures ranging from 300 to 450 °C and the yield was 60~80%. At temperatures exceeding 500 °C, large Ge particulates formed due to unfavorable growth kinetics. Although the reaction temperatures were below T_E, a solid nucleation particle has sufficiently high internal diffusion rates to permit GeNWs growth.

1.1.0.2 Non-Au catalysts in GeNW growth

In the mechanisms mentioned above, the metal catalyst, mainly Au, is an important factor to form GeNWs and determine their sizes. However, Au is a deep level impurity in Si and Ge that significantly degrades the carrier mobility and causes fast nonradiative electron-hole pair recombination.[83,84] Thus, Au seeded nanowires are relatively undesirable for electronic applications based on Si CMOS (complementary metal-oxide-semiconductor) technology, and other alternative metals would be strongly desired to use as seeds.

Early work investigated several metals, such as Ag, Cu, Ni, Pd, In, Sn and Bi, as catalyst in Ge and Si whisker growth.[78] Tuan and Korgel later prepared GeNWs by using

Ni as catalyst in SFLS methods at reaction temperatures ranging from 410 to 460 °C.[83] The growth temperature is well below the lowest Ni-Ge eutectic temperature (762 °C). Because the candidate metals have to satisfy both the compatibility of Si CMOS (such as Fe, Ni, Ti, and Co) and the corresponding very high-temperature eutectics with Si and Ge, this work expanded the applied range of the SFLS process, which was limited by organic decomposition temperature.

Unlike Ni, bismuth (Bi) is a low melting metal and can form a eutectic with Ge at 271.4 °C, which is well within the temperature window for conventional solvents. Buhro first showed that Bi nanocrystals could seed SLS growth of CdSe nanowires.[85] Korgel's group introduced Bi to GeNW synthesis. They found that GeI_2 was an effective precursor for Ge nanocrystal synthesis at 300 °C in trioctylphosphine (TOP) with sufficient reactivity.[62] The Bi nanocrystals were synthesized by room temperature reduction of bismuth(III) 2-ethylhexanoate ($Bi[OOCCH\text{-}(C_2H_5)C_4H_9]_3$) in dioctyl ether in the presence of TOP.[62] TOP serves as a capping ligand that prevents significant nanocrystal aggregation but does not interfere with nanowire growth. The precursor and nanocrystal were injected into preheated TOP at 365 °C and reacted for 10 min at 350 °C in the reaction vessel with stirring. GeNWs were formed as a black precipitate.[62] The best Ge nanowire product was obtained using a GeI_2:Bi mole ratio of 80:1. The wires were long and generally straight, ranging in diameter from 20 to 150 nm with an average of ~50 nm, with aspect ratios exceeding 100.

The solution-liquid-solid (SLS) mechanism is shown in Fig. 6. The critical condition for the process is that the highly reactive organic-free Ge precursor, GeI_2, disproportionates to Ge and GeI_4 with relatively high chemical yield at temperatures greater than ~330 °C using the assistance of TOP.[62] Control experiments where GeI_2 was injected without Bi nanocrystals into TOP at 365 °C showed Ge nanoparticle formation in just 5 min. With Bi present in the concentrations used for nanowire synthesis, Ge nanoparticles were not observed. Although small Ge clusters may nucleate homogeneously, their interfacial free energy is greatly lowered by incorporation into the much larger 20 nm Bi particles.[62]

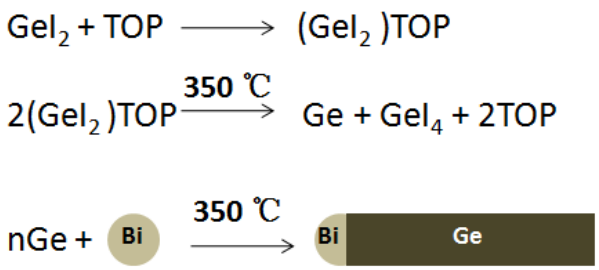

Figure 6. GeNW growth mechanism. (adapted from ref. 62.)

The latest work reported by Xiang et al. used germane (GeH_4, 10% in Ar) as a growth precursor and Bi as catalyst to synthesize GeNWs in a VLS process.[84] 1.5 nm Bi was deposited by electron beam evaporation onto fused quartz wafers. GeNWs grew at a temperature range from 270 to 400 °C and at GeH_4 gas pressures between 30 and 300 Torr. The optimal conditions leading to high density and high aspect ratio Ge NWs are 300 °C and 150 Torr of gas pressure. In another work, Yan and Lee did not deposit

catalyst Bi onto substrate initially.[86] They mixed bismuth, germanium, and carbon powders (molar ratio Bi:Ge:C= 0.05:1:1) and heated the source to 1000 °C for 60 min under an Ar flow of 200 sccm, then straight and uniform GeNWs formed on copper grid substrates. In this work, the Bi catalyst particles condensed at the low temperature region from the vapor generated via an in situ evaporation process. This one-step catalyst deposition and nanowire growth process is expected to minimize the oxidation of the Bi nanoparticles, due to the Ar protection atmosphere in the furnace during growth.

1.1.0.3 GeNW growth via catalyst-free process

In addition to metal-catalytic processes, much progress has been made in catalyst-free growth for compound semiconductor nanowires by various methods, including laser ablation, physical vapor deposition, and chemical vapor deposition. These catalyst-free anisotropic growth processes have been explained by a self catalytic VLS mechanism,[87] oxide-assisted growth,[88] dislocation-driven process,[89] or vapor solid growth.[90] Zaitseva et al. reported a self catalytic VLS process without metal catalyst.[87] They used either 5 mL of pure tetraethylgermane (TEG) or mixtures of 1.5 mL of TEG and 3.5 mL of different solvents as the growth precursor to grow GeNWs in the reactor in an Ar-filled glove box. In high boiling point (HBP) solvents containing long alkyl chains such as trioctylamine (TOA, bp 383 °C) and squalene (bp 392 °C), GeNWs were observed when reactions were carried out in the temperature range of 380–400 °C with additional short-term (10–30 min) heating to 430 °C.

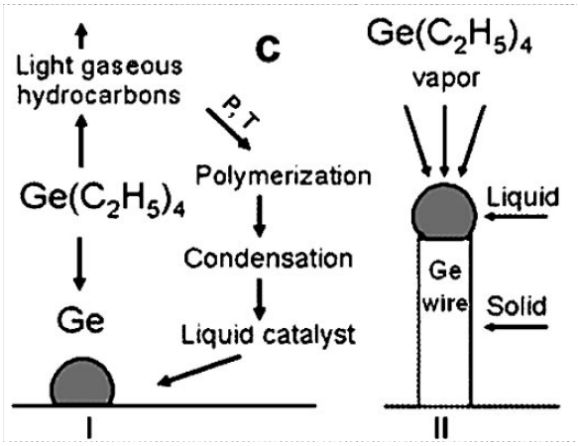

Figure 7. GeNW growth by unseeded VLS mechanism: I. Catalytic decomposition of TEG on the surface of a liquid droplet produced by condensation of HBP solvents or as a result of high-temperature-pressure polymerization process. II. Growth of a Ge NW. (adapted from ref. 87.)

Zaitseva et al. suggested a mechanism that is a complete analogue of the VLS mechanism, with the difference that the liquid component is replaced by an organic droplet (Fig. 7). The decomposition of TEG in the absence of catalysts starts at a very slow rate above 350 °C, becoming substantial only at the temperatures above 430 °C. During the cooling to temperatures in the range of 350–400 °C that follows, (which includes the boiling points of TOA and squalene), solvents condense to small droplets, while TEG (bp 167 °C) still exists as a vapor. The surface of the liquid droplets acts as a sink for vapor molecules, accelerating the process of the decomposition that deposits Ge atoms on the vapor-liquid interface, similar to the process that takes place on the surface of liquid Au–Ge alloy. Ge incorporates into the liquid, possibly through simple solubility but more likely because of the low diffusion resistance of small droplets.[87] It then

crystallizes on the solid-liquid interface between the droplet and substrate, similar to the traditional VLS mechanism.

Kim et al. built an oxide-assisted catalyst-free process for Ge semiconductor NW fabrication.[88] A piece of hydrogen-terminated Ge wafer was etched with ultrapure water to generate a reactive Ge-rich oxide (GeO_x) layer on the substrate surface. GeNW growth was initiated on the surface at 520 °C and 15 Torr using GeH_4 (10% diluted in H_2) for 2 min and then the anisotropic growth of the single crystal nanowires was carried out at a reduced temperature of 490 °C for 10 min to minimize nonspecific decomposition of GeH_4 on the nanowire surface.[88] The mechanism (suitable for both growth of Si and Ge NWs) can be understood with the vapor-solid (VS) growth model (Fig. 8). When the degree of reactant supersaturation is lower than that for homogeneous deposition or for the growth of bulk crystals, the precursors are adsorbed on the reactive thin oxide surface and decomposed to form nanocrystalline seeds, thus promoting anisotropic nanowires growth outward from the surface in a thermodynamically preferred direction.[88] According to SEM images, the process had a very sensitive control of the size distribution and morphology of nanowires. However, HRTEM images indicated that the crystalline

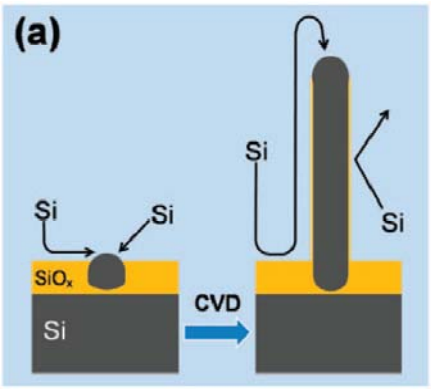

Figure 8. A schematic for the proposed catalyst-free Si or Ge nanowires growth model. (adapted from ref. 88.)

structures in the area close to surface had more defects with little surface roughness, as compared with the common VLS catalytic methods.

1.1.1 Electrical transport studies of GeNWs

Studies concerning the electronic and optical properties of nanomaterials have been extending our understanding of the solid state physics involved in quantum effects, which is relevant to the design and application of nanodevices. Gu et al. measured the typical temperature-dependent current–voltage characteristics on a single Ge nanowire with diameter of 120 nm (Fig. 9).[91] At temperatures higher than 100 K, linear current dependence on voltage was found, indicating ohmic contacts between the Ge nanowire and the Au electrodes.[91] The linear resistivity including contact resistance at room temperature ranged from 1.43×10^{-2} to 30 Ω cm, less than that of bulk Ge (47 Ω cm). Because the conductivity of doped bulk germanium is very sensitive to its surface states, Ge nanowire surface states may play an important role due to their high ratio of surface atoms. Therefore the observed high conductivity was also attributed to the surface states of Au-contained Ge nanowire devices.

Hanrath and Korgel reported that Ge nanowire (grown from Au seeded SFLS method) devices exhibited ohmic I-V curves with resistivity values ranging from 0.1 to 10 Ω cm.[92] Erts, Holmes et al. used both conductive atomic force microscopy (C-AFM) and macrocontact technology to measure the conductive properties of ordered arrays of semiconductor nanowires within aluminum oxide templates and obtained approximately

the same electrical resistivity results.[93] The resistivity for a single nanowire, based on a mean value obtained for a group of nanowires, was between 80~1000 Ω m for nanowires with a mean diameter of 100 nm and 140~3000 Ω m for nanowires with a mean diameter of 50 nm, respectively.[93] The result was much bigger than the previous two reports. Gu's work had a similar order of magnitude to the Korgel's, except a bigger resistivity range. It was perhaps limited by the early design of the previous experiment. Since the GeNWs were fabricated without Au catalyst in Holmes's report, the higher resistance was attributed to the Au free preparation process.

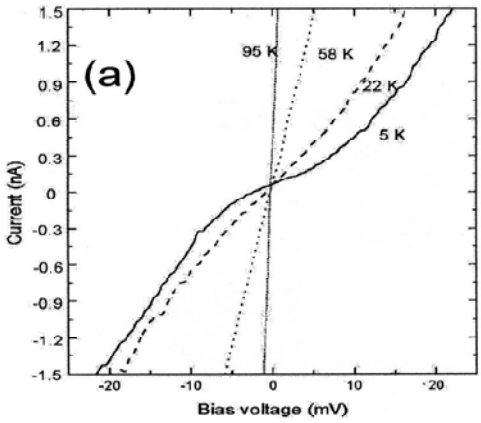

Figure 9 I–V curves of Ge nanowires at different temperatures. (adapted from ref. 91.)

1.1.2 Surface electronic states of GeNWs

The high surface areas of nanowires suggest that surface effects play dominant roles in determining additional properties such as Fermi level and depletion length.[94,95] When the energy density of surface states is very high ($>10^{12}/cm^2$) in a semiconductor, the

position of the Fermi level is determined by the neutral level of the surface states and becomes independent of doping concentration in a large range. This pinning effect can be quantitatively estimated for semiconductor nanowires. For a planar surface with a surface Fermi level pinning potential of φ_0, the screening length d is given by:[94]

$$d = \sqrt{\frac{4\pi\varepsilon_0\varepsilon\varphi_0}{2\pi n}} \qquad (1.1),$$

where ε_0 is the permittivity of a vacuum and ε, the dielectric constant of the semiconductor, n, the number of electrons. For a nanowire with radius R, the depletion length d (along the radial direction of the nanowire, and d << R) can be obtained by:

$$\frac{4\pi\varepsilon_0\varepsilon\varphi_0}{2\pi n} = \left(1 - \frac{d}{3R}\right) d^2 \qquad (1.2)\,,$$

which suggests that the screening length in a nanowire is longer than that in the planar surface case and the difference is more significant for smaller nanowires. This is a reasonable result since screening becomes less effective when approaching the core of a nanowire due to the reduced radial dimension.

The poor quality of the Ge/GeO_2 interface with a high density of surface states ($>10^{14}/cm^2$) causes substantial Fermi level pinning on the surface of GeNWs.[94] Wang and Dai carried out systematic X-ray photoelectron spectroscopy (XPS) on p- and n-type GeNWs, and found oxide-induced band bending on both types of GeNWs with opposite bending directions. For p-type GeNWs, the Fermi level is bent upwards, and for n-type GeNWs it is bent downwards, so both of them are pinned by the inter-band states (Fig. 10). Therefore, the surface/interface states are expected to be in the mid-gap.

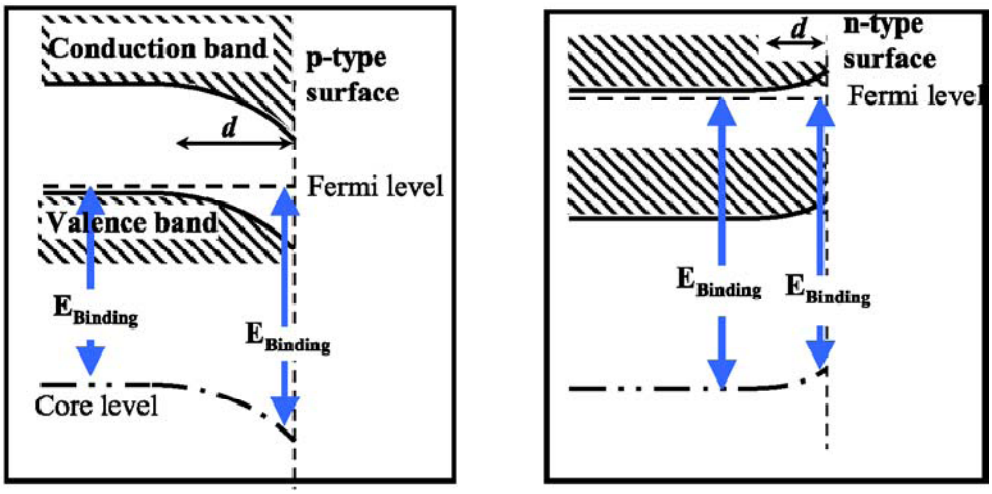

Figure 10 Band structures of *p*- and *n*-type Ge NWs. Opposite band bending is manifested as a result of Fermi level pinning due to surface states (adapted from ref. 94.)

1.1.3 Electronic devices based on GeNWs

High-k dielectric films, such as hafnium oxide and zirconium oxide, have been used to passivate the surface of GeNWs for the fabrication of Ge-based devices,[96-99] mainly FETs. The back-gated p-type Ge nanowire FETs reported by Dai et al. showed high I_{on}/I_{off} ratio ($\geq 10^3$) and low resistances (~500 kΩ).[94] The hole carrier mobility was higher than 600 cm^2V^{-1} s^{-1}, which is close to the highest reported value for Ge MOSFETs built on Ge wafers (~700 cm^2V^{-1} s^{-1}).

Cui et al. reported a method to synthesize GeNWs directly onto metal current collector substrates for use as Li battery anodes.[100,101] GeNWs grew onto stainless steel (SS) substrate by GeH_4 CVD process at a high temperature (500 °C), which was helpful for the adhesion of the GeNWs onto the substrate. GeNWs served as the working

electrode and Li foil as the counter electrode without adhesion. The electrochemical cycling of the GeNWs was found to be stable for 20 cycles at the C/20 rate (C-rate: the charging or discharging rate of a battery, expressed in terms of its total storage capacity in Ah or mAh. So a rate of 1C means transfer of all of the stored energy in one hour; 0.1C means 10% transfer in one hour, or full transfer in 10 hours; 5C means full transfer in 12 minutes, and so on). The first charge capacity was 2967 mAh/g (greater than the theoretical capacity, 1600 mAh/g), with a Coulombic efficiency of 39%. The Coulombic efficiency, the ratio of the number of charges that enter the battery during charging compared to the number that can be extracted from the battery during discharging, for the third set of 20 cycles is 84-96%, showing excellent reversible cycling after the surface reactions are completed. The capacity was very stable at the high C and 2C rates, indicating good Li diffusivity in the GeNWs. Although the capacity dropped at the 2C rate to ~600 mA.h/g, it was still much higher than the graphite capacity of 372 mA.h/g (the maximum theoretical specific capacity of Li-graphite anode).[101]

1.2 ZnO Nanowires and Tetrapods

1.2.1 ZnO nanowires

1.2.1.1 Growth of ZnO nanowires by VLS mechanism

ZnO is known as an excellent II-VI semiconductor with wide band gap (3.37 eV) and large exciton binding energy (~60 meV). As an outstanding optical material, the

photoluminescence (PL) of ZnO includes near band edge (NBE) ultraviolet emission and deep-level emission (usually broad green, blue peaks).[102-107]

For wide band-gap semiconductor materials, a high carrier concentration is usually required in order to reach an optical gain that is high enough for lasing action in an electron-hole plasma (EHP) process.[108,109] A high lasing threshold is necessary for EHP, commonly for conventional laser diode operation. As an alternative to an EHP process, excitonic recombination in semiconductors is a more efficient radiative process and can facilitate low-threshold stimulated emission.[110,111] To achieve efficient excitonic laser action at room temperature, the binding energy of the exciton must be much greater than the thermal energy at room temperature (26 meV). The high exciton binding energy makes ZnO a good candidate compared with ZnSe (22 meV) and GaN (25 meV).[108] ZnO nanostructures are expected to further lower the lasing threshold in semiconductor laser technology because quantum confinement yields a substantial density of states at the band edges and enhance radiative recombination. Over the past several years, ZnO nanostructures, such as ZnO nanowires, have attracted great attention and have become one of most important semiconductor nanomaterials studied as intensively as Si nanostructures and carbon nanotubes.[112-115]

To date, a large number of methods have been developed to synthesize ZnO nanowires, including chemical/physical vapor deposition[116-119] and solution phase synthesis.[120-122] Solution phase methods usually operate at low temperatures and have strength in massive production, but the relatively insufficient purity and crystallinity of

the product limits their applications for devices.[123] Yang et al. developed a vapor-phase transport process to grow ZnO nanowires via a VLS mechanism.[108] ZnO nanowires were grown on Au-coated silicon substrates by heating a 1:1 mixture of ZnO and graphite powder to 900~925 °C under a constant Ar flow (20-25 sccm) for 5~30 min. The ZnO nanowire layer appeared light or dark gray on the Si wafer after the reaction. The growth mechanism of ZnO nanowires in the thermal evaporation process can be presented in the following reactions, which occur at a source material (ZnO+C) temperature of 900~1300 °C:[123-125]

$$ZnO_{(s)} + C_{(s)} \rightarrow Zn_{(g)} + CO_{(g)} \quad (1)$$

$$CO_{(g)} + ZnO_{(s)} \rightarrow CO_{2(g)} + Zn_{(g)} \quad (2)$$

In the deposition area, gaseous products condense on the Au coated Si substrates through the following reactions:

$$Zn_{(g)} + CO_{(g)} \rightarrow ZnO_{(s)} + C_{(s)} \quad (3)$$

$$C_{(s)} + CO_{2(g)} \rightarrow 2CO_{(g)} \quad (4)$$

Thareja reported that Gibbs free energy (ΔG) have negative values for reactions (1), (2) and (4) and a positive value for reaction (3).[125] The reactions with negative values of Gibbs free energies imply instantaneous/spontaneous reactions. The reaction (3) initiates at the low temperature region.

Nanowires usually have a preferred growth direction, like Ge in the (111) and ZnO in (001). By using a-plane sapphire as substrate, Yang et al. obtained ZnO arrays in the (110) direction with nanowire sizes of ~20-40 nm. The size of ZnO nanowires could be controlled by the thickness of Au coating.

1.2.1.2 Dopant-modified ZnO nanowires

In the synthesis of ZnO nanowires, various dopants have been used to improve the optical, electrical, and/or structural properties of ZnO nanowires. For example, Al-doped ZnO nanowires exhibited a blue shift from 3.29 to 3.34 eV in the cathodoluminescence (CL) spectra.[126] These dopants almost span all groups in the periodic table including Li, Mg, Sc, Cr, Mn, Fe, Co, Ni, Cu, Au, Ga, Al, C, S, P, La, and Eu etc.[127] Although IIIB and IVB groups are not used in ZnO nanowire fabrication, similar work has been seen in ZnO film modifications.[128,129]

Zhang et al. fabricated Ga-doped ZnO (n-type) and N-doped ZnO nanowire arrays.[130,131] n-Type ZnO nanowires showed sharp near-band edge PL with negligible defect-related emission suggesting good crystal quality. The emission peak for the undoped ZnO nanowires is centered at 374 nm. Electrical transport properties of Ga-doped ZnO nanowires studied via single nanowire FET measurements show that increasing Ga_2O_3 in the source material from 0 to 1%at can realize tunable n-type conduction, with resistivity decreasing from 2.5×10^{-1} Ω cm to 2.2×10^{-3} Ω cm.[130] It indicated that the variation of electron concentration in Ga-doped ZnO nanowires was indeed dominated by Ga impurities.

Moreover, characterization of single ZnO NW FETs shows a transition from n-type conductivity in undoped ZnO NWs (8×10^{-3} Ω cm) to compensated high-resistive n-type (2.9 Ω cm), and finally to p-type conductivity (0.08 Ω cm) in N-doped NWs with

increasing N_2O in the reaction atmosphere. It means that the dopant (nitrogen) can be used to transform ZnO NWs from n-type to p-type.

Cui et al. reported a low temperature electrochemical approach to fabricate Cl-doped ZnO nanowire arrays, which were expected to reduce oxygen vacancies.[132] The solution of zinc nitrate, hexamethylenetetramine, and ammonium chloride was used as electrolyte. Cl-doped ZnO nanowires were grown on the Si wafer in a cathodization process at 90 °C for 1.5h. The ZnO UV/visible spectrum shows a remarkable reduction of O_2 vacancy-induced PL intensity with the increasing Cl dopant, and NBE ultraviolet emission shifts from 380 to 390 nm under the excitation of a 325 nm laser.[132]

There is a great deal of fundamental research ongoing with respect to ZnO NWs that may one day lead to enhanced performance in FETs, sensors, solar cells, LEDs, lasers, etc.[108,130,131,133] For example, Wang et al. reported the first nanogenerator based on ZnO nanowire-fiber composites, which can scavenge light-wind energy and body-movement energy due to the piezoelectric property of ZnO.[134]

1.2.2 ZnO tetrapods

1.2.2.1 Fabrication of ZnO tetrapods

Both Group IV and compound semiconductors typically display polymorphism, i.e. the existence of more than one stable crystal structure,[135] which allows the possibility of growing branched nanostructures, like ZnO tetrapods (TPs). ZnO TPs consist of a ZnO core in the zinc blende structure from which four similar ZnO arms extend in the

wurtzite structure. ZnO TPs have potential applications as sensors, electromagnetic and spintronics devices.[136-138]

ZnO TPs have been synthesized by oxidation of Zn powder[139] and evaporation of a mixture of Zn and silica powder with Fe_2O_3 used as a catalyst in the VL or VLS mechnism.[140] Surya et al. prepared ZnO TPs prepared under different conditions [in air (no flow), argon and nitrogen flow, with or without water vapor] by evaporating Zn powder in a quartz tube at 950 °C.[141] The quartz tube was inserted after the furnace has reached the desired temperature. They found that a mixture of TPs and nanowires was obtained for the gas flow, while for deposition in air only ZnO TPs were observed. Sun et al. used mixtures of ZnO and graphite as starting materials to fabricate ZnO TPs in a one-end sealed quartz tube at 1100~1200 °C.[142] The growth temperature was about 650–750 °C depending on the distance from the source region due to the temperature gradient. The temperature is a critical factor, which influences the vapor pressure and kinetic energy of vapor atoms. The high temperature is believed to be beneficial to multipod nucleus and the leg growth.

1.2.2.2 Properties and applications of ZnO tetrapods

Kim et al. measured the local resistances in the arms and in the junction in the ZnO-TPs separately by ac impedance spectroscopy.[143] The resistance at the junction is found to be greater than that in the bulk although the volume fraction of the junction is negligibly small compared to that of the arms. Buyanova et al. found that the PL

transient measured for the free exciton emission is significantly longer (τ_{slow}=14 ns, τ_{fast}=1ns, 280K, biexponential decay) in the tetrapods than in the reference bulk ZnO (0.5 ns).[144] Zhong also reported that PL decay time for ZnO TPs is 17.3 ns for the one-photon excitation case and 16.7 ns for the two-photon case.[145]

Zhang et al. designed ZnO TP-based multiterminal sensors for light detection. Different from double-terminal sensors, these sensors can give multiple responses to a single signal at the same time, which is helpful for weak signal measurements of nanodevices. Tests to detect light with different wavelengths with these structures indicated that they are sensitive to UV light and have a possible advantages in distinguishing authentic signals from noises and enhancing sensitivity.[138]

1.3 1D Core-shell Nanowires

1.3.1 Introduction

Core/shell nanowires or coaxial structures are of particular interest as novel class of nanomaterials that are characterized by a radial variation in composition and microstructure. The first radial core-shell structure, silicon and germanium core–shell and multishell nanowire heterostructures, were synthesized by Lieber's group in 2002.[146] The process consisted of the axial growth of the core nanowires based on VLS mechanism, and the shell growth based on homogeneous vapor deposition, which has been used widely to fabricate core-shell nanowires. Other popular technologies developed later include

thermal vapor deposition (TVD), atomic layer deposition (ALD), molecular beam epitaxy (MBE) and pulsed laser deposition (PLD). [147-152] Modifications to usual nanowire synthetic routes have allowed the realization of more complex core-shell nanowire systems, including GaN/GaP, GaN/InGaN, GaAs-$Ga_xIn_{1-x}P$, and metal oxides such as SnO_2/In_2O_3 and MgO/transition metal oxide.[153-158] The core and shell of the materials may be composed of metal, metal oxide, organic, inorganic, organic-inorganic hybrid, polymeric or dendritic nanoscale constituents. For example, organic-inorganic nanocomposites employ a strategy to combine the mechanical flexibility, optical properties, and electrical properties of conducting polymers with the high electrical conductivity and magnetic properties of metals.[159-163] These assembles not only provide a means for nanowires to avoid contamination or oxidation on the surface, but also reduce the impact of surface effects by packaging the very large surface-to-volume ratio of the nanowire core with a different shell. Various functions introduced to these core-shell structures expand extensively the field of potential applications such as field-effect transistor, solar cells, light emitting diodes, high electron mobility devices, and memory devices.[164-170] With surface modification, some distinct electronic properties are approached such as high mobility carrier transport, tunable band gaps, nonlinear optical gains, and giant magnetoresistance.[171-174]

1.3.2 Core-shell nanowire applications to solar cells

Work concerning p-n junction applications for solar cells in early stages indicated

that inexpensive candidate materials for use in photovoltaic applications generally have either a high level of impurities or a high density of defects, resulting in low minority-carrier diffusion lengths.[175] In solar cells, minority carriers excited by light is increased above that at equilibrium, the excess minority carriers will decay back to the equilibrium carrier concentration due to recombination processes.[176] The recombination rate is a critical parameter in a solar cell which depends on the number of excess minority carriers, and characterized by minority carrier lifetime τ and diffusion length L of a material. τ is the average time that a carrier can spend in an excited state after electron-hole generation before it recombines, and L the average distance a carrier can move from point of generation until it recombines, respectively.

The minority carrier lifetime and the diffusion length depend strongly on the type and magnitude of recombination processes in the semiconductor. For many types of silicon solar cells, the recombination rate will depend on the number of defects present in the material, and a doped semiconductor has a higher recombination rate because defects in the crystal act as recombination centers, reducing minority-carrier diffusion length (L) in the solar cell.[175] The diffusion length is related to the carrier lifetime by the diffusivity according to the following formula: $L = \sqrt{D\tau}$, where D is the diffusivity in m²/s.[176] For example, the lifetime can be as high as 1 ms in silicon, and the diffusion length is typically 100-300 μm for a single crystalline silicon solar cell.

These two parameters give an indication of material quality and suitability for solar cell use. A study of thin film polycrystalline silicon solar cells indicated that to achieve

17% conversion efficiency at a cell thickness of around 10 μm, an internal reflectance of more than 90% and minority-carrier diffusion length of 70 μm are necessary.[177] Additionally, efficient light trapping is necessary to attain high efficiency. Increasing the thickness of the base in film cell will therefore produce more light absorption but will not result in an increase in device efficiency. In the absence of sophisticated light-trapping schemes, materials with low diffusion lengths and low absorption coefficients therefore cannot be readily incorporated into planar solar-cell structures with high energy-conversion efficiency.

However, core/shell architectures exhibit a promising solution to these problems. An advantage of this structure is that carrier separation takes place in the radial versus the longer axial direction, with a carrier collection distance smaller or comparable to the minority carrier diffusion lengths. Atwater et al. found that radial p-n junction Si and GaAs nanorod cells tend to favor high doping levels to produce high cell efficiencies.[177] Although high doping will lead to a decreased charge-carrier mobility and a decreased depletion region width, high doping advantageously increases the built-in voltage (the internal or built-in potential across a solar cell is usually described as an upper limit to the open-circuit voltage of the cell under illumination).

Through tailoring the size of nanorods, carriers can traverse the cell even with low diffusion lengths. A theoretical study shows that the energy conversion efficiency reaches a limiting value as the thickness increases in the planar case.[176] In contrast, the efficiency of the radial p-n junction nanorod attains a maximum as a function of

thickness—if the thickness is increased further, the efficiency is reduced. These differences cause that extremely large efficiency gains from 1.5% to 11% are possible in silicon with very low diffusion lengths (L=100 nm).[176] The first solar cells based on nanorods were reported by Huynh et al. in 2005.[178] A photovoltaic device consisting of 7 nm by 60 nm CdSe nanorods and the conjugated polymer poly-3(hexylthiophene) was assembled from solution with an external quantum efficiency of over 54% and a monochromatic power conversion efficiency of 6.9% under 0.1 mW/cm^2 illumination at 515 nm. Under Air Mass (A.M.) 1.5 Global solar conditions, a power conversion efficiency of 1.7% was obtained. [178]

According to ASTM G173-03 and IEC 60904-3 international standards, air mass is used to evaluate how far light travels through the Earth's atmosphere. One air mass (AM1) is the thickness of the Earth's atmosphere. Air mass zero (AM0) describes the solar irradiance in space without the impact of the atmosphere. The power density of AM1.5 light is about 1,000 W/m^2 and 1,360 W/m^2 for AM0 light, which is considered to be the solar constant. In the photovoltaic test, the Standard Test Condition (STC) is defined as an insolation of 1000 W/m^2 (1 SUN) at 25 °C and with a solar spectral distribution equivalent to global AM1.5.

Peidong Yang's group used ZnO nanowire arrays to build a dye-sensitized solar cell and observed a full sun efficiency of 1.5%.[119] Later, they constructed ZnO/Al_2O_3 and ZnO-TiO_2 core-shell nanowire dye-sensitized solar cells by an ALD shell coating process.[179] It was found that TiO_2 shells (10-25 nm in thickness) cause a dramatic

increase in cell open-circuit voltage (VOC) and fill factor with little current fall off, which results in a substantial improvement in overall conversion efficiency, up to 2.25% under 100 mW/cm^2, AM 1.5 simulated sunlight.[179] The better performance of the ZnO-TiO_2 core-shell nanowire cells is a result of a radial surface field within each nanowire that decreases the rate of recombination in these devices.

More recent the combination of p-n heterojunction and nanowires has attracted attention. Lieber's group fabricated successfully p-type/intrinsic/ n-type (p-i-n) coaxial silicon nanowire solar cells.[163] Under AM 1.5 solar equivalent illumination, the p-i-n silicon nanowire elements yield a maximum power output of up to 200 pW per nanowire device and an apparent energy conversion efficiency of up to 3.4%, with stable and improved efficiencies achievable at high-flux illuminations (compared with organic and dye-sensitized solar cells).[180] It is the first individual photovoltaic nanodevice that can serve as a power source to drive functional nanoelectronic sensors and logic gates.

1.4 Porous Semiconductor Materials

1.4.1 Introduction

Most materials are to some extent porous. The control of porosity possesses significant industrial importance in the design of catalysts, industrial adsorbents, membranes and ceramics due to their effects on material properties such as density,

thermal conductivity and strength.[181] Porous materials can be classified by many methods. For example, the pores can be described as closed pores (ⓐ in Fig 11) and open pores (ⓑⓒⓓⓔand ⓕ in Fig 11) according to their availability to an external fluid. Different from the roughness of the external surface (ⓖ), *funnel*-shaped pores (ⓓ) or *slit*-shaped pores have irregularities that are deeper than they are wide.[181] According to pore size, porous materials can be defined by micropores (<2 nm), mesopores (2~50 nm) and macropores (>50 nm).

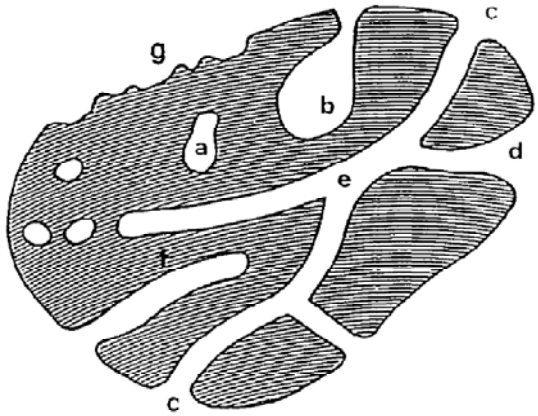

Figure 11. The schematic cross section of a porous solid. (adapted from ref. 181.)

Mesoporous materials have received great attention from both academia and industry because of their potential applications in various fields, such as bionanotechnology,[182-184] separation,[185, 186] catalysts[187, 188] and microelectronics.[189, 190] Perhaps due to their use in industrial applications, the development of mesoporous materials was highlighted by the early application and synthesis of zeolites as catalysts in 1950's and the preparation of

mesoporous silica with uniform pore size distribution from the layered polysilicate kanemite first reported by Kuroda and coworkers in 1990.[191-193]

An interesting parallel development timetable could be seen in porous semiconductor materials. Porous semiconductor structures were first produced by Uhlir at Bell Labs in 1950 on Si and Ge.[194] The field of porous semiconductors received a significant boost in 1990 when light emitting porous silicon was discovered by Canham.[195] Since then, significant progress has been made on the studies of the structural, optical, mechanical and electrical properties of porous semiconductors, which are critical to future applications such as optics, solar energy, and drug delivery/biosensing platforms.[184, 196-199] For example, aside from the common properties presented by mesoporous materials (including size tunability and surface modification), porous Si ($p>70\%$) dissolves completely in all simulated body fluids (SBFs), except in the simulated gastric fluid. The porous Si with medium porosity ($p<70\%$) is bioactive and slowly biodegradable, and the very low porous Si and macroporous Si are both quite bioinert materials similar to ordinary crystalline Si.[200, 201] Such a distinct biocompatibility continues to attract great attention for using porous Si in drug delivery.

1.4.2 Fabrication of Porous Semiconductors by Electrochemical Anodization

Porous semiconductors, including Group IV (Si and Ge), II-VI (CdTe, ZnTe, and CdS) and III-V (GaAs, InP, GaP, InSb, and GaN), have been fabricated by numerous physical and chemical methods,[202] such as anodic dissolution,[203] photochemical

etching,[204] chemical etching,[205] cathodic etching,[206] pulsed anodic etching,[207] vapor etching[208] and electroless etching.[209] Among them, electrochemical anodization is the most conventional processes because of the cost effectiveness and equipment required. In the most intensively investigated electrochemical anodic system, porous Si fabrication, the basic method is electrochemical dissolution of Si in HF based solutions. This is obtained by controlling either the anodic current (galvanostatic) or voltage (potentiostatic). In general, constant current is preferable as it allows better control of the porosity and thickness from sample to sample. In the simplest setup to fabricate porous semiconductors (top down), the target material (wafer, positive pole) and Pt (negative pole) are dipped into etchant as two electrodes and an etching current is applied between them. The porous layer is formed on the surfaces of a target wafer. Usually ethanol is added to the electrolyte to reduce formation of hydrogen bubbles and to improve the electrolyte penetration in the pores and, thus, uniformity of the PSi layer.[210]

1.4.3 Electrochemical anodization mechanism in porous Si fabrication

Hu and Kerr observed that the oxidation of the Si must be the rate-controlling step in the HF chemical etching with SiO_2 being removed as fast as it is formed.[211] The silicon surface is virtually inert against attack of hydrofluoric acid at low pH values, except that H^+ makes it H-terminated, which corresponds to low OH^- concentrations. Zhang et al. observed the presence of three regions depending on working potentials in the anodization of Si in HF as shown in Fig. 12,[212] namely pore formation, transition and

electropolishing regions. The electrochemical reaction at the interface is the rate limiting step in the PS formation region, while dissolution of SiO_2 is the rate limiting step in the electropolishing region. A model was constructed with two control reactions: SiO_2 formation by the reaction of H_2O and Si ion, and Si direct dissolution in HF. Thereby PS forms when the direct dissolution of Si by HF predominates. In electropolishing, the Si surface is completely covered by hydride species.

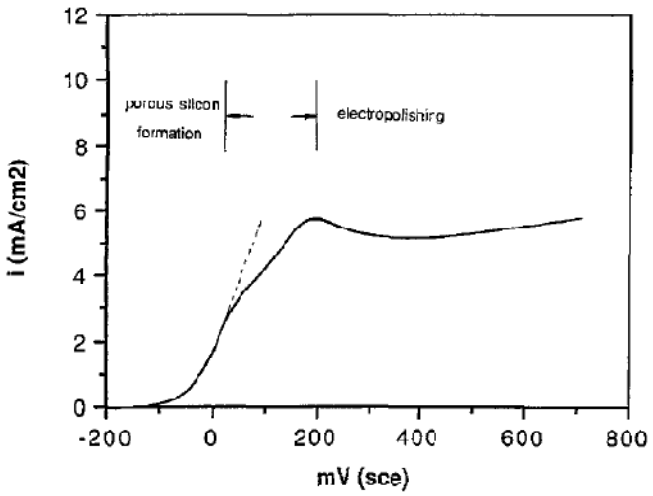

Figure 12. Current-potential curve of p^+ silicon sample in 1% HF solution with potential sweep rate of 2 mV/s. (adapted from ref. 212.)

Lehmann and Gösele demonstrated a mechanism for Si dissolution in HF as shown in Fig. 13.[203] For PS formation, a silicon surface saturated by hydrogen[213] is virtually inert against further attack of fluoride ions as long as no electronic holes (h^+) are available at the silicon electrode because the electronegativity of H is about that of Si and

the induced polarization is low. If a hole (h^+) reaches the surface, nucleophilic attack on Si-H bonds by fluoride ions can occur and a Si-F bond is established (step 1 in Fig. 13). Due to the polarizing influence of the bonded F, another F^- ion can attack and bond, causing generation of an H_2 molecule and injection of one electron into the electrode (step 2). Due to the polarization induced by the Si-F groups, the electron density of the Si-Si backbonds is lowered and these weakened bonds will now be attacked by HF or H_2O (steps 4 and 5) in a way that the silicon surface atoms remain bonded to hydrogen (step 5). If a silicon atom is removed from an atomically flat surface by this reaction, an atomic size dip remains. This change in surface geometry will change the electric field distribution in such a way that hole (h^+) transfer occurs at this location preferentially. Therefore, surface inhomogeneities are amplified. It has been shown that pores of about 1 μm will establish in a few minutes on polished n-type silicon surfaces by this process.[203] If the walls between the pores are depleted of holes (h^+), they will be protected against dissolution. Furthermore, the side wall of pores being prevented from dissolution is attributed to quantum confinement, which leads to an effective band gap increase in the etched narrow walls. Such a barrier to additional hole injections into this nanoscale region is energetically disfavored.

As a semiconductor with an indirect bandgap, the discovery of room-temperature visible PL from PS attracted interest in the optical properties of Si and opened a long-running debate on the origin of photoluminescence (PL) from porous Si. Although the quantum confinement effect can explain the PL phenomena in the visible light range

and has been widely acknowledged, some contradictions exist between its predictions and a number of experimental results.[214-216] The surface to volume ratio in light-emitting Si nanostructures becomes important. Thus the surface chemistry can have a significant effect on their electronic structure and optical properties, in addition to quantum confinement effects.[217] Numerous experiments have been done to investigate the impact of the crystalline structure and experimental conditions on the PL of PS, sometimes accompanied with chemical/physical surface modification.[218-228]

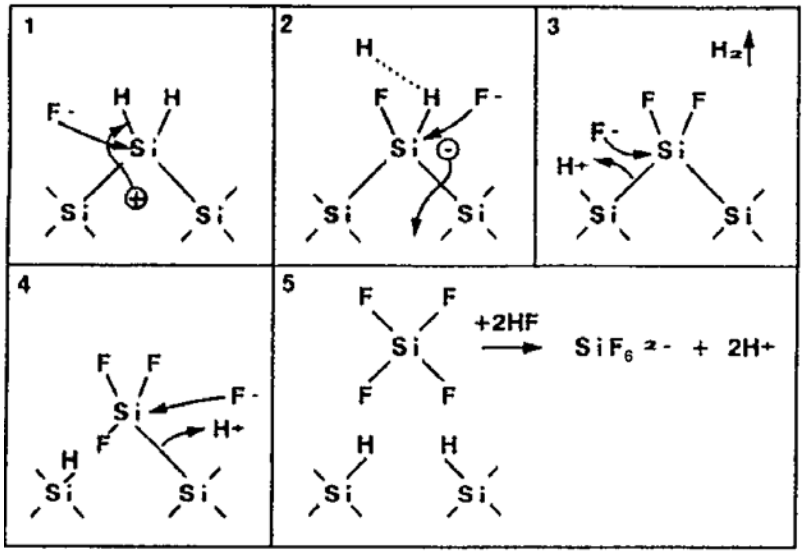

Figure 13. Anodic etching mechanism of silicon electrodes in hydrofluoric acid (HF) associated with PS formation. (adapted from ref. 213.)

1.4.4 Porous Ge fabrication

As the only semiconductor that shares some rather special characteristics with Si, much less work has been done for the fabrication of porous germanium (PG) in an anodic

process, when compared with PS.[229-237] The main reason leading to the effective replacement of Ge by Si as the leading element in semiconductor industry since 1960s is that Ge oxide is chemically unstable in contrast to SiO_2. In recent years, transistor structures incorporating some Ge alloy phase as a part of Si-based microelectronics are attracting increasing interest.[229] This is a consequence of Ge's enhanced carrier mobility and faster operation speed.

Bayliss et al. obtained PG by anodizing (111) p-type Ge wafer in HF/H_2O/ethanol (i.e. 1:2:1) solution for 10 min.[237] The PL maximum of PG was observed at ~730 nm. Choi and Buriak used a much milder etchant (1:1.8 of 48% HCl+EtOH v/v) to anodize (100) Ge wafers and obtained H-terminated PG with weak red light emission by involving a cathodization process after etching.[230] Kartopu et al. observed PG light emission at ~1.55 eV (800 nm) by anodizing n-type (100) and (111) Ge wafers in HF:H_3PO_4:H_2O_2 etching solution.[234] Föll et al. investigated systematically the impact of various etchants (HBr, HF, HCl, H_2SO_4 and other mixture solutions) on the pore morphology of PG formed in the process. Pores could be produced in all cases under optimized conditions, and HCl based electrolytes performed best.[229, 233] In HCl, H_2O and dimethylsulfoxide (DMSO) electrolyte, PG was obtained from both n- and p- type Ge anodization, although uniform pore nucleation in Ge is far more difficult than in most other semiconductors. They suggested that a rather large "leakage" current flowing through pore walls and all other surfaces results in "electropolishing" on top of the pore etching, which not only tends to make pores conical in shape, but also destroys the

original surface, often leaving a rough surface. However, if a dense array of pores could be achieved, pore walls were more stable, most likely because they only contained the space charge region (SCR) and thus no free carriers.

1.4.5 Disagreements involving pore formation in anodic etching

The PL mechanism is not the only controversial problem involving porous Si and Ge. A few points are listed below:[238-248]

Porosity formation and electropolishing: As mentioned above, the formation of porous silicon occurs when the current that flows through the interface is below a certain critical value, whereas above this critical value electropolishing prevails. Despite its importance, however, even the basic issue of why there is a transition from porous silicon formation to electropolishing is unresolved.[242] So far, there is no universal agreement among the pore nucleation and growth mechanisms proposed.

Pore arrays: The formation of an array of pores with submicrometer cross section in the single-crystal semiconductor-anode bulk was observed for the first time in studies of the electrochemical etching of silicon in hydrogen fluoride solutions.[240] Much later, pore arrays were found in other metal and semiconductor anodization with various electrolytes. All existing mechanisms are based on macroscopic consideration of the analyzed processes and follow from the assumption of the identity of chemical mechanisms of pore formation and anodic dissolution of semiconductors. Theoretical analysis of the kinetic equations describing the electrochemical etching of silicon have

only made it possible to show the feasibility of the existence of conditions causing the instability of the planar electrolyte – semiconductor interface to weak periodic perturbations of a profile with a density close to the actual pore density.[242,243] Considering pore arrays leading to the spontaneous formation of a complex spatial structure, Ulin and Konnikov attributed such arrays to a wide class of self-organization phenomena inherent to irreversible nonlinear processes in open systems far from the thermodynamic equilibrium state.[240] Without the need for direct involvement of free holes in electrochemical processes (like in Fig. 13), they introduced a mechanism about using an electric field to initiate matched nucleophilic substitution reactions between anions chemisorbed and atoms in the interface.[240] Such a reaction is accompanied by only partial dissociation of initial bonds in the crystal. The dissociation is controlled by the intermediate complex structure and in turn controls the preferential etching direction. Once the reaction is initiated, it can continue preferentially due to higher thermodynamic probability than other inactive surfaces, which results in pore arrays.

Voltage/Current oscillation: In the process of electrochemical anodization, the normally stable I-V relationships exhibit anomalous, but well-defined, current (potential) oscillations. The oscillations used to be correlated solely to the electropolishing regime, while stable oscillations may have been summarily dismissed as bubble formation or noise. However numerous references to "unstable" electrochemical behavior have been reported in the pore formation region.[248] For example, strong visible oscillating light emission was observed that is correlated with current oscillations during electrochemical

GaP pore etching in HF and HBr electrolytes,[246] which has been attributed to a direct coupling between electron transfer at the semiconductor–electrolyte interface and the light emission mechanism.

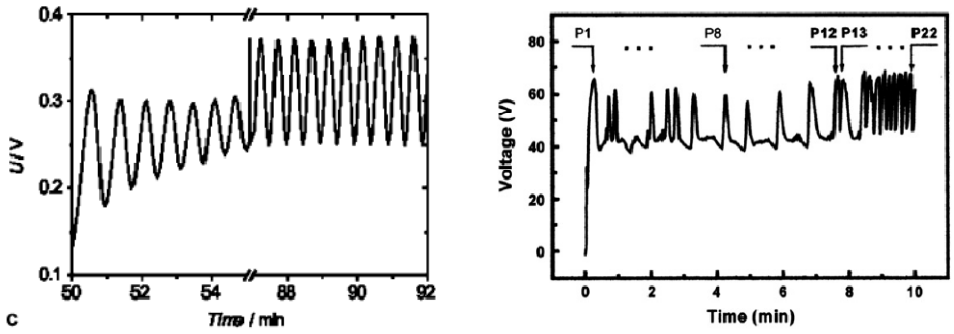

Figure 14. Voltage oscillations in the anodization process for: (left) PG in 5% HCl / DMSO electrolyte (adapted from ref. 229.) and porous InP in HCl. (adapted from ref. 249.)

A number of papers deal with the investigation of current oscillations in PS anodization, which is supposed to be strongly coupled to the growth of the silicon oxide on the surface of the electrode.[244] Föll et al. put forth a mechanism to explain such oscillations (Fig. 14). In the current ‘‘burst’’ model, local current flows start as soon as the local field strength is high enough: the current ‘‘bursts’’. They induce direct Si dissolution or oxidation and stop. The oxide is then chemically dissolved and the cycle starts again. Since the Si exhibits a high reactivity just after dissolution, the next current ‘‘burst’’ will likely take place at the same locations. However the H-termination induces a surface passivation and hampers further ‘‘bursts’’ until it reaches a situation similar to the one before the first event. The H-termination is thus the main synchronizing force

because it correlates with the nucleation phenomena. The second reason for the phase locking between pores at high pore density is the overlapping of the space charge regions surrounding each pore. This model has been extended to III-V semiconductors.[202, 244]

1.5 Electrospinning

Among the various nanostructures that have recently been developed for use in practical applications, nanofibers have received increased attention in the last 20 years.[250-253] Electrospinning significantly contributes to this advance through providing a cost-effective and reliable process to fabricate nanofibers with the ability to control their compositional, structural and functional properties. In electrospinning, polymer nanofibers may be obtained by the application of a strong electrical field (e.g. 20 kV) between a grounded target and a polymer solution that is pumped from a storage chamber through a small capillary orifice (Fig. 15). Fibers are collected as a non-woven mesh or membrane on a collector plate that acts as the counter electrode. The fibers range in diameter between 10 and tens of micrometers depending on the solution and the process conditions.

Theoretically, electrospinning was divided into three distinct sections in fiber formation, namely the Taylor cone formation, the thinning stage, and the drying of the fiber.[254] To a drop in the end of syringe, the drop surface and shape may have variety of situations with the interaction of gravitational forces and interfacial forces (surface

tension) and electrostatic forces. To form a Taylor cone, there is a force balance to the drop where gravity and electric polarization stress tend to elongate the droplet from within, aided by tangential electric stress on the cone surface (Fig. 16).[254] Viscous drag

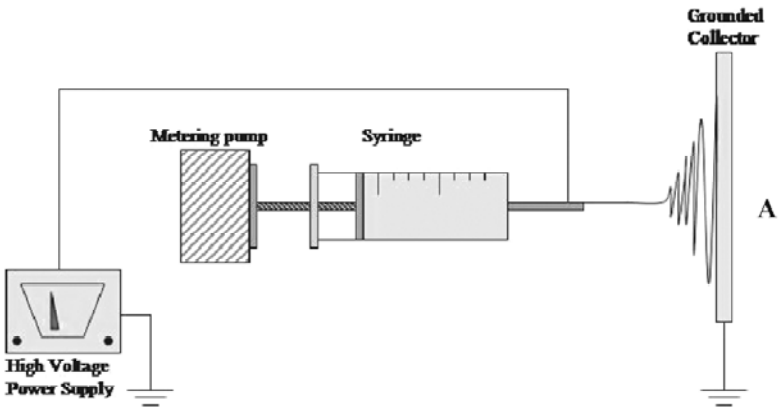

Figure 15. Schematic illustration of laboratory scale electrospinning setup. (adapted from ref. 250.)

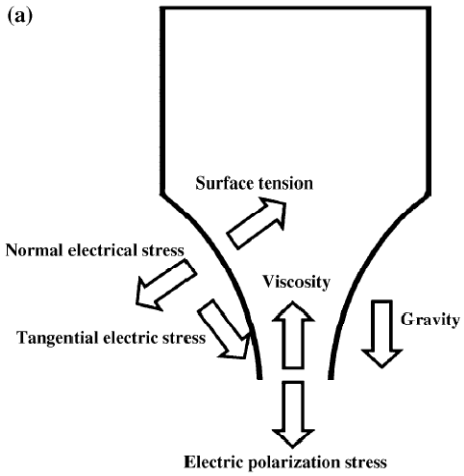

Figure 16. Schematics of the forces on a droplet at the end of a syringe from gravity, surface tension, and electrostatic forces. (adapted from ref. 254.)

slows down the formation of the cone. In addition, there are two more forces active on the surface of the droplet/forming cone. These are the surface tension that tries to minimize the surface area pulling the surface vertically in and an opposing force which is the normal electrical stress that tries to maximize the distance between electrical charges on the surface by enlarging the surface area.[254]

When the electric field is large enough, the droplet is deformed into the Taylor cone. As soon as the electrostatic repulsive forces overcome the surface tension, a fine charged jet is ejected that is typically 1/100 in diameter of the needle opening. After leaving the cone this jet then moves toward the counter electrode. During the traveling time the jet will become unstable. In this second stage, there are a total of three possible instabilities: one, where droplets are formed, which is referred to as Rayleigh instability; two, where swollen structures are visible, which is referred to as axisymmetric instability; and three, where a non-axisymmetric bending of the fiber occurs. This last bending instability is the most important one that needs to be achieved, as it is responsible for thinning the fibers from about a micron into the nanometer range.[255]

Nanofibers with extremely small diameters are of large surface-to-mass ratio, high porosity, and superior mechanical performance (dependent on composition). Moreover, the fiber can be functionalized by locating molecules at the surface of the fiber thus satisfying the engineering requirement by tailoring the fiber surface compositions and morphologies. This has led to diverse applications of nanofibers in tissue engineering, wound healing, drug delivery, medical implants, dental applications, biosensors,

military protective clothing, filtration media, and other industrial applications.[254] Table 1 reveals a broad set of ceramic systems synthesized by electrospinning.

Table 1. A List of Inorganic Oxides Derived from Electrospinning (adapted from ref. 254.)

Ceramic	Precursor	Comments
Al_2O_3	1. Aluminum di-sec-butoxide ethylacetoacetate 2. Ethanol 3. HCl	Aged sol; α-Al_2O_3 formed
GeO_2	1. Germanium isopropoxide 2. PVAC 3. Acetone	Sol–gel; α-quartz like structure
Mn_2O_3–Mn_3O_4	1. Manganese acetate 2. PVA	Sol–gel; calcination controlled phase formation
Co_3O_4	1. Cobalt acetate 2. PVA	Sol–gel
Nb_2O_5	1. Niobium ethoxide 2. Acetic acid in ethanol 3. PVAC	Sol–gel
TiO_2	1. Titanium butoxide 2. P-123 ($EO_{20}PO_{70}EO_{20}$) (BASF) 3. HCl	Sol–gel; mesoporous fibers
NiO/ZnO	1. Nickel acetate 2. Zinc acetate 3. PVA	Sol–gel; two phase ceramic Fibers
PVP–TiO_2	1. Ttitanium isopropoxide 2. Acetic acid 3. PVP 4. Mineral oil	Sol–gel; remove mineral oil to get hollow fibers; removal of PVP by calcinations makes hollow anatase nanofibers
SnO_2	1. $C_{22}H_{44}O_4Sn$ 2. PEO 3. $CHCl_3$	Sol–gel
TiO_2	1.Titanium isopropoxide 2. Polystyrene 3. DMF–THF 4. PVP	Sol–gel; highly porous rutile nanofibers
La_2CuO_4	1. Lanthanum nitrate 2. Copper (II) nitrate 3. PVP	Co-precipitation
SiO_2	1. Tetraethylorthosilicate 2. Ethanol 3. HCl	Sol–gel
$BaTiO_3$	1. Barium acetate 2. Titanium isopropoxide 3. PVP 4. Ethanol 5. Acetic acid	Sol–gel

PVP, poly(vinyl pyrrolidone); PVA, poly(vinyl alcohol); PEO, polyethylene oxide.

Table 1. (continued)

Ceramic	Precursor	Comments
$NiFe_2O_4$	1. Iron (II) ethylhexano isopropoxide 2. Nickel ethylhexano isopropoxide 3. Acetic acid+PVP	Sol–gel; glove box; hydrolysis after spinning
Fe_3O_4	1. Iron (II) chloride+iron (III) chloride+graft copolymer 2. PEO or PVA	Initial co-precipitation reaction; no polymer burnout
$Pb(Zr_{0.52}Ti_{0.48})O_3$	1. Zirconium propoxide 2. Titanium isopropoxide 3. Lead (II) ethylhexaonate 4. Xylene only	E-spin from precursors only; hydrolysis from atmosphere
$MgTiO_3$	1. Magnesium ethoxide 2. Titanium isopropoxide 3. 2-Methoxyethanol in N_2 4. Polyvinylacetate in DMF	Sol first, then polymer addition
$NiTiO_3$	1. Nickel acetate 2. Ethanol 3. HNO_3 4. Titanium isopropoxide 5. Polyvinylacetate in DMF	Sol first, then polymer addition
Al_2O_3–B_2O_3	1. Aluminum acetate 2. Boric acid (1 g) 3. PVA	Hydrolyzed in PVA; 5 h ageing before spinning
CeO_2	1. Cerium nitrate 2. PVA	PPT (co-precipitation)
ZrO_2	1. Zirconium oxychloride 2. PVA	Sol–gel

1.6 Erbium photoluminescence

Erbium (^{68}Er) is a rare earth element with an electronic configuration of [Xe] $4f^{12}$ $6s^2$. As an ion, erbium usually loses one 4f electron and both of the 6s electrons to form Er^{3+} whose electronic configuration is [Xe] $4f^{11}$. The 11 4f electrons are shielded from the surrounding matrix by closed 5s and 5p shells, resulting in rather sharp optical intra-4*f* transitions at 1.54 μm ($^4I_{13/2} \rightarrow {}^4I_{15/2}$) in Er-doped materials.[256] This is an important telecommunication wavelength since standard silica-based optical fibers have their maximum transparency at this wavelength.

Since the absorption cross section（the ability of a molecule to absorb a photon of a particular wavelength and polarization）of Er^{3+} ions for stimulated emission are very small (typically on the order of 10^{-21} cm^2), concentrations of 10^{19}-10^{20} Er/cm^3 are required to achieve a reasonable gain over a length of a few centimeters.[257] However, high concentration of Er^{3+} ions can also cause other problems, such as excitation migration and non-radiative quenching, due to the complicated PL mechanism of Er^{3+} ions.

Generally, Er^{3+} ions generate light emission by direct excitation of erbium ions and/or carrier-mediated excitation of erbium ions that is assisted by a sensitizer. [258-261] In the direct excitation process, Er^{3+} ions are excited to the corresponding energy level and then relax to first excited energy level ($^4I_{13/2}$) via a series of nonradiative multi-phonon emissions (an Auger process). Er^{3+} PL at 1.54 μm results from the subsequent transition from $^4I_{13/2}$ to $^4I_{15/2}$ (the ground state) as shown in Fig. 17a.[260] In this mode, the pump efficiency is closely related to the wavelengths of the optical excitations.

In carrier-mediated excitation mode shown in Fig. 17b,[260] host materials absorb incoming pumping photons to form free excitons, that could be traped at Er-related defects (through Auger process) to form bound excitons. These bound excitons further lower their energy through an Auger relaxation process and then excite Er^{3+} ions from the ground state to the first excited state ($^4I_{15/2} \rightarrow {}^4I_{13/2}$) via energy resonance, which contributes to Er^{3+} PL at 1.54 μm in a radiative relaxation.[260] For example, Yb^{3+} ions can be introduced into the Er doped waveguide. The Yb ions have a large absorption cross-section around 980 nm, and can transfer their energy non-radiatively to the $^4I_{11/2}$ erbium level.[257]

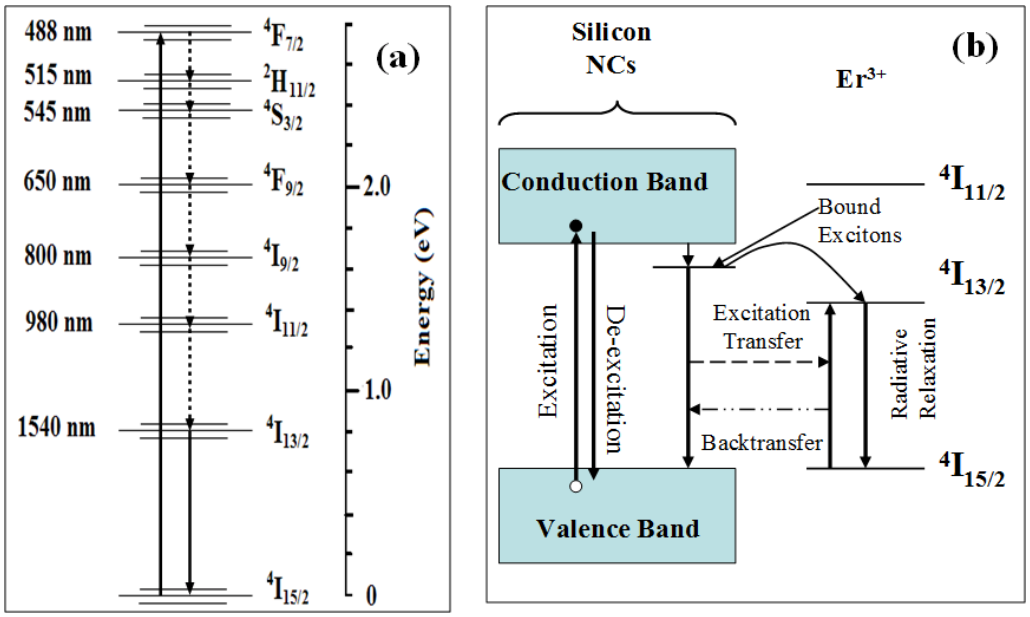

Figure 17. Schematic diagrams of (a) direct excitation of erbium ions excited by 488 nm laser; and (b) carrier-mediated excitation of erbium assisted by sensitizer of Si nanocrystals. (adapted from ref. 260.)

At high erbium concentrations, other excitation processes can happen in Er ions. An Er^{3+} ion at the first excited state can de-excite by transferring its energy to a neighboring Er^{3+} ion at the first excited state, resulting in the neighboring erbium ion to be excited to a higher energy level, namely cooperative up-conversion, which can cause the decrease of the PL intensity at 1540 nm.[257] In another model, excited state absorption, an excited erbium ion absorbs an incoming photon, and is further excited to higher energy level, which can also greatly limit the optical gain of the Er^{3+} PL intensity.[257] Moreover, an excited Er ion can transfer its energy to a nearby, unexcited Er ion. Such an excitation migration does not necessarily reduce the Er population density, but can become detrimental to the gain if some Er ions are strongly coupled to non-radiative quenching sites.[257] Therefore, the host materials must have a high solubility for erbium ions; otherwise Er ions will precipitate from the host matrix resulting in the decrease of the Er-related PL intensity. This requirement is based on a direct excitation of erbium ions. In the case of carrier-mediated excitation of erbium ions, the concentration can be much lower while a reasonable PL intensity is achievable.

Due to the intricate electronic structure, Er-doped semiconductor materials have many interesting optical phenomena. Affected by the electric field in the host, the Stark effect is often observed in the Er spectral lines. Stark splitting is an indicator for symmetry changes of different ligand fields.[261] Higher Stark levels represent a lower symmetry of Er^{3+} sites in the host matrix and higher coordination numbers. Additionally, Er^{3+} is the most popular as well as one of the most efficient ions to generate an upconversion,[258]

which is of great interest in industrial applications such as color displays, optical data storage, biomedical diagnostics, sensors, and undersea optical communications.[259-261]

Erbium-doped semiconductors have been studied widely. Er-doped ZnO films have proved reliable materials for light-emitting diodes, laser diodes, and optical amplifiers operating at 1.54 μm in the waveguide structure as well as electrode materials for carrier injection because of their high electrical conductivity and transparency.[262-264] Er-doped Ge materials have also been studied by many groups. A previous report showed that the oxidation of Ge improves Er PL in the case of Er-doped Ge film without coupling phenomenon observed between Ge and Er atoms.[265] These authors attributed the PL improvement to the enhancement of pumping efficiency resulting from quantum confinement effects and a close energy between Ge excitons and the 1540 nm transition of the Er^{3+} ions. Vergnat et al. reported the probable existence of a non-optical dipole–dipole interaction from Ge nanocrystals to Er^{3+} ions.[266] Moreover, Jensen and Larsen et al assigned an energy transfer between the GeO_x defect states and the Er ions to the increase of Er PL in the study of Er-doped GeO_x because of the disappearance of large band around 800 nm related to GeO_x PL. [267] However, the intensity of Er PL decreased greatly after annealing at 450 °C, when GeO_x is converted to GeO_2 (an insulator).

The Coffer group has been engaged in studies of Er-doped Group IV bulk or nanoscale materials for more than ten years. In 1997, John St. John investigated the luminescence of erbium-doped porous SiO_2 layers by allowing a 10~25 μl solution of the Er salt ($Er(NO_3)_3 \cdot 5H_2O$) to evaporate, followed by spark processing.[268] The Er^{3+} PL was

observed at 1540, 560 and 670 nm, corresponding to the near-IR $^4I_{13/2} \rightarrow {}^4I_{15/2}$, $^4S_{13/2} \rightarrow {}^4I_{15/2}$ and $^4F_{9/2} \rightarrow {}^4I_{15/2}$ visible transitions, respectively. At higher erbium concentrations, self-quenching occurs, probably due to erbium clustering or precipitates. Later, St. John prepared discrete erbium-doped silicon nanoparticles with sizes ranging from 11~15 nm by the co-pyrolysis of the mixture of disilane/He and $Er(TMHD)_3$ (TMHD=2,2,6,6-tetramethyl-3,5-heptanedionato)/He. The near-IR PL intensity is observed to be a sublinear function of the pump laser power, which is the signal of carrier-mediated process in Er^{3+} PL. This work created a method for the fabrication of a wide variety of rare earth-doped Si nanoparticles with tunable emission maxima by the selection of a particular rare earth ion.[269]

J. Ji's work in our group involved the fabrication and characterization of composite films composed of poly(phenylene vinylene) (PPV) and Er-doped Si nanocrystals. It was found that the presence of Er-doped Si nanoparticles in the film strongly impacts the steady-state photoluminescence of the PPV, whereas the presence or absence of solvent chosen for the nanocrystals influences the carrier transport and resultant visible electroluminescence of light-emitting diodes fabricated from these materials.[270]

Z. Wang fabricated Si/Er core-shell nanowires, one of the earliest reported core-shell nanostructures, by a two step CVD method in 2002.[271] Si nanowires were synthesized by the pyrolysis and deposition of SiH_4 at 600 °C for 2 min at a flow rate of 40 sccm, diluted with additional He (3000 sccm). Erbium incorporation was achieved by the CVD of $Er(TMHD)_3$ at a temperature of 600 °C in He carrier gas. After a vacuum

high-temperature anneal, the characteristic near-IR PL associated with Er^{3+} transitions was obtained. The crystalline core-shell nanowires were characterized by HRTEM.

J. Wu first fabricated single crystal GeNWs by evaporating Ge powder in a physical vapor deposition process in 2004 as described in Chapter 1.1.0.1.[66] Modified by Er-doping (5.4~17.9%wt), as-prepared core-shell nanowires exhibited impressive Er^{3+} PL at 1.54 μm. PLE spectra confirmed the presence of a carrier-mediated pathway in Er^{3+} transitions after 600 °C annealing. His later work focused on the fabrication of Er-doped group IV oxide and SnO_2 nanofibers derived from sol–gel/electrospinning methods.[272,273] He found that the PL intensity of Er-doped GeO_2 fibers is almost 10 times stronger than that of Er-doped SiO_2 fibers. The PL of Er_2O_3, Er-doped SnO_2, and Er-doped SiO_2 fibers arises from the direct excitation of erbium ions, whereas a carrier-mediated process is the underlying reason for the erbium photoluminescence in Er-doped GeO_2 nanofibers that are annealed at relatively lower annealing temperatures (<700 °C).

CHAPTER II.

Fabrication and Photoluminescence of ZnO/Er-modified core-shell Ge nanowires

2.0 Overview

As mentioned in Chapter 1, there has been rapid growth in fundamental studies of semiconductor nanowires, which have relevance to the development of new nanoscale electronic platforms as well as biotechnology. GeNWs are of pointed interest because of their charge carrier mobility, but long-term chemical stability of their surfaces is a significant concern. One-dimensional (1D) radial core/shell nanowire heterostructures provide a strategy to not only functionalize nanowires, but also to improve the surface properties.[94,95] Additionally, Er-doped GeNWs possess favorable properties for potential applications in optoelectronics and optics, due to the near infrared $^4I_{13/2} \rightarrow {}^4I_{15/2}$ luminescence transition of this rare earth in a +3 oxidation state.[66] From a broad perspective, the selection of shell materials has to consider the compatibility of core and shell materials, in terms of both chemical reactivity and structural properties of each lattice.

In this chapter, ZnO/Er^{3+} modified Ge core-shell NWs were fabricated by a vapor-liquid-solid (VLS) method for the core followed by different thermal vapor deposition techniques for the shell component. ZnO has been used as host material for Er because ZnO provides erbium with an oxygen coordination sphere, which is helpful for an efficient Er near infrared PL.[274,275] Recall that ZnO itself is a useful wide bandgap semiconductor (3.37 eV) with two types of luminescence peaks, including near-band-edge (NBE) ultraviolet emission and deep-level visible emission.

It is important to note that Zn/ZnO and Ge can form a zinc germanate phase (Zn_2GeO_4) with a relatively larger bandgap (4.68 eV).[276] Use of larger bandgap shell materials is very useful in studies of carrier confinement in core-shell nanostructures. On a fundamental level, it is also important to determine the relative stability of a given core-shell architecture and the corresponding conditions regard for alloy formation and the photophysical properties of each.

Structural characterization was principally achieved by scanning electron microscopy (SEM, JEOL-6100) with an energy dispersive X-ray spectroscopy (EDX) system, high resolution transmission electron microscopy (HRTEM, JEOL-2100), and X-ray diffraction (XRD, Philips-3100).

ZnO photophysical properties were measured using photoluminescence (PL) spectroscopy. The signal was excited by a CW Kimmon IK5452R-E HeCd laser with a wavelength of 325 nm. A variable frequency chopper was employed to provide a reference frequency. The samples were mounted inside an evacuated Janis CCS-150 cryostat having a temperature range between 8 and 325 K. The PL signal was probed by a Spex 1401 monochromator with a spectral resolution of 0.18 cm^{-1} and an RCA C31034 photomultiplier tube detector connected to a Stanford Research-830 lock-in amplifier for a background noise reduction.

The near infrared wavelength PL was measured using an Applied Detector Corp. liquid N_2-cooled Ge detector in conjunction with a Stanford Research Systems

Chopper/Lock-in amplifier and an Acton Research Corp. 0.25 m monochromator. Excitation was provided by a Coherent Ar^+ laser, mainly at 488 nm. A Hummer VII sputtering system (Anatech, Ltd.) or Veeco thermal evaporator was used to deposit Au catalysts onto a given substrate.

2.1 Experimental Methods

2.1.1 Preparation of Ge nanowires

Germanium nanowires were fabricated using a previously-developed approach in our lab.[66] The 5~10 nm Au film is deposited onto selected substrates (5 mm × 15 mm) by sputtering system or thermal evaporation in vacuum (2×10^{-6} MPa). Then an alumina boat loaded with Ge power (Strem) & carbon power (in a molar ratio 1:3) and Au-coated substrates (on another boat) are placed in a 30mm quartz tube reactor with locations as shown in Fig. 18. The Ge source boat is put inside the furnace and the collecting boat is located in a downstream position 1~1.5 cm away from the edge of the tube oven. After 1.5h annealing at 850 °C in 300 sccm He carrier gas, the Ge source is heated to 990 °C for 1.5h. The temperature of the Ge NWs growth is ~560 °C. At the end of the reaction period, a thick brown film can be seen on the substrate.

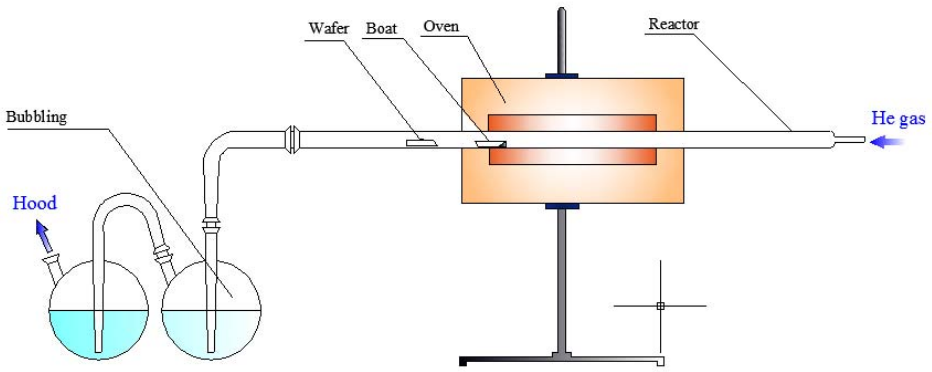

Figure 18. Reactor setup for preparing GeNWs.

2.1.2 Er-doping

Chemical vapor deposition (CVD) was employed to deposit Er onto Ge nanowires. Wafer samples containing Ge nanowires were placed within the quartz reactor located at the middle of the tube furnace (Fig. 19a). Another alumina boat containing an Er precursor (Strem Chemicals, $Er(TMHD)_3$, TMHD=tris(2,2,6,6-tetramethyl-3,5-heptanedionate)) was placed in the upstream position within 5 mm of the edge of the furnace. This Er precursor was sublimed at ~170 °C and entered the furnace (500 °C) with a He gas flow of 300 sccm where it decomposed and deposited onto the Ge nanowire sample.

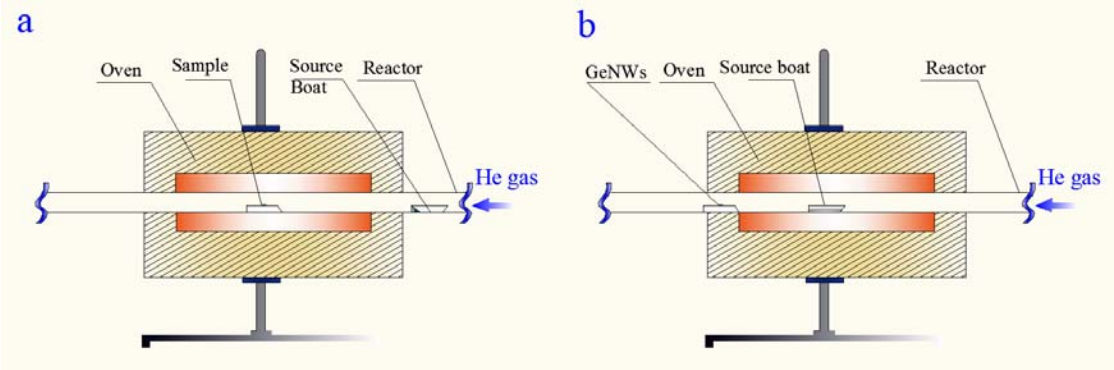

Figure 19. Diagram of (a) Er-doping or Zn deposition with Zn precursor; (b) Zn deposition with Zn granule.

2.1.3 Zn shell fabrication

ZnO shells were formed by initial Zn deposition followed by annealing in O_2. Two different approaches were used, CVD and physical vapor deposition (PVD). In the CVD process, a Zn precursor (zinc acetylacetonate hydrate, Gelest) sublimed at ~140 °C and then decomposed in the furnace (500 °C to form a surface layer onto GeNWs. The experimental setup was the same as that used for Er-doping, as shown in Fig. 19a. In the PVD process, 50 mg of Zn granules (Aldrich, 100 mesh, 99.8%) were evaporated at 440~500 °C in He gas (300 sccm), with the Zn vapor deposited onto the surface of Er-doped or bare Ge nanowires in a cooler region of the reactor as shown in Fig. 19b.

The PL associated with Er^{3+} and ZnO is highly dependent on the annealing condition of ZnO/Er/Ge NWs in oxygen. In this work, Zn-coated GeNWs need to be annealed in O_2 to grow the ZnO shell at a temperature range 600~700 °C, which is also necessary to

obtain a relatively high intensity of Er^{3+} PL.[66,277] This annealing was conducted in a quartz reactor with 50 sccm O_2 flow and a heating rate of 200 °C per hour.

2.2 Results and Discussion

2.2.1 GeNWs prepared with different catalyst and substrates

Fig. 20 shows typical SEM images of GeNWs grown by the vapor transport method described above. In this method, the Au catalyst has a significant impact on the NW structure. When the thickness of sputtered Au film was more than 10 nm or the Au thermal evaporation duration was longer than 60 s, the size distribution became wider. In this case, the GeNWs with big diameters (>200 nm) could be found on the top of GeNW layer as shown in Fig. 20a. Under the conditions utilized, GeNWs catalyzed by thermal-coated Au (Au evaporation duration ~45 s) have more uniform sizes than those NWs produced with sputtering Au as catalyst (Fig. 20b). The diameter of GeNWs on the top was also a little larger than that beneath them. It expected that GeNWs near the top of the film possess a sufficient Ge vapor concentration to expand their sizes, while those

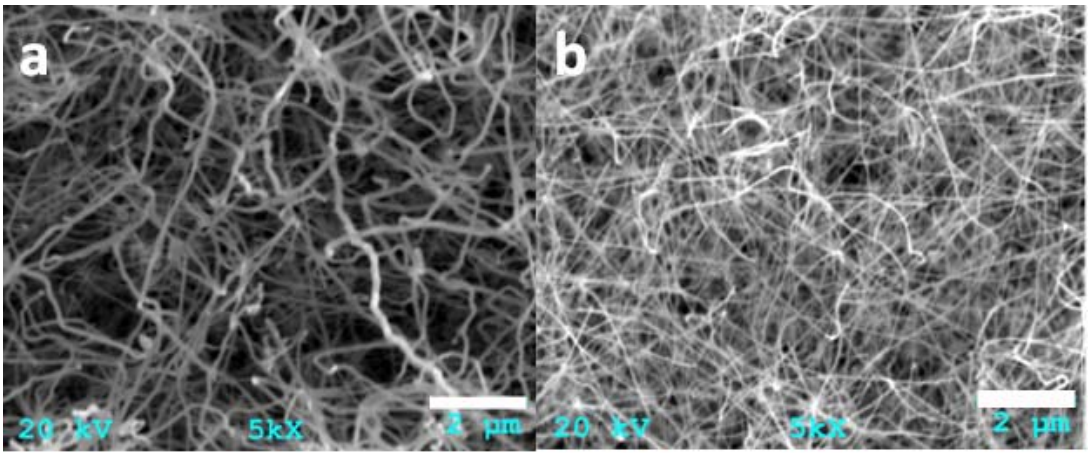

Figure 20. GeNWs fabricated by (a) 10 nm sputtering Au catalyst film. (b) Thermo-evaporated Au catalyst (45s). Scale bars are 2 µm.

close to the bottom of the substrate are inhibited presumably due to mass transfer limitations. Given this consideration, graphite cloth is likely the best open structure for the reactant gas to penetrate. Indeed, GeNWs grown on graphite cloth showed very uniform morphologies (Fig. 21a) with the diameter ranging from 4 nm to 40 nm (much smaller than those grown on Si wafer), perhaps because the round cross-section of graphite cloth fiber limits the Au diffusion on the surface to form small islands. A HRTEM image (Fig. 21b) demonstrates that these GeNWs have high quality crystalline structure, usually with ~3 nm oxide layer. The histogram in Fig. 22 shows that GeNWs have a narrow size distribution if catalyzed by thermal coated Au film on Si or sputtered Au on graphite cloth. GeNWs grown using a sputtered Au catalyst on Si substrates produced a relatively broad size distribution of NWs.

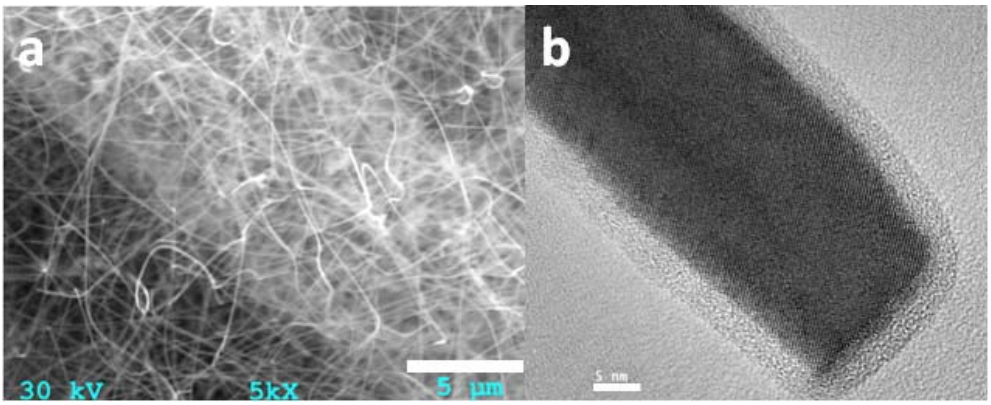

Figure 21. (a) SEM image of GeNWs fabricated on graphite cloth. Scale bar, 5 µm. (b) HRTEM image of a GeNW. Scale bar, 5 nm.

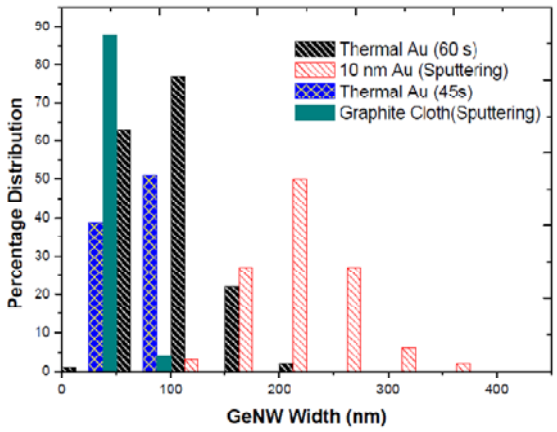

Figure 22. Histogram representing the size distribution of GeNWs grown from different Au catalyst and substrates. The average diameters of GeNWs are 114, 51, 230 and 30 nm, corresponding to samples prepared from Au catalyst thermally evaporated by 60s and 45s, sputtering Au as well as from sputtering Au on graphite cloth, respectively.

2.2.2 The influence of Zn shell source and substrate on Zn/Er/Ge NW morphology/structure: initial SEM analysis

SEM suggests that CVD methods (using a Zn precursor) provide a very uniform surface coating (Figs. 23a,c). There are typically some Zn particles observed on samples

modified by physical vapor deposition (using Zn granule) as shown in Figs. 23b,d. This is attributed to an inhomogeneous dispersion of Zn vapor in the He carrier gas. Small Zn liquid droplets presumably agglomerated to form Zn seeds on Si in low temperature areas of the substrates. These seeds kept growing and then formed some big particles (~8 μm) covered by GeNW network layer. Graphite cloth apparently abated the agglomeration.

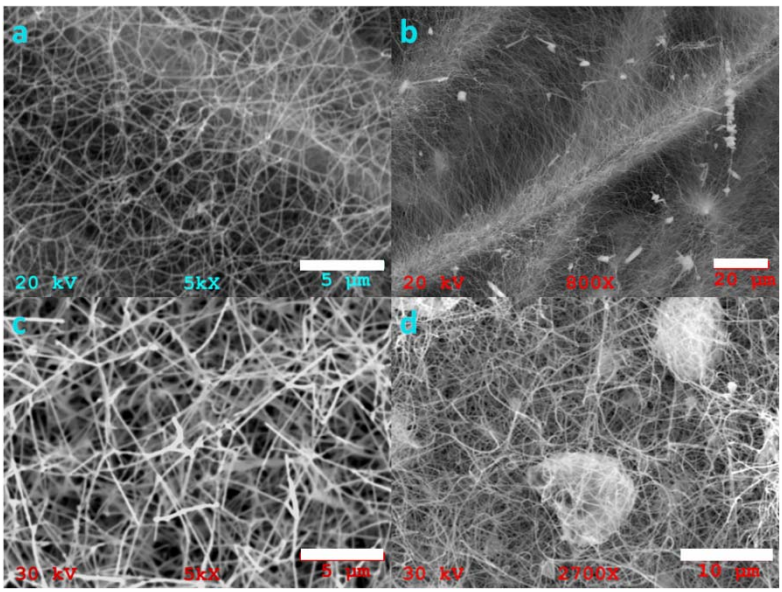

Figure 23. SEM images of Zn/Er/Ge NWs fabricated on (a) graphite cloth, with Zn precursor. (b) Graphite cloth, with Zn granule, (c) Si wafer, with Zn precursor. (d) Si wafer, with Zn granule. Scale bars are 5 μm, 20μm, 5μm and 10μm, respectively.

2.2.3 Zn/Er/Ge NWs Grown on Graphite Cloth

Zn shells by CVD: Examination of the Zn/Er coated GeNWs prepared by CVD by higher resolution TEM images reveals the formation of rough outer surfaces at the

nanoscale (Fig. 24). One possible explanation for these rough surfaces in Figs. 24a,c is that graphite could react with O-containing species generated by the decomposition of

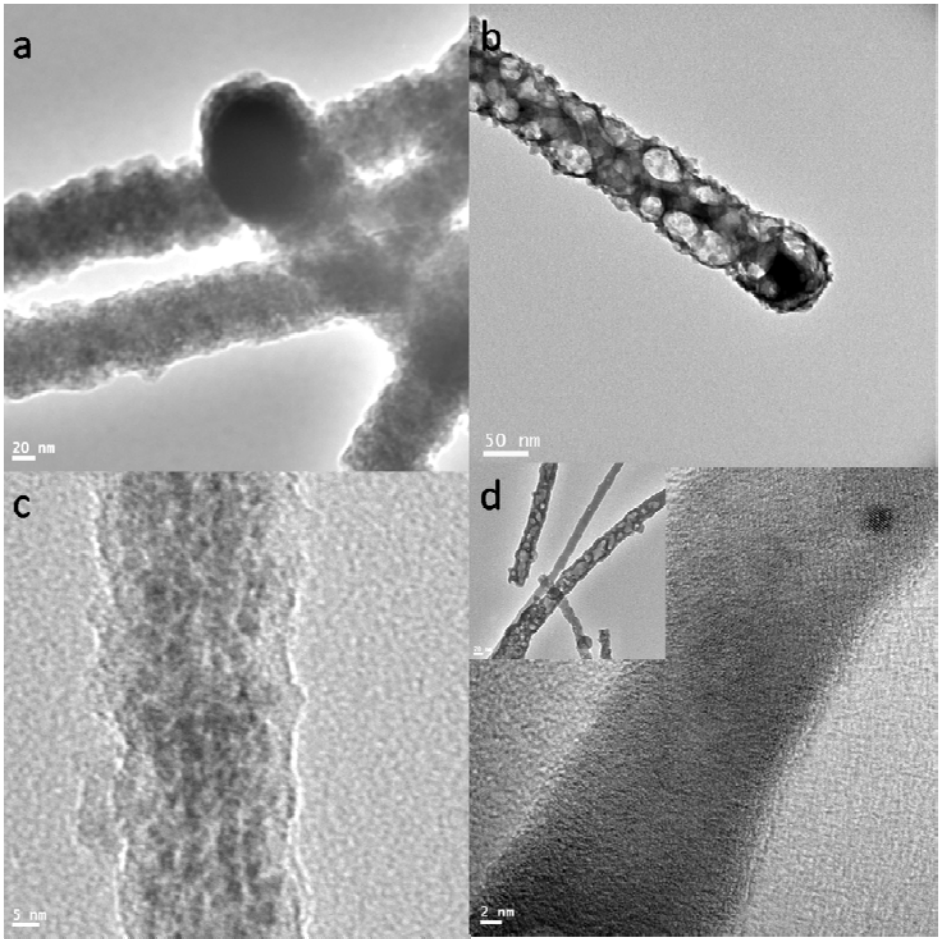

Figure 24. TEM image of Zn/Er/Ge NWs fabricated on graphite cloth with (a) and (b) 20 mg Er precursor and 70 mg Zn precursor respectively; (c) and (d) with 5 mg Er precursor and 35 mg Zn precursor before and after annealing at 700°C for 30 min, respectively. The inset shows a low magnification TEM image of Er/Zn modified GeNWs with a thin porous coating layer.

oxygen-containing precursors, and likely producing CO_2, which would make the deposition unable to form a uniform coating. With large amounts of precursors used (>70

mg), the outer surface layer looked porous. After annealing in O_2 at 700 °C for 30 min, porous Zn/Er modified GeNWs were fabricated (Fig. 24b). When the mass of precursors was lowered to 35 mg, porous layer on the surface of GeNWs became thin after annealing (the inset of Fig. 24d). Some nanowires revealed a polycrystalline surface (Fig. 24d).

Zn shells by PVD: As an alternative deposition source, Zn granules were used. Preliminary experiments showed that the morphology of the Zn surface coating on bare GeNWs was hard to control (as shown in Fig. 25) if the Zn evaporation temperature is allowed to go higher than the Zn boiling point (907 °C). A large number of flower-shaped or solid particles of micron size were observed on the top of the GeNWs. Therefore, a temperature range from 440~500 °C was tested to conduct Zn-coating.

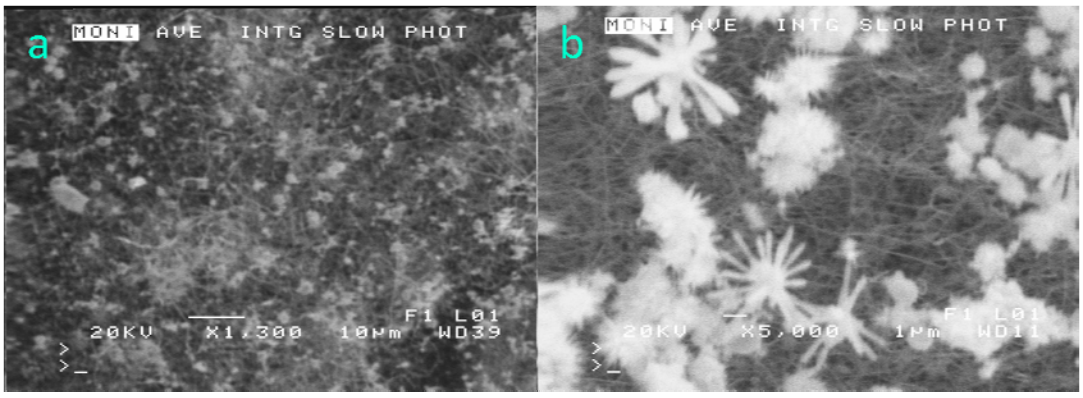

Figure 25. SEM image of Zn -coated GeNWs fabricated on Si (a) at 1250 °C for 1 min (b) at 980 °C for 30 min.

Zn/Ge NWs (without Er) with shells grown using the PVD method are shown in Fig. 26. The low magnification image indicates that the amorphous coating has a thickness ~8-13 nm with relatively smooth surfaces. In this case, stacking faults (Figs. 26c, d) were observed frequently on the GeNW core along the (111) growth direction, according to

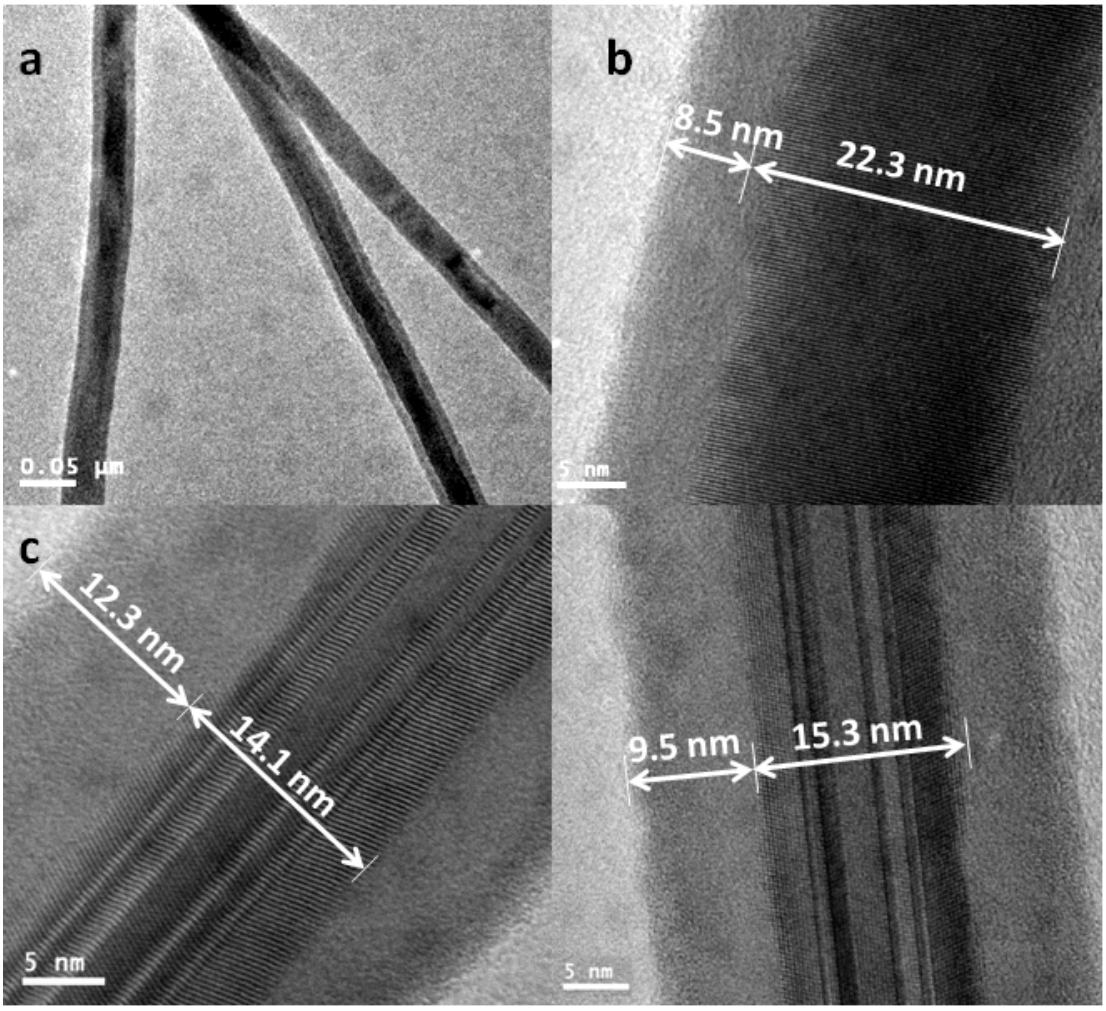

Figure 26. Zn-modified core-shell GeNWs fabricated on graphite cloth at 440 °C for 1 h (Zn granule source). (a) Low magnification TEM images, (b) HRTEM image with a typical (111) GeNW core. (c) (d) HRTEM image with Stacking faults on (111) GeNW cores.

d-spacing measurements (~0.32 nm). Such a high density of stacking faults were never found among numerous HRTEM images of bare GeNWs and other core-shell GeNWs modified by both Zn and Er. One possible reason is that the thermally induced stress during shell formation causes the dislocation. Furthermore, if the coating is not very thick or the thickness ratio of shell/core is not very high, (e.g. values shown in Fig. 26b), stacking faults were not formed. Another possible factor is that the amorphous oxide layer could act as a buffer to relax the thermal induced stress, which reduced the formation of stacking faults in other core-shell structures with Er-doping. The typical mass ratio of Zn/Ge in this type of NW is ~0.09 as measured by electron dispersive X-ray (EDX) spectroscopy.

The method above indicated that it is feasible to make uniform coatings of Zn onto GeNWs on graphite substrate by using Zn granules as a source in a PVD process. Subsequent work produced structures with an Er layer between the Zn shell and Ge core. TEM images of Zn/Er/Ge NWs annealed at 600 °C in O_2 for 30 min are shown in Fig. 27. The d-spacing measurement indicated that the amorphous Zn coating has been converted into a polycrystalline shell (Fig. 27a), but that the component was not ZnO. It suggests that graphite cloth substrates consumed most of O_2 and kept the Zn coating from oxidation. Zn diffusion during annealing could cause an inhomogeneous redistribution of the Zn (Fig. 27b). Fig. 27c shows the core-shell structure in some as-fabricated nanowires.

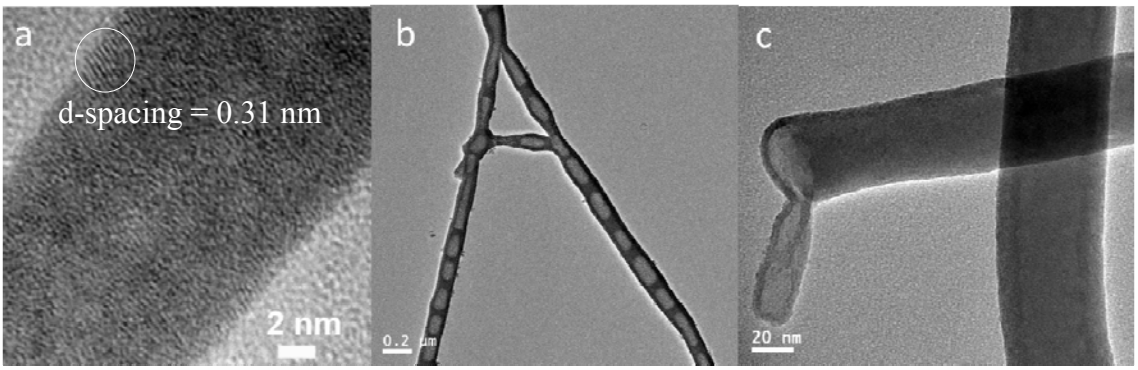

Figure 27. Zn/Er/Ge NWs on graphite cloth (3 mg Er precursor; Zn granule, 440 °C for 1 h; Annealing at 600 °C in O_2 for 30 min). (a) Porous surface TEM image. (b) HRTEM polycrystalline surface image. (c) A cross section of core-shell structures.

2.2.4 Zn/Er/Ge NWs grown on Si substrates

CVD vs. PVD process. In a typical CVD experiment, 1~2 mg Er precursor and 20 mg Zn precursor were used to form a surface layer with 5~10%wt Er and 10~12%wt Zn concentration at a total thickness of ~12 nm. In the PVD process (using Zn granule as source), the coating thickness is controlled by evaporation temperature (450~500 °C) and duration (1~2h). EDX spectra revealed that the concentration of Er, Zn and Ge varied because of varying GeNW diameters (ranging from 10 to 40 nm, prepared from thermally evaporated Au catalyst). HRTEM images exhibit clearly the amorphous shell and single crystalline GeNW core in both Fig. 28 (CVD) and Fig. 29 (PVD).

In comparing the HRTEM images of Fig. 28 and Fig. 29, a different contrast is observed in the shell formed by PVD (Fig. 29), than that using CVD (Fig. 28). Additionally, the shell surface of samples observed in Fig. 29 is more smooth and stable

under the electron beam of the TEM than that of Fig. 28. Organic residues from Zn precursor decomposition in the shell likely contributed to the unstable coating surface and made the Zn layer not as dense as those using Zn granules.

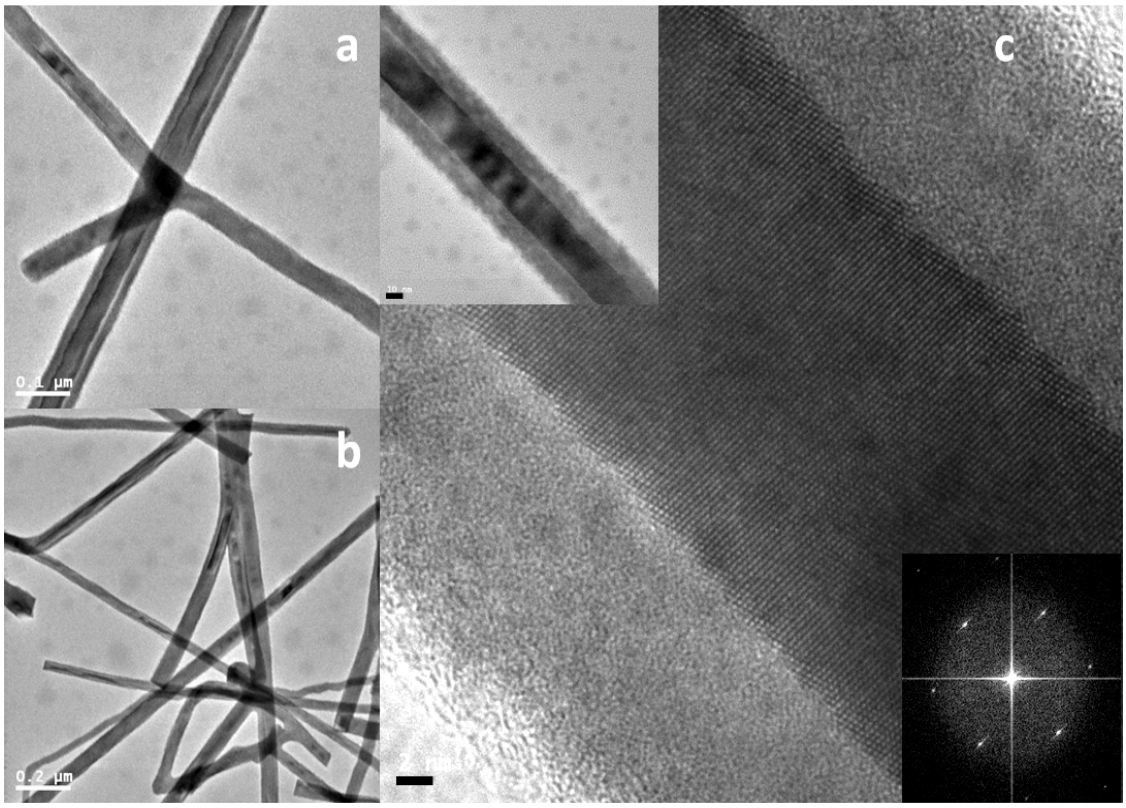

Figure 28. Zn/Er/Ge core-shell NWs on Si wafer (1.8 mg Er precursor; 20 mg Zn precursor). (a) (b) Low magnification TEM images (c) HRTEM image. Scale bar, 2 nm. (Top inset: TEM image of the same nanowire with lower magnification. Scale bar, 10 nm; Bottom inset: Fast-Fourier-Transformation (FFT) image).

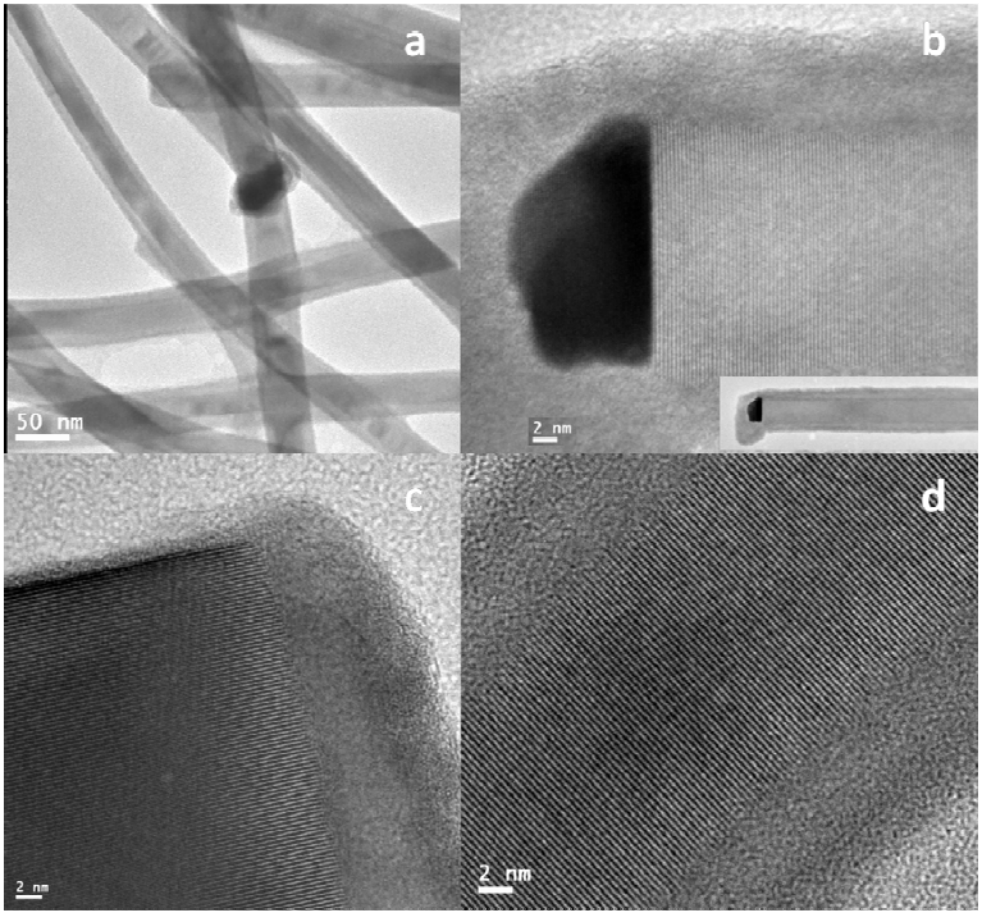

Figure 29. Zn/Er/Ge core-shell NWs on Si wafer (1.8 mg Er precursor; Zn granule, 440 °C for 1 h). (a) Low magnification TEM images. (b) (c) (d) HRTEM images. The inset in (b): TEM image of the same nanowire with lower magnification.

Annealing Zn/Er/Ge NWs with surface CVD coating. In order to form a stable ZnO shell and enhance Er^{3+} PL at room temperature, the annealing process must be carefully controlled to yield the desired morphology and crystalline structure of ZnO/Er/Ge NWs with shell structure formed by either CVD or PVD. Usually Zn/Er/Ge NWs were annealed at 600~700°C for 30 min in O_2 with a slow temperature ramp rate (200 °C/min). For the CVD process, EDX mapping experiments (Fig. 30) show that Zn (12 %) and Er (5 %) species were distributed uniformly on the surface of GeNWs.

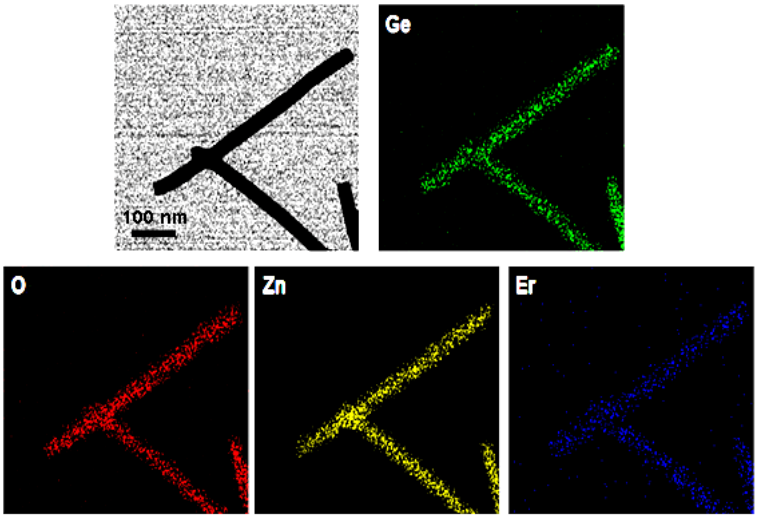

Figure 30. SEM, EDX mapping of annealed ZnO/Er/Ge NWs in O_2, 600 °C, 1h (using Zn precursor as Zn source).

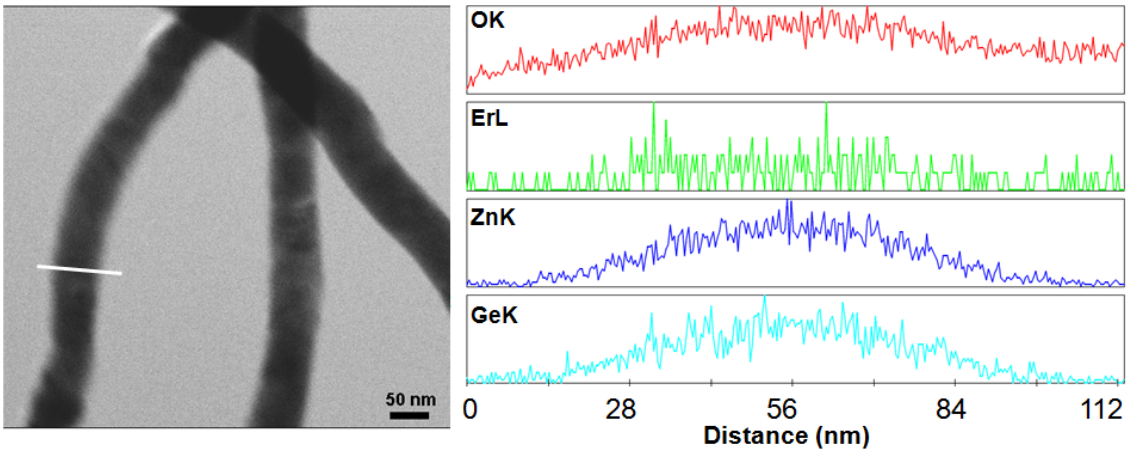

Figure 31. SME, EDX linescan spectrum of annealed ZnO/Er/Ge NWs in O_2, 700 °C, 30 min (using Zn precursor as Zn source).

A linescan spectrum for this type of sample (Fig. 31) indicates that Ge, Zn and O have a similar characteristic line-shape, which implies the formation of an alloy such as Zn_2GeO_4. The Er trace, with a very low concentration in the shell, appeared somewhat different.

Again, for the surface coatings prepared by CVD, corresponding TEM images (Fig. 32) illustrated that ZnO/Er/Ge NWs have diameters ~45 nm after annealing at 700 °C in O_2 for 30 min. An oxidation process, accompanied with alloy formation, blurred the interface of most core-shell structures, although the shell (~10 nm thickness) can still be observed in some samples (Fig. 32b). The HRTEM image of Fig. 32c clearly exhibits the presence of zinc germanate on the surface of ZnO/Er/Ge NWs (d = ~ 0.71 nm, corresponding to (110) plane, which is parallel to the longitudinal direction of GeNWs).

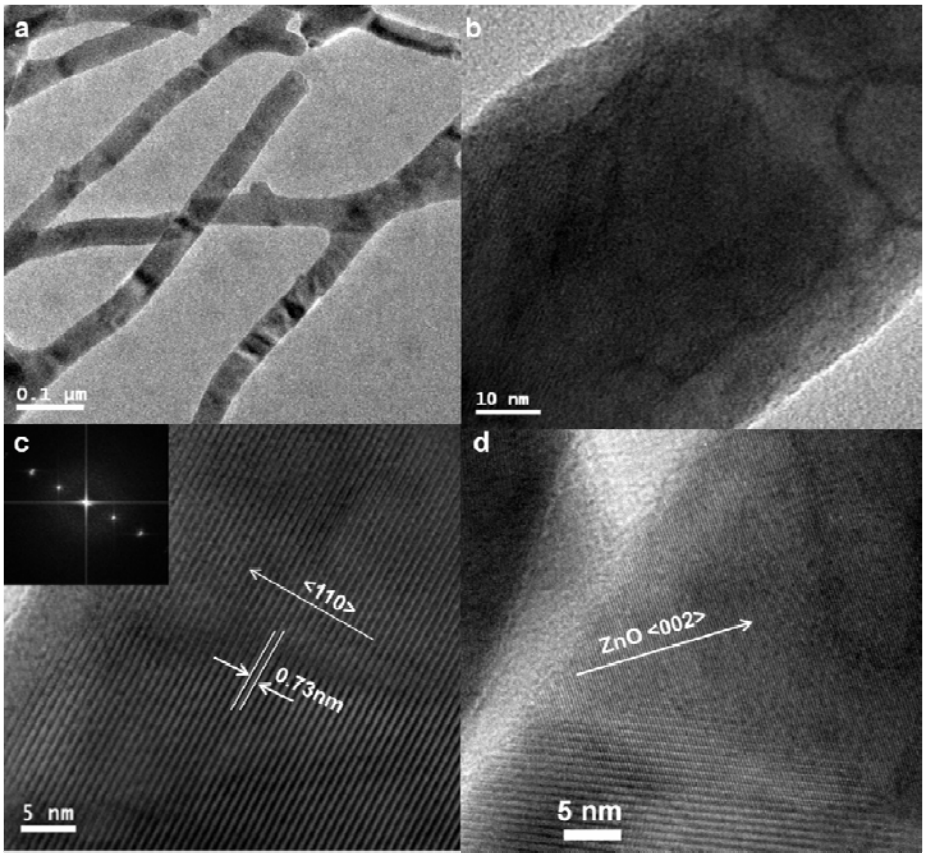

Figure 32. TEM images of annealed Zn/Er/Ge NWs in O_2, 700 °C, 30 min (1.8 mg Er precursor; 20 mg Zn precursor). a. low magnification, b. core-shell structure, c, d. HRTEM image of zinc germanate and ZnO lattice.

In addition to zinc germanate phase, a d-spacing of 0.27 nm shown in Fig. 32d is assigned to ZnO (002) plane, a value expanded slightly by the presence of Er and Ge atoms in the ZnO lattice.[278] Thus, the surface of annealed ZnO/Er/Ge NWs consists of a majority of zinc germanate and a minor ZnO component in the given annealing condition. If a thin Zn layer, e. g. 5~10 nm, is deposited onto the surface of GeNWs, the alloy formation possibly does not consume all of the Ge. Therefore, the Ge content distribution presumably is descending radially from core to surface.

Annealing Zn/Er/Ge NWs with surface coating by PVD. In contrast, use of the PVD method with Zn granules results in an inhibition of Zn_2GeO_4 formation during annealing by a dense amorphous Zn shell. Fig. 33 reveals that the ZnO preferred growth direction is along the (110) and ($\bar{2}$110) planes. In Fig. 33a, the (110) plane of ZnO shell is identical to the GeNW growth direction. A distinct core-shell interface boundary could not be displayed clearly, except for an inconspicuous contrast difference. For ZnO growing along ($\bar{2}$110) direction (as shown in Fig. 33b, d-spacing ~0.16 nm),[279] the core-shell crystalline structures on annealed ZnO/Er/Ge NWs were clearly observed. The top inset shows a low magnification image of ZnO/Er/Ge NWs with Moiré fringes; the corresponding fast Fourier transform (FFT) diffraction pattern is determined by a single crystalline (wurtzite) ZnO shell in (1$\bar{1}$00) plane. Additionally, FFT analysis also confirmed ($\bar{2}$110) growth direction of ZnO shell along GeNWs according to d-spacing calculations (~0.16 nm). Some satellite spots appear around the basic reflections of ZnO due to double diffraction.

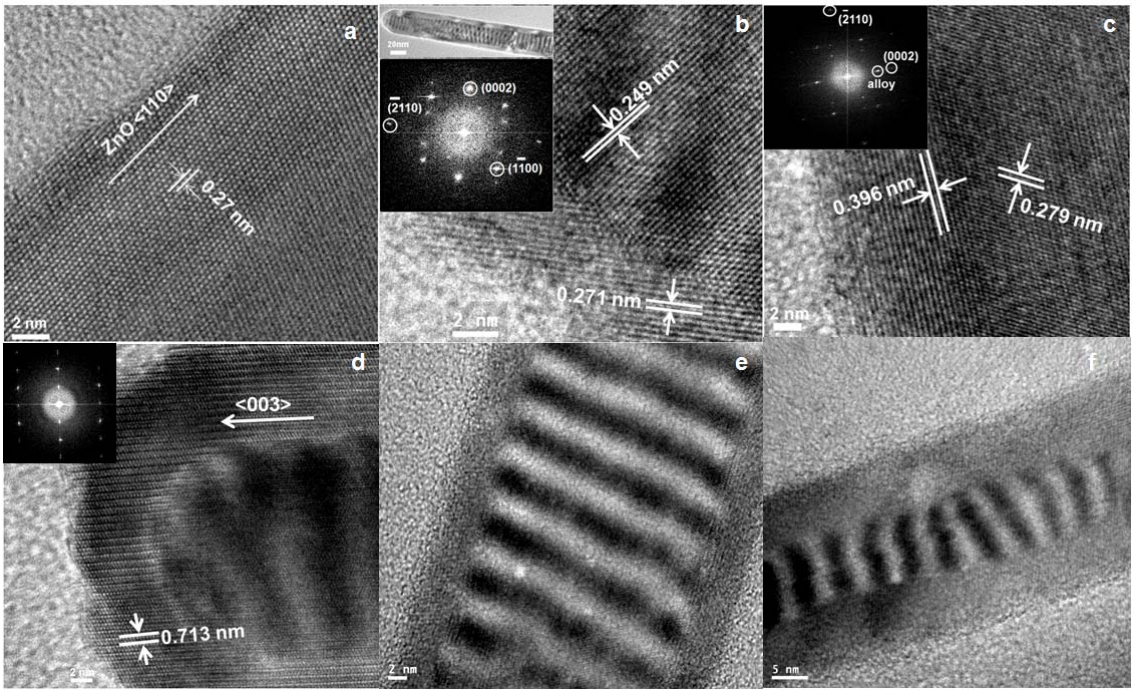

Figure 33. TEM images of ZnO/Er/Ge NWs in O_2, 700 °C, 30 min (using Zn granules as Zn source) with a. ZnO shell in (110) direction; b. ZnO shell in ($\bar{2}$110) direction. The top inset is the low magnification image. The bottom one is FFT image. Scale bar: 2 nm. c. Zn/Ge alloy shell in ($\bar{2}$110) direction and FFT image (the inset). Crystal structures indicated the presence of alloy. Scale bar: 2 nm; d. zinc germanate shell. Scale bar: 2 nm. e, f. Moiré fringes in ZnO/Er/Ge NWs with different ratio of shell and core sizes.

A gradual reduction in d-spacing in shell from surface to core was observed in Fig. 33c. It is notable that d-spacing (~0.418 nm) in the outer surface is somewhat larger than that near the boundary of core and shell (~0.396 nm). With the increasing O and Ge diffusion into shell, the d-spacing in the axial direction became larger. A ZnO (002) plane reflection could be still identified in the FFT image (see inset). A brighter spot (labeled by a white circle) closer to the origin corresponds to the altered shell crystalline structure. It is not possible to assign a suitable ZnO or Zn_2GeO_4 lattice index to the observed d-spacing of

0.396 nm. Presumably such a value represents an intermediate phase between ZnO and Zn_2GeO_4. The evidence is shown in Fig. 33d, where Zn_2GeO_4 shell was observed with a growth direction along (003) plane.[276,280]

Role of diffusion and surface strain. Therefore, it is suggested that the O and Ge diffusion rate into the shell is a critical factor to affect Zn_2GeO_4 formation and crystallinity structure at the given temperature during annealing, which adds to the possible number of crystalline structures in the shell. Compared with the CVD process employing a zinc precursor, an amorphous Zn layer formed by Zn granule evaporation (PVD) restrained Ge quick diffusion in the shell and increased the likelihood of forming ZnO on the outer surface, instead of zinc germanate (shown in Fig. 32). The Moiré fringes appearing in the TEM images of core-shell ZnO/Er/Ge NWs (using a Zn granule source), are attributed to the epitaxial orientation between ZnO and Ge as well as the zone axis incidence of the electron beam, rather than staking faults caused by misfit-induced strains (Figs. 33e,f). The spacing of the Moiré fringes is given by:[279]

$$D = \frac{d_{core} \times d_{shell}}{|d_{shell} - d_{core}|} \qquad (1)$$

where d_{core} and d_{shell} are the corresponding d spacing of the overlapping planes for the Ge core and ZnO shell. The spacing of moiré fringes observed in our images range from 4.8~5.5 nm. Using these values and that of the ZnO shell growing in the ($\bar{2}$110) plane (d=0.16 nm) in eq. (1), the calculated d-spacing of the Ge core is ~ 0.16 nm, corresponding to the Ge (222) plane.[281] This is consistent with growth of the core GeNWs in (111) planes,

which is a preferential direction in GeNW fabrication (Figs. 38c,d). The natural mismatch m between the two lattices is[279]:

$$m = \frac{|d_{shell} - d_{core}|}{d_{core}} \qquad (2)$$

The value of $|d_{shell} - d_{core}|$ is 0.005 nm, so m=3%. This means that the mismatch between core and shell is very small if the GeNW core has the (111) growth direction, identical with the ($\bar{2}$110) plane of ZnO shell. To such well packed core-shell structures, the Moiré fringes looks like periodic arrays (Fig. 33e). However, in most conditions, the array was disordered or eliminated by the electron beam (Fig. 33f), which implies that the crystal structure in the core was affected by core-shell strain. The deformation of GeNWs was often found in the area close to the tip (also due to strain) (Fig. 33e), although HRTEM images did not show the existence of a significant number of stacking faults.

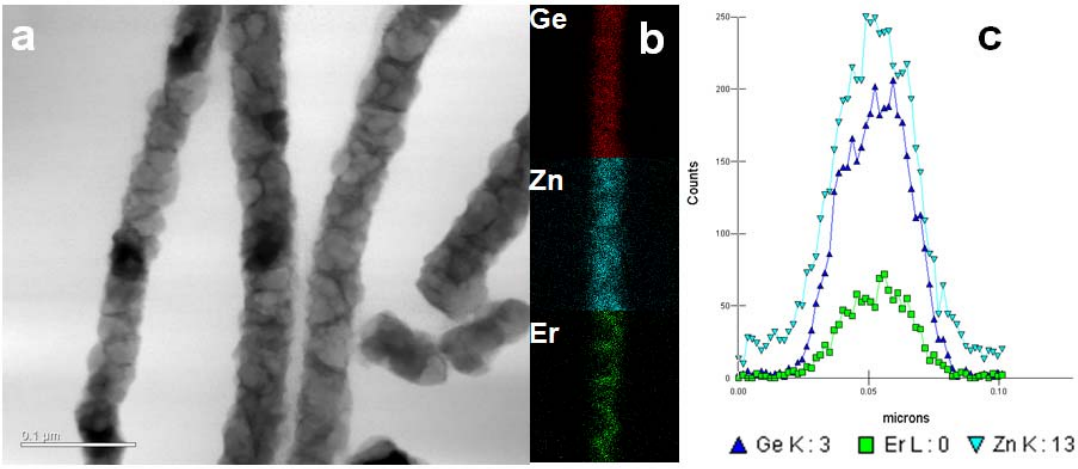

Figure 34. (a) TEM image of Zn/Er/Ge NWs annealed in O_2, 700 °C, 2h (Zn precursor, 200 mg); (b) Elemental mapping; (c) Intersection linescan.

Impact of thick Zn coatings by CVD. Annealed Zn/Er/Ge core-shell NWs fabricated by a CVD process did not exhibit similar Moiré fringes. A sample was fabricated with a thick Zn layer (60 %wt) by using 200 mg Zn precursor and annealing the core-shell nanowires at 700 °C in O_2 for 2h. These NWs lost their smooth surface and core-shell structure (Fig. 34a) because of the volume expansion caused by oxidation process; the associated electron diffraction spectrum (not shown here) exhibited a polycrystalline structure. By increasing the amount of Zn deposited, the roughening effect observed after annealing resulted in Zn/Er redistribution on the surface of ZnO/Er/Ge core-shell NWs as shown in the EDX maps of Fig. 34b.

2.2.5 XRD Spectra of ZnO/Er/Ge NWs

The XRD spectrum in Fig. 35 indicates that crystalline Ge peaks (2θ = 25.6°, 27.0°, 45.1° and 53.4°) are still present in Zn/Er/Ge core-shell NWs modified by Zn granule vapor after annealing at 700 °C in O_2 for 30 min. Such features disappeared in the case of GeNWs exposed to the Zn precursor (Fig. 35). One possible reason is that there are a large number of sub-micrometre particles, or nanocrystallites in these nanowires, that diminish the characteristic peaks.[282] As a reference, the XRD spectra of Ge and GeO_2 are also shown in Fig. 36.

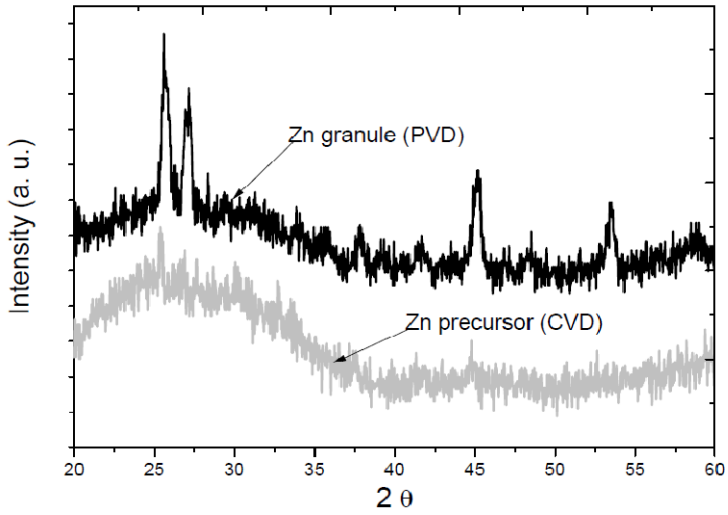

Figure 35. XRD spectra of annealed ZnO/Er/Ge NWs at 700 °C in O_2 for 30 min.

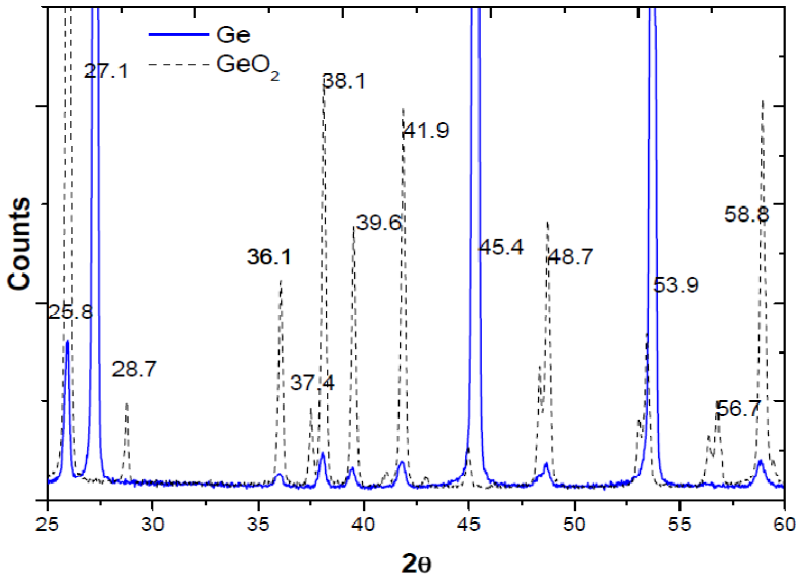

Figure 36. XRD spectra of standard Ge and GeO_2 samples.

2.2.6 Photoluminescence Spectra of ZnO/Er/Ge NWs

Typical near IR PL for annealed Zn/Er/Ge NWs are shown in Fig. 37. The Zn precursor process (CVD) provides a higher Er^{3+} PL intensity, which is consistent with the observation of better Er diffusion and oxidation in the shell because of a less dense Zn coating. An Er preannealing process (500 °C in O_2 for 30 min) was necessary to increase Er^{3+} PL intensity before Zn deposition, presumably due to formation of more Er-O species.

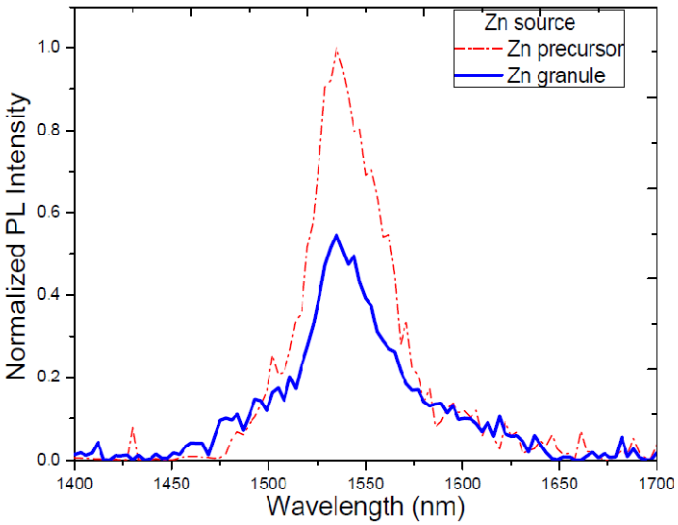

Figure 37. PL of annealed Zn/Er/Ge NWs at 700 °C in O_2 for 30 min. (λ_{ex}=488 nm)

In collaboration with Prof. Yuri M. Strzhemechny of the TCU Physics Department, UV/visible PL measurements were employed to assess the photophysical properties of ZnO formed on the surface of core-shell NWs (Fig. 38). The ZnO UV/visible spectrum of ZnO/Er/Ge NWs with ZnO surface coating by a PVD process (the black trace in Fig. 38) exhibits ZnO near-band-edge (NBE) ultraviolet emission and a deep-level trap

feature at 3.30 eV (375 nm) and 2.25 eV (550 nm) respectively, while the spectrum from ZnO/Er/Ge NWs modified by a CVD process (the grey trace in Fig. 38) displays a different spectrum with intensity in the 2.4~2.9 eV range, but without any distinctive ZnO NBE features. By comparing with the literature,[283, 284] the broad peak in the gray spectrum was attributed to the blue-green emission of Zn_2GeO_4, which correlates to oxygen defects.

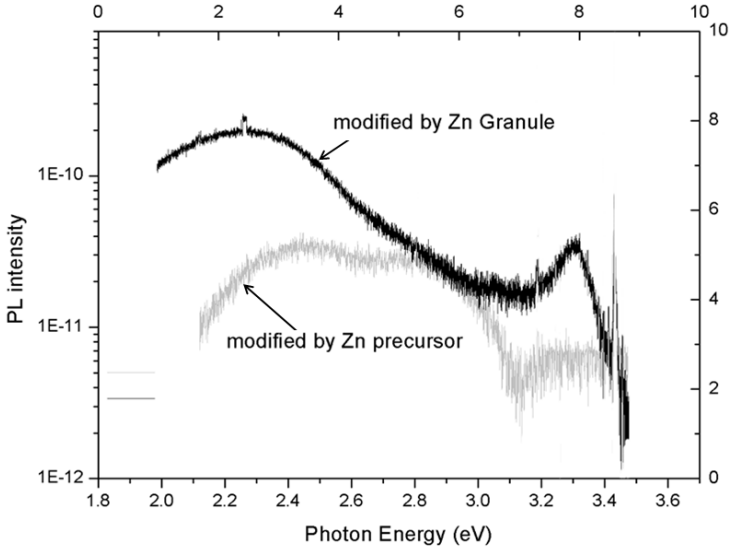

Figure 38. Room temperature ZnO UV/visible PL for Zn/Er/Ge core-shell NWs with surface modification by Zn precursor and granule, respectively. (λ_{ex}=325 nm)

In order to enhance both Er^{3+} and ZnO PL intensity of ZnO/Er/Ge NWs prepared by a CVD method, one strategy is to increase the mass of Zn precursor applied. When the concentration of Zn is up to ~40% (wt) on the NWs, the thicker Zn layer can form more

ZnO phase on the surface of ZnO/Er/Ge NWs, which contributes to an enhanced light emission in the visible as shown in Fig. 39, even though some of it likely forms Zn_2GeO_4 with Ge core during annealing. The spectra in Fig. 39 reveals that there could be an energy transfer from ZnO to Er^{3+} ion because of the enhanced emission intensity above 520 nm in the spectrum of ZnO/Er/Ge NWs in Fig. 39, consistent with possible upconversion in the visible. Such a drop could not be observed in ZnO/Ge NWs without Er^{3+} ions.

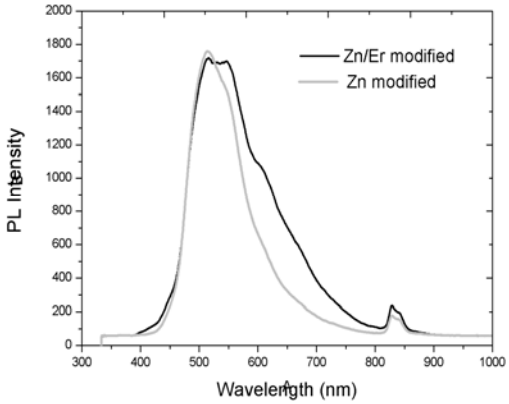

Figure 39. Fluorescence microscopy spectra of ZnO for Zn- and Zn/Er-modified Ge core-shell NWs. Annealing temperature: 500 °C in O_2 for 1h. (λ_{ex}=370 nm)

ZnO/Er/Ge NWs with a thick Zn layer (100 mg Zn precursor, CVD) exhibit strong Er^{3+} PL intensity at 1.54 μm after annealing at 700 °C in O_2 for 1 h as shown in Fig. 40a. At a cost of higher Er^{3+} & ZnO light emission, the discrete core-shell structures of Ge NWs were lost. For Zn/Er/Ge NWs, the thickness of outer Zn coating has no remarkable effect on Er^{3+} PL intensity. For example, strong Er^{3+} PL can also be observed, even with a thick Zn coating by using 200 mg Zn precursors (Zn concentration ~60%wt).

In this work, the impact of Er location on Er^{3+} PL is investigated based on Zn/Er-modified Ge NWs prepared by the CVD process. ZnO/Er/Ge NW sandwich structures (Er in the middle layer) provide higher Er^{3+} PL intensity than Er/ZnO/Ge NWs (Er layer located on the surface) as shown in Fig. 40b.

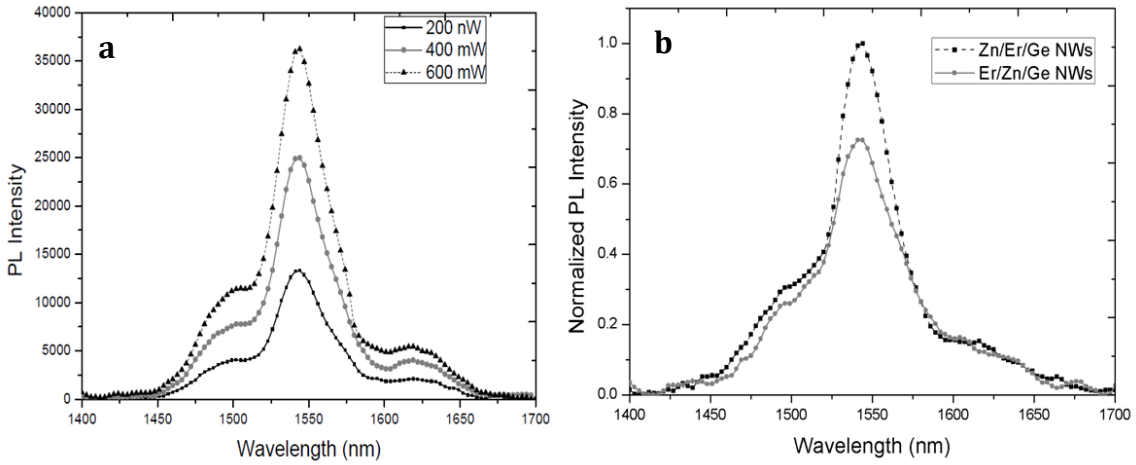

Figure 40. (a) Er^{3+} PL spectra of ZnO/Er/Ge nanowires excited by 488 nm laser at different powers. (Zn 30%; Er 2.5%; Ge 67.5%). (b) Er^{3+} PL spectra of ZnO/Er/Ge and Er/ZnO/Ge nanowires excited by 488 nm laser. (Zn 30%; Er 8%; Ge 62%).

In ZnO/Er/Ge sandwich structures (CVD route), it is found that 2~3% (wt) Er concentration provided the best light emission in terms of PL intensity and line shape (Fig. 40a). Poor or no PL could be obtained in the condition of Er concentration less than 1% (wt). A strong PL signal with good line shape can still be observed without quenching from the sample with very high Er concentration (20%wt) as shown in Fig. 41a. Such a concentration-dependent Er^{3+} PL can also be observed in Er/ZnO/Ge NW structures (Er on the surface).

The Er^{3+} PL excitation mechanism can be probed by measurements of excitation spectra at excitation wavelengths of 476, 488, 496, 502 and 514 nm. The typical Er^{3+} PLE spectrum is shown in Fig. 41b. The highest Er^{3+} PL intensity observed at 488 nm and an ascending at 514 nm excitation wavelength confirm a direct excitation pathway in this work, because erbium ions can be directly excited into ligand field states when 488 and 514 nm wavelengths are used.[272]

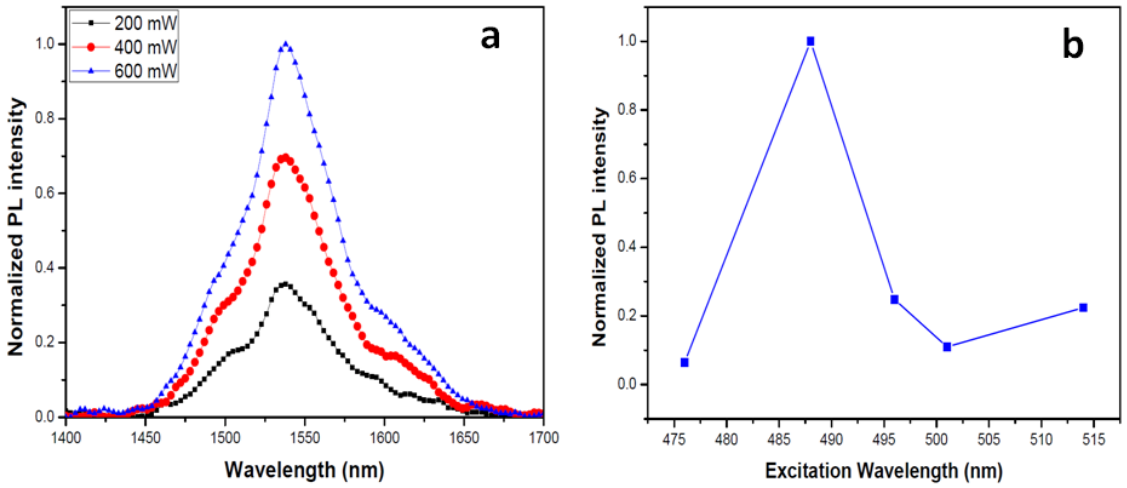

Figure 41. (a) Er^{3+} PL spectra of ZnO/Er/Ge nanowires with high Er concentrations (Zn 12%; Er 20%; Ge 66%), excited by 488nm laser at different powers. (b) the corresponding PL excitation spectrum. Annealing temperature: 700 °C (1 h).

2.3 Summary

This chapter describes processes to fabricate ZnO/Er-modified GeNWs and their corresponding structural characterization. GeNWs grown on Si wafer or graphite cloth substrates are synthesized by physical vapor deposition (PVD). Although graphite cloth provides a better mass transfer environment for GeNWs growth with high yield and quality than Si wafer, it can react with O-containing species and affect the formation of a uniform core-shell structure in the CVD method. The carbon reduction property of graphite also makes Zn hard to oxidize during annealing.

Furthermore, the nature of Zn source had significant impact on the crystalline structure and photophysical properties of ZnO/Er/Ge NWs. In the Zn granule process (PVD), Zn/Er/Ge NWs can provide high composition of ZnO in the surface during annealing by inhibiting Ge diffusion towards the shell and zinc germanate formation, which is helpful to ZnO UV/visible PL. The Zn precursor surface deposition process provided more appropriate conditions to form Zn_2GeO_4 which is useful to enhance Er^{3+} PL, but diminishes ZnO luminescence. Dual wavelength light emission is observed in both processes. Heavily ZnO coated Er/Ge NWs (Zn precursor) exhibit very impressive Er^{3+} and ZnO UV/visible PL. Evidence for energy transfer from ZnO to Er at wavelength 520 nm was observed. It is found that 2~3 % (wt) Er concentrations and the Zn/Er/Ge sandwich structure were preferred for dual wavelength light emission.

CHAPTER III.

Dual Wavelength Emissive ZnO Tetrapods: Effects of Erbium/Germanium Modification

3.0 Overview

The higher exposed surface area of ZnO in nanostructured form is providing interesting phenomena of relevance to energy conversion, spintronics, piezobased devices, and other applications.[108,112,115,123] ZnO tetrapods (TPs) are one intriguing variant in this regard, with a controllable morphology based on a single crystal core.[136-138]

To improve the properties of electrical and optical devices, doping is a necessary strategy. As a promising host material for Er^{3+}, ZnO provides erbium with an oxygen coordination sphere which is helpful to an efficient Er-based near-infrared photoluminescence (PL).[274,275,278] Er-doped ZnO films have proven to be reliable materials for light-emitting diodes, laser diodes, and optical amplifiers operating at 1.54 μm, as well as electrode materials for carrier injection because of their high electrical conductivity and transparency.[262-264]

In this Chapter, the results of experiments involving the synthesis of ZnO TPs by heating Zn granules in air are described. Er^{3+} ions are then introduced onto the surface of ZnO tetrapod structures by chemical vapor deposition (CVD). Since previous reports have noted the ability of oxidized germanium species to improve the near-IR PL intensity of Er-doped Ge nanowires (NWs) as well as Er-doped SnO_2 nanofibers,[279] Ge was deposited via vapor transport onto the surface of Er^{3+}/ZnO TPs to generate an analogous enhancing effect. As prepared samples were characterized by scanning electron microscopy (SEM, JEOL-6100) with X-ray energy dispersive spectroscopy (EDX) system attached, high resolution transmission electron microscopy (HRTEM, JEOL-2100) and X-ray diffraction

(XRD, Philips-3100). All PL spectral measurements were carried out using the instrumental set-ups described in Chapter II.

3.1 Experimental Methods

3.1.1 ZnO TP fabrication

ZnO TPs were grown by ZnO in air without any carrier gas or catalyst. An alumina boat loaded with 80~110 mg Zn particles was placed inside the quartz reactor with one sealed end (see Fig. 42). Another boat was placed in the reactor at a distance of 1~3 cm away from the Zn source boat to collect the ZnO TPs products. White ZnO TPs were formed on the collection boat while the temperature of the reactor was heated to ~990 ºC at a ramp rate of ~30 ºC /min; the reactor temperature remained at 990 ºC for 20~30 min.

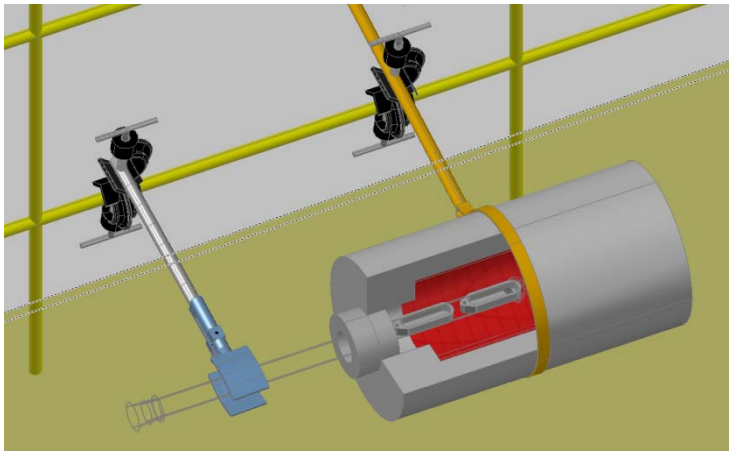

Figure 42. Schematic view of the setup for ZnO TP fabrication.

3.1.2 Er-doping and Ge surface modification

The incorporation of Er on the surface of TPs is achieved through the chemical vapor deposition of $Er(TMHD)_3$. The setup has been introduced in Chapter II (Fig. 19a). An alumina boat loaded with ZnO TPs (10-20 mg) was placed in a quartz tube reactor (of 24 mm inner diameter) heated by a ceramic furnace up to 500 °C (at a rate of 30 °C/min). The Er precursor (20 mg) was heated to ~145 °C (also in an alumina boat), and the vapor was carried downstream by He gas with a flow rate of 300 sccm to the furnace, with the distance between the precursor boat and the tetrapod-containing alumina boat set at approximately 6 cm. Ge deposition was fulfilled via the heating of Ge powder (15 mg) at 990 °C in helium gas (300 sccm) for 1 h, followed by cooling downstream to form a Ge layer on the surface of Er-doped or undoped ZnO TPs. A Ge source to tetrapod container separation again of 6 cm was maintained.

3.2 Results and Discussion

3.2.1 Zn granule size and mass dependence on the fabrication of ZnO TPs

In the ZnO TP fabrication process, Zn granules were evaporated at ~ 990 °C. With an increase of Zn concentration in the gas phase, Zn vapor diffused towards the open end of the reactor and reacted with O_2 to form ZnO TPs in the low temperature area (~670 °C, measured by thermocouple.). Usually 90 mg of Zn could produce ~15 mg ZnO TPs (13% yield). Most of the Zn (~87%) formed ZnO powder and still stayed in the Zn source boat. Zn granule size was an important factor to the success of ZnO TP

fabrication. A high surface area Zn powder (200 mesh) did not provide ZnO TP products because the surface of those small particles have been covered by a thick ZnO layer during the increasing temperature stage, which hindered the Zn evaporation rate. Therefore, the amount of Zn vapor in the gas phase could not reach the required concentration in the low temperature area to form ZnO TPs. Zn granules with 3~5 mm diameters were preferred to synthesize ZnO TPs in this work. Typical ZnO TPs are shown in Fig. 43a and b. The arms are ~32 μm. If the Zn granules were larger than 5 mm in diameter, a white ZnO shell could be left on the source boat after Zn evaporation. The surface morphologies of the interior of the Zn granule remaining after the conclusion of the experiment is shown in Fig. 43c, while the exterior granule surface was covered by Zn TPs (Fig. 43d) with arm lengths of ~10 μm.

The amount of Zn used has significant effects on the morphology of ZnO TPs for a given reaction system. If the Zn mass was less than 80 mg, only ZnO powder formed due to low Zn vapor concentration in air phase. A large number of ZnO particles, sheets, polypods and tetrapods generated in very high concentrated Zn vapor from large mass of Zn evaporation (>130 mg). Such effects are illustrated below from Fig. 44 to Fig. 47, corresponding to 172, 130, 110 and 93 mg of Zn reacting at 990 °C for 30 min, respectively.

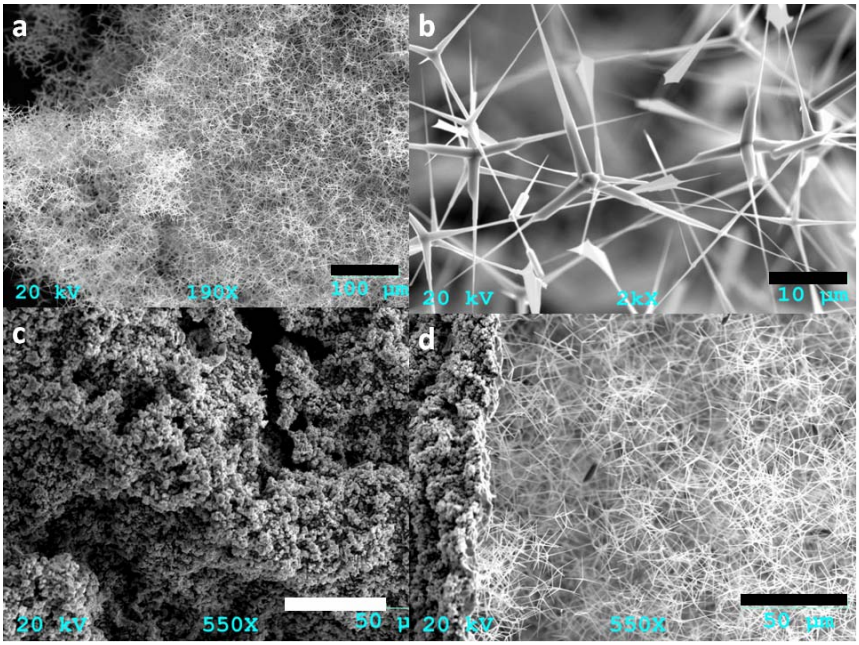

Figure 43. SEM images of (a) (b) representative ZnO TPs at different magnifications; (c) the interior surface morphology of ZnO shell; and (d) outer surface of ZnO shell covered by ZnO TPs. Scale bars: (a) 100 µm, (b) 10 µm, (c) 50 µm, and (d) 50 µm.

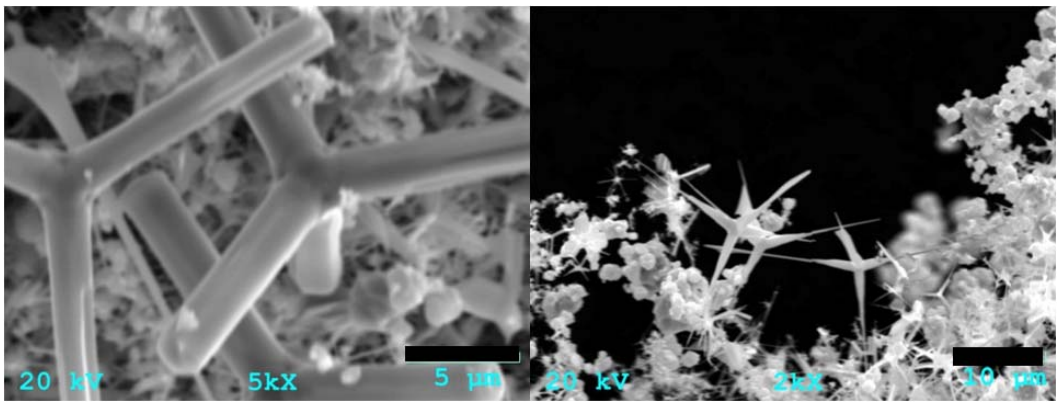

Figure 44. SEM images of ZnO TPs (172 mg Zn, 990 °C, 30 min). Scale bars: 5 µm (left), 10 µm (right).

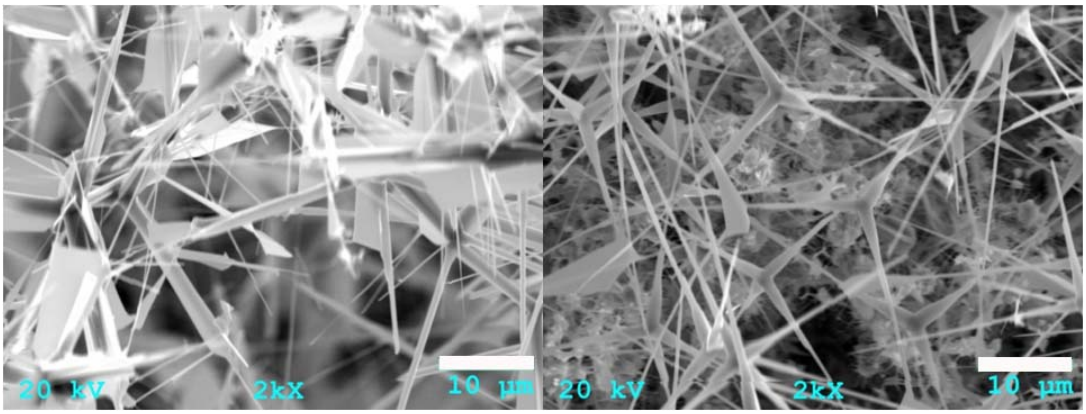

Figure 45. SEM images of ZnO TPs (130 mg Zn, 990 °C, 30 min). Scale bars: 10 µm.

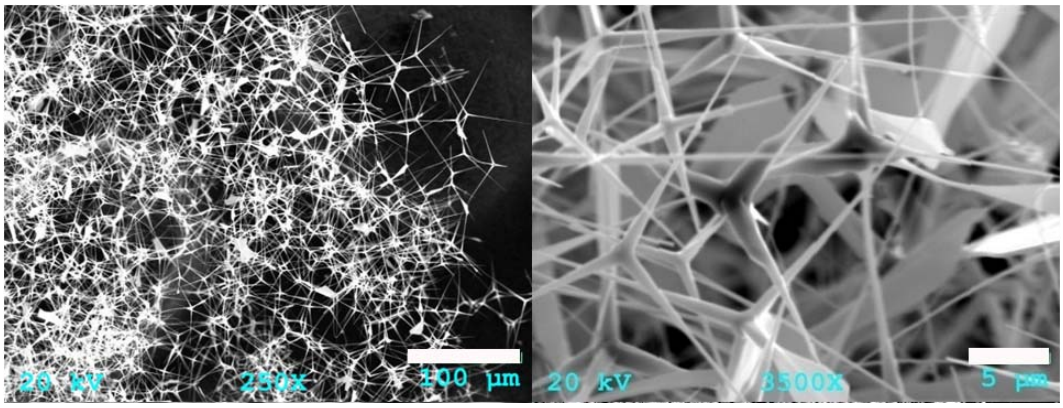

Figure 46. SEM images of ZnO TPs (110 mg Zn, 990 °C, 30 min). Scale bars: 100 µm (left), 5 µm (right).

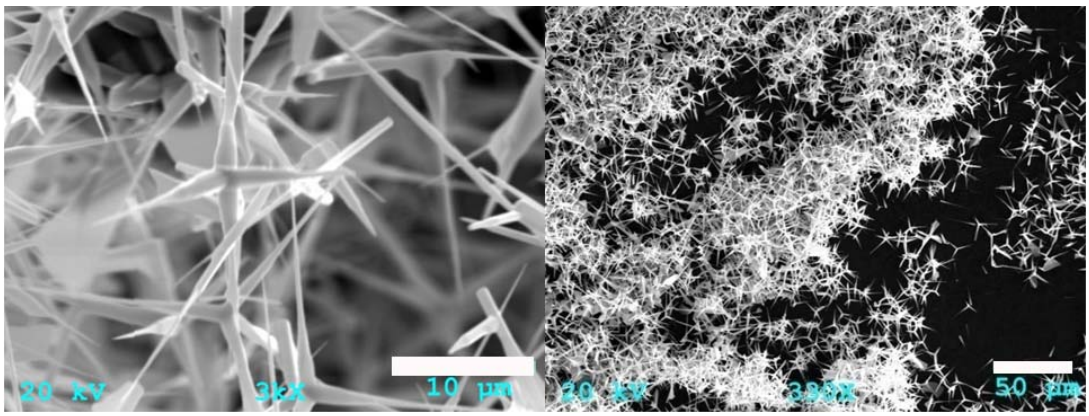

Figure 47. SEM images of ZnO TPs (93 mg Zn, 990 °C, 30 min). Scale bars: 10 µm (left), 50 µm (right).

These images suggest that a large number of ZnO beads and sheets are formed in conditions with high Zn vapor concentration (or relatively low O_2 concentration). In the given setup, ZnO TPs were not found on the collection boat if Zn mass was lower than 90 mg. However, if the reaction temperature is increased to 1010 °C, ZnO TPs could also be produced with Zn amounts smaller than 90 mg as shown in Figs. 48 and 49. Compared with reactions at 990 °C, ZnO TP morphologies were more sensitive to the amount of Zn mass used. A large number of ZnO TPs with small size were produced due to a faster growth rate induced by high temperature. ZnO TPs products could not be found if the temperature was lowered to 980 °C. The arm length of TPs usually ranges from 10~30 μm. A weak explosion could be observed with sound and light if Zn masses over 200 mg were used. It provided a pressure to send small Zn TPs ~20 cm far away from the collection boat toward the outside of the furnace as shown in Fig. 50. The smallest arm length could be even less than 1 μm.

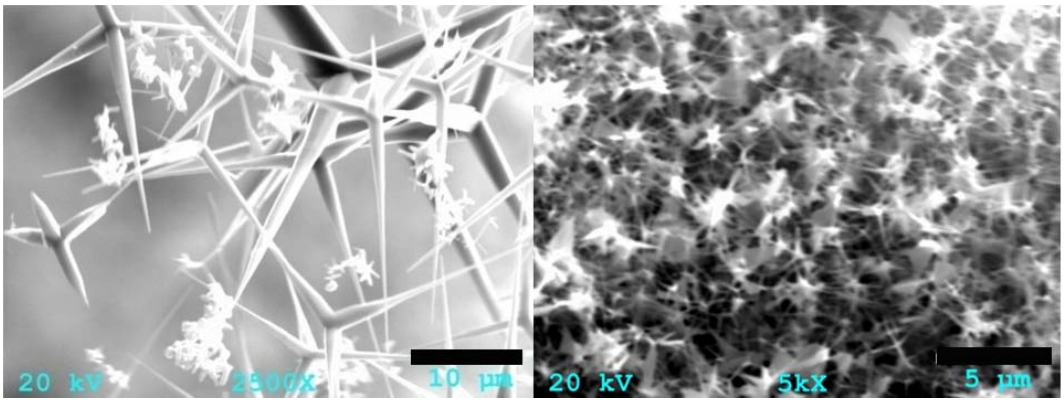

Figure 48. SEM images of ZnO TPs (89 mg Zn, 1010 °C, 30 min). Scale bars: 10 μm (left), 5 μm (right).

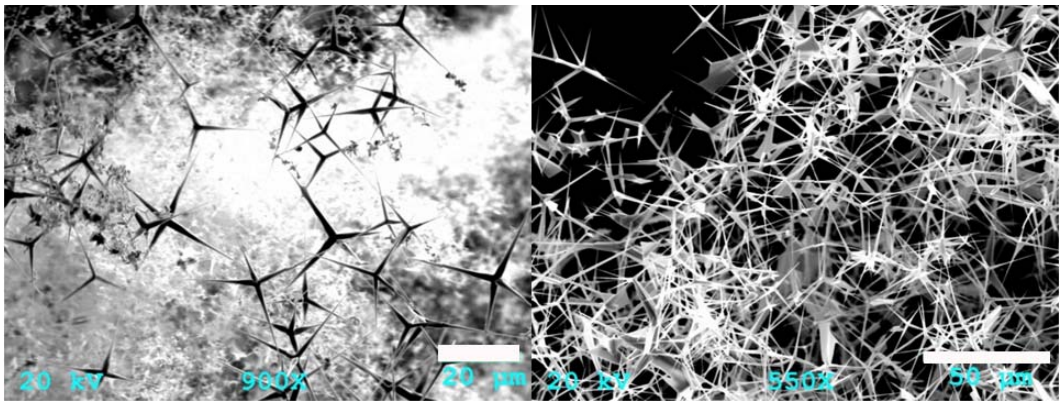

Figure 49. SEM images of ZnO TPs (81 mg Zn, 1010 °C, 30 min). Scale bars: 20 µm (left), 50 µm (right).

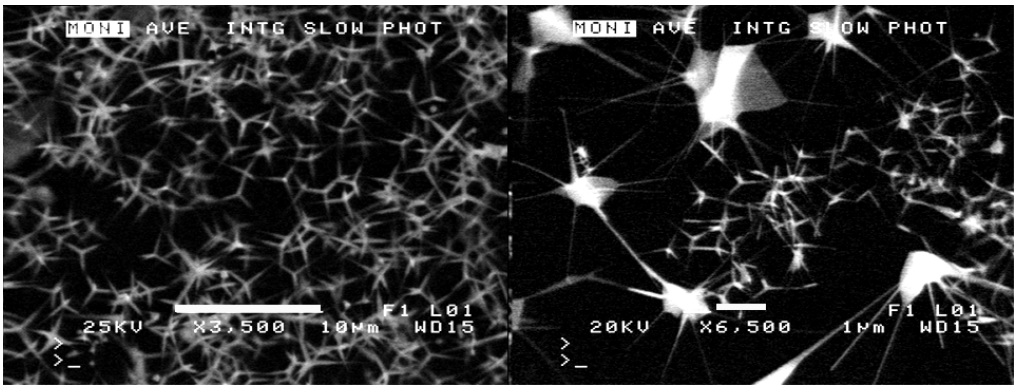

Figure 50. SEM images of ZnO TPs with small sizes (explosion, 920 °C, 1 min). Scale bars: 10 µm (left), 1 µm (right).

The morphology of ZnO TPs is also location-dependent along the deposition area. The sharp arm of ZnO TPs always correlated with a relatively higher concentration of O_2 in the deposition area close to the open end of the reactor. ZnO sheets or thick arm TPs (Fig. 51) formed more frequently towards the furnace center, along with a decreasing O_2 concentration, according to SEM images of ZnO TPs sampled from different deposition areas.

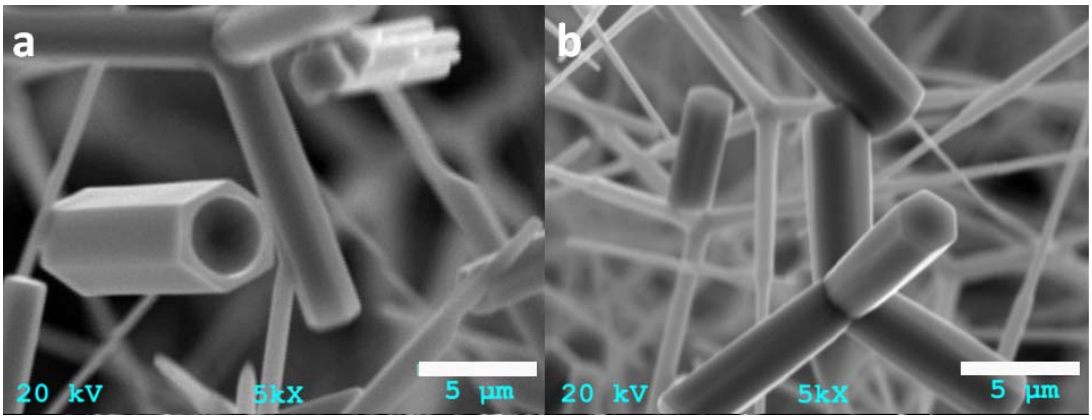

Figure 51. SEM images of ZnO TPs with rod-shaped arms. (a) 95 mg Zn, 990 °C, 30 min; (b) 122 mg Zn, 990 °C, 30 min. Scale bars: 20 µm (left), 50 µm (right).

3.2.2 Er and Ge surface modification

In this work, two kinds of doped structures were fabricated. One has an Er-doped layer introduced between the Ge coating and the ZnO TP core (hereafter referred to as Ge/Er^{3+}/ZnO TPs). The other structure has a Ge middle layer acting as a sandwich between the Er and the ZnO TP core (hereafter described as Er^{3+}/Ge/ ZnO TPs). When imaged by SEM, the tetrapod morphology shows no remarkable change after a typical incorporation of 1-3 wt% Er (Fig. 52). In terms of composition, energy dispersive X-ray (EDX) spectra show varying amounts of the expected elements as a function of location in the tetrapod, due to the differences in ZnO thickness in the central area and legs. For example, typically the Er or Ge concentration at the tip of a leg is about 2-3 times that observed near the center of the tetrapod. Under conditions of extended Ge exposure (~25 wt % in the central area), the ZnO TPs surface remains relatively smooth at low magnification (Fig. 53).

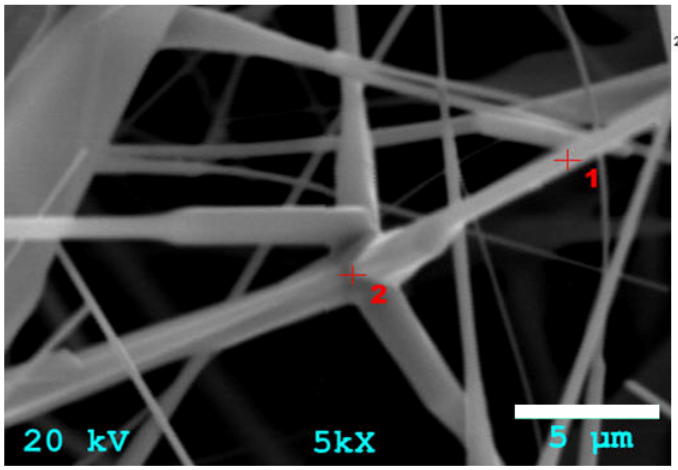

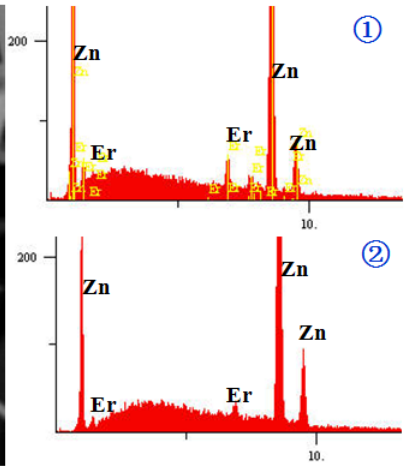

Elt.	Line	Intensity (c/s)	Atomic %	Atomic Ratio	Conc	①
Zn	Ka	73.64	98.586	1.0000	96.462	wt.%
Er	La	5.94	1.414	.0143	3.538	wt.%
			100.000		100.000	wt.%

Elt.	Line	Intensity (c/s)	Atomic %	Atomic Ratio	Conc	②
Zn	Ka	82.03	99.682	1.0000	99.190	wt.%
Er	La	2.22	.318	.0032	.810	wt.%
			100.000		100.000	wt.%

Figure 52. SEM image and EDX of representative ZnO TPs doped by 15 mg $Er(TMHD)_3$. The labels of (1) and (2) on the EDX spectra and analysis (bottom) correspond to the two investigated points in the SEM image.

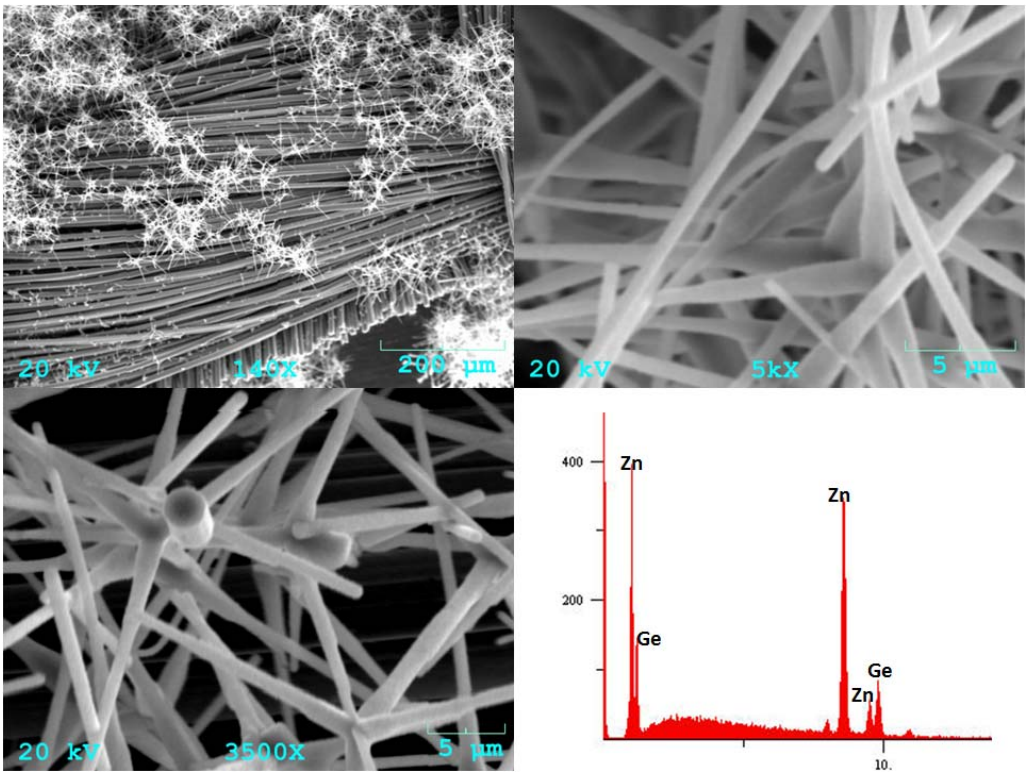

Figure 53. SEM images and EDX of representative ZnO TPs coated with 25%(wt) Ge.

The two Er-doped TPs structures containing Ge have similar morphologies. The image of Ge/Er^{3+}/ZnO TPs and the corresponding EDX spectrum (Fig. 54) show the presence of ~1.5% Er and ~8% Ge in central areas after 1 h of annealing at 900 ºC in O_2. Some slight charging is observed after such treatment.

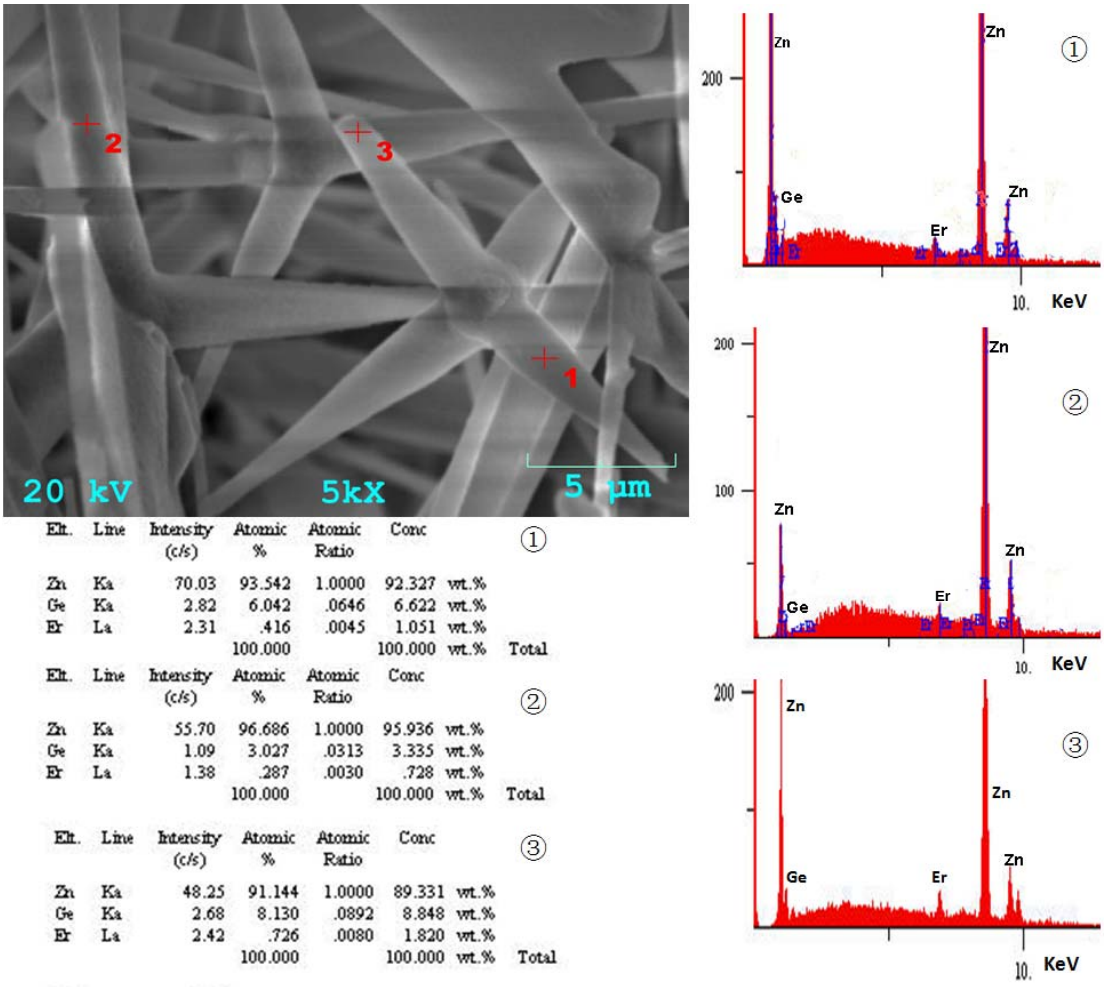

Elt.	Line	Intensity (c/s)	Atomic %	Atomic Ratio	Conc		
							①
Zn	Ka	70.03	93.542	1.0000	92.327	wt.%	
Ge	Ka	2.82	6.042	.0646	6.622	wt.%	
Er	La	2.31	.416	.0045	1.051	wt.%	
			100.000		100.000	wt.%	Total

Elt.	Line	Intensity (c/s)	Atomic %	Atomic Ratio	Conc		
							②
Zn	Ka	55.70	96.686	1.0000	95.936	wt.%	
Ge	Ka	1.09	3.027	.0313	3.335	wt.%	
Er	La	1.38	.287	.0030	.728	wt.%	
			100.000		100.000	wt.%	Total

Elt.	Line	Intensity (c/s)	Atomic %	Atomic Ratio	Conc		
							③
Zn	Ka	48.25	91.144	1.0000	89.331	wt.%	
Ge	Ka	2.68	8.130	.0892	8.848	wt.%	
Er	La	2.42	.726	.0080	1.820	wt.%	
			100.000		100.000	wt.%	Total

Figure 54 SEM image and EDX of representative Ge/Er^{3+}/ZnO TPs (after 1h annealing at 900 ºC in O_2). The labels of (1), (2) and (3) on the EDX spectra and analysis correspond to the three investigated points in the SEM image. Scale bar 5µm.

3.2.3 ZnO TP morphologies characterized by TEM

TEM images revealed that ZnO TPs have smooth surfaces before Ge/Er modification. The size of arm tips could be diverse due to growth conditions as shown in Fig. 55a and Fig. 56a. HRTEM images prove that the tips of ZnO TPs have a preferential growth direction along the (002) plane according to d-spacing measurements (0.266 nm) in both Fig. 55b and Fig. 56b. With the surface modification by Ge/Er and annealing in O_2 at 900 ºC for 1h, some measurable surface roughness and associated protuberances were observed upon deposition of Er and Ge of 20-30 nm thickness. The morphology increases the surface area and possibly plays a role in the enhancement of the quantum efficiency of the Er^{3+} PL.[285, 286]

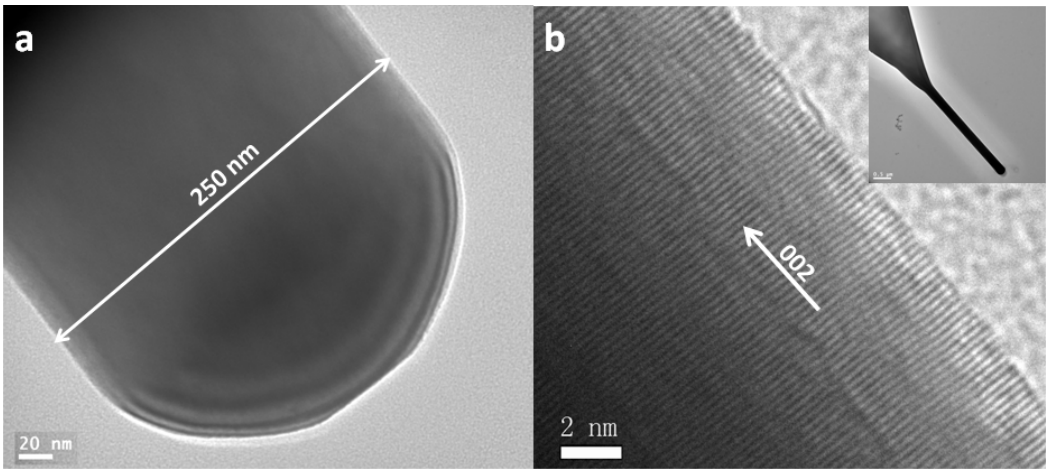

Figure 55. (a) TEM images and (b) HRTEM images of a tip surface of ZnO TPs. The inset shows the tip images at low magnifications.

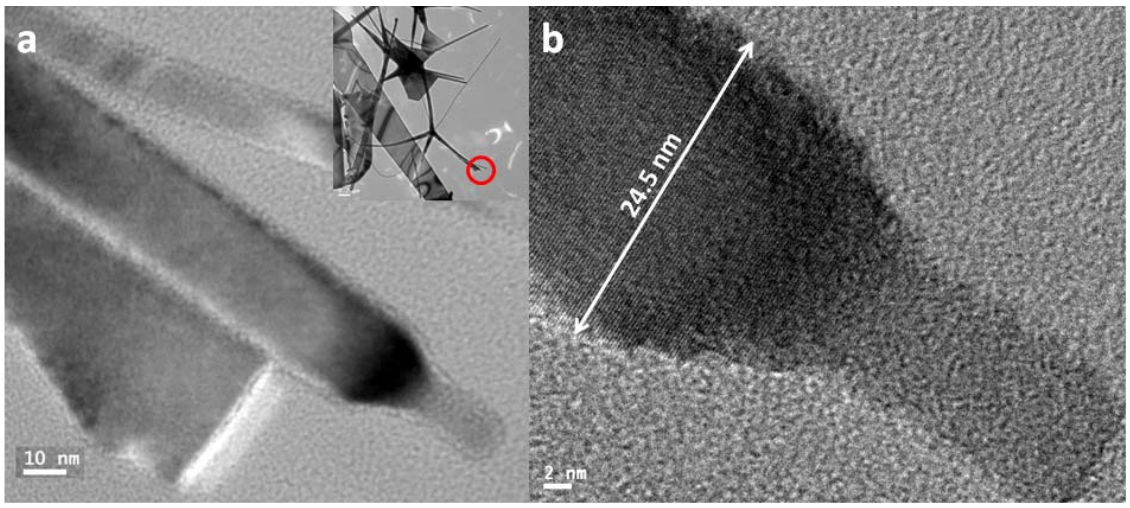

Figure 56. (a) TEM images and (b) HRTEM images of a tip surface of ZnO TPs. The red circle in the inset shows the area selected for zoom in.

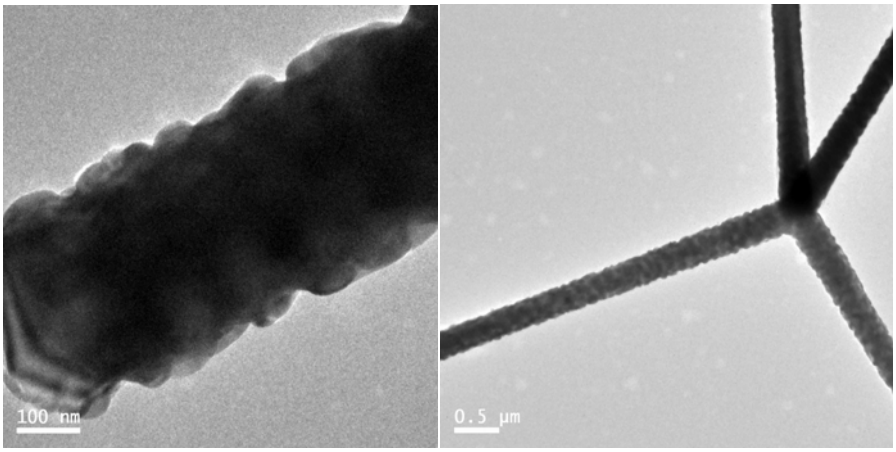

Figure 57. TEM images of the rough surface of Ge/Er^{3+}/ZnO TPs at different magnifications.

HRTEM images show that Ge and ZnO have formed a zinc germanate (Zn_2GeO_4) phase on the surface of Ge/Er^{3+}/ZnO TPs during annealing. The zinc germanate in Fig. 58 was present in a separate phase with clear boundaries to neighboring ZnO crystalline phases. They could also be present in as a mixture of phases as shown in Fig. 59. A Fast

Fourier Transform (FFT) image (the inset in Fig. 59) indicates that ZnO (100) and Zn_2GeO_4 (116) planes share the same spots labeled by a white circle.

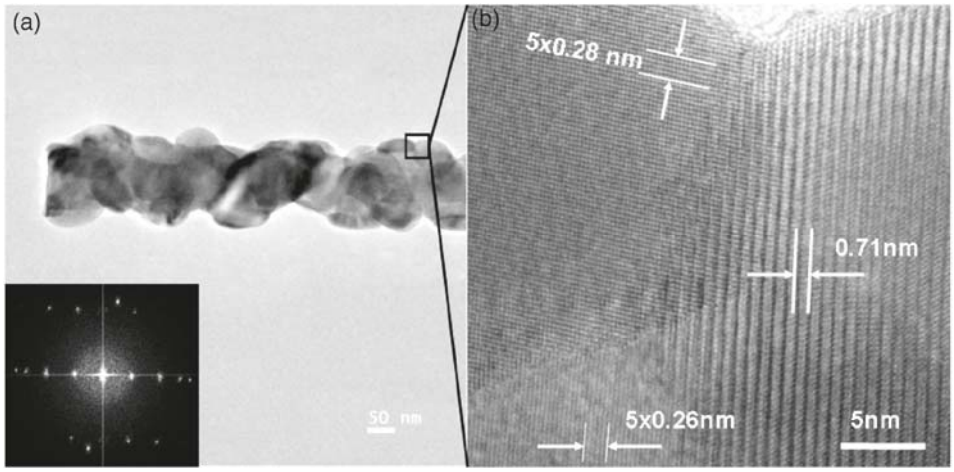

Figure 58. (a) TEM image of a tetrapod arm exposed to Ge vapor, followed by an Er precursor. (Inset: FFT image). (b) HREM image showing the lattice features associated with ZnO and Zn_2GeO_4.

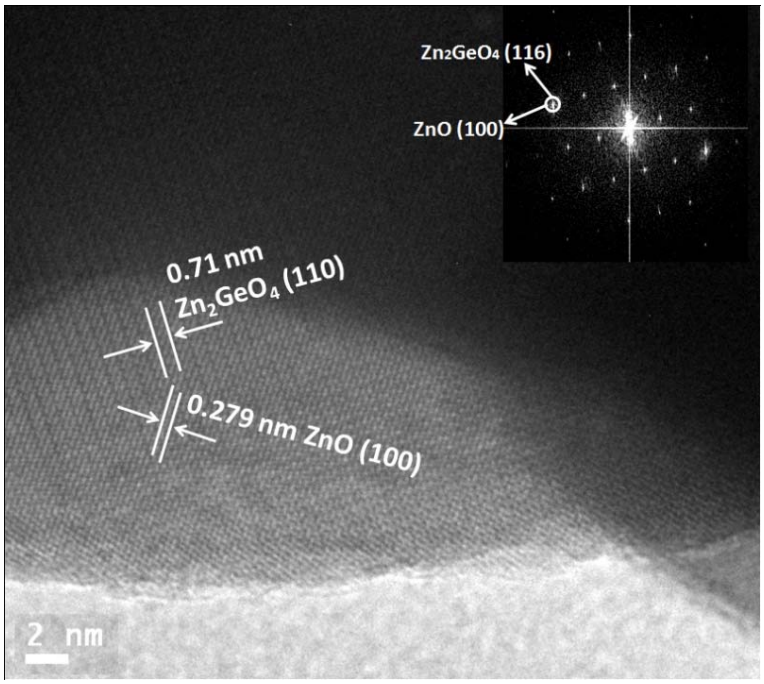

Figure 59. HRTEM images of Ge/Er^{3+}/ZnO TPs with a mixture of crystalline composition of ZnO and Zn_2GeO_4. Inset: FFT of this corresponding lattice image.

3.2.4 XRD Spectra

XRD spectra (Fig. 60) show an enhancement of crystallinity after the annealing temperature was increased from 700℃ to 900℃. For the Er^{3+}/Ge/ZnO sample, some weak peaks are identified, suggesting the possible presence of Er_2O_3 (111) (2θ ≈ 30°), Zn_2GeO_4 (2θ ≈ 30.54° and 33.06°), and GeO_2 (2θ ≈ 26.94°).[287-289] The Ge/Er/ZnO structure does not exhibit these peaks, presumably because of relatively lower Ge/Er concentrations.

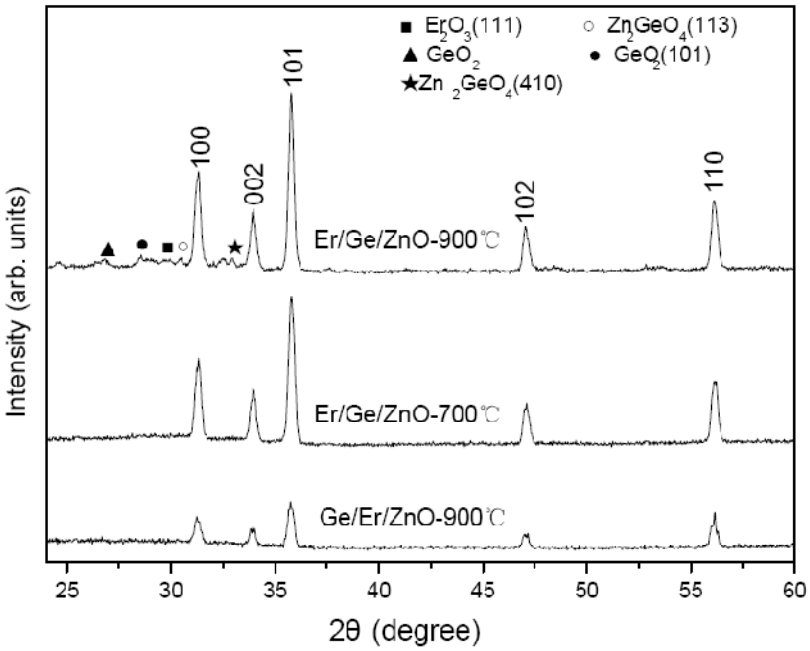

Figure 60. X-ray diffraction pattern of Er & Ge modified ZnO TPs after annealing at different temperatures.

3.2.5 Room Temperature Er^{3+} Photoluminescence Spectra

Because no PL spectra could be achieved at room temperature from Ge/Er^{3+}/ZnO TPs annealed at 700 ºC, it is necessary to employ a relatively high temperature anneal (900 ºC) to sufficiently activate the Er^{3+} PL at 1540 nm luminescence associated with the

($^4I_{13/2} \rightarrow {}^4I_{15/2}$) transition; the PL spectrum is shown in Fig. 61. This annealing condition is likely a consequence of the relative strength of the polar Zn-O framework and the energy required to allow insertion of Er-oxo species into the surface layers. Such treatment provides the necessary noncentrosymmetric oxygen-rich coordination environment for optical activity.

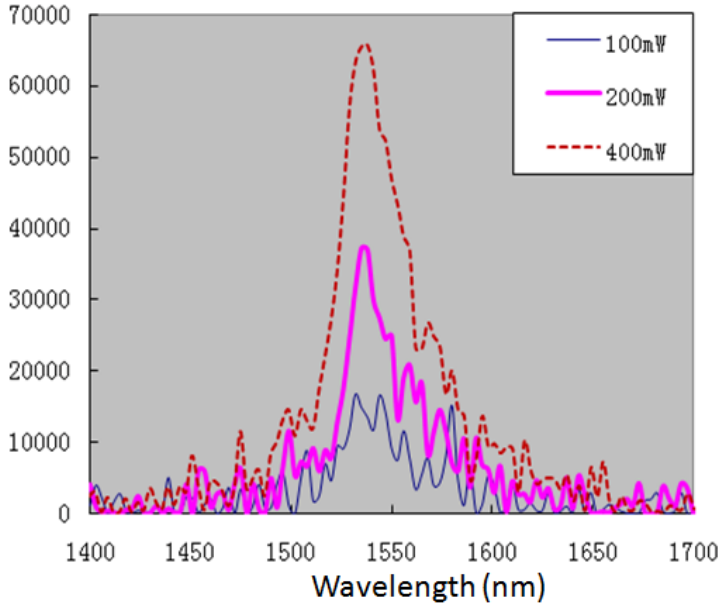

Figure 61. Room temperature Er^{3+} PL from Er^{3+}/ZnO TPs (~2.5 wt% Er) annealed at 900 ºC in O_2 for 1 h. Excitation wavelength: 488 nm.

After the sample in Fig. 61 was deposited with ~10% Ge and annealed at 900 ºC in O_2 for 1h, the PL of Ge/Er^{3+}/ZnO was greatly improved in terms of intensity and line-shape as shown in Fig. 62a. The PL intensity of Er-doped ZnO TPs increases by ~10 times after Ge deposition. A result of direct excitation of Er^{3+} was confirmed by excitation wavelength dependence experiments when excitation wavelengths were changed from

476 nm to 514 nm (Fig. 62b). This is expected as a consequence of the oxygen-rich environment and subsequent complete oxidation of the germanium to an insulating matrix.

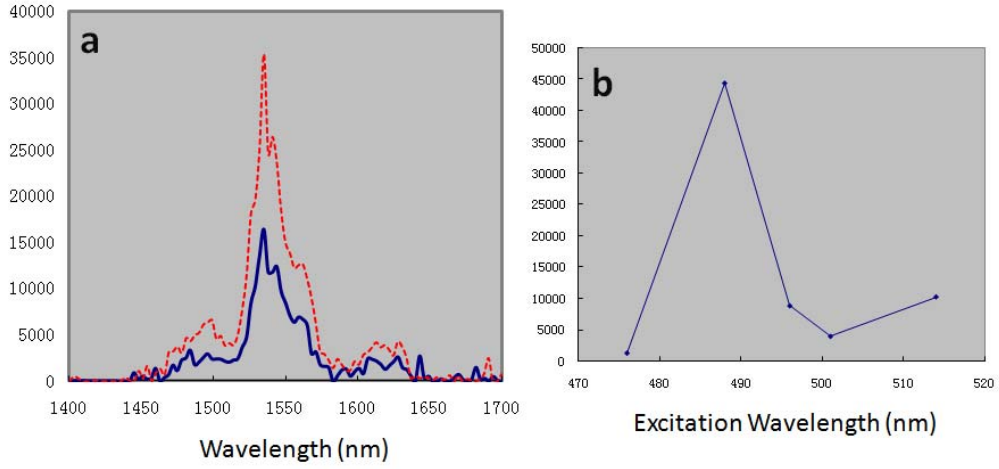

Figure 62. Room temperature Er^{3+} PL from Ge/Er^{3+}/ZnO TPs (a) Annealed at 900 ºC in O_2 for 1h. The excitation powers were 200 mW (solid line) and 400 mW (dashed line), respectively. (b) Photoluminescence excitation. Excitation wavelength: 488 nm.

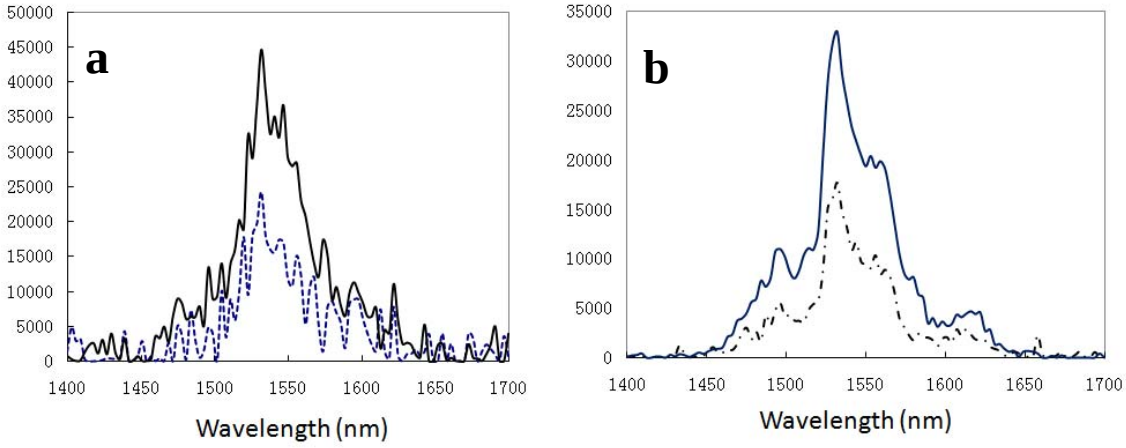

Figure 63. Room temperature Er^{3+} PL from Er^{3+}/Ge/ZnO TPs (a) Annealed at 700 ºC in O_2 for 1h. The excitation powers were 200 mW (solid line) and 400 mW (dashed line), respectively. (b) Annealed at 900 ºC in O_2 for 1h. The excitation powers were 100 mW (solid line) and 200 mW (dashed line). Excitation wavelength: 488 nm.

Er^{3+}/Ge/ZnO TP structures exhibit weak light emission at 1540 nm after annealing at 700 ºC (Fig. 63a). By increasing the annealing temperature to 900 ºC, Er^{3+} PL obtains improvement as expected (Fig. 63b), in terms of the PL intensity and lineshape. These results indicate that incorporation of Ge increases PL efficiency in this system. A possible reason is that it permits increased solubility of the rare earth ions relative to that of the zinc oxide surface (thereby reducing Er-Er interactions and associated self-quenching).

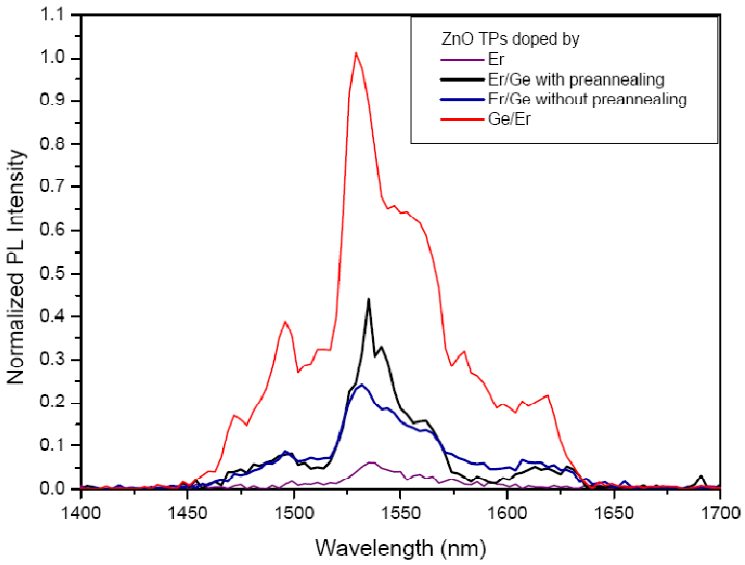

Figure 64. Room temperature photoluminescence spectra of ZnO TPs with doped structures: (a) Er^{3+}/Ge/ZnO; (b) Ge/Er^{3+}/ZnO with preannealing applied in O_2 for 1 h before Ge deposition; (c) Ge/Er^{3+}/ZnO without preannealing; (d) Er^{3+}/ZnO. All spectra were excited by a laser power of 200 mW, and all samples have been annealed in O_2 at 900 ºC for 1 h.

For the Ge/ Er^{3+}/ZnO structures, a preannealing step (700 ºC, 1 h) applied before Ge deposition is slightly helpful in increasing the Er^{3+} PL intensity as shown in Fig. 64.

Switching the order of addition of Ge and Er^{3+} has a much more significant effect on Er^{3+} emission intensity; Ge exposure, followed by Er^{3+}, yields a more intense variant, presumably because of more efficient excitation higher pump efficiency without shielding from Ge or its oxide. This is expected as a consequence of the oxygen-rich environment and subsequent complete oxidation of the germanium to an insulating matrix. It is also interesting to note that the Er^{3+} PL associated with ZnO TPs apparently shows more Stark splitting,[261,290] representing a lower symmetry of Er^{3+} sites in the host matrix and higher coordination numbers. A blue shift of the peak at 1540 nm was observed with a maximum value of 11 nm, especially with Ge deposition.

3.2.6 UV/visible photoluminescence measurements

Again, with the assistance of Yuri M. Strzhemechny, UV/visible PL measurements were used to assess the impact of erbium and germanium incorporation on the photophysical properties of ZnO TPs. The PL of ZnO typically includes near-band-edge (NBE) ultraviolet emission and deep-level trap features (usually broad peaks in the visible region). ZnO TPs show three low-temperature NBE emission lines at 3.367, 3.315, and 3.226 eV, and one or more peaks in the visible.[104-107, 291] In the studies reported here, intense deep defect emission appears at ~2.4 eV in both room and low temperature PL spectra (Fig. 65a). One relatively weak near-band gap emission broad peak was observed

at 3.163 eV in the room temperature PL spectrum. By contrast, low temperature PL spectrum shows 5 peaks from 3.021 to 3.357 eV that can be assigned to surface defect-related excitation and bound exciton complexes.[261, 292] The presence of the Er^{3+} ions

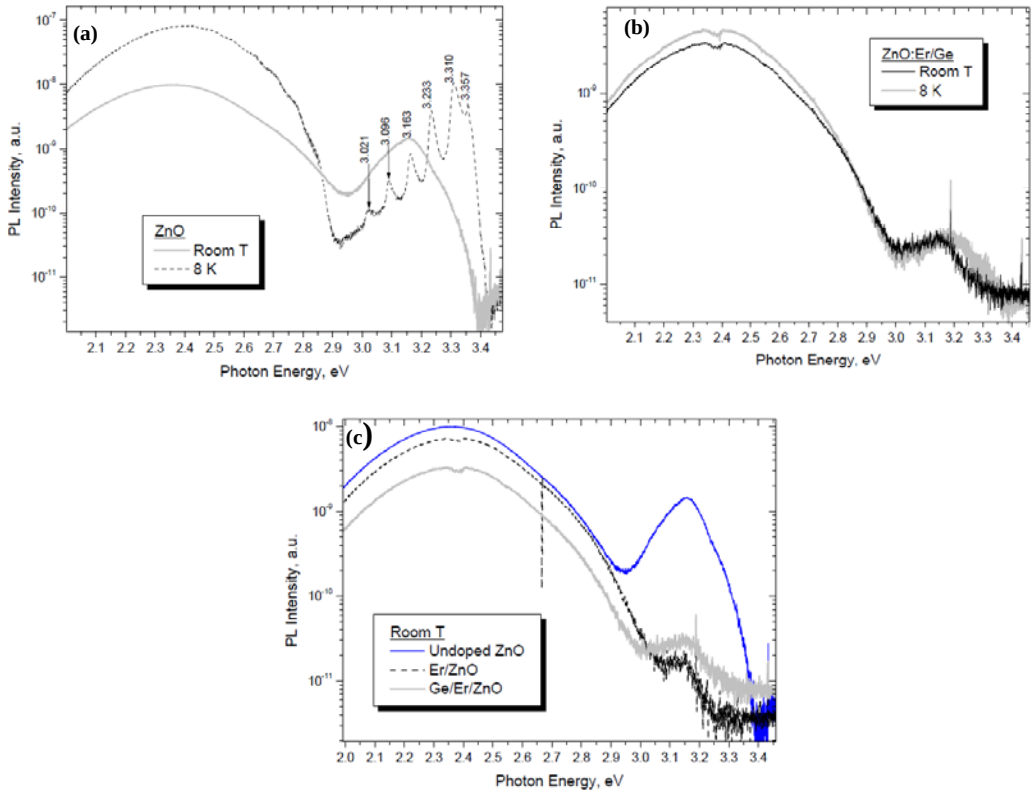

Figure 65. UV/visible PL spectra of ZnO TPs at room temperature and low temperature (8K) for (a) Undoped ZnO TPs; (b) Ge/Er-doped ZnO TPs; (c) ZnO, Er-doped ZnO and Ge/Er-doped ZnO TPs.

demonstrates a quenching effect on the ZnO band-edge emission (Fig. 65b). Most significantly, it is noteworthy that a relatively weak adsorption structure appears at 2.383 eV (520 nm) after Er^{3+} deposition. The adsorption is caused by Er^{3+} doping and is enhanced by Ge deposition (Figs. 65b,c); the increased intensity of this feature with Ge

incorporation also directly correlates with the enhanced Er^{3+} PL intensity observed in this type of structure in Fig. 64. The fact that the absorption structure is relatively insensitive to temperature from 8 K to room temperature confirms the intrashell nature of this transition. The energy transfer from ZnO to Er^{3+} ions can probably be associated with the $^2H_{11/2}$ level because of a second order cooperative upconversion interaction between Er^{3+} ions in the $^4I_{11/2}$ state (populated from the $^4I_{9/2}$ state) and ZnO. [256, 293, 294]

3.3 Summary

In this chapter, ZnO TPs were fabricated by Zn granule evaporation in air at ~990℃ in a one-end-sealed quartz reactor. The amount of Zn granules used as source significantly affects the morphology and size of ZnO, which correlates to oxygen concentration. The arm size of ZnO TPs (shorter but bigger) and the amount of ZnO sheets produced could be increased considerably in a gas phase with high Zn vapor concentration or low O_2 content. It implies that the morphology of ZnO TPs is location-dependent along the deposition area.

Furthermore, Er^{3+} ions, both with and without a germanium (Ge) sensitizer layer, have been introduced onto the surface of ZnO tetrapod structures. Such structures, characterized by electron microscopy and X-ray diffraction, are found to emit at both the UV/ visible and near-infrared as a consequence of the presence of ZnO/ Er^{3+}. Considerable enhancement of Er^{3+} PL was made possible by Ge deposition, with the most significant enhancement observed when the erbium ions are deposited closer to the outer surface (Er^{3+}/Ge/ZnO). Energy transfer between ZnO and Er^{3+} took place with a wavelength of 520 nm verified by ZnO PL spectra, with Ge deposition again facilitating the process.

It is also interesting to note that the Er^{3+} PL associated with ZnO TP apparently shows more Stark splitting than other system we have investigated. With the change of surface optical structure, a blue shift was observed in the Er PL at 1540 nm with a maximum of 11 nm. The possible utility of these and related types of structures in energy conversion and photonics warrants further investigation.

CHAPTER IV.

Emissive Er/ZnO/ Silicon and Germanium Oxide Nanofibers Derived from an Electrospinning Process

4.0 Overview

The incorporation of optically active erbium ions into oxide matrices is a targeted component of a long-term strategy toward the fabrication of integrated optoelectronic circuits operating at 1.5 μm.[272] Previous workers in our laboratories have fabricated various erbium-containing Si or Ge nanostructures with strong Er^{3+} ion photoluminescence.[268-273] Ji Wu in our group reported a facile method to fabricate strongly emissive SnO_2 nanofibers containing erbium ions in relatively high concentrations by combining electrospinning techniques and sol-gel processing.[273] His further work revealed that an oxidized Ge layer, as sensitizer deposited onto Er-doped SnO_2 nanofibers, could result in a significant enhancement (~2 orders of magnitude) of the room-temperature luminescence at 1540 nm due to a carrier mediated excitation process.[295]

In Chapters III and IV, surface modification of nanostructures based on Er-doped Ge nanowires and ZnO tetrapods was investigated. Both Er^{3+} and ZnO photoluminescence (PL) can be observed from such structures, the properties of which depend upon the surface crystal structure involving alloy formation of zinc germanate. The presence of Ge in these nanostructures can enhance Er^{3+} PL remarkably, while ZnO does not provide similar enhancement to Er^{3+} PL, only providing its own light emission in the UV/Visible range. However, the weak absorption features in ZnO visible PL spectra at 520 nm suggested the presence of energy transfer from ZnO to Er^{3+}, which implies a complex interaction between such species in these nanostructures containing Er, GeO_x and ZnO.

In this Chapter, Er/SiO_2/ZnO and Er/GeO_x/ZnO nanofibers (stabilized by PVP or PEO) were fabricated to further investigate the impact of ZnO on Er^{3+} PL. Solutions containing Zn, Er and Si/Ge precursors undergo various forms of hydrolysis and polycondensation reactions during electrospinning to form the metal or semiconductor oxide. Compared to VLS methods, electrospinning is an efficient process to fabricate 1D nanoscale materials in high yield. In principle, sol-gel methods can provide precise control of the composition of solid state products. A homogeneous distribution of elements, especially the dispersion of Er^{3+}, is conducive to the formation of Er-O complexes and the reduction of Er agglomeration, which strongly influences the intensity of Er^{3+} photoluminescence (PL).[296] Nanofiber products were characterized by a combination of SEM, TEM, EDX, XRD and PL measurements, as described in previous chapters.

4.1Experimental Methods

4.1.1 Fabrication of Er-doped SiO_2/ZnO PVP nanofibers

To prepare Er-doped SiO_2/ZnO PVP nanofibers, typically 0.45 g polyvinylpyrrolidone (PVP, 0.60 g, Mw = 1.3 M, Aldrich) and 0.14~0.28 g zinc acetate hydrate (Gelest) were dissolved into 3 ml MeOH (99.99%, Pharmco) to form solution I (as shown in Table 2), and then 0.007~0.050 g Er(III) *i*-propoxide (99.9%, Strem) and 1.3~2.2 ml tetraethyl orthosilicate (TEOS, 98%, Aldrich) were dissolved into a mixture of 1.0 ml MeOH and 0.5 ml acetic acid (Mallinckrodt AR) to form solution II. Solution I and solution

II were mixed by vortex shaking. The mixture was then loaded into a glass syringe equipped with a 21 gauge stainless steel needle for electrospinning (Fig. 15). A 25 kV accelerating voltage (DC) was applied to the solution through the metal needle, 15 cm away from a drum covered by a piece of aluminum foil for the fiber collection. As-fabricated nanofibers were exposed to air for complete hydrolysis for 24 h.

Table 2. Typical compositions of Er-doped SiO_2/ZnO PVP reaction mixtures.

	Er concentration (%wt) in nanofibers measured by EDX					
	16		9		3	
	Sol-I	Sol-II	Sol-I	Sol-II	Sol-I	Sol-II
PVP (g)	0.45		0.45		0.45	
MeOH (ml)	2.0	1.0	2.0	1.0	2.0	1.0
	3.0		3.0		3.0	
Zn precursor (g)	0.28		0.14		0.28	
HOAc (ml)		0.5		0.5		0.5
Er precursor (g)		0.05		0.020		0.0070
TEOS (ml)		1.34		2.2		2.2
Mass of Si (g)	0.25		0.4		0.4	
Mass of Zn (g)	0.083		0.042		0.083	
Mass of Er (g)	0.021		0.0097		0.0034	
Er concentration (%wt)	5.9		2.1		0.6	

4.1.2 Fabrication of Er-doped GeO_x/ZnO PEO nanofibers

To prepare Er-doped GeO_x/ZnO nanofibers, typically 0.02~0.1 g poly(ethylene oxide) (PEO, Mw=900,000, Aldrich) was dissolved into 3 ml $CHCl_3$ (99.5%, Pharmco) to form solution I, and then 0.005~0.025 g Er(III) i-propoxide (99.9%, Strem), 0.07 ml tetraethoxygermane (TEOG, Gelest), and 0.14 g zinc acetate hydrate (Gelest) were dissolved into a mixture of 2.0 ml MeOH (99.99%, Pharmco) and 0.5 ml acetic acid

(Mallinckrodt AR) to form solution II. Solution I and solution II were mixed by vortex shaking and then used for electrospinning. The electrospinning setup was the same as described above. Such mixtures typically provide 1~6%wt Er and 7~16%wt Zn concentration in as-fabricated nanofibers, which is comparable to the elemental composition for a typical Er/ZnO-modified core-shell GeNW described in Chapter II.

4.1.3 Fabrication of Er/ZnO/ Si and Ge oxide nanofibers

As-prepared nanofibers need to be annealed in O_2 for 2~8 h at temperatures of 500, 600, 650, 700, or 900 °C before PL measurements. The polymer template was decomposed during annealing, and the annealing can also significantly enhance the Er^{3+} PL intensity due to the reduction of Er-Er interactions and additional oxygen insertion reaction.

4.2 Results and Discussion

4.2.1 Characterization of Er-doped SiO_2/ZnO PVP nanofibers

4.2.1.1 Morphology of Er-doped SiO_2/ZnO nanofibers

SEM images of Er-doped SiO_2/ZnO nanofibers are shown in Fig. 66a with a ratio of Er:Si:Zn ~ 16:49:35 (%wt). The average diameter of these nanofibers is ~180 nm and the

histogram of the corresponding size distribution is shown in Fig. 67. The morphologies of nanofibers became bent and some fused together after annealing in air for 1h at 500, 600 or 650 °C as shown in Figs. 66b, c and d, respectively.

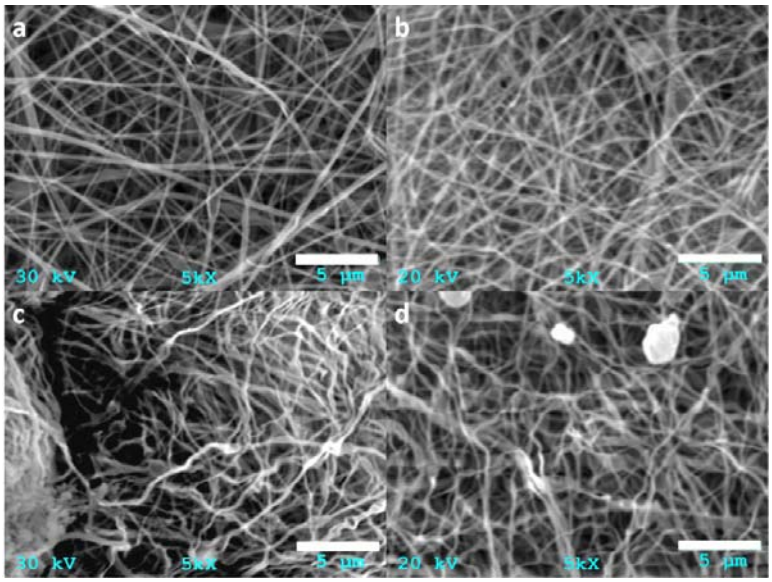

Figure 66. SEM images of Er-doped SiO_2/ZnO PVP nanofibers (16 wt % Er concentration) before annealing (a) and after annealing in air for 1h at (b) 500 °C, (c) 600 °C, (d) 650 °C. All scale bars are 5 µm.

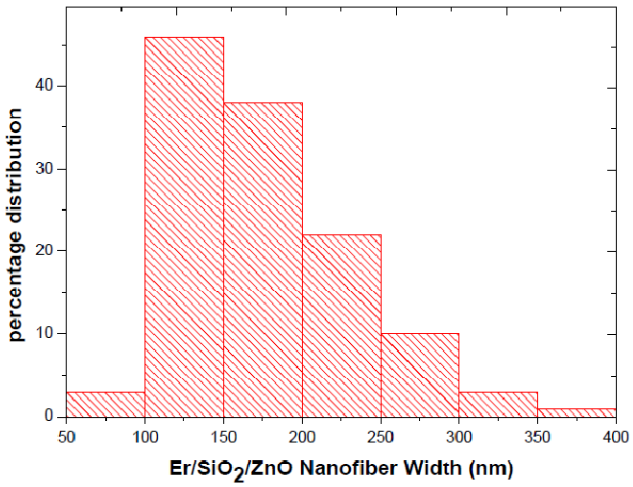

Figure 67. Histogram representing the size distribution of Er-doped SiO_2/ZnO PVP nanofibers without annealing.

4.2.1.2 PL spectra of Er-doped SiO_2/ZnO nanofibers

Fig. 68 shows the annealing temperature dependent Er^{3+} PL spectra of Er-doped SiO_2/ZnO PVP nanofibers measured at room temperature. The PL intensity from a sample annealed at 650 °C is enhanced by 85% relative to one annealed at 600 °C and ~1400% compared to one annealed at 500 °C.

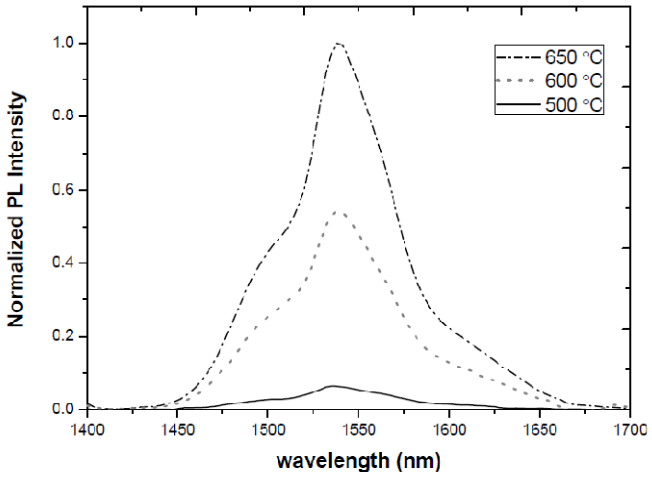

Figure 68. Er^{3+} ion PL spectra of Er-doped SiO_2/ZnO nanofibers at different annealing temperatures (Er:Si:Zn =16:49:35, %wt).

4.2.1.3 Carrier-mediated photoluminescence

Erbium PL excitation spectra of Er-doped SiO_2/ZnO nanofibers are shown in Fig. 69. Spectrum B shows a steady diminution of Er^{3+} PL intensity excited by increasing excitation wavelength ranging from 476 to 514 nm. The normalized PL intensity for Er-doped Ge NWs as a function of excitation wavelength suggests a type of carrier-mediated pathway.[272,268] Spectra A also reveals a similar excitation wavelength

dependence as spectrum B, except for a little lower PL intensity when excited by the 488 nm line, which also implies the presence of carrier-mediated excitation. Since erbium ions can be directly excited into ligand field states when 488 and 514 nm wavelengths are used, spectrum C of Fig. 69 shows a direct excitation pathway due to higher Er^{3+} PL intensity observed by using 488 nm and 514 nm excitation. Considering the earlier observation that spectra B and C are from samples with similar composition, the enhanced PL efficiency at 514 nm could result from the higher annealing temperature of 600 °C.[272]

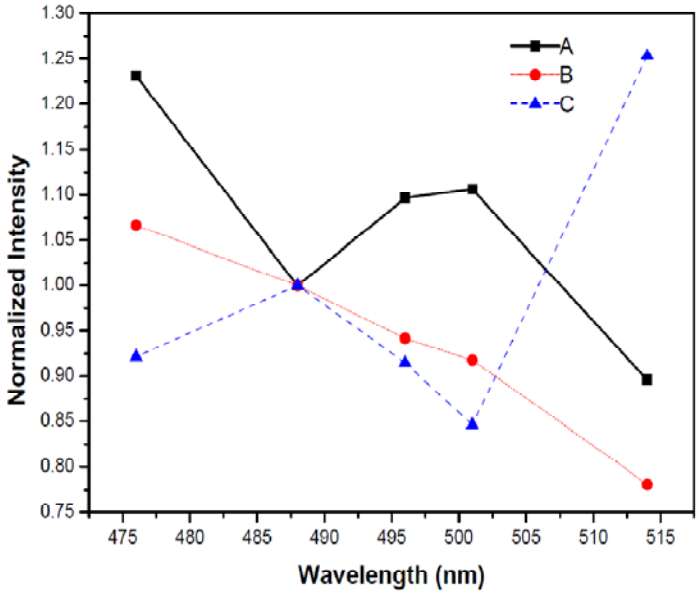

Figure 69. PL excitation spectra of Er-doped SiO_2/ZnO nanofibers with (a) the composition of Er:Si:Zn =4:61:35, annealing temperature:700 °C. (b) Er:Si:Zn =10:35:54, annealing temperature:500 °C. (c) Er:Si:Zn=10:38:52, annealing temperature: 600 °C.

4.2.2 Characterization of Er-doped GeO_x/ZnO PEO nanofibers

4.2.2.1 Morphology of Er-doped GeO_x/ZnO PEO nanofibers

Although PVP proved to be a good host material for the fabrication of Er-doped SiO_2/ZnO nanofibers, it is not compatible with TEOG in this case due to gel formation during the mixing process. PCL (polycaprolactone, Mw=65,000, Aldrich) can be used to fabricate Er-doped GeO_x/ZnO nanofibers, but it requires longer times (2~3 h) to dissolve into $CHCl_3$. In contrast, PEO dissolves readily in methanol, and is miscible with the other sol-gel precursors. SEM image and an EDX spectrum of Er-doped GeO_x/ZnO PEO nanofibers are shown in Fig. 70a before annealing. Their morphologies (average diameter ~400 nm) did not change significantly after annealing at 600 °C in air for 4 h (Fig. 70b). After annealing at higher temperature (700 °C), Er-doped GeO_x/ZnO PEO nanofibers fused together with increased sizes (average diameter ~540 nm) and the network structures formed as shown in Fig. 70c. EDX spectra indicated that the composition of as-fabricated nanofibers remains relatively constant before and after annealing.

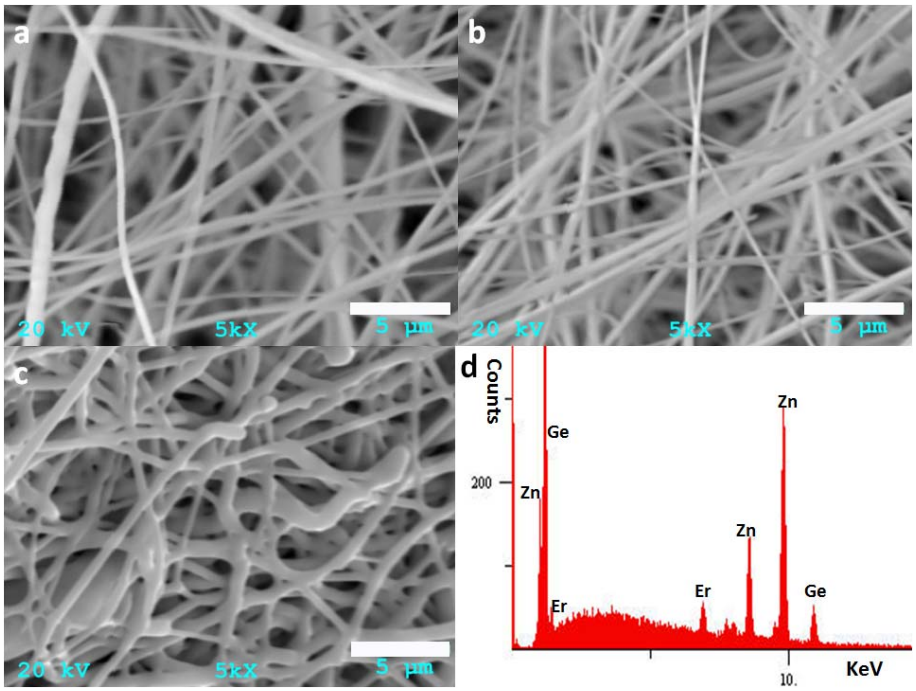

Figure 70. SEM images of typical Er-doped GeO_x/ZnO nanofibers. (a) Before annealing; and after annealing in air for 4 h at (b) 600 °C and (c) 700 °C. All scale bars are 5 µm. (d) EDX spectrum of Er-doped GeO_x/ZnO nanofibers before annealing. The ratio of nanofibers (Er:Ge:Zn) is 19:75:6 (wt).

In order to reduce the fusion of nanofibers caused by melting during annealing, one approach is to decrease the mass of polymer used relative to the mass of Zn/Er/Ge precursor used, which relatively increases the proportion of precursors to polymer. An associated advantage is that the diameter of as-prepared nanofibers could be decreased. Fig. 71 shows the size distribution of Er-doped GeO_x/ZnO PEO nanofibers as a function of PEO concentration. The average diameters of nanofibers are 400 nm, 510 nm, and 1.2 µm, corresponding to masses of PEO used of 0.02, 0.04 and 0.1 g, respectively.

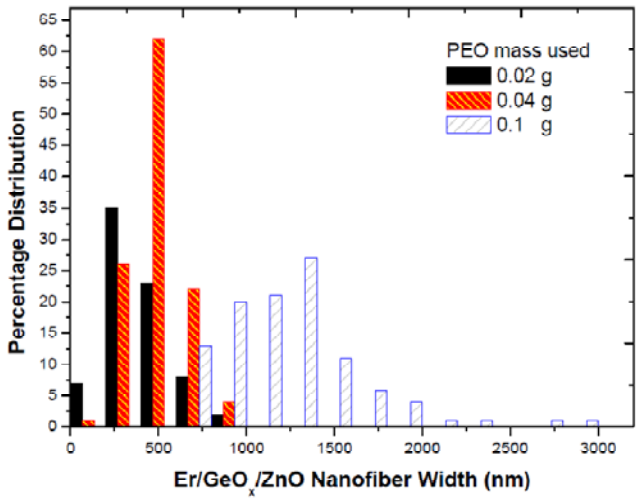

Figure 71. Histogram representing the size distribution of Er-doped GeO_x/ZnO nanofibers with the different PEO mass used.

4.2.2.2 Photoluminescence spectra of Er-doped GeO_x/ZnO nanofibers

Er-doped GeO_x/ZnO PEO fibers demonstrate a stronger Er^{3+} PL intensity, which is surprising given the relatively weak emission of Er/ZnO-modified core-shell GeNWs described in Chapter II. Fig. 72 shows that the Er^{3+} PL intensity of Er/GeO_x/ZnO nanofibers (2.6% atom Er, annealing at 700 °C for 4 h) excited by a laser power of 10 mW is close to that of Er/SiO_2/ZnO nanofibers excited by 100 mW laser power, and 2 times more intense than that of an Er-doped SiO_2 glass standard sample. The PL measurement conditions are listed in Table 3. Additionally, a higher Er concentration (2.6%atom Er) also displays higher Er^{3+} PL intensity by ~20 times than the sample with lower Er concentration (0.4% atom Er) without obvious Er-Er interaction quenching, which means that Er^{3+} ions have very uniform dispersion in such a nanofiber system. PLE

spectral measurements also show that the Er PL results from the direct ligand field excitation in samples having a composition of Er/Ge/Zn ~ 2.6:74.7:22.7 (%atom).

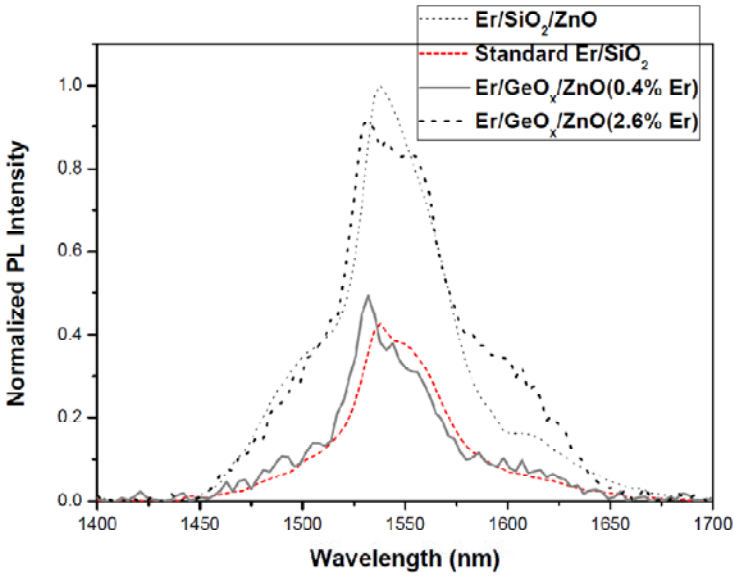

Figure 72. Er^{3+} ion PL spectra from $Er/SiO_2/ZnO$ nanofibers, standard Er/SiO_2 glass, and $Er/GeO_x/ZnO$ nanofibers with different Er concentrations. The composition of samples is listed in Table 3.

Table 3. The composition of samples in Fig. 72 and PL measurement conditions.

	Composition (%atom)				Annealing Temperature and Time	Excitation power (mW)
	Er	Ge	Si	Zn		
Er-doped SiO_2 glass	0.5	------	99.5	------	------	100
$Er/SiO_2/ZnO$	0.9	------	79.5	19.6	700 °C 4 h	100
$Er/GeO_x/ZnO$	0.4	79.7	------	19.9		100
$Er/GeO_x/ZnO$	2.6	74.7		22.7		10

4.2.2.3 XRD Spectra of Er-doped GeO_x/ZnO nanofibers

XRD spectra shown in Fig. 73 indicate that the concentration of Er^{3+} in the nanofiber can influence the crystal structure of GeO_x/ZnO. For Er-doped GeO_x nanofibers, the amorphous Ge oxo species have transformed to GeO_2 crystals after annealing at 700 °C (Spectrum a in Fig. 73). In the presence of Zn (18%wt), Ge (~81%wt) can form a Zn_2GeO_4 alloy phase. Spectrum b in Fig. 73 shows that the crystalline phases contain both Zn_2GeO_4 and GeO_2 crystals with 1%wt Er content. Compared with spectrum a, spectrum b

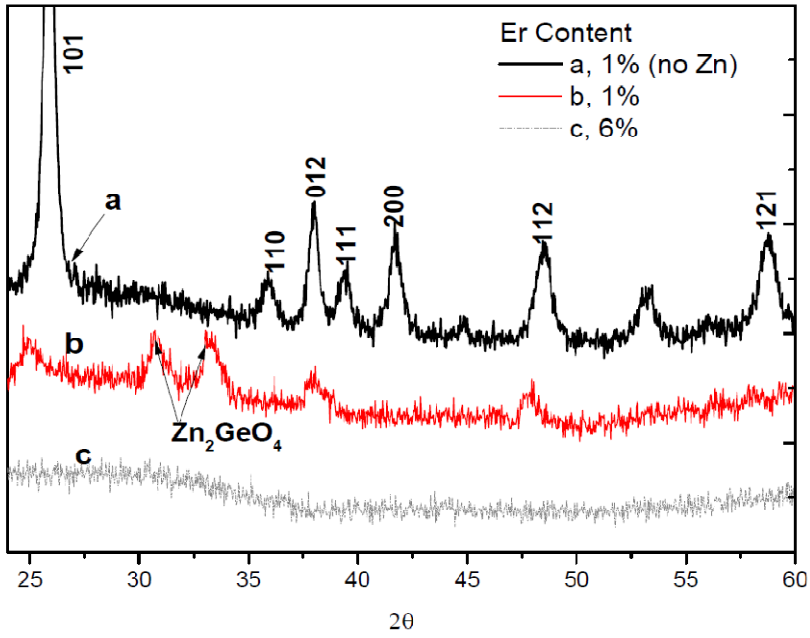

Figure 73. XRD spectra of Er/GeO_x/ZnO nanofibers (1%wt and 6%wt Er) with same ratio of Zn and Ge as well as Er/GeO_x nanofibers (1%wt Er). All samples were annealed at 700 °C in air for 4 h.

reveals more broad peaks, which means a smaller crystallite size or more strain in this system.[296,297] When the Er content increases up to 6%wt, all characteristic peaks diminish

(Fig. 73c). Such a sample can provide very strong Er^{3+} PL. This result implies that Er doping likely hinders crystallization of any new phases. Such a disordered phase contributes to the reduction of Er-Er interactions and the striking Er^{3+} PL even in very high Er concentrations e.g. ~18%wt.

4.3 Summary

In this Chapter, Er/SiO_2/ZnO PVP nanofibers and Er/GeO_x/ZnO PEO nanofibers were fabricated by electrospinning of selected sol-gel precursor solutions. These types of nanofibers exhibited strong Er^{3+} near IR photoluminescence at 1.54 μm after annealing to remove the polymer template.

Photocarrier-mediated excitation processes were frequently observed in Er/SiO_2/ZnO nanofibers, with a composition and annealing temperature dependence. Not surprising, the Er^{3+} PL preferred a direct excitation mechanism with higher annealing temperature. The room temperature quenching caused by Er-Er interactions does not have any remarkable effects on the intensity of Er^{3+} PL in the nanofibers described here, even with very high Er concentrations (~18% wt) due to well-dispersed Er locations.

GeO_x can significantly enhance Er^{3+} PL. The high Er concentration in GeO_x/ZnO nanofibers possibly inhibits crystalline phase formation, which contributes to the more uniform dispersion for Er (according to XRD spectral analysis). Thus the intensity of Er^{3+} PL was not diminished by increasing Er concentration, as compared with other literature reports involving Er-implanted Si systems.[256,296] Such an observation is also consistent with results from Er/ZnO-modified GeNWs in Chapters II and III.

CHAPTER V

The Fabrication of Fluorine-doped ZnO Nanowires

5.0 Overview

One of the most promising applications of doped ZnO nanostructures is with regard to transparent conductivity. Transparent conductors are materials with low electrical resistivity (~10^{-4} Ω.cm) and high transmittance of visible light (>85%).[298-300] This standard classifies thin metal films and metal oxide films as the best transparent conductor materials. However, a large number of free electrons effect the transparence of metals, thereby the requirement in the thickness of metal film is very strict. Large band gap semiconducting metal oxides such as indium oxide, cadmium oxide, tin oxide and zinc oxide can be doped with impurity atoms to reduce their resistivity while retaining high transparency in the visible spectrum.[298] Compared with others, ZnO has several advantages including non-toxicity, widespread availability from natural sources, and chemical stability. Al-doped ZnO transparent conductor films have been commercialized.[301] Unlike indium and other Group III elements as p-type dopants in ZnO, fluorine and other n-type dopants have been studied far less. Fluorine-doped ZnO is a good candidate to be used as a high quality transparent electrode in solar cell applications.[300]

Studies have shown that oxygen chemisorbed on nanocrystal surface三 serves as traps for charge carriers, thus increasing the interfacial potential and lowering carrier mobility. Doping with halogen atoms can be very effective in preventing oxygen adsorption on surfaces.[132,298,299] For example, an experimental strategy has been developed for incorporating F ions into ZnO nanocrystalline films via oxidizing ZnF_2

film.[298] The results indeed show that the presence of F ions inside and outside of nanocrystals can effectively eliminate the well-known defect-associated visible emission.

ZnO NWs recently have been investigated intensively for potential applications in FETs, sensors, solar cells, LEDs, lasers, H_2-storage, etc.[108,130,131,133] However, F-doped ZnO NWs prepared through VLS mechanism have not been reported to our knowledge. The improved electrical conductivity of ZnO NWs by F-doping is expected to be conducive for electron collection in solar cells. In this work, F-doped ZnO nanowires were fabricated by heating the mixture of ZnO powder, ZnF_2, and carbon powder (or graphite powder), with or without a carrier gas (Ar).[112,124] Different substrates, including Si wafers, graphite cloth, and sapphire (all coated with Au catalyst) were used to grow ZnO NWs. Furthermore, F-doped ZnO shell/ZnO core nanowires have also been synthesized by chemical vapor deposition. As-prepared samples were characterized by a combination of electron microscopies and X-ray diffraction (XRD) as described in previous chapters. Low-temperature ZnO PL was recorded in the labs of Professor Strzhemechny using the set-up described in Chapter II.

5.1 Experimental Methods

5.1.1 F-doped ZnO NW fabrication

In this work, two kinds of methods were used to fabricate F-doped ZnO NWs. In the first one, a one end-sealed quartz reactor is used to grow F-doped ZnO NWs (without gas

flow). When the temperature of the reactor has reached 880~900 °C, a source loaded with the mixture of ZnO powder, carbon powder and ZnF_2 powder (mass ratio, 20:25:1) was inserted into the reactor (22 mm) and located in the middle of the furnace. Another boat containing a given substrate (Si, sapphire or graphite cloth, coated with 5~10 nm Au catalyst) was then pushed into the reactor and left substrates 2~6 cm away from the compound source. By increasing the temperature to 930 °C and maintaining it for 1h, F-doped ZnO NWs could be formed on the substrates.

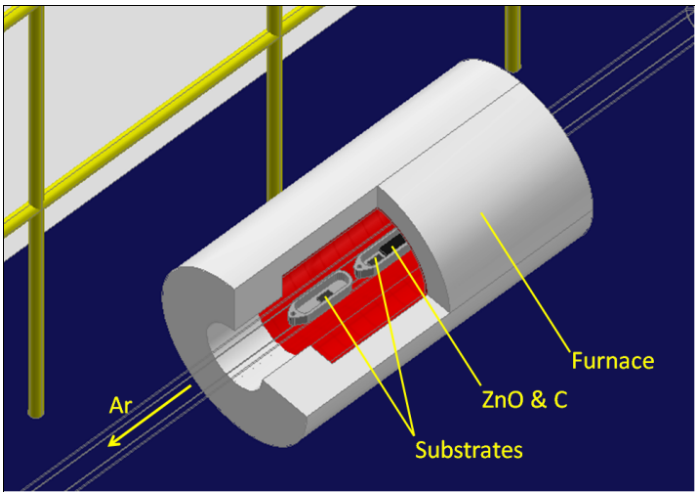

Figure 74. Scheme of F-doped ZnO fabrication reactor.

In the second method, F-doped ZnO NWs were synthesized under conditions using Ar carrier gas (50~190 sccm). The location of compound source and substrates (Si or sapphire wafer) is shown in Fig. 74 with separation distances of 5~7 cm. A typical mass ratio (ZnO:C:ZnF_2) was 200:30:1. When the reactor temperature reaches 900 °C, O_2 is introduced into the system at a flow ratio of 1/40 (relative to the amount of carrier gas).

The white or gray F-doped ZnO NWs could be found after the reaction when a temperature range from 900 to 950 °C for 20 min is used.

5.1.2 F-doped ZnO/ZnO core-shell nanowire fabrication

ZnO shells were formed on the ZnO cores by Zn deposition, followed by annealing in O_2. CVD and PVD processes were used to make Zn coating on the surface of F-doped ZnO NWs, respectively. In the CVD process, Zn precursor (zinc acetylacetonate hydrate, Gelest) was sublimed at ~140 °C and then decomposed in the furnace (500 °C) to form a surface layer onto F-doped ZnO NWs. The experimental setup is same as shown in Fig. 19a. In another procedure, 50 mg Zn granules (Aldrich, 100 mesh, 99.8%) were evaporated at 440~500 °C in He gas (300 sccm), and then Zn vapor cooled down and deposited onto the surface of F-doped ZnO NWs. The setup is same as shown in Fig. 19b.

5.2 Results and Discussion

5.2.1 F-doped ZnO NWs grown in method I (without carrier gas)

5.2.1.1 On Si or sapphire substrate

As described in Chapter I, ZnO is reduced by carbon to form Zn vapor at high temperatures, and then Zn is condensed on the substrate at lower temperatures to form ZnO NWs. However, carbon powder is easily consumed in oxygen-rich surroundings at

high temperature. The compound source boat had to be inserted into the reactor when the temperature was ready in method I because one end of reactor is open to air. Usually a cork stopper was used to seal the reactor after source and wafer boats were placed into the reactor. Additionally, the ZnF_2 melting point (872 °C) needs to be considered for the selection of reaction temperature. The presence of ZnF_2 vapor is necessary to fulfill F-doping. Therefore boats were inserted into the reactor at 880~900 °C. The reaction temperature is important to successfully synthesize nanowires, which is directly related

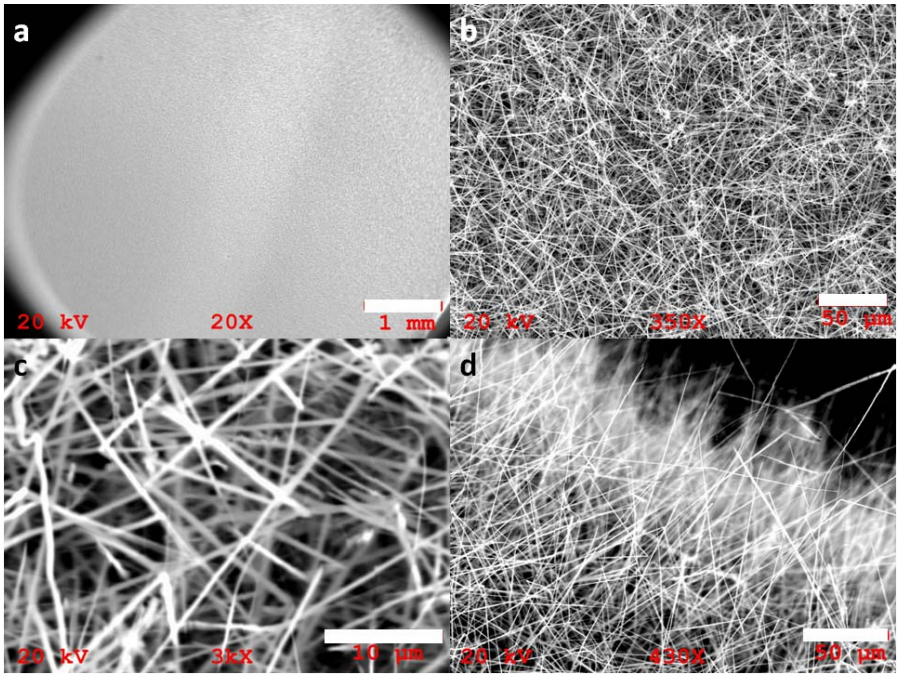

Figure 75. SEM images of F-doped ZnO NWs in different magnification. Scale bars in (a) (b) (c) and (d) are 1 mm, 50 µm, 10 µm and 50 µm, respectively.

to the vapor composition in the reactor, especially in the region between the sealed end and the deposition area. Although a wide range of reaction temperatures have been used(from 680 to 1100 °C) for ZnO NWs fabrication via CVD methods,[295,302] the

optimum temperature is found to be about 930 °C. As-grown F-doped ZnO NWs are shown in Fig. 75. The average NW diameter is ~440 nm, with sizes ranging from 150 nm to 800 nm. Increasing amounts of $ZnO/C/ZnF_2$ has a remarkable impact on the morphology of ZnO NWs, including the formation of bigger feature sizes (~1.7 μm) in Fig. 76(a), increasing amount of undesired particles (b), more nanobelts (c) and nanorods (d). High concentrations of Zn in the gas phase (relative to a lower O_2 concentration) always results in larger size, Zn-rich nanostructures.

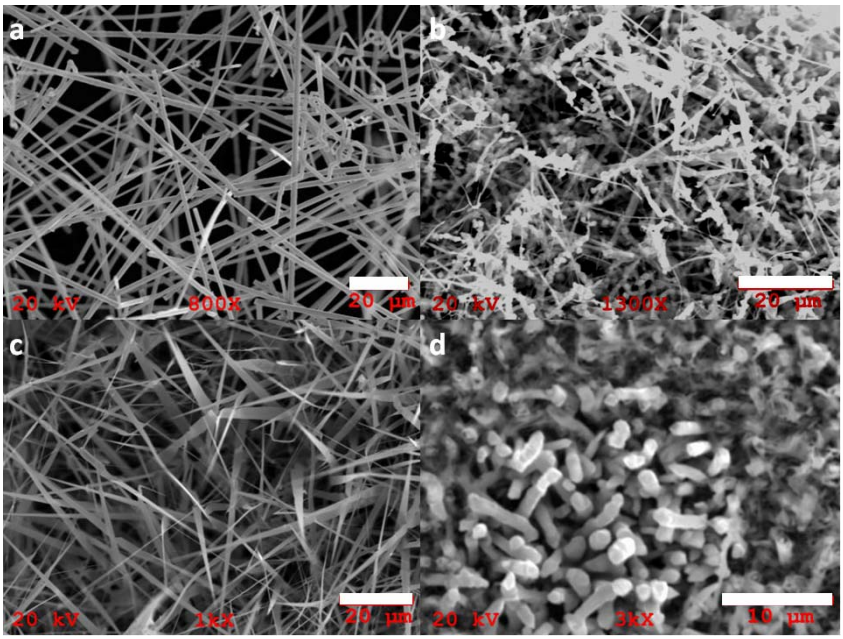

Figure 76. SEM images of ZnO NWs with large amount of compound sources (100 mg ZnO, 50 mg C). Scale bars in (a)(b)(c) and (d) are 20 μm, 20 μm, 20 μm and 10 μm, respectively.

In this work, the typical amount of ZnO mass used was about 20~40 mg with the same amount of carbon powder. If the reaction temperature is increased, the deposition

area can move toward the low temperature area. Such an effect can also be achieved by increasing the amount of ZnO/C used, which is useful to locate the suitable position for optimal ZnO NW growth. ZnO NWs only grow in the deposition area near the open end of the reactor. Toward the sealed end, ZnO formed in the type of nanorods as shown in Fig. 77. In a reactor containing water vapor, the morphology of ZnO looks flocked (Fig. 78).

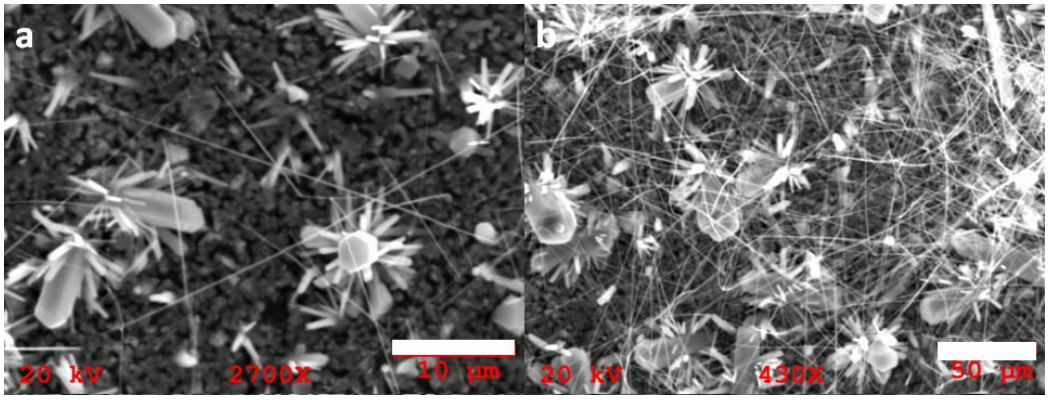

Figure 77. SEM images of flower-like F-doped ZnO NWs grown on the wafer close to the source boat (compound sources: 40 mg ZnO, 30 mg C, 2 mg ZnF_2). Scale bars in (a) and (b) are 10 µm and 50 µm, respectively.

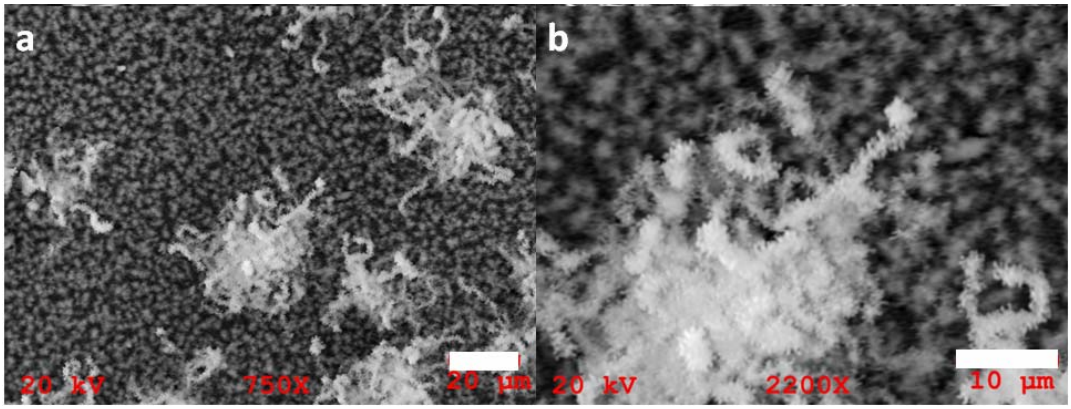

Figure 78. SEM images of flocked F-doped ZnO NWs. Scale bars in (a) and (b) are 20 µm and 10 µm, respectively.

In a given reactor, the diameter and the volume contained in the furnace are the most important parameters, which determine the operational flexibility of experiments. For example, it is found that if the reaction temperature was higher than 950 °C, large ZnO microwires (3-9 μm) with rough surfaces could be found in the side of deposition area near the open end of the reactor. A possible reason is that higher temperatures shrink the effective deposition area, and thus Zn vapor concentrations continuously supply the rapid growth of ZnO at high temperatures and high O_2 concentrations to form such microwires as shown in Fig. 79.

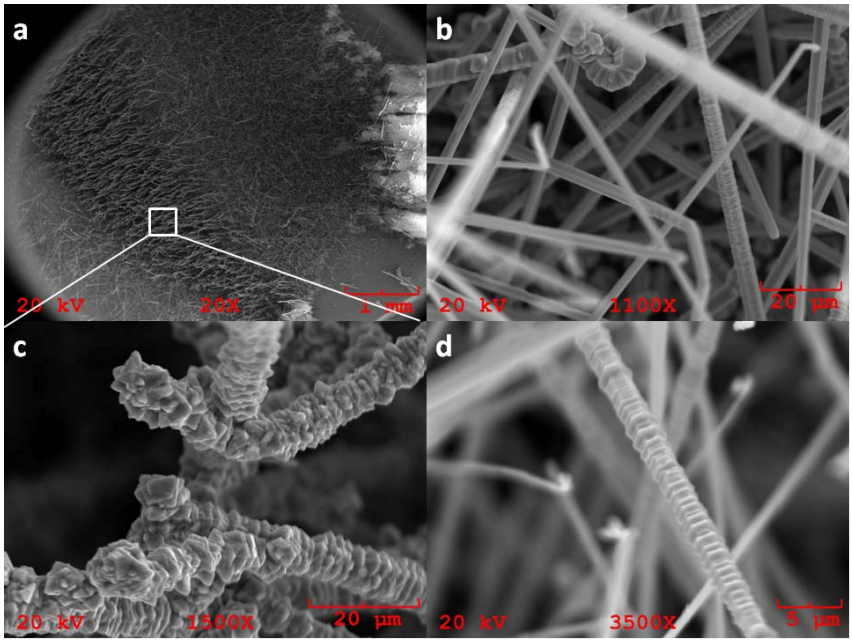

Figure 79. SEM images of micron-scale F-doped ZnO NWs. Scale bars in (a)(b)(c) and (d) are 1 mm, 20 μm, 20 μm and 5 μm, respectively.

Nanowires usually have preferential growth directions, e. g. ZnO NWs grow along

the (001) direction, which can be affected by the substrate used to grow nanowires. ZnO can grow epitaxially on a- and c-plane sapphire (lattice constant a = 0.475 nm, c =1.294 nm), due to their hexagonal crystal structures and very small lattice mismatch (<0.08%).[102] However, here we did not find any remarkable difference between Si wafers and sapphire in terms of morphologies of ZnO NWs, perhaps because rapid NW growth inhibited the epitaxial seeding process.

5.2.1.2 On graphite cloth

Under the conditions utilized, F-doped ZnO NWs grown on Si or sapphire possessed relatively large widths (~440 nm). Reducing the size of Au catalyst from 10 nm to 2 nm did not generate an effective reduction in NW width. Graphite cloth exhibits a capacity to limit the size of GeNWs as mentioned in Chapter II, because the curved surface of graphite fibers hinders the Au diffusion to form big islands. Another predictable effect is that the reducing surface of graphite fibers could slow down ZnO NWs growth, for the O_2 concentration would be decreased by the reaction of graphite and O_2. F-doped ZnO NWs grown on graphite cloth are shown in Fig. 80. F-doped ZnO NWs display very good coverage and uniform size distribution on this substrate. The average diameter is ~154 nm, much less than that on Si or sapphire substrates. In areas of the reactor closer to the source boat, the diameter of ZnO NWs became larger with needle-like shape, as shown in Fig. 80d. The base of ZnO needles is ~800 nm.

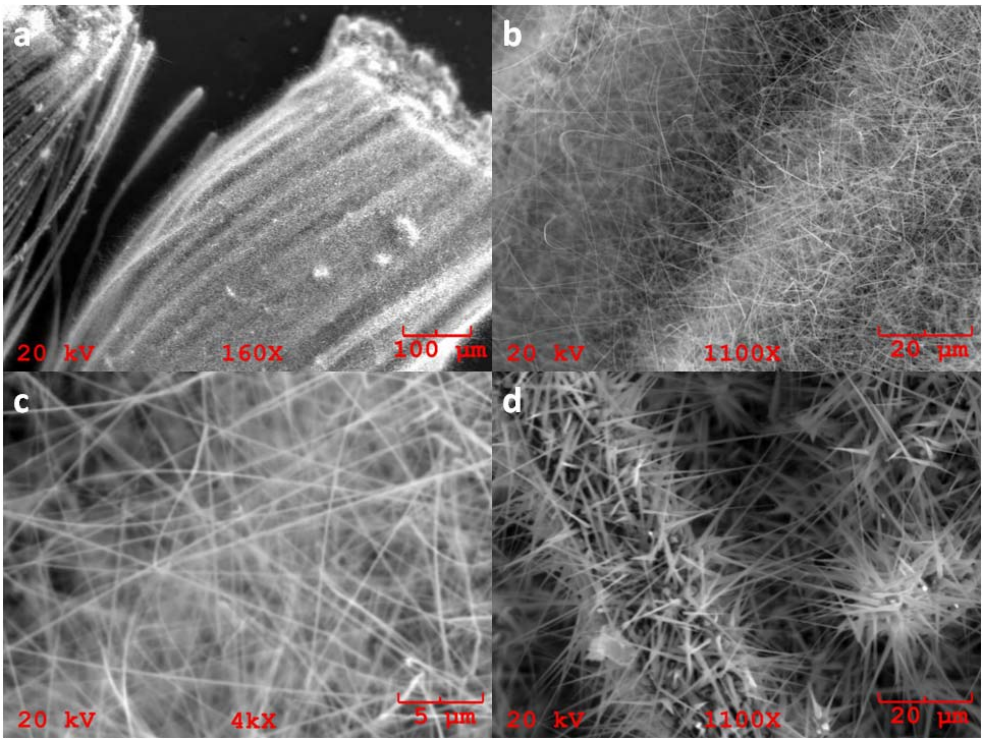

Figure 80. SEM images of F-doped ZnO NWs grown on graphite cloth.

5.2.1.3 Morphology and composition of F-doped ZnO NWs characterized by HRTEM and EDX

TEM images of F-doped ZnO NWs (on Si wafers) are shown in Fig. 81 at different magnifications. The HRTEM image shows a nanowire with a (002) growth direction. However, an EDX spectrum (Fig. 82) indicates that these F-doped ZnO NWs are zinc-rich with varying ratios of Zn & O. The typical F content was about 2~6%(wt).

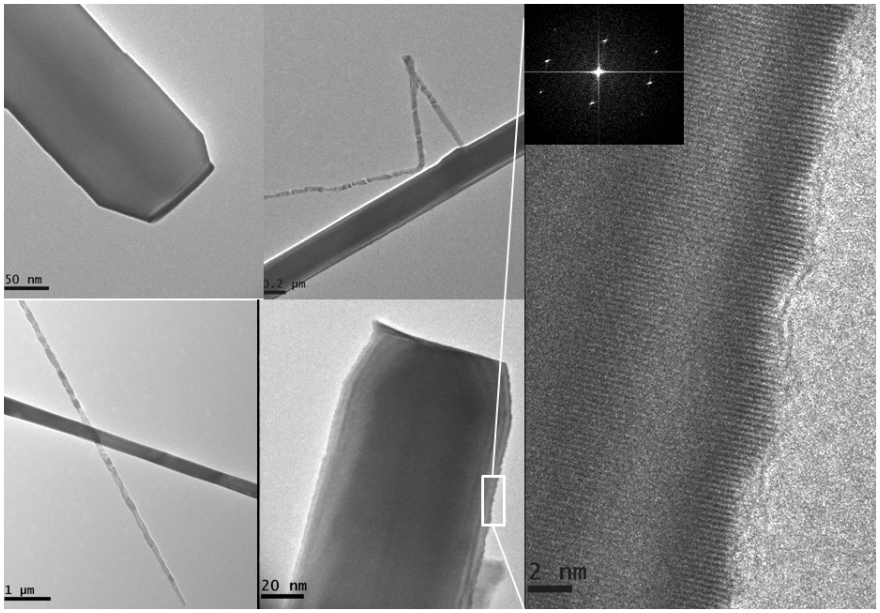

Figure 81. TEM images of F-doped ZnO NWs grown on Si wafer.

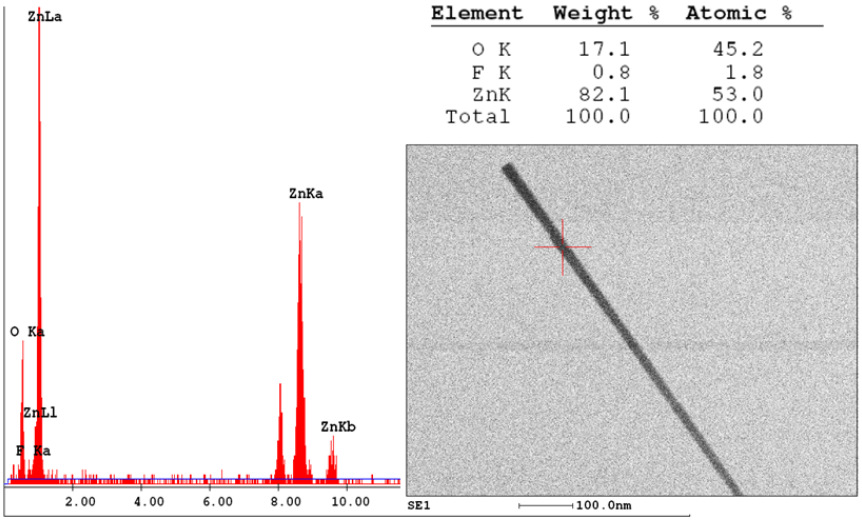

Figure 82. EDX spectrum of F-doped ZnO NWs grown on Si wafer.

F-doped ZnO NWs grown on graphite cloth often remain with the Au catalyst at the tip as shown in Fig. 83, which confirms that the Au catalyst controls the size of as-grown nanowires. A distinct core-shell structure (Fig. 84) is found by using TEM to characterize those samples having been annealed in O_2 at 700 °C for 1h. Both core and shell grow along the (001) plane, thereby two (001) spots can be found in the fast Fourier transform (FFT) image. However, it is hard to identify which process (synthesis or preannealing) that contributes to the formation of such a structure based on this one observation.

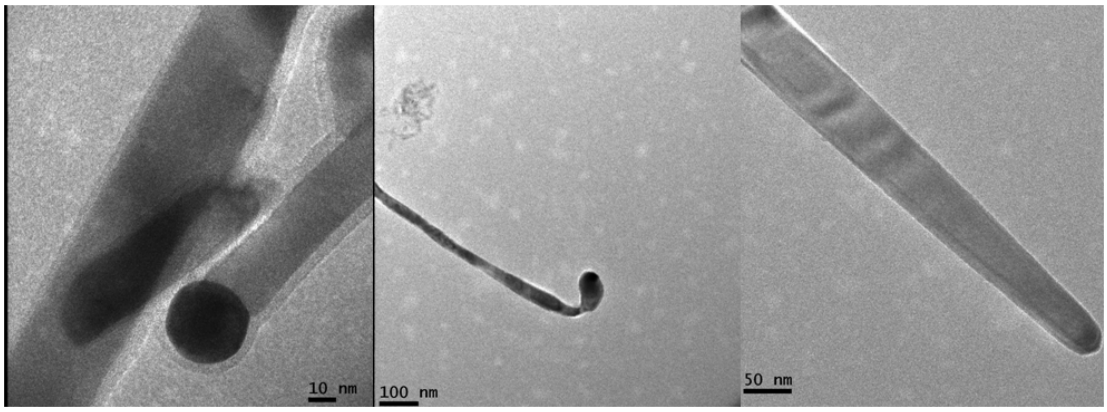

Figure 83. TEM images of F-doped ZnO NWs grown on graphite cloth.

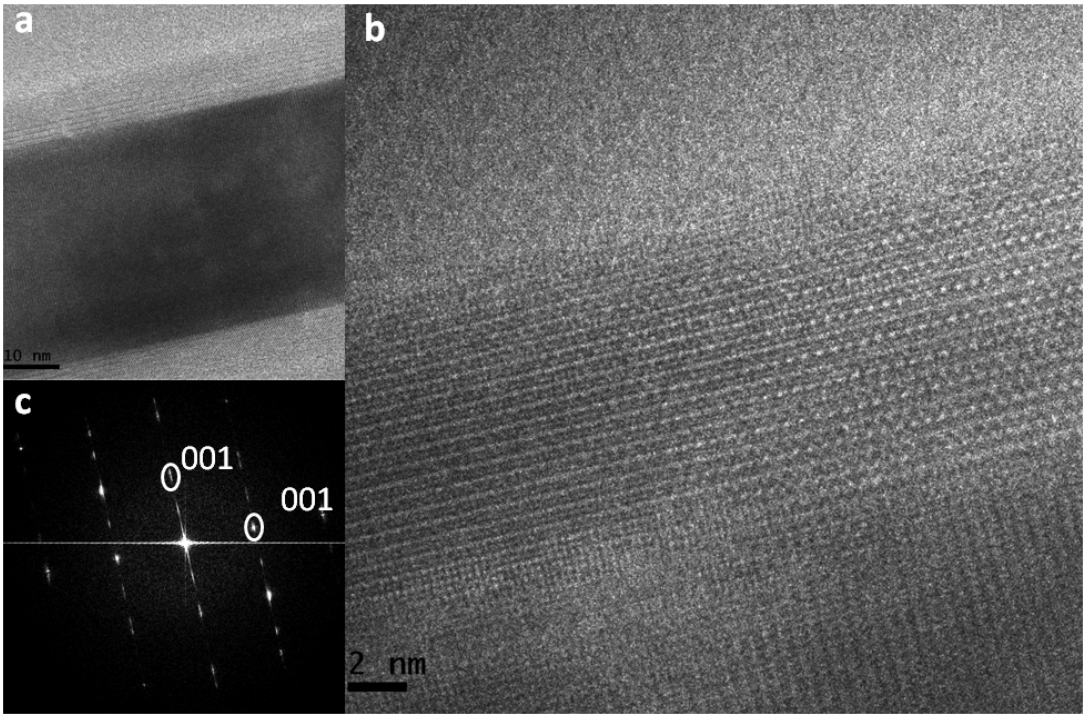

Figure 84. (a) HRTEM images of F-doped ZnO core-shell NW grown on graphite cloth, with higher magnifications (b), and the corresponding FFT image.

5.2.2 F-doped ZnO NWs grown by method II (with carrier gas)

The goal of this new method was to give better control over the vapor composition, which significantly impacts the morphology of products. With method I, no ZnO NW arrays could be fabricated even on sapphire substrates (c- or a-plane). Carrier gas can dilute the reactant composition in the gas phase in order to control the growth rate of nanowires. Various carrier gas rates were investigated and the optimal gas flow was found to be ~ 60 sccm, in conjunction with a reaction temperature of 930 °C for 20 min. The corresponding mass ratio of ZnO/graphite powder/ZnF_2 is 300:45:2. The morphology of F-doped ZnO NWs grown on Si substrates in method II is shown in Fig. 85a. However, we also find that ZnO NWs (Figs. 85b, c) grow vertically without a

predeposited ZnO buffer layer.[295] It is interesting to note that the XRD spectrum (Fig. 86) shows that these ZnO NW arrays did not have any preferential growth epitaxy. In contrast, ZnO NW arrays with or without F-doping on c-sapphire both reveal[a preferential growth along the (002) direction.

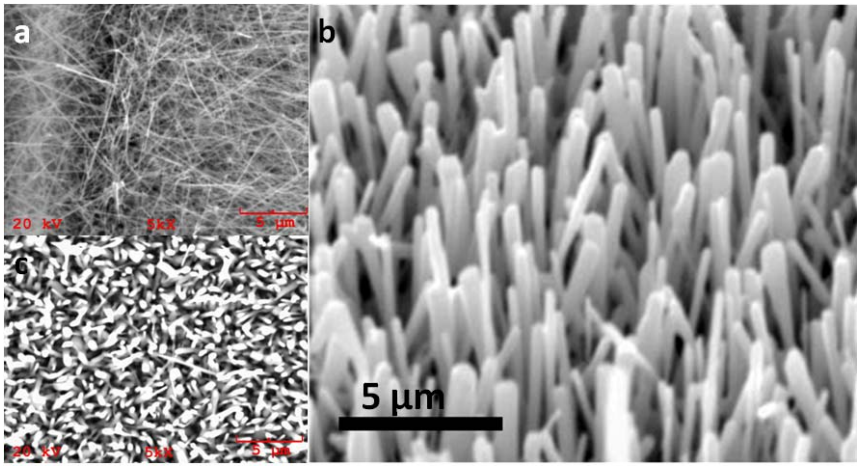

Figure 85. SEM images of ZnO NWs grown on Si wafer. (a) With F-doping. (b)(c) Without F-doping. Image (b) is the view of image (c) with 40° tilt.

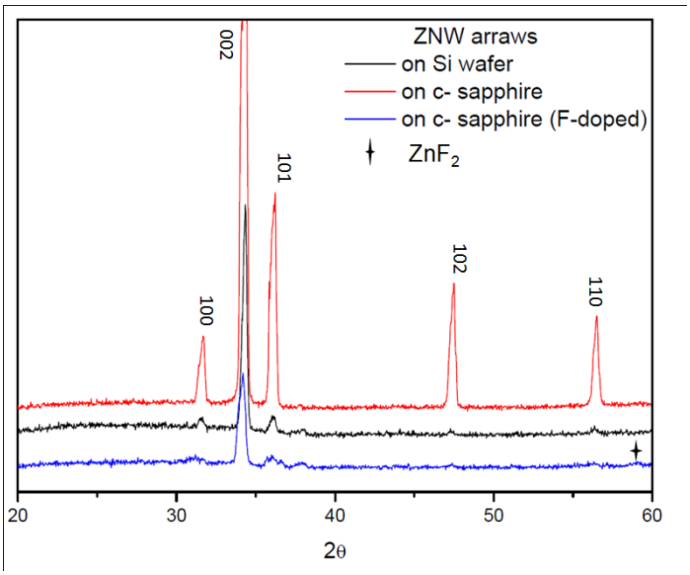

Figure 86. XRD spectra of ZnO NW arrays on Si wafer and c-sapphire substrates.

Fig. 87 shows the morphology of F-doped ZnO NW arrays grown on c- and a- plane sapphire substrates. O_2 could not be introduced to the reaction system until the reaction temperature is up to 900 °C (beyond the melting point of ZnF_2, 872 °C) for F-doping. Thus the composition in the gas phase is dynamic during nanowire growth, which caused complicated shifts of reaction equilibrium involved in the carbon thermal reduction (as described in Chapter I). For example, the reaction between the ZnO and carbon is reversible above 900 °C, which may cause a large amount of reevaporation (ZnO NWs formed react with CO and produce Zn vapor). Therefore, more precise experimental control is necessary to make results more repeatable in the fabrication of F-doped ZnO NW arrays.

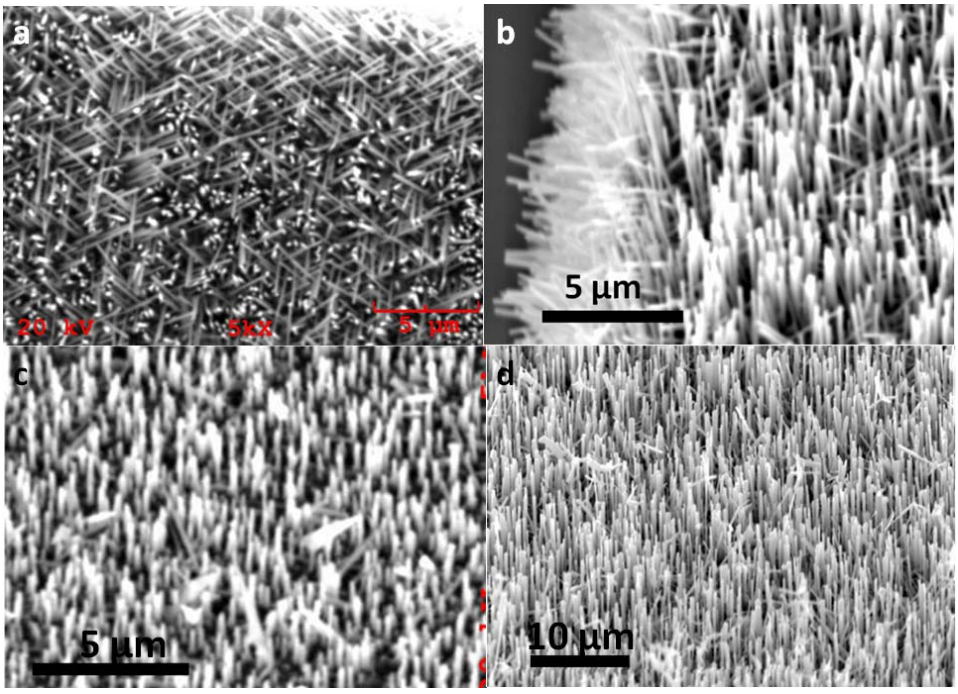

Figure 87. SEM images of F-doped ZnO NW arrays. (a)(b) On c-plane sapphire. (c)(d) On a-plane sapphire. Images of (b) (c) and (d) were obtained with 40° tilt.

Additionally, the fabrication of ZnO NWs was conducted at atmospheric pressure in this work. Previous work has shown that the pressure of the reactor system strongly affects the supersaturation level of the vapor which is critical to the morphology of ZnO NWs.[236,303] The supersaturation level seems to be higher at low pressures and decreases at higher pressures. At low pressures, this higher supersaturation leads to secondary nucleation and different types of growth since the environment is far away from thermal equilibrium. This non-equilibrium kinetic growth may create a low-surface-energy tip that allows molecules to diffuse away easily to energetic side surfaces causing the growth of nanobelts and sheets and platelets, which affects the morphology of ZnO NW arrays.[236]

5.2.3 Photoluminescence of F-doped ZnO NWs

For the F-doped ZnO NWs prepared in these studies, ZnO UV/visible PL measurements only show defect PL in the visible. Low F-doped (4%wt) ZnO NWs (~150 nm) at 8K and undoped ZnO NW arrays share the highest light emission measured because of higher PL efficiency at low temperature and lower carrier scattering in undoped samples (Fig. 88 ① and ②). ZnO NWs with similar F-doping exhibit same level of light emission, except for a small size-dependent red shift can be observed in the sample with bigger size (~600 nm).

Halogen doping has been used to reduce the number of oxygen vacancies during

ZnO growth.[126,299] Heavily doped fluorine could also reduce the emission due to the increased impurity scattering and structure defects scattering. These impacts contribute to the poor visible PL of heavily F-doped ZnO NWs (Fig. 88⑤).

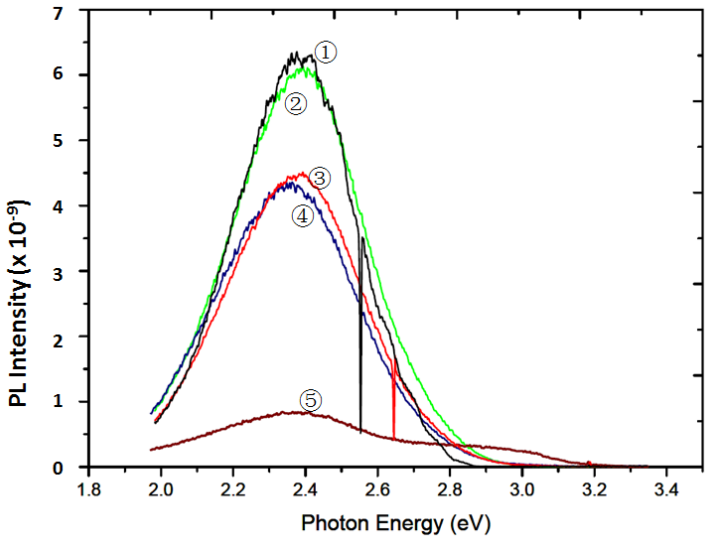

Figure 88. ZnO UV/visible photoluminescence spectra. (1) Low F-doped (4%wt) at 8K; (2) ZnO NW arrays; (3) Low F-doped (4%wt); (4) Low F-doped (4%wt) ZnO NWs with relatively larger sizes (~600 nm); (5) Heavily F-doped (20%wt).

5.2.4 F-doped ZnO/ZnO core-shell nanowires

5.2.4.1 Zn/ZnO shell using Zn granules (PVD)

Compared with the results of Zn deposition on GeNWs (described in Chapter III), the ZnO core surface seems less reactive, presumably reflecting a lower surface energy than that of GeNWs. Usually a ~10 nm Zn coating could be formed in the former within 1h of vapor exposure, while only a 2.5~5 nm Zn shell was obtained in a 3 h reaction period as shown in Fig. 89. The HRTEM image shows that the interface between

amorphous Zn layer and ZnO NW displays a tendency of crystal growth along the (001) plane. However, the identification of core-shell boundary in this case becomes challenging due to their same crystal structure. Some distinct ZnO/F-doped ZnO core-shell structures are shown in Fig. 90 after annealing in O_2 for 1h at 600 °C.

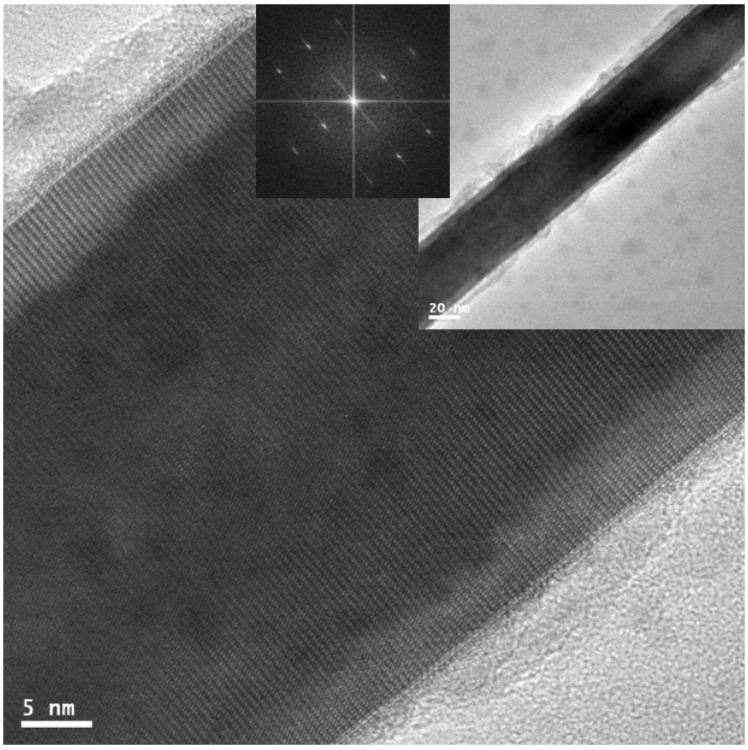

Figure 89. F-doped ZnO NWs with Zn shell by evaporating Zn granule at 460 °C, 3h (before annealing in O_2).

The thicknesses of ZnO shells are 5 nm, 2.7 nm, 2.7 nm and 2.9 nm in Figs. 90a, b, c and d, respectively. The duration for Zn evaporation for all samples was 3 h. Compared with the NW morphologies of Fig. 89, the Zn shell in these structures had transformed to a single crystal after annealing, which caused contrast with the zinc-rich nanowire core. Usually ZnO has a preferential growth epitaxy (001), as shown in Figs. 90c, d. Some

nicks could be observed on the shell perhaps because of Zn diffusion driven by a requirement to reduce surface energy. The shell in (d) shows a different diffraction pattern from (c). The reason is that the spots of (001) planes were absent with the diffraction of the core.

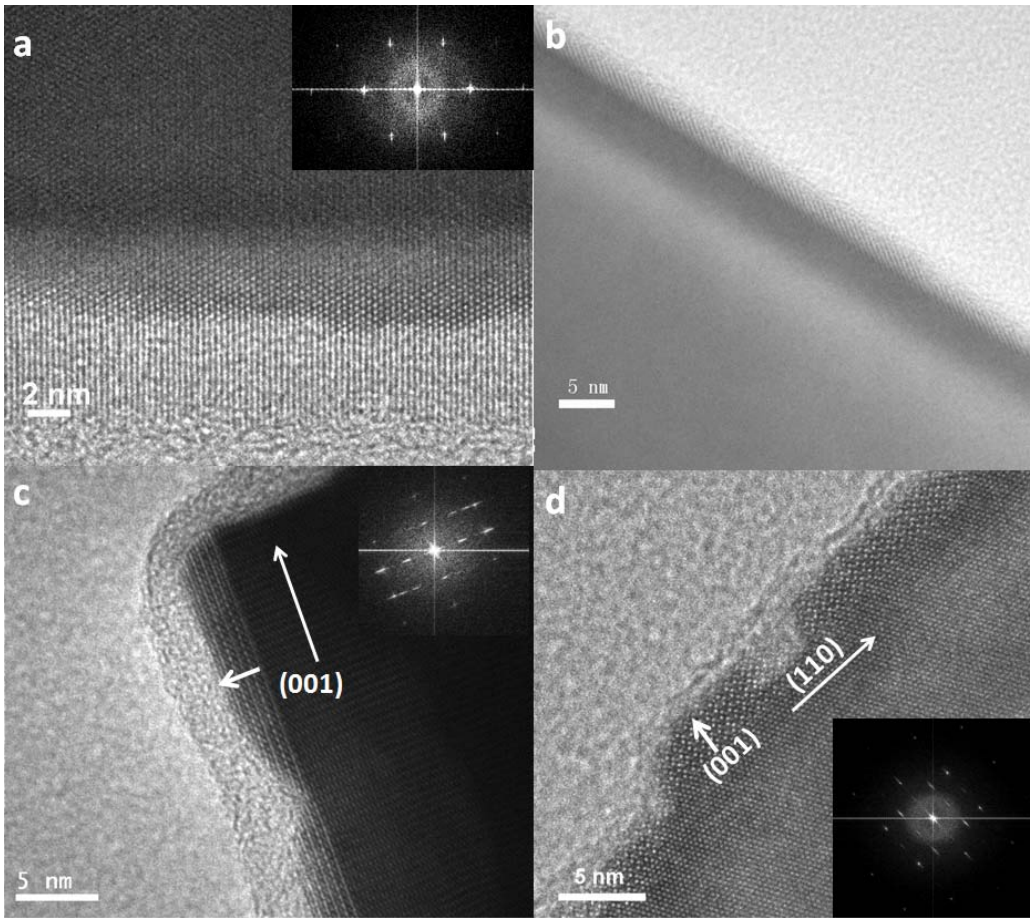

Figure 90. HRTEM images of annealed F-doped ZnO core/ZnO shell NWs (PVD process).

5.2.4.2 Zn/ZnO shell using Zn precursors (CVD)

Zn shells formed by CVD were not very stable under the TEM beam as shown in Figs. 91a,b. The thickness of shell is ~4 nm with the use of 10 mg Zn precursor.

Although the Zn shell looks more uniform than that in Fig. 89, the core-shell structure and crystal growth is poor, compared with those described in Fig. 90.

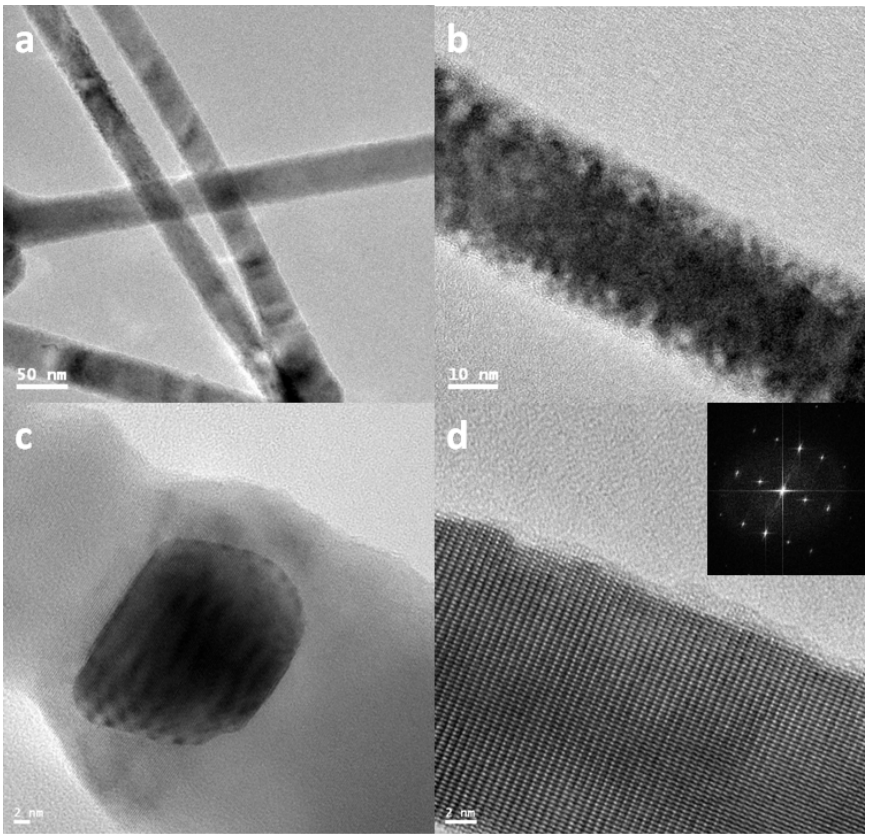

Figure 91. TEM images of F-doped ZnO NWs with Zn shell by CVD (10 mg Zn precursor used). (a) (b) before annealing; (c) (d) after annealing at 600 °C for 1 h.

5.2.4.3 Composition analysis

Fig. 92 shows the EDX spectrum, linescan and map of ZnO/F-doped ZnO core-shell nanowires. The oxygen content was higher than the Zn content after annealing at 600 °C. The EDX mapping indicates the presence of fluorine with a uniform distribution. However, linescans could not locate the fluorine distribution along the cross section due

to the low resolution and very thin shell.

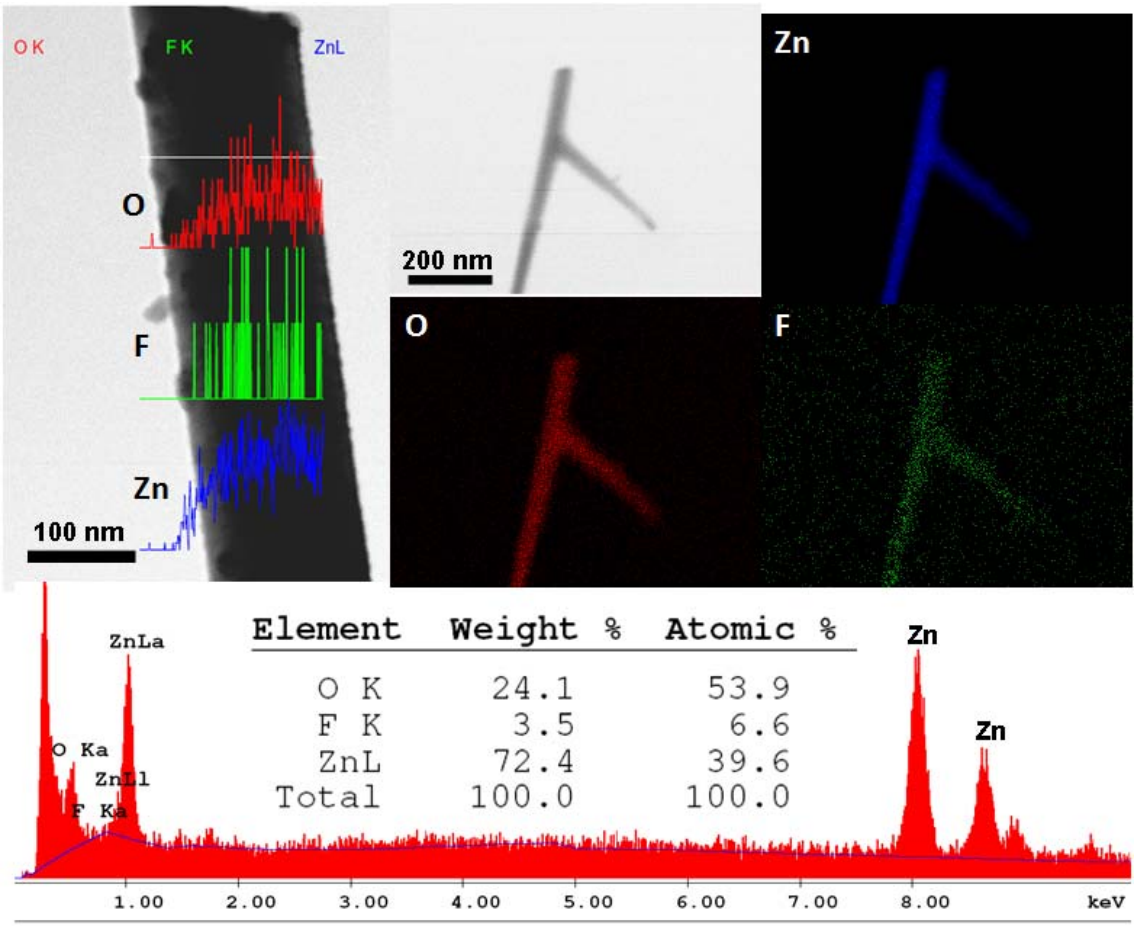

Figure 92. EDX spectrum, linescan and mapping on ZnO/F-doped ZnO NWs (annealing at 600 °C for 1 h).

5.3 Summary

In this chapter, F-doped ZnO nanowires were fabricated on different substrates by CVD methods using two types of experimental procedures: with or without carrier gas (Ar). In method I, use of graphite cloth substrates reveals better size-control (with an average diameter ~154 nm) than other substrates. No ZnO NW arrays could be observed on sapphire substrates due to very rapid growth rates.

In method II, F-doped ZnO NWs and arrays were synthesized in an Ar carrier gas with O_2. HRTEM images show clear single crystal structures from as-prepared nanowires, although they are zinc-rich, as measured by EDX. The fluorine content can be controlled by the amount of ZnF_2 used. ZnO UV/visible PL spectra indicate that F-doping diminished the intensity of defect light emission at ~2.4 eV.

ZnO/F-doped ZnO core-shell NWs were fabricated either by PVD or CVD processes, as well as a subsequent annealing in O_2. Compared with the CVD procedure, the PVD method provides better crystalline shell structures after annealing, although the morphology of as-grown nanowires looks not as uniform as CVD before annealing, because the agglomeration of small liquid Zn droplets could increase the roughness of surface layer before annealing. The typical shell thickness ranges from 2~5 nm.

CHAPTER VI.

Electrochemical Fabrication of Porous Ge Nanowires

6.0 Overview

Porous semiconductors elicit great interest as a consequence of their increased surface area and nanostructured features, thereby creating materials with opportunities for enhanced performance in optics, solar energy, and drug delivery/biosensing platforms. Traditional fabrication methods for semiconductors such as silicon (Si) have emphasized anodic or open circuit electrochemistry from bulk single crystals, thereby producing supported thin films or freestanding microparticles of the given matrix.[195] Contrasting with a number of studies on porosifying bulk material, the notion of creating one dimensional (1D) structures of even higher surface areas/porosities by porosifying nanowires is a difficult challenge, and has only recently been addressed in the case of etching silicon NWs.[304-306] Although sharing some rather special characteristics with Si, Ge is not etched as easily with regards to control of morphology in terms of pore nucleation and growth.[232, 233] The corresponding mechanism has been studied for bulk Ge, but controversies and confusion still remain.[238-248]

In this work, porous Ge nanowires (GeNWs) were fabricated by anodization of undoped single crystalline GeNWs (grown on Si wafer or graphite cloth) using ethanolic HCl with or without an initial cathodic Cu electrodeposition step. Based on periodic pit/pore structures shown on the surface of etched nanowires, it is demonstrated that these structures reflect carrier diffusion whose periodic localization corresponds to the GeNW surface energy barrier in a given electrolyte in the Ge oxidation reaction during

the anodization process. A new mechanism is put forth to interpret experimental results, which highlights the role of a anodic etching in the nanowire. The morphology of etched nanowires was principally characterized by SEM, TEM, and PL measurements, as described in previous chapters. The necessary bias for etching was provided by a Keithley 236 source measure unit.

6.1 Experimental Methods

6.1.1 Anodization

The germanium nanowires used in these experiments were grown using the vapor transport method as described in Chapter III. Samples were grown on 5 × 15 mm gold-coated (100) Si wafers or graphite cloth (GC) surfaces through a VLS approach; GeNWs (average diameter: 60 nm on Si wafer; 30 nm on GC substrate) were etched in a Pyrex electrolytic cell (Fig. 93). The substrate containing GeNWs was placed into the electrolyte vertically and served as anode. A 5×15 mm platinum foil as cathode was located 1 cm away from the anode in a parallel fashion. Ethanolic HCl solutions (varying from 1:1 to 1:16 of 37.5% HCl:EtOH v/v) were used as the electrolyte. Anodization proceeded under a constant current or voltage. GeNWs were sonicated in acetone after etching and dispersed onto Cu grids for TEM characterization immediately to minimize surface oxidation of the etched nanostructures.

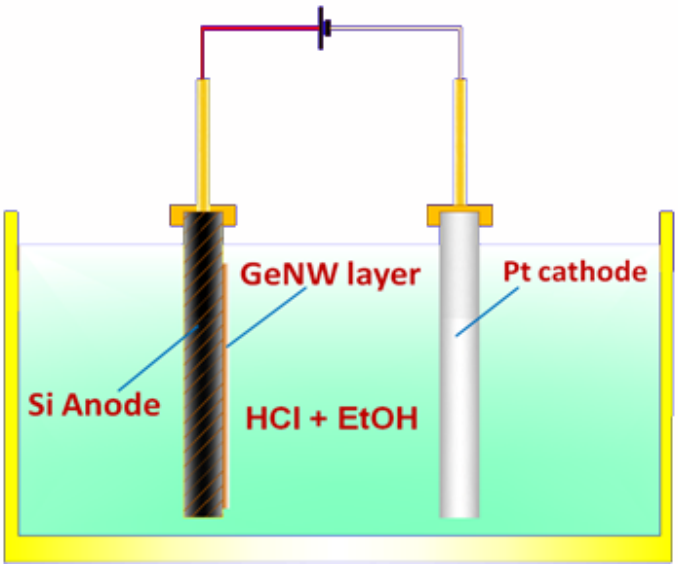

Figure 93. Schematic view of the GeNW anodization setup.

6.1.2 Copper electrodeposition

In selected experiments, a copper deposition step was added to the GeNW/substrate surface by applying cathodic bias to a saturated $Cu(NO_3)_2$, $CuSO_4$, or $CuCl_2$ solution before anodization; the magnitude of applied bias selected for a given experiment is identical to the magnitude of anodic bias in the subsequent HCl etching step.

6.2 Results and Discussion

6.2.1 Anodization of GeNWs on GC substrate.

GeNWs grown on Si and GC substrates are shown in the TEM images of Fig. 94. These images indicate that the surface of GeNWs is smooth before anodization. The average diameter of GeNWs on GC is ~ 30 nm with a relative narrow size distribution,

ranging from 4 nm to 40 nm. A few GeNWs over 100 nm could be observed by increasing the reaction temperature or prolonging reaction duration in the fabrication process. For GeNWs grown on Si wafer substrates, large diameter nanowires were a little easier to obtain by the use of larger Au catalyst thicknesses up to 10~15 nm. However, most nanowires possess sizes in the 20~60 nm range as shown in Figs. 94c, d (4~10 times smaller than the wider GeNWs in Fig. 94c).

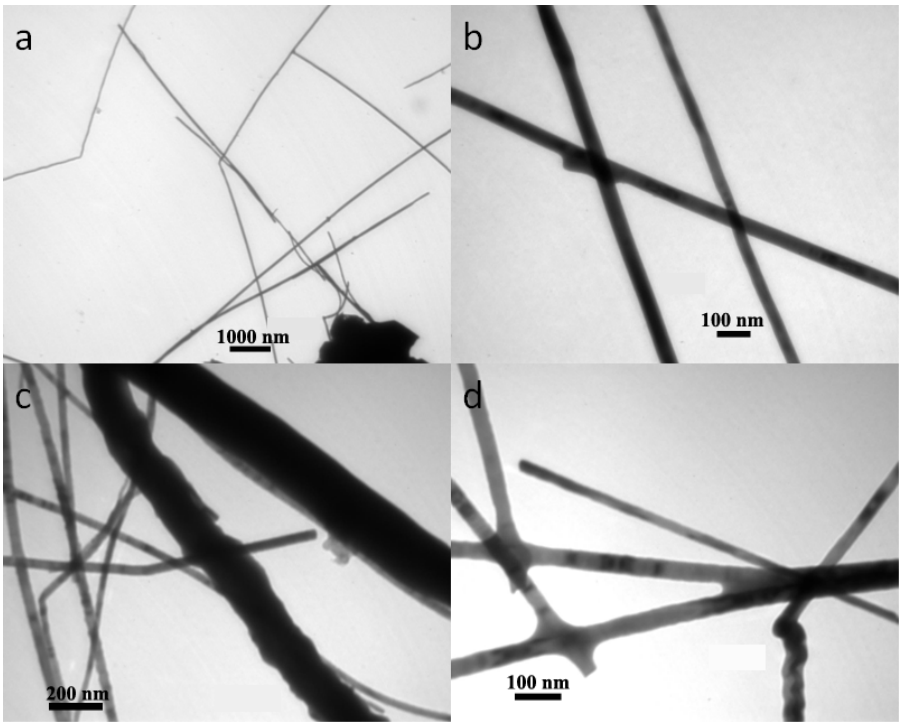

Figure 94. TEM images of GeNWs before anodization on: (a) (b) GC substrates; (c) (d) Si wafer. The scale bars are 1 μm, 100 nm, 200 nm and 100 nm in (a) (b) (c) and (d), respectively.

Preliminary experiments indicated that GeNWs on graphite cloth substrates quickly oxidized and dissolved into etchant within 1 min under etching conditions of high HCl

concentration (> 1:4) and etching current density higher than 13 mA/cm^2. Some current or voltage oscillations were observed, so the etching condition only refers to the steady state values (current or voltage) in each experiment. Fig. 95 exhibits morphologies of etched GeNWs at a current density of 13 mA/cm^2, where etched GeNWs (diameters >100 nm) reveal roughened surfaces with pores. Fig. 95e shows pit arrays due to the relatively larger size of the nanowire (~ 200 nm). However, no etched surfaces were observed for GeNWs in the size range from 20~40 nm.

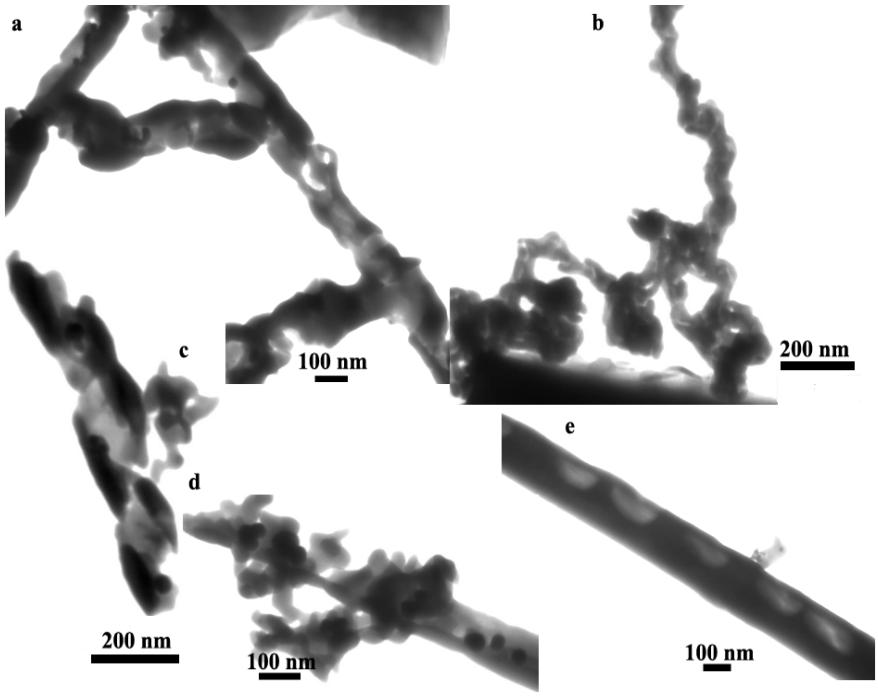

Figure 95. TEM images of GeNWs after anodization (13 mA/cm^2, HCl:EtOH=1:2, 1 min).

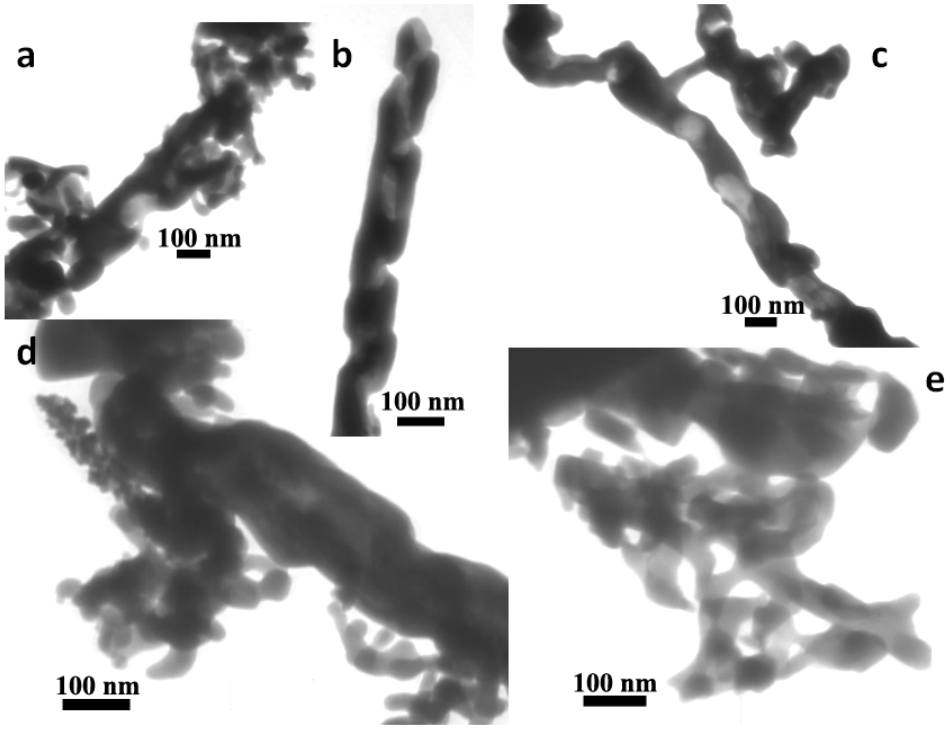

Figure 96. TEM images of etched GeNWs grown on GC substrates (6.5 mA/cm^2, HCl:EtOH=1:2, 2 min).

Upon reducing current density values to 6.5 mA/cm^2, more pore arrays and networks could be formed, but the disordered morphologies and curve shapes hindered further analysis (Fig. 96). The etched nanostructures with pore networks could dissolve partially at conditions with high current density and high HCl concentration.

With decreasing HCl concentration, both Ge oxidation and dissolution slowed down, which enabled pits to be observed on the surface of GeNWs, even with very small NW widths (~4 nm). If GeNWs were cleaved into smaller fragments during the anodization and settled at the bottom of the electrolytic cell, these lost GeNWs could not be collected for TEM characterization. This is presumably the reason why no small etched GeNW could be found in the etching conditions with large current density and high HCl

concentration as mentioned above (Figs. 95 and 96). Usually pits distribute preferentially on one side of a given nanowire, instead of both sides as shown in Fig. 97. The reason is that electrical field determines the preferential etching direction. Additionally, this result matches the traditional electrochemical theory that mass transfer (diffusion and convection) has remarkable effects on the reaction and dissolution at the solid-liquid interface.[239] HCl is consumed in the anode process. The supply of HCl at the GeNW surface is determined by its mass transfer. The side of GeNWs toward the platinum electrode is more open to the electrolyte with less spatial hindrance from GeNW networks, which contributes to better mass transfer and faster dissolution than the opposite side.

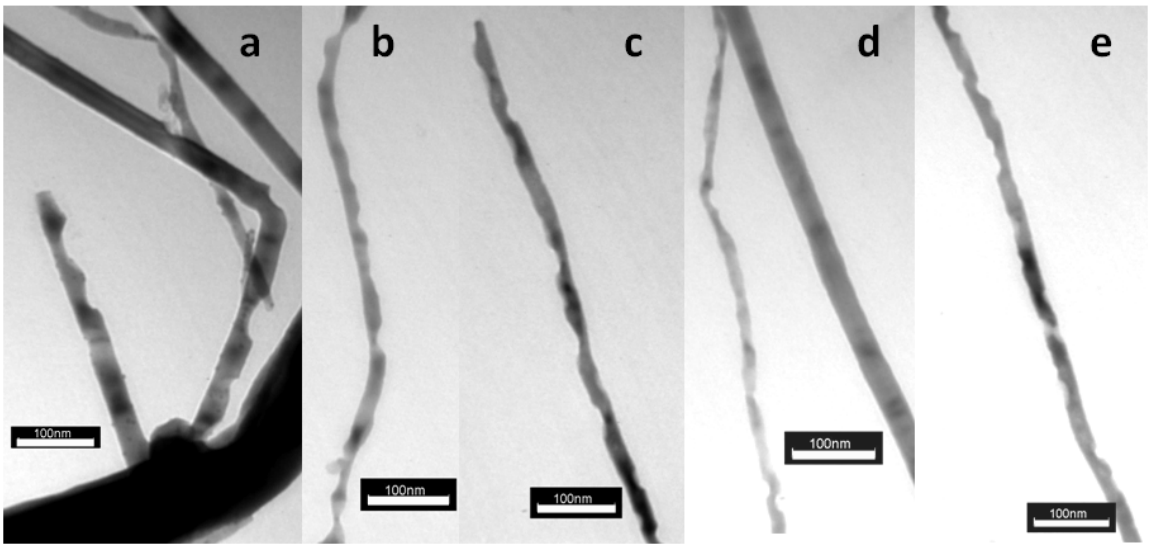

Figure 97. TEM images of etched GeNWs grown on GC substrates (6.5 mA/cm^2, HCl:EtOH=1:16, 1.5 min).

HRTEM images shown in Fig. 98 display some structural details of an etched

GeNW surface. The anodization did not considerably damage the crystalline structure of GeNWs. The amorphous layer caused by anodization is only ~1 nm in the left image, and ~2 nm in the right. No thick oxide layer can be found, which means that the oxidation process is the control step, instead of the dissolution step.

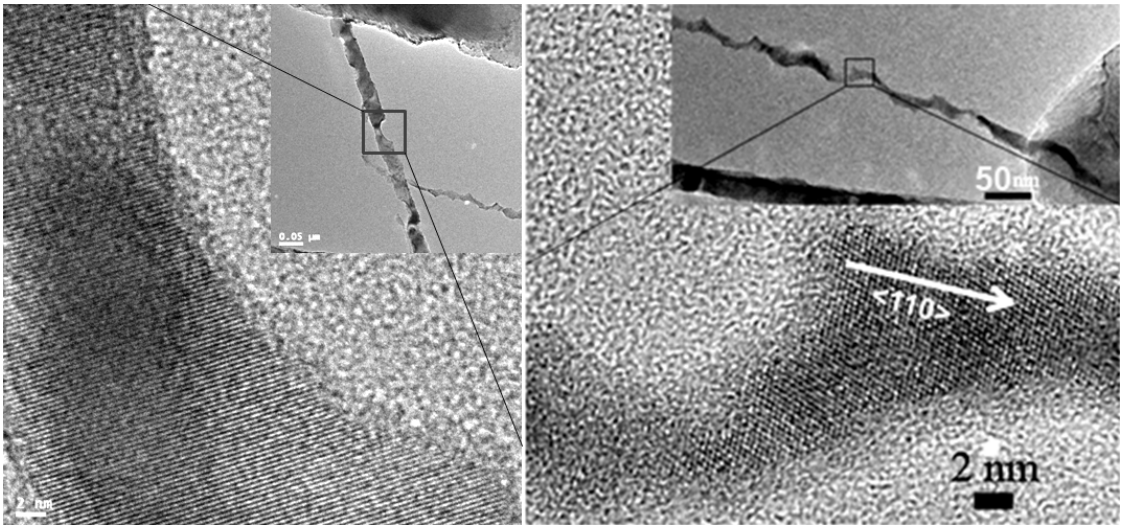

Figure 98. HRTEM images of etched GeNWs grown on GC substrates (6.5 mA/cm^2, HCl:EtOH=1:16, 1.5 min).

By keeping HCl concentration (1:16) constant and reducing current density to 0.65 mA/cm^2 with a longer etch duration of 10 min, etched GeNWs only show rough surfaces without apparent pits or wave-like morphologies (Fig. 99). The maximum roughness is only about ~2 nm. In other words, a Ge oxidation reaction tends to occur only in the surface with the less depth of the etched features due to lower current density and electric field. Such a uniform etching made it possible to observe etched GeNWs with very small diameter (~6 nm) without losing them due to fragmentation.

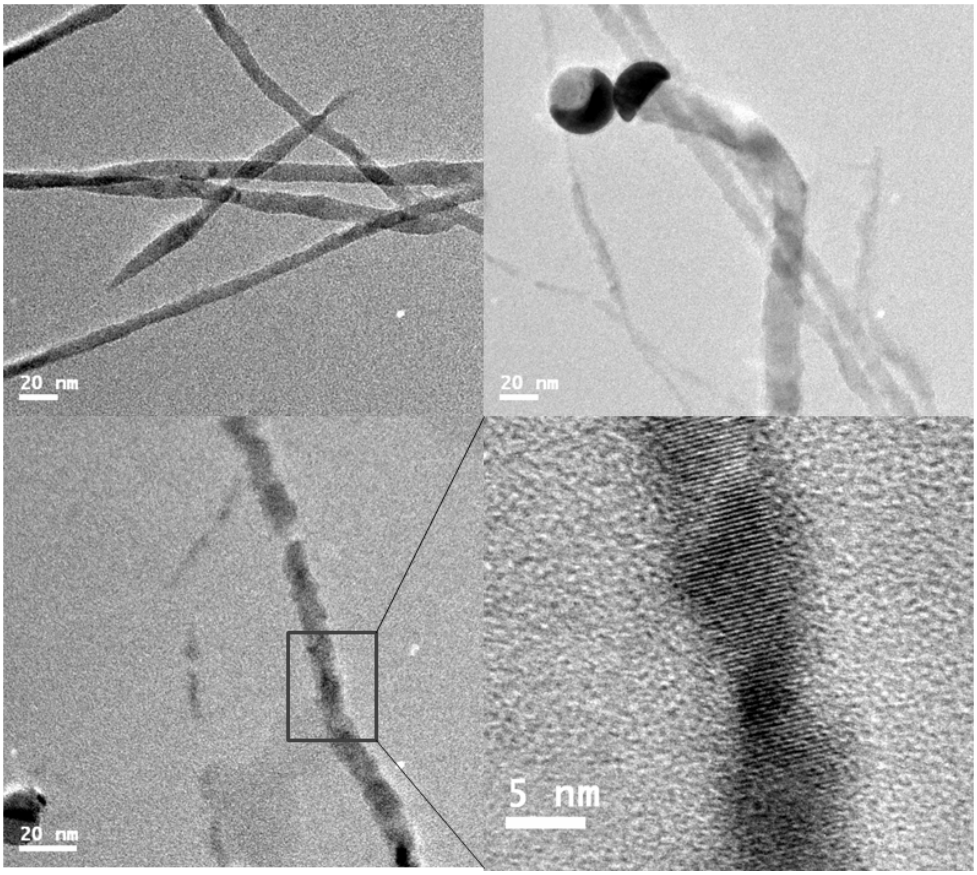

Figure 99. HRTEM images of etched GeNWs grown on GC substrates (0.65 mA/cm^2, HCl:EtOH=1:16, 10 min).

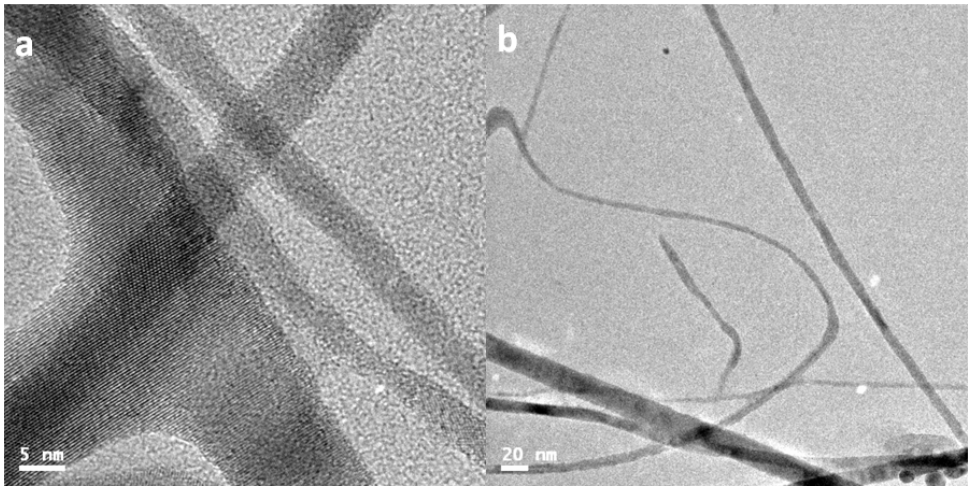

Figure 100. HRTEM images of etched GeNWs grown on GC substrates (0.065 mA/cm^2, HCl:EtOH=1:16, 10 min).

If current density is decreased further to 0.065 mA/cm^2 in 1:16 electrolyte (along with an increased duration to 20 min), a tendency toward more uniform surface etching became more apparent as shown in Fig. 100. Numerous thin GeNWs (< 5 nm) could be found. For GeNWs larger than 10 nm wide, it is difficult to determine the impact of such a low current density. However, if the size of GeNWs is less than 5 nm, the single crystal

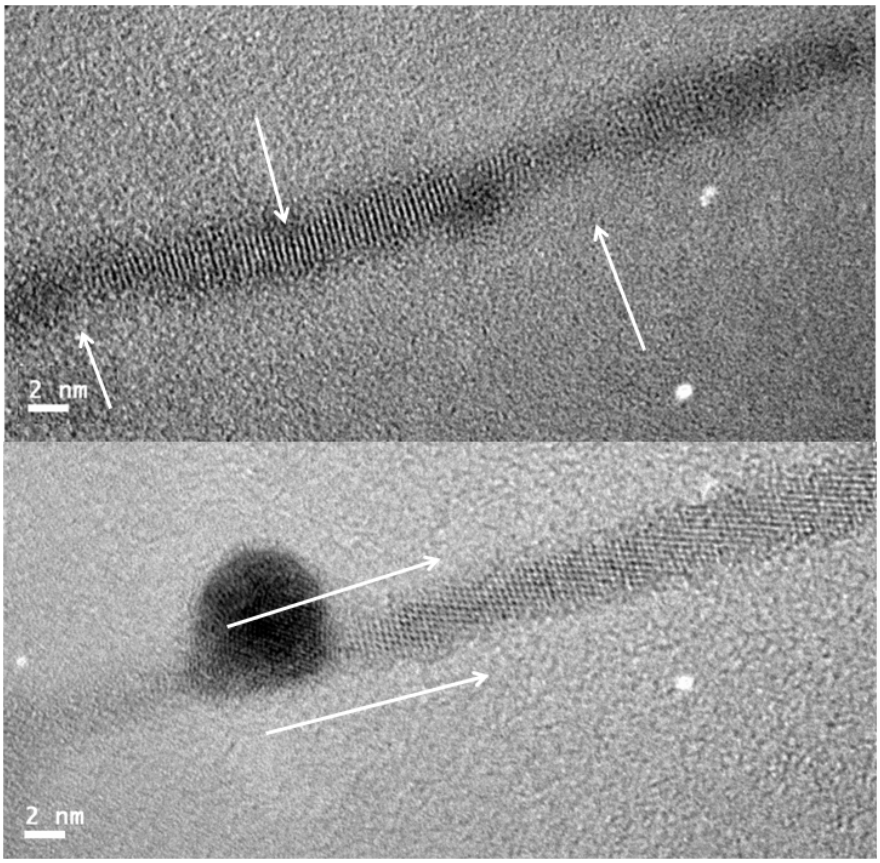

Figure 101. HRTEM images of etched GeNWs with a size less than 5 nm. (0.065 mA/cm^2, HCl:EtOH=1:16, 10 min).

structures explored by HRTEM images could still provide details about the preferential etching direction as labeled by white arrows in Fig. 101 due to the higher sensitivity to

the diminishing diameter. Because chemical, electroless and anodic etching phenomena can take place simultaneously or successively,[202] by combining the above observations above, we suggest that mainly anodic-etching contributes to the pore arrays and network formation with preferential etching direction and location. The application of strong bias should reduce open circuit chemical reduction (dissolution) of nanowire thickness.

6.2.2 Anodization of GeNWs on Si wafer substrates

Although graphite cloth possesses large internal spaces for ideal mass transfer, GeNWs grown on this substrate have a small size range, mainly with diameters less than 30 nm. The curved surface of graphite fibers hinders gold catalyst diffusion from forming big islands on the surface of graphite fiber, which in turn limits the size of GeNWs. More commonly, a Si wafer was used as substrate to grow GeNWs. Preliminary experiments indicated that the entire GeNW layer peeled from the Si wafer substrate and floated over the etchant at anodic current densities greater than 26 mA/cm^2 within 2 min. The bright and polished wafer surface was exposed after etching. TEM images showed that these delaminated GeNWs (collected by filter paper) remain smooth without any visual pits (Fig. 102).

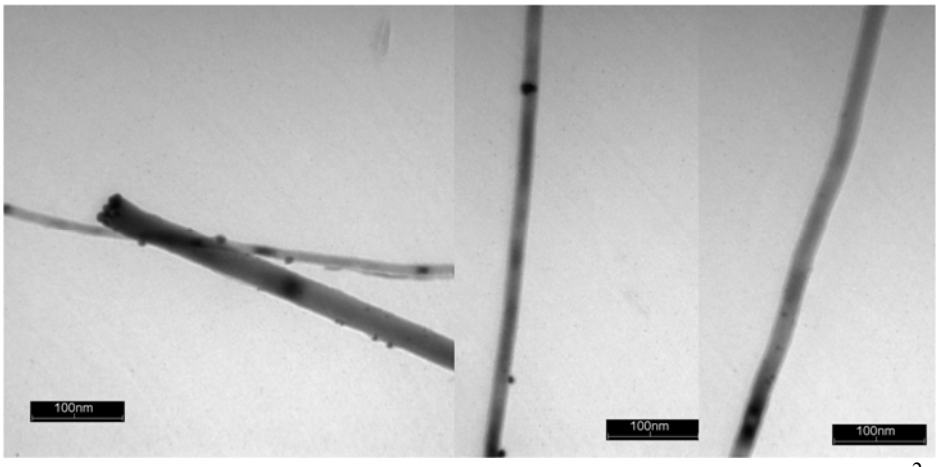

Figure 102. TEM images of GeNWs peeled from Si wafer (39 mA/cm^2, 2 min, HCl:EtOH=1:2).

Upon decreasing the current density to 13~26 mA/cm^3 in a 1:1 etchant for 5 min, GeNWs were broken into small pieces, forming dendritic bundles (Fig. 103a). Black arrows highlight the etched features in each position. The black circled area of Fig. 103a was magnified and shown in the HRTEM image of Fig. 103b. It revealed that those small fragments retain their crystal character without an obvious oxide layer. An etched GeNW fragment exhibits a highly curved morphology (Fig. 103c). The front tip of the core has been sharpened without loss of the single crystal structure, while pore wall framework is amorphous. A high etching current density (26 mA/cm^2) is preferred to form porous structures, as discussed above, although it also dissolves them quickly. As a dislocation structure, twin nanowires like one in Fig. 81d, are observed to be etched through one or both sides of boundary preferentially. A possible reason is that the interface in twinned GeNWs works as a screen and confines electron motions to two separate sides. Among etched GeNWs with twin structures, no evidence was observed that pits formed just on the boundary.

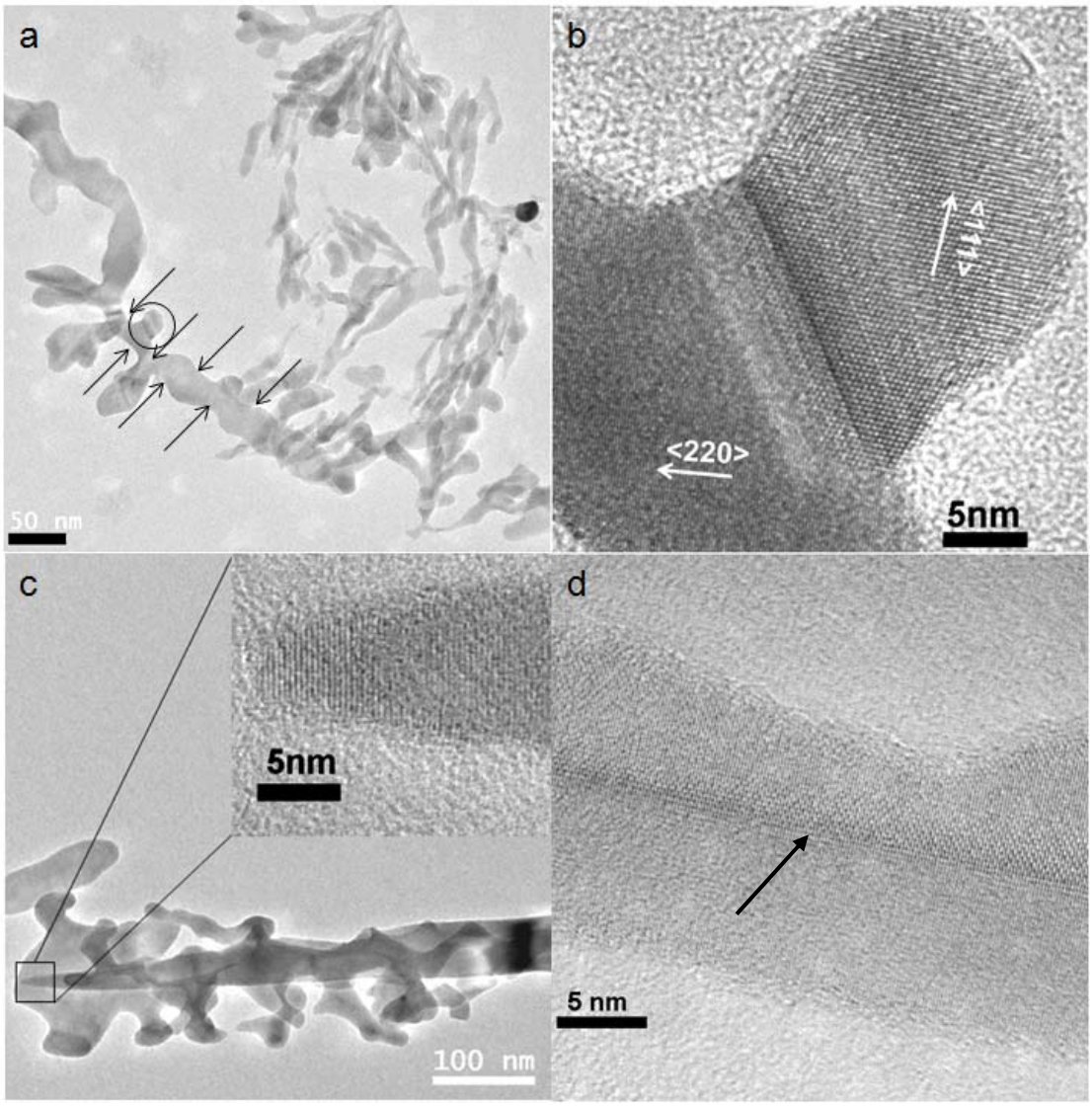

Figure 103. TEM images of Ge NWs etched in 1:1 HCl/ethanol. Current density and duration in (a) (b): 13 mA/cm^2, 5 min; (c) 26 mA/cm^2, 5 min; (d) 6.5 mA/cm^2, 20 min (the black arrow refers to a twin boundary.)

Usually the etching process of GeNWs on Si wafers needs a longer duration (> 5 min) to provide visible etching effects due to a slower etching rate than that on GC substrates. So a high HCl concentration (> 1:4) with corresponding high current density (13~26 mA/cm^2) is helpful to cause deep etching on GeNWs, but with a dissolution of etched structures. A high current density (13~26 mA/cm^2) and low HCl concentration (<

1:12) can create pore arrays similar to those on GC substrates as shown in Fig. 98. However, decreasing the working current density to a low value (< 6.5 mA/cm^2) usually results in no observable etched features on the GeNW surface. These observations indicate that high HCl concentrations are not preferred in porous GeNW fabrication.

6.2.3 Anodization of GeNWs grown on Si wafer with Cu electrodeposition.

In selected experiments, a thin layer of copper was electrodeposited on the surface of NWs and substrates by using a saturated Cu salt solution ($Cu(NO_3)_2$, $CuSO_4$, or $CuCl_2$) as Cu source in a cathodic process. The main objective for the introduction of copper plating firstly is to stabilize the base of nanowires attached to Si wafer substrates, which prevents GeNWs from peeling off before they are etched adequately according to the preliminary experiments using high current densities. Left untreated, the contact interface between substrates and GeNWs becomes an accumulation area for electrons because at high current densities electrons would rather move along the substrate surface than penetrate a given GeNW. Increased carrier injection of these point contacts leads to structural instabilities and NW delamination. The electrodeposition is a self-selective process to cover these oxidation-active areas preferentially with Cu, and then works as a passivation mask in the anodization that follows. Additionally, copper electrodeposition results in preferential GeNW oxidation because germanium is of a lower standard electrode potential (Ge/Ge^{2+} 0.26V) than copper (Cu/Cu^{2+} 0.34V).

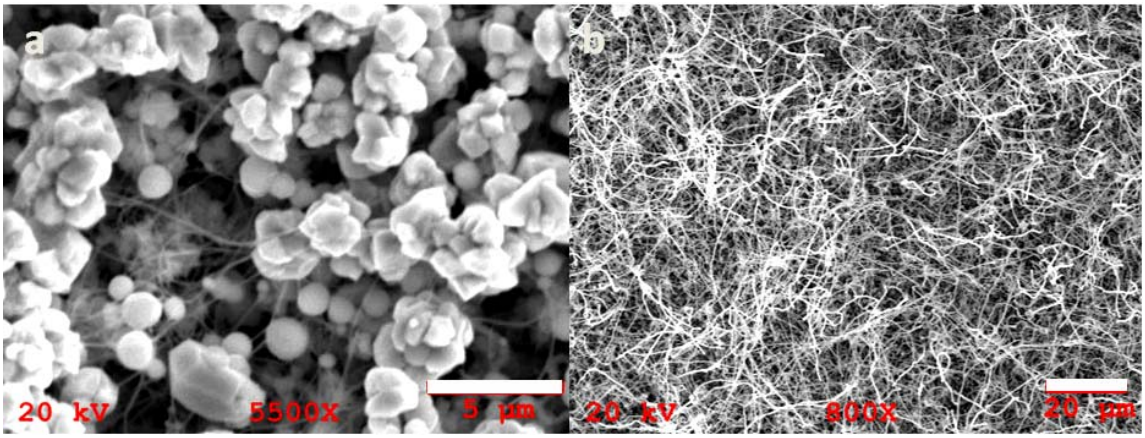

Figure 104. SEM images of GeNWs after electrodeposition in saturated $Cu(NO_3)_2$ with 6.5 mA/cm^2 current density for 5min. (a) Si wafer edge (scale bar, 5 µm) and (b) central area (scale bar, 20 µm).

SEM images (Fig. 104) show that copper was mainly deposited onto the edge of a given Si wafer, and little on the surface of GeNWs. It means that bare Si wafer is the most active area for particle deposition in the cathodic process. Therefore, in the opposite process of anodization, the Si surface should be also an active area for electrons passing through, which decreases the current diffusion through GeNWs. Passivation in such areas could increase the etching current moving through GeNWs correspondingly. The copper coating would presumably be oxidized again in the subsequent anodization process. TEM images and EDX spectra of etched GeNWs did not detect the presence of Cu unless the anodization duration was less than that used in the Cu cathodization process.

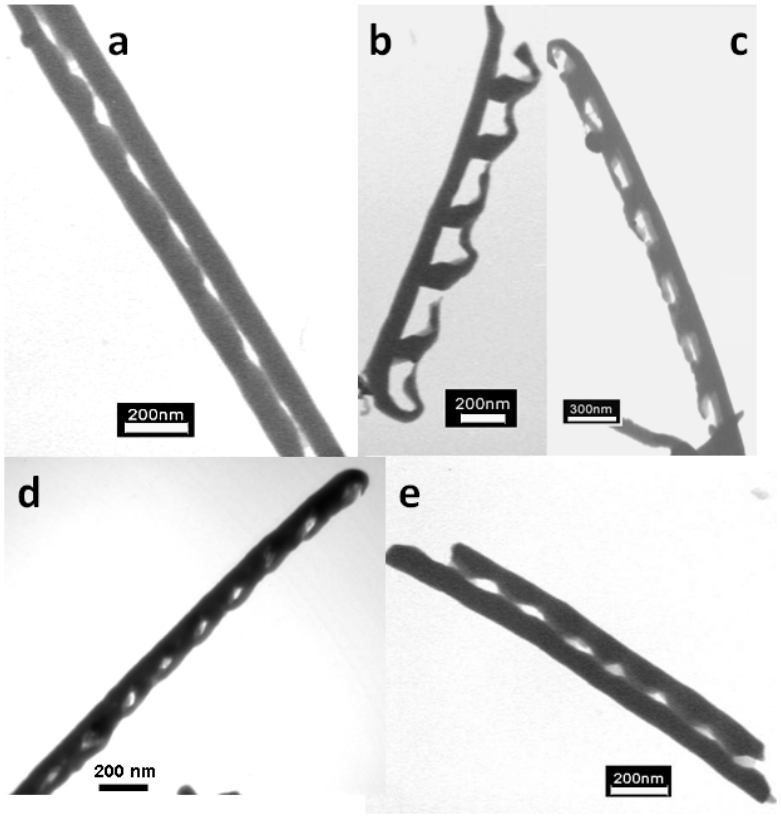

Figure 105. TEM images of etched GeNWs with Cu electrodeposition in saturated $Cu(NO_3)_2$ with anodization conditions: (a) (b) 13 mA/cm^2, 20 min, 1:1; (c) 13 mA/cm^2, 15 min, 1:2; (d) (e) 6.5 mA/cm^2, 30 min, 1:1. The current density in Cu plating was the same as that in the following anodization process and the duration was 5 min.

With the assistance of Cu electrodeposition, effective etching on GeNWs increases. TEM images in Fig. 105 exhibit pore arrays on GeNWs (fabrication conditions: 6.5~13 mA/cm^2, 1:1 or 1:2 ethanolic HCl). The periodic feature spacing (d_{FS}) between two neighbor pores in a etched GeNW ranges from 200 to 300 nm. The angle of pores reflects the spatial position of each GeNW in the electric field direction because the preferential etching is assumed to be determined by the electric field. Other GeNWs etched under similar conditions show morphologies including only pits along one side (Figs. 106a, b), etched at both middle areas and sidewalls (Figs. 106c, d, and e), and

heavily etched GeNWs (Figs. 106f, g).

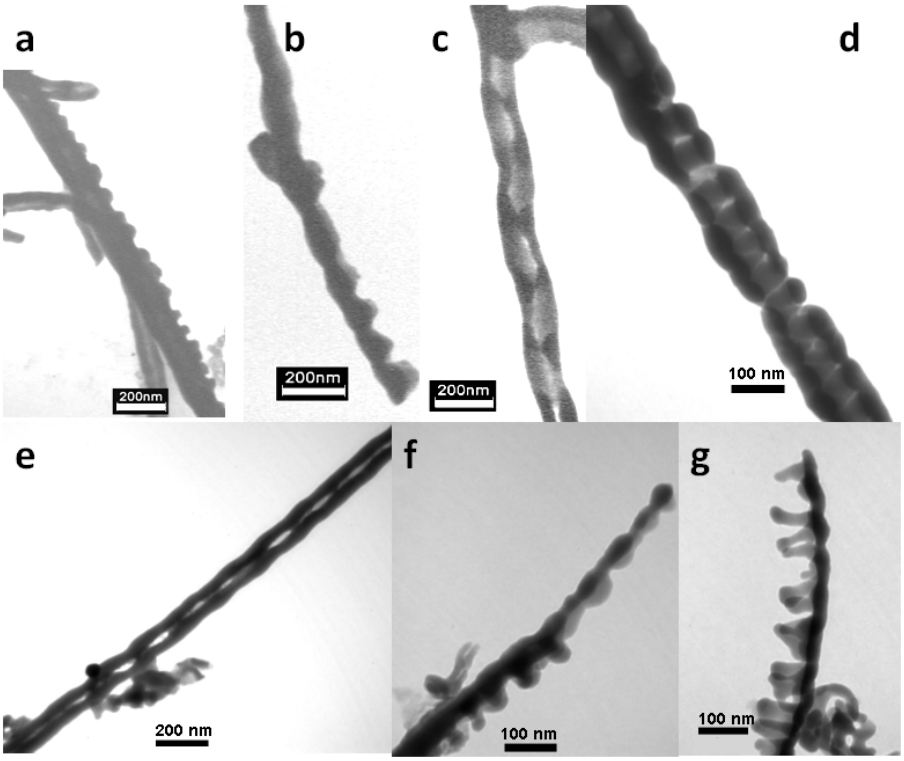

Figure 106. Other morphologies of etched GeNWs with Cu electrodeposition in saturated $Cu(NO_3)_2$ with anodization conditions: (a) (b) (c) 13 mA/cm^2, 5 min, 1:1; (d) 13 mA/cm^2, 12 min, 1:2; (e) (f) (g) 6.5 mA/cm^2, 30 min, 1:1; The current density in Cu plating was same as that in the following anodization process and the duration was 5 min.

Experiments in Figs. 105,106 were conducted in high HCl electrolyte concentrations (1:1~2). Etched structures from GeNWs with diameters less than 60 nm were rarely observed. According to the measurement of etched depths in these NWs ranging from 50~80 nm, it is believed that those small GeNWs have been dispersed into the electrolytic cell, such that only relatively larger diameter of GeNWs remain. In this experimental system, the morphology of etched GeNWs differ in thousands of ways

from heavily etched to little etched because of the variations in charge density at a given nanowire surface. Based on our goal to fabricate porous GeNWs, thus pit arrays and porous networks were used as a standard to evaluate the impacts of etchant and bias applied. Although we observed numerous pore arrays in high HCl etchant with various current densities from 5.5~13 mA/cm^2 and duration from 3 min to 30 min, pore networks were never observed for this substrate.

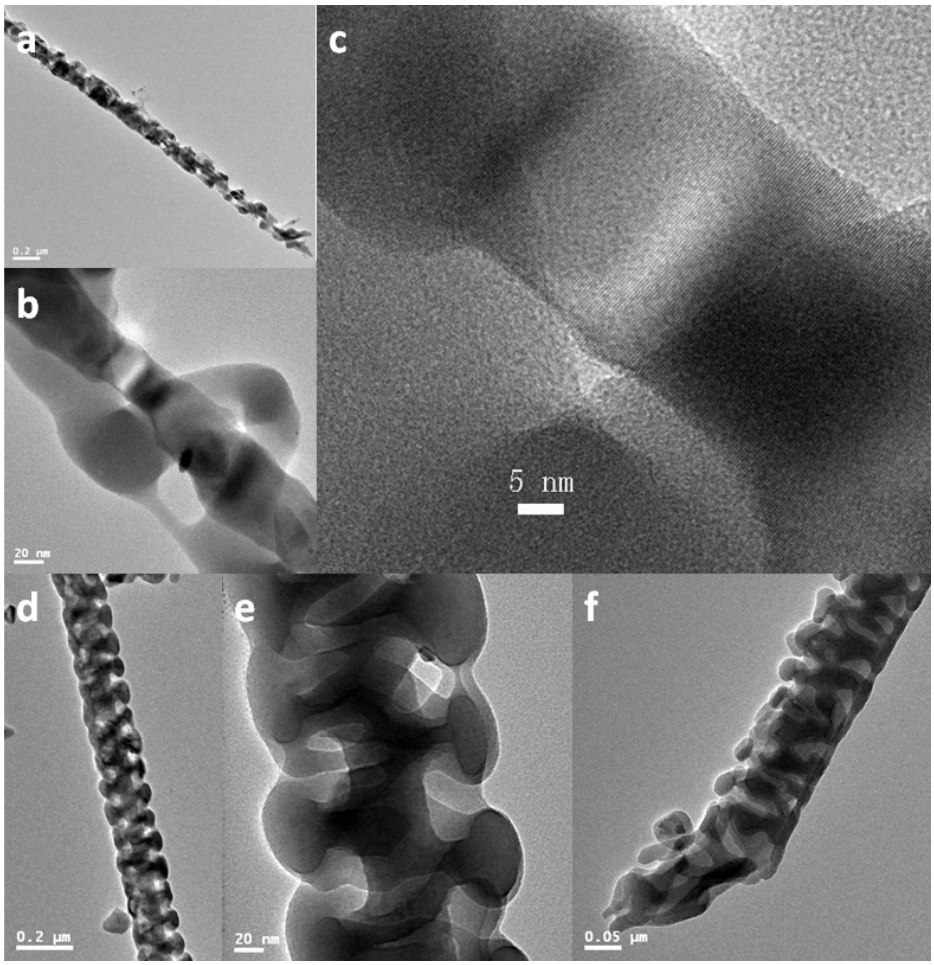

Figure 107. TEM images of etched GeNWs with an initial Cu electrodeposition in saturated $Cu(NO_3)_2$; with anodization conditions: 1.3 mA/cm^2, 30 min, 1:12. The current density in Cu plating was the same as that in the following anodization process and its duration was 30 min.

In contrast, porous GeNWs can be fabricated in highly diluted etchant (< 1:12) with low current densities. Figs. 107a,c exhibit an etched GeNW with single crystal core and etched helical shell under constant current density (1.3 mA/cm^2). The same core could be seen in the spine-like etched GeNW in Figs. 107d,e, but not f. Although the structures of porous GeNWs are much more complicated to analyze in terms of etching direction than pore arrays, this periodic feature could always be found in such structures.

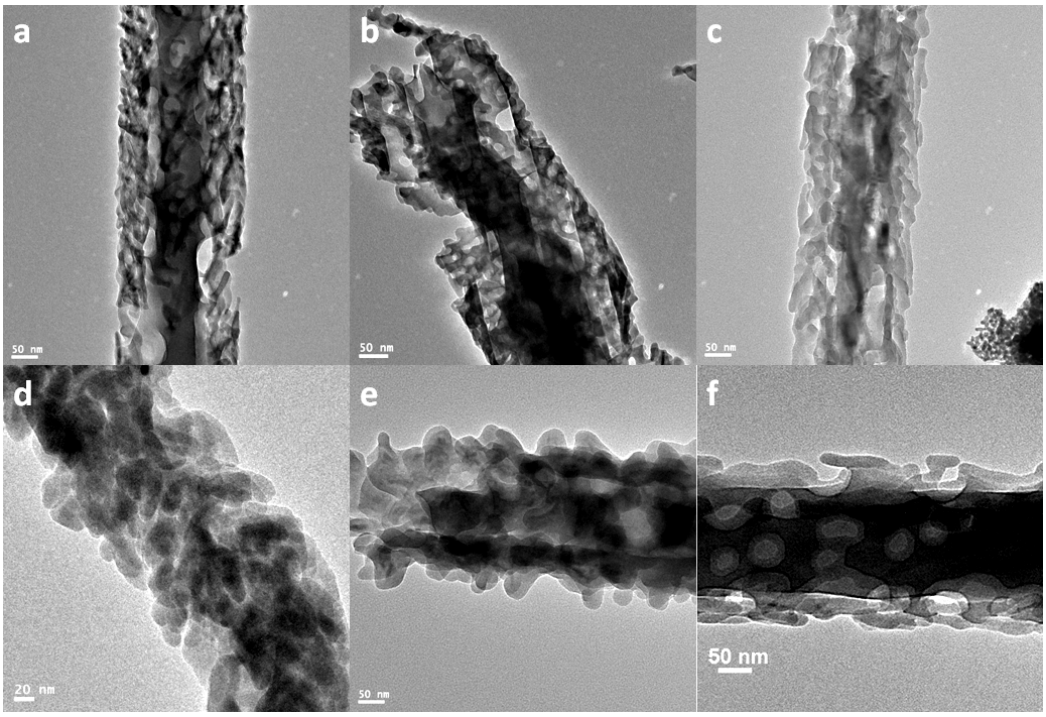

Figure 108. TEM images of etched GeNWs with an initial Cu electrodeposition step in saturated $Cu(NO_3)_2$; anodization conditions: (a) (b) 4V, 10 min, 1:12. (c) 4V, 20 min, 1:12. (d) 4V, 10 min, 1:12. (e) (f) 8V, 30 min, 1:16. The voltage and duration in Cu plating was the same as that in the following anodization process.

Under constant voltage, porous GeNWs could be also obtained using voltage values from 4~8 V as shown in Fig. 108. In this approach, the current always diminished gradually during anodization, which is helpful to protect the sidewalls in etched porous networks (because of oxidation), but at a cost of pore penetration depth, compared with constant current (Fig. 107).

6.2.4 Helical structures of etched GeNWs.

Helical structures were always associated with a strong anodic bias (13 mA/cm^2) applied with the assistance of Cu plating. However, it is hard to believe that such an ordered structure could be provided by random electrochemical oxidation process (based

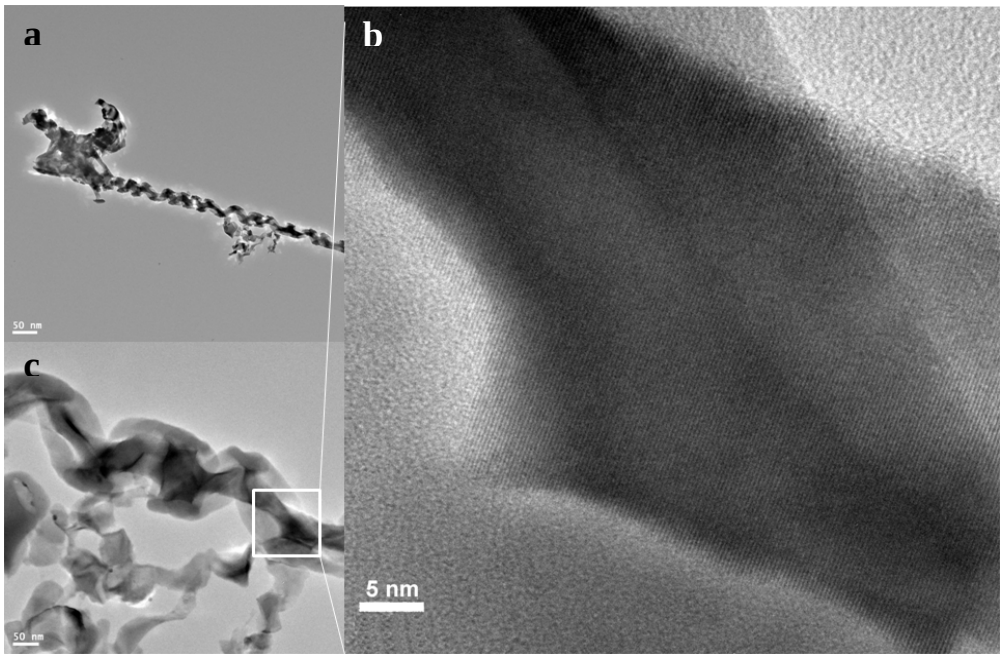

Figure 109. TEM images of etched GeNWs with an initial Cu electrodeposition step in saturated $Cu(NO_3)_2$; anodization conditions: 26 mA/cm^2, 20 s, and then, 4V, 5 min, 1:16. Cu plating: 1.3 mA/cm^2 , 10 min.

on a traditional mechanism), and some curved Ge nanoribbons formed in the VLS process also made it difficult to confirm if the helical structure resulted from anodization. This confusion eventually was resolved by the analysis of additional HRTEM images.

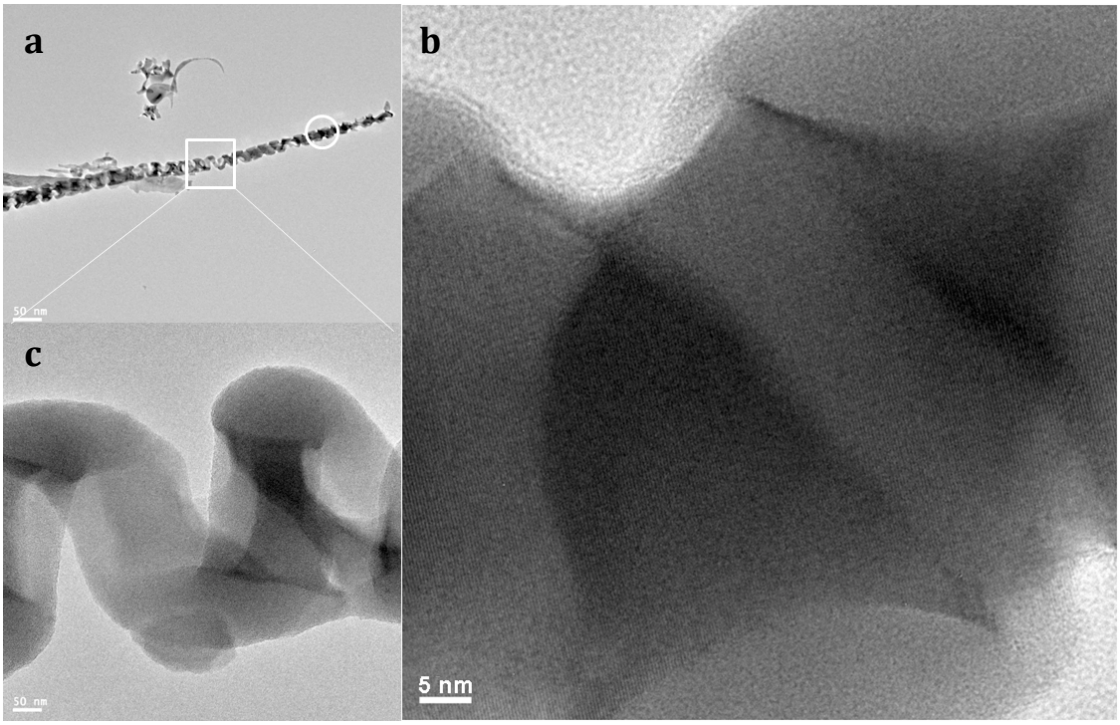

Figure 110. TEM images of etched GeNWs with an initial Cu electrodeposition step in saturated $Cu(NO_3)_2$; anodization conditions: 20 V, 20 s, followed by 4V, 5 min, 1:16. Cu plating: 1.3 mA/cm^2 , 10 min. The white circle in the top left image corresponds to the right HRTEM image.

Figs. 109 and 110 show two GeNWs with a helical track caused by etching. Two extra factors, high current density (26 mA/cm^2) or high voltage (20 V) for only 20 seconds, mainly contributed to the formation of a helix (rather than Cu plating, lower bias and HCl concentration). The helical structures include amorphous ribbons and single crystal GeNW cores. The HRTEM image in Fig. 109 indicates that the single crystal core was

etching and without damaging the surrounding ribbon. Fig. 109c shows that the core was dissolved in that particular area. The formation of a helical ribbon structure can be seen in the HRTEM image (Fig. 110), where the etched track surrounds the single crystal GeNW core growing along (110) direction with an angle of 32°.

6.2.5 Photoluminescence of etched GeNWs.

Typical room temperature PL measurements in the UV/Visible of etched GeNWs reveal two peaks at 2.94 eV (420 nm) and 2.32 eV (534 nm) respectively (Fig. 111). Both emission features are enhanced in terms of intensity at low temperature (8K), with the 2.94 eV peak more prominently affected. The 2.32 eV is assigned to etching defects (dangling bonds) because the PL intensity diminished in low temperature. Sun and Tolbert et al. reported that hexagonal nanoporous Ge provides light emission at 1.2~1.3 eV, and a strong PL at 2.0 eV for GeO_x.[231] Mei et al. reported that GeNWs did not show any PL at room temperature.[307] A weak PL feature at 3.19 eV (389 nm) was observed only at 77 K, which was attributed to the Ge oxide at the tip of the nanorods. Su et al. observed three peaks at 471 nm (2.63 eV), 448 nm (2.76 eV) and 411 nm(3.02 eV) in the room-temperature PL measurements from GeO_2 nanowire arrays.[308] In our experiment, HRTEM images indicate that the amorphous layer on the surface of etched GeNWs is less than 3 nm. Additionally, the PL measured for these etched NWs was conducted in a vacuum environment. Therefore, it strongly believed that the PL of etched GeNWs at

2.94 eV results from etched porous GeNWs.

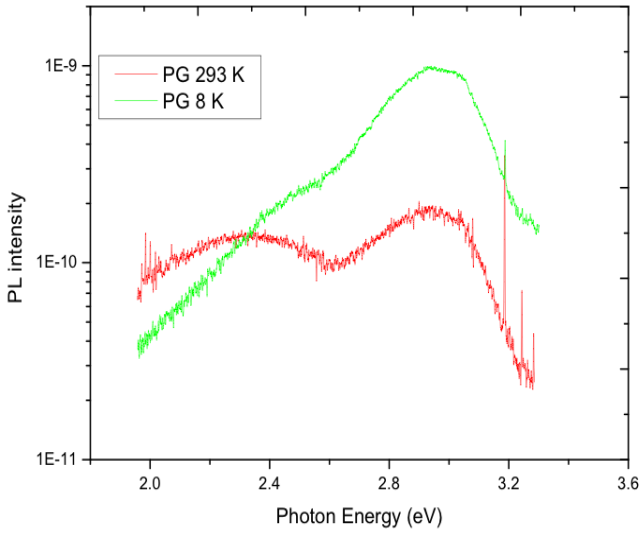

Figure 111. PL of etched GeNWs, with a λ_{ex} = 325 nm at both room temperature and 8K.

6.2.6 Electrochemical anodization mechanism.

Analysis of etching mechanisms in bulk single crystals is often challenging due to issues with sample preparation for TEM (ion milling, polishing etc.). In contrast, a great advantage in examing GeNWs porosification is that direct observations of etching effects could be characterized by HRTEM without extensive sample preparation. The foregoing data presentation has shown that chemical etching in ethanolic HCl only provides a slow and uniform dissolution of the surface of GeNWs with diminishing bias, while pore formation prefers the application of strong bias. Reducing HCl concentration is a critical step to the fabrication of porous GeNW networks. It means that chemical etching is

necessary, but must be restrained strictly in such an anodization process. Therefore, it is important to highlight the role of anodic bias in the electrochemical etching mechanism.

The frequent observation of pore arrays on the surface of etched GeNWs indicates that the etching process expresses a periodic behavior. One assumption is that at the beginning of pit array formation, pit nucleation areas on the surface of GeNWs have the highest electron hole (h^+) density, and separated at fixed distances. In other words, those areas which have sufficient electrical potential to overcome surface energy barrier, permit Ge oxidation and dissolution. The simplest answer to a symmetric potential distribution is that carrier transport in GeNWs occurs with a periodic wave-like potential.

In a study of electrochemical potential distribution along a quantum wire connected with two electron reservoirs, Pernas and Flores et al found that for a perfect 1D chain, the electrochemical potential oscillates around a zero mean value along the chain, with a wavelength related to the Fermi wavelength of the free electrons.[309,310] According to De Broglie equation,[58] the wavelength (λ) of electrons is correlated to their momentum (p) as:

$$\lambda = \frac{h}{p} \qquad (6.1)$$

where h is Planck's constant. Since the kinetic energy (E) of an electron with mass (m) is related to its momentum by the classical relation:

$$E = \frac{p^2}{2m} \qquad (6.2)$$

Therefore, the relationship of energy and wavelength of electrons is given by:

$$E = \frac{h^2}{2m\lambda^2} \qquad (6.3)$$

We measured d_{FS} values on GeNWs with etched pore arrays without consideration of specific anodization conditions, and then employed these values (ranging from 25 nm to 450 nm) as Fermi wavelength (λ) in Eq. 6.3. The result shows that the energy level is size-dependent as shown in Fig. 112. The surface energy barrier of GeNWs increases exponentially with GeNW diameter descending when their diameters are smaller than 38 nm. Such a size effect is predominant over any other etching conditions at this stage. As a specific illustration of the clear size-dependence of d_{FS}, the d_{FS} values measured from a GeNW shown in Fig. 113 decrease from 113 nm to 70 nm, corresponding to descending GeNW diameters from 79 nm to 55 nm.

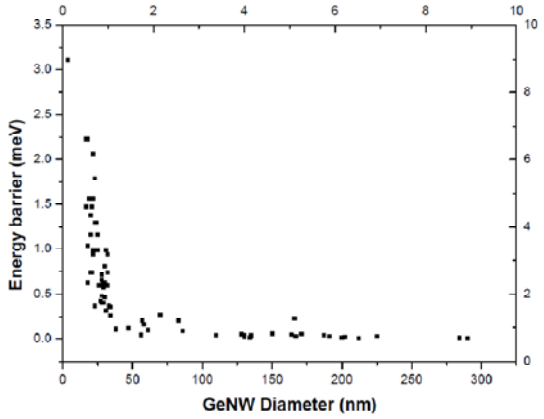

Figure 112. Size-dependent surface energy barrier distribution (electron mass m_p=9.1x10^{-31} kg) .

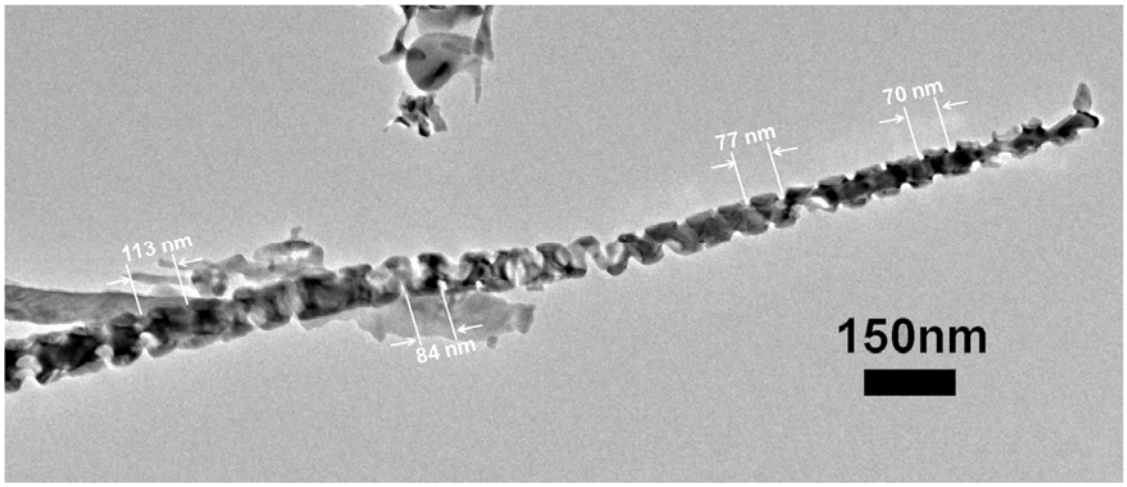

Figure 113. TEM image of etched GeNW with the size-dependent feature spacing distribution. Etching conditions is same as that in Fig. 110.

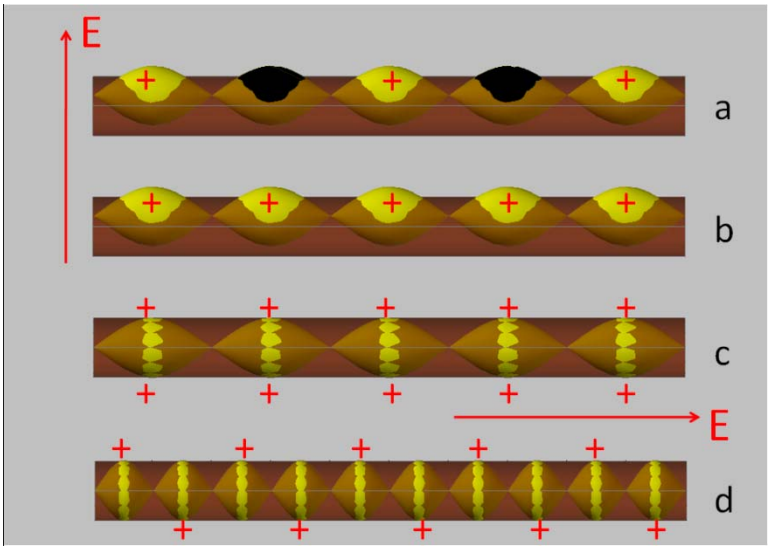

Figure 114. Schematic view of the impact of electric field on pore locations.

Fig. 114 shows the impact of electric field on pore location. For example, if the GeNWs are normal to the electric field, holes are pushed to one side, thus pores only form on the side (Figs. 114a,b). If NWs are parallel to the electric field, pores can form on both sides (Figs. 114c,d). Helical structures (Figs. 109,110) indicates that the pore

location change from one side to another side periodically with the mode in Fig. 114d, rather than c. Therefore, for GeNWs normal to the electric field, the pore location should be formed with the mode in Fig. 91a, but not b. Thus the d_{FS} just corresponds to one Fermi wavelength.

By comparing the periodic feature spacing (d_{FS}) with the observed diameter of the etched structure, a d_{FS} is 0.5~2.5 times as much as that of nanowire diameter (Fig. 114). It means that pore arrays could be formed only when the Fermi wavelength of electrons in a given GeNW is close to its diameter. If the ratio of d_{FS}/d_{NW} (GeNW diameter) is $\leqslant 1$, pore networks can be formed.

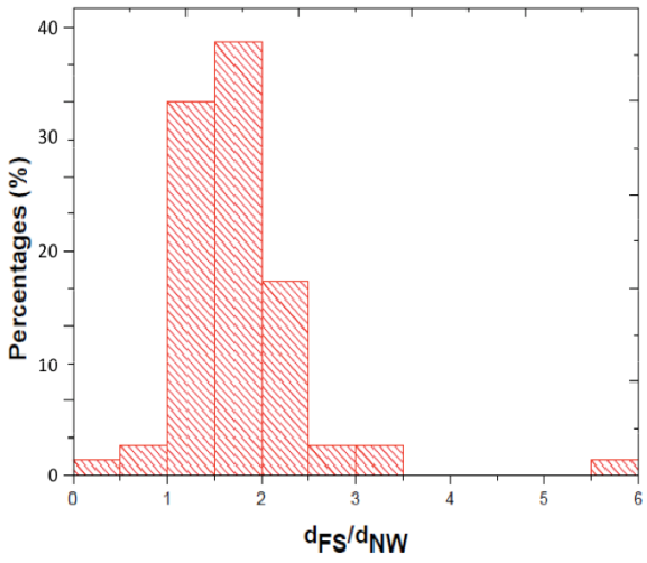

Figure 115. Relationship between feature size (pore distance) and GeNW diameter.

6.3 Summary

In this work, the fabrication of porous Ge nanowires by the anodization of Ge nanowires (grown on Si substrates or graphite fibers) using ethanolic HCl as an electrolyte is described. With a decreasing of applied bias, the morphology of etched GeNWs characterized by HRTEM display a transition from pore array and network formation, surface roughness to uniform oxidation on the surface. Porous GeNWs were fabricated by anodizing GeNW on Si wafer substrates in a low ratio of HCl & EtOH (<1:12) with current densities ranging from 1.3~6.5 mA/cm^2 or constant voltage (4~8 V). An initial cathodic Cu electrodeposition (CBD) step is critical to the pore formation by stabilizing the nanowires and passivating the Si surface. Periodic pore structures are the most significant properties on etched GeNWs with feature spacing (d_{FS}) from 20~450 nm.

By looking at pores as the active area of Ge oxidation reactions, (where holes have higher energy), pore formation involves a discrete electron potential distribution along 1D GeNWs. Potential charge distribution in the NWs studies suggest that the electrochemical potential oscillates around a zero mean value along the chain, with a wavelength related to the Fermi wavelength of the conduction band electrons. Therefore, the pore arrays reflect such a potential distribution along GeNWs and the d_{FS} values correspond to the Fermi wavelength of carriers in an anodization process.

Based on feature spacing values (d_{FS}), the electron energy was calculated. Using a simple De Broglie mode, it was found that the surface potential energy is

diameter-dependent with an exponential increase at a threshold diameter of ~ 38 nm. Therefore, it is more difficult to form a pore network structure in NWs with diameters close to the minimal NW diameter threshold. A strong bias is necessary to fabricate porous GeNWs in such cases. When the Fermi wavelength of carriers is less than the diameter of GeNWs, porous GeNWs with networks can be formed.

VII Concluding Remarks

The work presented in this dissertation focused on the fabrication of one dimensional nanostructures, including Er/Zn-modified core-shell GeNWs, Ge/Er-modified ZnO tetrapods, Er/ZnO/Si and Ge oxide nanofibers, and F-doped ZnO core/ZnO shell NWs, and their characterization by using SEM, HRTEM, XRD and PL measurements. In addition, porous GeNWs were fabricated by electrochemical anodization.

In Chapter II, ZnO/Er-modified core-shell GeNWs were fabricated by using a CVD or PVD process to form a surface layer onto the surface of GeNWs. The nature of the Zn source significantly impacted on the crystalline structure and photophysical properties of ZnO/Er/Ge NWs. The PVD process used to form Zn shells can provide high concentrations of ZnO in the surface during annealing by inhibiting Ge diffusion towards the shell and zinc germanate formation, which is helpful to ZnO UV/visible PL. The CVD process provided more appropriate conditions to form Zn_2GeO_4, which diminished ZnO luminescence. Dual wavelength light emission is observed in as-prepared nanostructures fabricated by using both CVD and PVD processes. Heavily ZnO coated Er/Ge NWs (Zn precursor) exhibits very strong Er^{3+} ion and ZnO UV/visible PL. It is found that 2~ 3 % (wt) Er concentrations and the Zn/Er/Ge sandwich structure were preferred for optical dual wavelength light emission (Er and ZnO PL).

In Chapter III, ZnO TPs were fabricated by Zn granule evaporation in air at 990 ˚C.

Er^{3+} doped ZnO tetrapods, both with and without a germanium (Ge) sensitizer layer, are found to emit at both the UV/visible and near-infrared. Considerable enhancement of Er^{3+} PL was made possible by Ge deposition, with the most significant enhancement observed when the erbium ions are deposited closer to the outer surface (Er^{3+}/Ge/ZnO). Energy transfer between ZnO and Er^{3+} took place with a wavelength of 520 nm verified by ZnO PL spectra, with Ge deposition again facilitating the process. Compared with other systems that have been investigated, the Er^{3+} PL associated with ZnO TP apparently shows more Stark splitting.

Chapter IV describes the fabrication of Er/SiO_2/ZnO PVP nanofibers and Er/GeO_x/ZnO PEO nanofibers by using electrospinning of selected sol-gel precursor solutions. These nanofibers exhibited strong Er^{3+} near IR photoluminescence at 1.54 μm after annealing to remove the polymer template. Photocarrier-mediated excitation processes were observed in Er/SiO_2/ZnO nanofibers, with a composition and annealing temperature dependence. Higher annealing temperatures resulted in Er^{3+} PL following a direct ligand field excitation mechanism. Room temperature near IR PL quenching was not observed even with very high Er concentrations (~18% wt) due to well-dispersed Er locations and very disordered crystalline structures in as-prepared nanofibers.

In Chapter V, F-doped ZnO nanowires were fabricated on different substrates by a carbon thermal evaporation process. F-doped ZnO NWs grown on graphite cloth substrates possess smaller widths (~154 nm) than those on Si or sapphire substrates in the process without a carrier gas. In the gas flow of Ar and O_2, F-doped ZnO NW arrays

were synthesized with a preferential growth direction along the (002) planes. The fluorine content can be controlled by the amount of ZnF_2 used. UV/visible PL spectra indicate that F-doping diminished the intensity of defect light emission at ~2.4 eV. ZnO/F-doped ZnO core-shell NWs were fabricated either by PVD or CVD processes. Compared with the CVD procedure, the PVD method provides better crystalline shell structures after annealing, with a typical shell thickness ranges from 2~5 nm.

In Chapter VI, porous Ge nanowires were fabricated by the anodization of Ge nanowires in ethanolic HCl electrolyte. A transition from pore arrays/networks to roughened surfaces to polished surfaces was observed with a decreasing of applied bias. Porous GeNWs can be fabricated by anodizing GeNWs grown on Si wafer substrates in low ratio of HCl:EtOH (<1:12) with current densities ranging from 1.3~6.5 mA/cm^2 or constant voltage (4~8 V). An initial cathodic Cu electrodeposition step can be used to stabilize the nanowires and passivate the Si surface, which contributes to a more effective anodic etching.

For the periodic features in etched GeNWs with feature spacing (d_{FS}) ranging from 20~450 nm, one possible reason is that the electrochemical potential along GeNWs is not uniform. Previous work suggested that the electrochemical potential along 1D quantum wire, as a function of bias intensity, could have oscillations with a wavelength related to the Fermi wavelength of the free electrons. Therefore, the pore arrays reflect such a potential distribution along GeNWs and the d_{FS} values correspond to the Fermi wavelength of carriers in an anodization process. Based on a simple De Broglie model,

the electron energy was calculated by using feature spacing values (d_{FS}) as the Fermi wavelength. It was found that the surface potential energy is size-dependent with an exponential increase at a threshold diameter of ~ 38 nm. Therefore, it is more difficult to form a pore network structure in NWs with diameters close to a minimal NW diameter threshold. A strong bias is necessary to fabricate porous GeNWs in such case. When the Fermi wavelength of carriers is ≤ the diameter of GeNWs, porous GeNWs with networks can be formed.

The studies in this dissertation reveal a potential for as-prepared Ge or/and ZnO based nanostructures to be used in photoelectronics and photovoltaics, etc.

References

1. C. N. R. Rao, and A. K. Cheetham, *J. Mater. Chem.* **2001**, 11, 2887-2894.

2. J. Weber, R. Singhal, S. Zekri and A. Kumar, *Int. Mater. Rev.* **2008**, 53, 245-255.

3. G. E. Moore, in *Int. Elec. Devices Mtg (IEDM) Technical Digest* 75, 11 (IEEE, Piscataway, New Jersey, **1975**).

4. G. C. Osbourn, *Phys. Rev. B* **1983**, 5126-5128.

5. G. C. Osbourn, R. M. Biefeld, and P. L. Gourley, *Appl. Phys. Lett.* **1982**, 41, 172-174.

6. W. D. Laidig, Y. F. Lin, and P. J. Caldwell, *J. Appl. Phys.* 1985, 57, 33-38.

7. N. Hey, *IEE Rev.* **2003**, 46-48.

8. T. J. Beveridge, and R. G. E. Murray, *J. Bacteriol.* **1980**, 141, 876-887.

9. D. Bhattacharya, and R. K. Gupta, *Crit. Rev. Biotechnol.* **2005**, 25, 199-204.

10. H.W. Kroto, J. R. Heath, S. C. O'Brien, R.F. Curl, and R. E. Smalley, *Nature* **1985**, 318, 162-163.

11. J. Chen, and F. Wu, *Appl. Phys. A* **2004**, 78, 989-994.

12. S. Iijima, *Nature* **1991**, 354, 56-58.

13. L.W. Zhong, *Annu. Rev. Phys. Chem.* **2004**, 55,159-196.

14. H. Huang, E. E. Remsen, T. Kowalewski, and K. L. Wooley *J. Am. Chem. Soc.* **1999**, 121, 3805-3806.

15. D. Golberg, Y. Bando, T. Sato, N. Grobert, M. Reyes-Reyes, H. Terrones, and

M.Terrones, *J. Chem. Phys.* **2002**, 116, 8523-8532.

16. T. J. Trentler, K. M. Hickman, S. C. Goel, A. M. Viano, P. C. Gibbons, and W. E. Buhro, *Science* **1995**, 270, 1791-94.

17. L. C. Campos, M. Tonezzer, A. S. Ferlauto, V. Grillo, R. Magalhães-Paniago, S. Oliveira, L.O. Ladeira, and R. G. Lacerda, *Adv. Mater.* **2008**, 20, 1499-1504.

18. H. J. Dai, E. W. Wong, Y. Z. Lu, S. S. Fan, and C. M. Lieber, *Nature* **1995**, 375, 769-772.

19. L. Manna, E. C. Scher, and A. P. Alivisatos, *J. Am. Chem. Soc.* **2000**, 122, 12700-12706.

20. R. Q. Guo, J. Nishimura, M. Ueda, M. Higashihata, D. Nakamura, and T. Okada, *Appl. Phys. A* **2007**, 89, 141-144.

21. Y. Zhang, K. Suenaga, C. Colliex, and S. Iijima, *Science* **1998,** 281, 973-975.

22. Z. L. Wang, Z. R. Dai, R. P. Gao, Z. G. Bai, and J. L. Gole. *Appl. Phys. Lett.* **2000**, 77, 3349-3351.

23. R. Feynman, *Eng. Sci. (California Institute of Technology)* **1960**, 23, 22-36.

24. M. Schulz, *Nature* **1999**, 399,729-730.

25. L. Mazzola, *Nat. Biotechnol.* **2003**, 21, 1137-1143.

26. J. Drbohlavova, V. Adam, R. Kizek, and J. Hubalek, *Int. J. Mol. Sci.* **2009**, 10, 656-673.

27. J. Sharma, R. Chhabra, A. Cheng, J. Brownell, Y. Liu, and H. Yan, *Science* **2009**, 323,112-116.

28. A. Javey, S-W. Nam, R. S. Friedman, H. Yan, and C. M. Lieber, *Nano Lett*, **2007**, 7, 773-777.

29. G. A. Somorjai, F. Tao, J. Y. Park, *Top Catal.* **2008**, 47, 1–14.

30. D. Loveridge, P. Dewick and S. Randles, *Tech. Anal. Strat. Manag.* **2008**, 20, 29-43.

31. D. Bhattacharya and R. K. Gupta, *Crit. Rev. in Biotechnol.* **2005**, 25, 199-204.

32. M. C. Mcalpine, R. S. Friendman, and C. M. Lieber, *Proc. IEEE.* **2005**, 93, 1357-1363.

33. J. M. Xu, *Synth. Met.* **2000**, 115, 1-3.

34. T. Zhai, X. Fang, M. Liao, X. Xu, H. Zeng; B. Yoshio, D. Golberg, *Sensors* **2009**, 9, 6504-6529.

35. C. D. Franco, A. Elia, V. Spagnolo, G. Scamarcio, P. M. Lugarà, E. Ieva, N. Cioffi, L. Torsi, G. Bruno, M. Losurdo, M. A. Garcia, S. D. Wolter, A. Brown, M. Ricco, *Sensors* **2009**, 9, 3337-3356.

36. J. Martinez, R. V. Martínez and R. Garcia, *Nano Lett.* **2008**, 8, 3636-3639.

37. M. S. Gudiksen, K. N. Maher, L. Ouyang, and H. Park, *Nano Lett.* **2005**, 5, 2257-2261.

38. H. Kim, Y. Cho, H. Lee, S. Il Kim, S. R. Ryu, D. Y. Kim, T. W. Kang, and K. S. Chung, *Nano Lett.* **2004**, 4, 1059-1062.

39. L. Kim, P. O. Anikeeva, S. A. Coe-Sullivan, J. S. Steckel, M. G. Bawendi and V. Bulovi, *Nano Lett.* **2008**, 8, 4513-4517.

40. I. Sakamoto, T. Yamaguchi, H. Nagao, K. Nishikawa, *AIP Conf. Proc.* **2004**, 708,

795-796.

41. I. Gur, N. A. Fromer, C-P. Chen, A. G. Kanaras, and A. P. Alivisatos, *Nano Lett.* **2007**, 7, 409-414.

42. P. Kervalishvili, *Rev. Adv. Mater. Sci.* **2007**, 14, 71-80.

43. K-Q. Peng, X. Wang, X-L Wu and S-T. Lee, *Nano Lett.* **2009**, 9, 3704-3709.

44. J. F. Scott, *Ferroelectrics* **2005**, 314, 207-222.

45. J-M. Shieh, J. Y. Huang, W.-C. Yu, J-D Huang, Y-C. Wang, C-W. Chen, C-K. Wang, W-H. Huang, A-T. Cho, H-C. Kuo, B-T. Dai, F-L. Yang, C-L. Pan, *Appl. Phys. Lett.* **2009**, 95, 143501-3.

46. S. Hacohen-Gourgy, B. Almog, G. Deutscher, *Appl. Phys. Lett.* **2008**, 92, 152502-1-3.

47. K. Matsumoto, *Int. J. High Speed Electron. Syst.* **2000**, 10, 1, 83-91.

48. P. Utko, P. E. Lindelof, K. Gloos, *Appl. Phys. Lett.* 2006, 88, 202113-3.

49. P. Chen, X. Ma, and D. Yang, *J. Appl. Phys.* **2007**,101, 053103-1-4.

50. N. Azad and Y. Rojanasakul, *Am. J. Drug Deliv.* **2006**, 4, 79-88.

51. O. V. Salata, *J. Nanobiotechnology* **2004**, 2, 1-6.

52. T. A. Taton, *Trends Biotechnol.* **2002**, 20, 277-279.

53. G. Balasundaram, and T. J. Webster, *J. Mater. Chem.* **2006**, 16, 3737–3745.

54. A. Nduwimana, R. N. Musin, A. M. Smith, and X-Q. Wang, *Nano Lett.* **2008**, 8, 3341-3344.

55. R. S. Wagner, and W. C. Ellis. *Appl. Phys. Lett.* **1964**, 4, 89-90.

56. Y. Maeda, N. Tsukamoto, Y. Yazawa, Y. Kanemitsu, and Y. Masumoto, *Appl. Phys. Lett.* **1991**, 59, 3168-3170.

57. *CRC Handbook of Chemistry and Physics*, 4-13 78th ed.; Lide, D. R., Ed.; CRC Press: Boca Raton, FL, **1998**.

58. J. I. Pankove, *Optical Processes in Semicaonductors,* Dover Publications Inc, NY, 1971, p412.

59. A. M. Morales, C. M. Lieber, *Science* **1998**, 279, 208-211.

60. P. S. Shah, T. Hanrath, K. P. Johnston, and B. A. Korgel, *J. Phys. Chem. B,* **2004**, 108, 9574-9587.

61. T. Hanrath, B. Korgel, *J. Am. Chem. Soc.* **2002**,124, 1424-1429.

62. X. Lu, D. D. Fanfair, K. P. Johnston, and B. A. Korgel, *J. Am. Chem. Soc.* **2005**, 127, 15718-15719.

63. D. Wang, Y. Chang, Q. Wang, J. Cao, D. B. Farmer, R. G. Gordon, and H. Dai, *J. Am. Chem. Soc.* **2004**, 126, 11602-11611.

64. T. I. Kamins, X. Li, R. S. Williams, *Nano Lett.* **2004**, 4, 503-506.

65. H. Jagannathan, M. Deal, Y. Nishi, J. Woodruff, C. Chidsey, P. C. Mclntyre, *J. Appl. Phys.* **2006**, 100, 024318-1-10.

66. J. Wu, P. Punchaipetch, R. M. Wallace, and J. L. Coffer, *Adv. Mater.*, **2004**, 16, 1444-1448.

67. P. Nguyen, H. T. Ng, and M. Meyyappan, *Adv. Mater.* **2005**, 17, 549-553.

68. X. H. Sun, C. Didychuk, T. K. Sham, and N. B. Wong, *Nanotechnology* **2006**, 17,

2925-2930.

69. P. J. Poole, J. Lefebvre, and J. Fraser, *Appl. Phys. Lett.* **2003**, 83, 2055- 2057.

70. B. Mandl, J. Stangl, T. Martensson, A. Mikkelsen, J. Eriksson, L. S. Karlsson, G. Bauer, L. Samuelson, and W. Seifert, *Nano Lett.* **2006**, 6, 1817-1821.

71. C. Fang, H. Foell, and J. Carstensen, *Nano Lett.* **2006,** 6, 1578-1580.

72. W. Han, L. Wu, Y. Zhu, and M. Strongin, *Microsc. Microanal.* **2005**, 11(Suppl 2), 1549.

73. N. R. B. Colemana, K. M. Ryana, T. R. Spaldinga, J. D. Holmes, and M. A. Morris, *Chem. Phys. Lett*. **2001**，343, 1-6.

74. Y. F. Mei, Z. M. Li, R. M. Chu, Z. K. Tang, G. G. Siu, R. K. Y. Fu, P. K. Chu, W. W. Wu, and K. W. Cheah, *Appl. Phys. Lett.* **2005**，86, 02l 111-1-3.

75. T. Hanrath, and B. A. Korgel, *Adv. Mater.* **2003**, 15, 437-441.

76. V. Schmidt and U. Gösele, *Science*, **2007,** 316, 698-699.

77. S. Kodambaka, J. Tersoff, and M. C. Reuter, F. M. Ross, *Science* **2007**, 316, 729-732.

78. G. A. Bootsma, and H. J. Gassen, *J. Crystal Growth* **1971**, 10, 223-227.

79. A. I. Persson, M. W. Larsson, S. Stenström, B. J. Ohlsson, L. Samuelson, and L. R. Wallenberg, *Nat. Mater.* **2004**, 3, 677-681.

80. D. Wang, and H. Dai, *Angew. Chem. Int. Ed.* **2002**, 41, 4783-4786.

81. F. D. Wang, A. G. Dong, J. W. Sun, R. Tang, H. Yu, and W. E. Buhro, *Inorg. Chem.* **2006**, 45, 7511-7521.

82. J. L. Lensch-Falk, E. R. Hemesath, F. J. Lopez, and L. J. Lauhon, *J. Am. Chem. Soc.* **2007**, 129, 10670-10671.

83. H-Y. Tuan, D. C. Lee, T. Hanrath, and B. A. Korgel, *Chem. Mater.* **2005**, 17, 5705-5711.

84. Y. Xiang, L. Cao, J. Arbiol, M. L. Brongersma, A. F. i. Morral, *Appl. Phys. Lett.* **2009**, 94, 163101-1-3.

85. H.Yu, J. B. Li, R. A. Loomis, P. C. Gibbons, L. W. Wang, W. E. Buhro, *J. Am. Chem. Soc.* **2003**, 125, 16168-16169.

86. C. Yan and P. S. Lee, *J. Phys. Chem. C*, **2009**, 113, 2208-2211.

87. N. Zaitseva, J. Harper, D. Gerion, and C. Saw, *Appl. Phys. Lett.* **2005**, 86, 053105-1-3.

88. B-S. Kim, T-W. Koo, J-H. Lee, D. S. Kim, Y. C. Jung, S. W. Hwang, B. L. Choi, E. K. Lee, J. M. Kim, and D. Whang, *Nano Lett.* **2009**, 9, 864-869.

89. J. Zhu, H. Peng, A. F. Marshall, D. M. Barnett, W. D. Nix, Y. Cui, *Nat. Nanotechnol.* **2008**, 3, 477-481.

90. K. Ikejiri, J. Noborisaka, S. Hara, J. Motohisa, and T. Fukui, *J. Cryst. Growth* **2007**, 298, 616-619.

91. G. Gu, M. Burghard, G. T. Kim, G. S. Düsberg, P. W. Chiu, V. Krstic, S. Roth, and W. Q. Han, *J. Appl . Phys.* **2001**，90, 5747-5751.

92. T. Hanrath, B. A. Korgel, *J. Phys. Chem. B* **2005**, 109, 5518-5524.

93. D. Erts, B. Polyakov, B. Daly, M. A. Morris, S. Ellingboe, J. Boland, and J. D.

Holmes, *J. Phys. Chem. B* **2006**, 110, 820-826.

94. D.wang, H. Dai, *Appl. Phys. A* **2006**, 85, 217-225.

95. D. Wang, *Pure Appl. Chem.* **2007**, 79, 55-65.

96. P. Nguyen, H. T. Ng, M. Meyyappan, *Adv. Mater.* **2005**, 17, 549-553.

97. D. W. Wang, Y. L. Chang, Z. Liu, H. J. Dai, *J. Am. Chem. Soc.* **2005**, 127, 11871-11875.

98. X. Wu, J. S. Kulkarni, G. Collins, N. Petkov, D. Almécija, J. J. Boland, D. Erts, and J. D. Holmes, *Chem. Mater.* **2008**, 20, 5954-5967.

99. D. W. Wang, Q. Wang, A. Javey, R. Tu, H. J. Dai, H. Kim, P. C. McIntyre, T. Krishnamohan, and K. C. Saraswat, *Appl. Phys. Lett.* **2003**, *83*, 2432-2434.

100. K. A. Dick, K. Deppert, L. S. Karlsson, L. R. Wallenberg, L. Samuelson, W. Seifert, *Adv. Funct. Mater*. **2005**, 15, 1603-1610.

101. C. K. Chan, X. F. Zhang, and Y. Cui, *Nano Lett.* **2008**, 8, 307-309.

102. P. Yang, H. Yan, S. Mao, R. Russo, J. Johnson, R. Saykally, N. Morris, J. Pham, R. He, and H. J. Choi, *Adv. Funct. Mater.* **2002**, 12 , 323-331.

103. X. Y. Kong, Y. Ding, and Z. L. Wang, *J. Phys. Chem. B* **2004**, 108 (2), 570-574.

104. J. Fallert, R. Hauschild, F. Stelzl, A. Urban, M. Wissinger, H. Zhou, C. Klingshirn, and H. Kalt, *J. Appl. Phys.* **2007**, 101, 073506-1-4.

105. W. Cheng, P. Wu, X. Zou, and T. Xiao, *J. App. Phys.* **2006**, 100, 054311-1-4.

106. A. B. Djurišić, H. L. Yu, W. C. H. Choy, K. W. Cheah, and W. K. Chan, *App. Phys. Lett.* **2004**, 84, 2635-2637.

107. M. N. Jung, S. H. Park, S. Y. Ha, S. J. Oh, Y. R. Cho, J. S. Park, I. H. Im, B. H. Kood, T. Yao, and J.H. Chang, *Phys. E* **2008**, 40, 2761-2764.

108. M. H. Huang, S. Mao, H. Feick, H. Yan, Y. Wu, H. Kind, E. Weber, R. Russo, P. Yang, *Science* **2001**, 292, 1897-1899.

109. C. Klingshirn, *J. Cryst. Growth* **1992**, 117, 753-757

110. Y. Kayamura, *Phys. Rev. B* **1988,** 38, 9797-9805.

111. W. Wegscheider, L. N. Pfeiffer, M. M. Dignam, A. Pinczuk, K. W. West, S. L. McCall, and R. Hull, *Phys. Rev. Lett.* **1993**, 71, 4071-4074.

112. J. Rybczynski, D. Banerjee, A. Kosiorek, M. Giersig, and Z. F. Ren, *Nano Lett.* **2004**, 4, 2037-2040.

113. M. H. Huang, S. Mao, H. Feick, H. Yan, Y. Wu, H. Kind, E. Weber, R. Russo, and P. Yang, *Science* **2001**, 292,1897-1899.

114. M-C. Jeong, B-Y. Oh, W. Lee, and J-M. Myoung, *J. Crystal Growth* **2004**, 268, 149-154.

115. Y. Cheng, P. Xiong, L. Fields, J. P. Zheng, R. S. Yang, and Z. L. Wang, *App. Phys. Lett.* **2006**, 89, 093114-1-3.

116. T-W. Koo and D. Whang, *Nano*, **2008,** 3, 477-482.

117. W. I. Park, D. H. Kim, S. W. Jung, and G. C. Yia, *Appl. Phys. Lett.* **2002**, 80, 4232-4234.

118. C. Xu, K. Rho, J. Chun, and D-E. Kim, *Appl. Phys. Lett.* **2005**, 87, 253104-1-3.

119. X. Wang, J. Song and Z. L. Wang, *J. Mater. Chem.* **2007**, 17, 711-720.

120. Y. Li, G. W. Meng, L. D. Zhang and F. Phillipp, *Appl. Phys. Lett.* **2000**, 76, 2011-2013.

121. L. E. Greene, M. Law, J. Goldberger, F. Kim, J. C. Johnson, Y. Zhang, R. J. Saykally and P. Yang, *Angew. Chem. Ind. Ed.* **2003**,115, 3139-3142.

122. C.-J. Kim, K. Kang, Y. S. Woo, K.-G. Ryu, H. Moon, J.-M. Kim, D.-S. Zang and M.-H. Jo, *Adv. Mater.* **2007**, 19, 3637-3642.

123. M. Law, L. E. Greene, J. C. Johnson, R. Saykally and P. Yang, *Nature Mater.* **2005**, 4, 455-459.

124. B. D. Yao, Y. F. Chan, and N. Wang, *Appl. Phys. Lett.* **2002**, 81, 757-759.

125. A. Mohanta and R. Thareja, *J. Appl. Phys.* **2008**, 104, 044906-6.

126. R. C. Wang, C. P. Liu, J. L. Huang, and S. J. Chen, *Appl. Phys. Lett.* **2006**, *88*, 023111-1-3.

127. Representative ZnO Dopant References: (a) B. Y. Geng, G. Z. Wang, Z. Jiang, T. Xie, S. H. Sun, G. W. Meng, and L. D. Zhang, *Appl. Phys. Lett.* **2003**, 82, 4791-4793. (b) Y.Q. Chang, D. B. Wang, X. H. Luo, X. Y. Xu, X. H. Chen, L. Li, C. P. Chen, R.M. Wang, J. Xu, and D. P. Yu, *Appl. Phys. Lett.* **2003**, 83, 4020-4022. (c) Q. Wan, Q. H. Li, Y. J. Chen, T. H. Wang, X. L. He, X. G. Gao, and J. P. Li, *Appl. Phys. Lett.* **2004**, 84, 3085-3087. (d) S-M. Zhou, X.-H. Zhang, X-M. Meng, K. Zou, X. Fan, S-K. Lee, and S-T. Wu, *Nanotechnology* **2004**, 15, 1152-1155. (e) W. Lee, M-C. Jeong, and J-M. Myoung, *Appl. Phys. Lett.* **2004**, 85, 6167-6169. (f) S-M. Zhou, X-H. Zhang, X-M. Meng, X. Fan, S-K. Wu, and S-T. Lee, *Physica E,* 2005, 25, 587-591.

(g) S. Y. Bae, C. W. Na, J. H. Kang, and J. Park, *J. Phys. Chem. B* **2005**, 109, 2526-2531. (h) J. B. Cui, and U. J. Gibson, *Appl. Phys. Lett.* **2005**, 87, 133108-1-3. (i) H. Pan, Y. Zhu, H. Sun, Y. Feng, H. Sow, and J. Lin, *Nanotechnology* **2006**, 17, 5096-5100. (j) J. Wang; M. J. Zhou, S. K. Hark, Q. Li, D. Tang, M. W. Chu, and C. H. Chen, *Appl. Phys. Lett.* **2006**, 89, 221917. (k) G. N. Panin, A. N. Baranov, O. V. Kononenko, S. V. Dubonos, and T. W. Kang, *AIP Conf. Proc.* **2007**, 893, 743-744. (l) P. Mohanty, B. Kim, and J. Park, *Mater. Sci. Eng. B* **2007**, 138, 224-227. (m) N. Hongsith, C. Viriyaworasakul, P. Mangkorntong, N. Mangkorntong, and S. Choopun, *Ceramics International*, **2008**, 34, 823-826. (n) T. Jia, W. Wang, F. Long, Z. Fu, H. Wang, and Q. Zhang, *J. Alloys Comp.* **2009**, 484, 410-415. (o) K. Hyunwook and J. R. Chelikowsky, *Appl. Phys.Lett.* **2009**, 95, 263108-1-3. (p) B. Wang, J. Iqbal, X. Shan, G. Huang, H. Fu, R. Yu, and D. Yu, *Mater. Chem. Phys.* **2009**, 113, 103-106.

128. Y. R. Park and K. J. Kim, *Solid State Commun.* **2002**, 123, 147-150.

129. J.M. Lin, Y.Z. Zhang, Z.Z. Ye, X.Q. Gu, X.H. Pan, Y.F. Yang, J.G. Lu, H.P. He and B.H. Zhao, *Appl. Surf. Sci.* **2009**, 255, 6460-6463.

130. G. D. Yuan, W. J. Zhang, J. S. Jie, X. Fan, J. A. Zapien, Y. H. Leung, L. B. Luo, P. Wang, C. S. Lee, and S. T. Lee, *Nano Lett.* **2008**, 8, 2591-2597.

131. G.-D. Yuan, W.-J. Zhang, J-S. Jie, X. Fan, J-X. Tang, I. Shafiq, Z-Z. Ye, C-S. Lee, and S-T. Lee, *Adv. Mater.* **2008**, 20, 168-173.

132. J. B. Cui, Y. C. Soo, and T. P. Chen, U. J. Gibson, *J. Phys. Chem. C* **2008**, 112, 4475-4479.

133. Q. Wana C. L. Lin and X. B. Yu, T. H. Wang, *Appl. Phys. Lett*. **2004**, 84, 124-126.

134. Y. Qin, X. Wang, and Z. L. Wang, *Nature* **2008**, 451, 809-814.

135. M. C. Newton and P. A. Warburton, *Mater. Today.* **2007**, 10, 50-54.

136. Y. F. Hsu, Y. Y. Xi, C. T. Yi, A. B. Djurišić, and W. K. Chan, *J. App. Phys.* **2008**, 103, 83114-1-4.

137. V. A. L. Roy, A. B. Djurišić, H. Liu, X. X. Zhang, Y. H. Leung, M. H. Xie, J. Gao, H. F. Lui, and C. Surya, *App. Phys. Lett.* **2004**, 84, 756-758.

138. Z. Zhang, L. Sun, Y. Zhao, Z. Liu, D. Liu, L.Cao, B. Zou, W. Zhou, C. Gu, and S. Xie, *Nano Lett.* **2008**, 8, 652-655.

139. Y. Dai, Y. Zhang, Q. K. Li, and C. W. Nan, *Chem. Phys. Lett.* **2002**, 358, 83-86.

140. C. C. Tang, S. S. Fan, M. L. de la Chapelle, and P. Li, *Chem. Phys. Lett.* **2001**, 333, 12-15.

141. V. A. L. Roy, A. B. Djurišić, W. K. Chan, J. Gao, H. F. Lui and C. Surya, *App. Phys. Lett.* **2003**, 83, 141-143.

142. K. Zhenga, C. X. Xua, G. P. Zhua, X. Lia, J. P. Liua, Y. Yang, and X. W. Sun, *Physica E* **2008**, 40, 2677-2681.

143. J. Huh, G-T. Kim, J. S. Lee, and S. Kim, *Appl. Phys. Lett.* **2008**, 93, 042111-1-3.

144. S-K. Lee, S. L. Chen, D. Hongxing, L. Sun, Z. Chen, W. M. Chen, and I. A. Buyanova, *Appl. Phys. Lett.* **2010**, 96, 083104-1-3.

145. Y. C. Zhong, K. S.Wong, A. B. Djuriši´c, and Y.F. Hsu, *Appl Phys B* **2009**, 97,

125-128.

146. L. J. Lauhon, M. S. Gudiksen, D. L. Wang and C. M. Lieber *Nature* **2002,** 420, 57-61.

147. H-W. Kim, S-H. Shim and J-W. Lee, *Nanotechnology* **2008**, 19, 45601-1-6.

148. H. Wang, M. Upmanyu, and C. V. Ciobanu, *Nano Lett.* **2008**, 8, 4305-4311.

149. F. Jabeen, S. Rubini, V. Grillo, L. Felisari, and F. Martelli, *Appl. Phys. Lett.* **2008**, 93, 083117-1-3.

150. S. Park, J. Jun, H. W. Kim, and C. Lee, *Solid State Commun.* **2009**, 149, 315-318.

151. L-W. Yin, M-S. Li, Y. Bando, D. Golberg, X. Yuan, and T. Sekiguchi, *Adv. Funct. Mater.* **2007**, 17, 270-276.

152. B. Q. Cao, J. Zúnniga-Pérez, N. Boukos, C. Czekalla, H. Hilmer, J. Lenzner, A .Travlos, M. Lorenz, and M. Grundmann, *Nanotechnology* **2009**, 20, 305701-1-8.

153. F. Qian, Y. Li, S. Gradecak, D. Wang, C. J. Barrelet, and C. M. Lieber, *Nano Lett.* **2004**, 4, 1975-1979.

154. H.-M. Lin, Y.-L. Chen, J. Yang, Y.-C. Liu, K-M. Yin, J-J. Kai, F-R. Chen, L-C. Chen, Y.-F. Chen, C-C. Chen, *Nano Lett.* **2003**, 3, 537-541.

155. N. Sköld, L. S. Karlsson, M. W. Larsson, M.-E. Pistol, W. Seifert, J. Trägardh, and L. Samuelson, *Nano Lett.* **2005**, 5, 1943-1947.

156. D-W. Kim, I-S. Hwang, S. J. Kwon, H-Y. Kang, K-S. Park, Y-J. Choi, K-J. Choi, and J-G. Park, *Nano Lett.* **2007**, 7, 3041-3045.

157. S. Han, C. Li, Z. Liu, B. Lei, D. Zhang, W. Jin, X. Liu, T. Tang, and C. Zhou, *Nano*

Lett. **2004**, 4, 1241-1246.

158. T. Asefa, C. T. Duncanc, and K. K. Sharma, *Analyst* **2009**, 134, 1980-1990.

159. M. Lahav, E. A. Weiss, Q. Xu, and G. M. Whitesides, *Nano Lett.* **2006**, 6, 2166-2171.

160. V. M. Cepak, C. Hulteen, J. G. Che, K. B. Jirage, B. B. Lakshmi, E. R. Fisher, and C. R. Martin, *J. Mater. Res.* **1998**, 13, 3070-3080.

161. S. Park, J-H. Lim, S-W. Chung, and C. Mirkin, *Science* **2004**, 303, 348-351.

162. M. Bognitzki, H. Hou, M. Ishaque, T. Frese, M. Hellwig, C. Schwarte, A. Schaper, J. H.Wendorff, and A. Greiner, *Adv. Mater.* **2000**, 12, 637-640.

163. B. Tian, X. Zheng, T. J. Kempa, Y. Fang, N. Yu, G. Yu, J. Huang, and C. M. Lieber, *Nature* **2007**, 449, 885-889.

164. A. L. Pan, L. Yao, Y. Qin, Y. Yang, D. S. Kim, R. Yu, B. Zou, P. Werner, M. Zacharias, and U. Gösele, *Nano Lett.* **2008**, 8, 3413-3417.

165. Y. Jung, S. H. Lee, A. T. Jennings, and R. Agarwal, *Nano. Lett.* **2008**, 8, 2056-2062.

166. L. Zhang, R. Tu, and H. Dai, *Nano. Lett.* **2006**, 6, 2785-2789.

167. F. Qian, S. Gradecak, Y. Li, C. Y. Wen, and C. M. Lieber, *Nano Lett.* **2005**, 5, 2287-2291.

168. T. Mokari, S. E. Habas, M. Zhang, P. D. Yang, *Angew. Chem. Int. Ed.* **2008**, 47, 5605-5608.

169. O. Hayden, A. B. Greytak, and D. C. Bell, *Adv. Mater.* **2005**, 17, 701-704.

170. Y. L. Chueh, L. J. Chou, and Z. L. Wang, *Angew. Chem., Int. Ed.* **2006**, 45,

7773-7778.

171. X. F. Duan, Y. Huang, R. Agarwal, and C. M. Lieber, *Nature* **2003**, 421, 241-245.

172. X. F. Duan, Y. Huang, Y. Cui, J. Wang, and C. M. Lieber, *Nature* **2001**, 409, 66-69.

173. C. Thelander, T. Martensson, M. T. Bjork, B. J. Ohlsson, M. W. Larsson, L. R. Wallenberg, and L. Samuelson, *Appl. Phys. Lett.* **2003**, 83, 2052-2054.

174. H. J. Choi, J. C. Johnson, R. He, S. K. Lee, F. Kim, P. Pauzauskie, J. Goldberger, R. J. Saykally, and P. Yang, *J. Phys. Chem. B* **2003**, 107, 8721-8725.

175. V. Schlosser, *IEEE Trans. Electron Devices* **1984**, 31, 610-613.

176. B. M. Kayes, H. A. Atwater, and N. S. Lewis, *J. Appl. Phys.* **2005**, 97, 114302-1-11.

177. M. Imaizumi, T. Ito, M. Yamaguchi, and K. Kaneko, *J. Appl. Phys.* **1997**, 81, 7635-7640.

178. W. U. Huynh, J. J. Dittmer, and A. P. Alivisatos, *Science* **2002**, 295, 2425-2427.

179. M. Law，L. E. Greene，A. Radenovic，T. Kuykendall，J. Liphard，and P. D. Yang，*J. Phys. Chem. B* **2006**，110, 22652-22663.

180 N. S. Lewis, *Science* **2007**, 315, 798-801.

181. J. Rouquerol, D. Avnir, C. W. Fairbridge, D. H. Everett, J. H. Haynes, N. Pernicone, J. D. F. Ramsay, K. S. W. Sing, and K. K. Unger, *Pure & Appl. Chem* **1994**, 66, 1739-1758.

182. L. T. Canham, C. L. Reeves, J. P. Newey, M. R. Houlton, T. I. Cox, J. M. Buriak, and M. P. Stewart, *Adv. Mater.* **1999**, 11,1505-1507.

183. A. Vaseashta, and D. Dimova-Malinovska, *Adv. Mater.* **2005**, 6, 312-318.

184. J. L. Coffer, J-L. Montchamp, J. B. Aimone, and R. P. Weis, *Phys. Stat. Sol. (a)* **2003**,197, 336-339.

185. M.B. Rao, and S. Sircar, *J. Membr. Sci.* **1996**, 110, 109-118.

186. J. Lee, S. Han, and T. Hyeon, *J. Mater. Chem.* **2004**, 14, 478-486.

187. M.A. Harmer, W.E. Farneth, and Q. Sun, *J. Am. Chem. Soc.* **1996**, 118, 7708-7715.

188. F. Schüth, *Annu. Rev. Mater. Res.* **2005**. 35, 209-238.

189. K. Maex, M. R. Baklanov, D. Shamiryan, F. Iacopi, S. H. Brongersma, and Z. S.Yanovitskaya, *J. Appl. Phys.* **2003**, 93, 8793-8841.

190. P. Arora and Z. Zhang, *Chem. Rev.* **2004**, 104, 4419-4462.

191. N.K. Raman, M.T. Anderson, C.T. Brinker, *Chem. Mater.* **1996,** 8, 1682-1701.

192. T. Yanagisawa, T. Shimizu, K. Kuroda, C. Kato, *Bull. Chem. Soc. Jpn.* **1990**, 63, 988-992.

193. A. Vinua, T. Moria, and K. Arigab, *Sci. Technol. Adv. Mater.* **2006**, 7, 753-771.

194. X. G. Zhang, *Electrochemistry of Silicon and Its Oxides*, Kluwer Academic, Hornell, New York, **2001**, 87.

195. L. T. Canham, *Appl. Phys. Lett.* **1990**, 57, 1046-1048.

196. G. S. Armatas, and M. G. Kanatzidis, *Science* **2006**, 313, 817-820.

197. J. Wei, J. M. Buriak, and G. Siuzdak, *Nature* **1999**, 399, 243-246.

198. T. Ma, M. Akiyama, E. Abe, and I. Imai, *Nano Lett.* **2005**, 5, 2543-2547.

199. X. Wang, Z. Tian, T. Yu, H. Tian, J. Zhang, S. Yuan, X. Zhang; Z. Li and Z. Zou, *Nanotechnology*, **2010**, 21, 065703-1-5.

200. L. T. Canham, J. P. Newey, C. L. Reeves, M. R. Houlton, A. Loni, A. J. Simons, and T. I. Cox, *Adv. Mater.* **1996**, 8, 847-849.

201. J. Salonen, A. M. Kaukonen, J. Hirvonen, and V-P Lehto, *J. Pharm. Sci.* **2008**, 97, 632-653.

202. L. Santinacci, and T. Djenizian, *C. R. Chimie* **2008**, 11, 964-983.

203. V. Lehmann, and U. Gösele, *Appl. Phys. Lett.* **1991**, 58, 856-858.

204. J-L. Maurice, A. Rivière, A. Alapini and C. Lévy-Clément, *Appl. Phys. Lett.* **1995**, 66, 1665-1667.

205. A. Starovoitov, and S. Bayliss, *Appl. Phys. Lett.* **1998**, 73, 1284-1286.

206. S. Menezes, B. Miller, K. J. Bachmann, *J. Vac. Sci. Technol. B* **1983**, 1, 48-53.

207. X-Y. Hou, and H-L. Fan, *Appl. Phys. Lett.* **1996**, 68, 2323-2325.

208. S. Shih, K. H. Jung, and D. L. Kwong, M. Kovar and J. M. White, *Appl. Phys. Lett*. **1993**, 62, 1904-1906.

209. K. Peng, X. Wang, and S-T. Lee, *Appl. Phys. Lett.* **2008**, 92, 163103-1-3. .

210. A. Halimaoui, *Porous silicon: Material processing, properties and applications.* In: Vial JC, Derrien J, editors. *Porous Silicon Science and Technology*. France: Springer-Verlag. **1995**. 33-52.

211. S. M. Hu and D. R. Kerr, *J. Electrochem. Soc.* 1967, 114, 414.

212. X. G. Zhang, S. D. Collins, and R. L. Smith, *J. Electrochem. Soc.* **1989**, 136, 1561-1565.

213. Y. Kato, T. Ito, and A. Hiraki, *Jpn. J. Appl. Phys.* **1988**, 27, L1406-L1409.

214. S. Godefroo, M. Hayne, M. Jivanescu, A. Stesmans, M. Zacharias, O. I. Lebedev, G. Van Tendeloo, V. V. Moshchalkov, *Nat. Nanotechnology*, **2008**, 3, 174-178.

215. J.-S. Lee, and N.-H. Cho, *Appl. Surf. Sci.* **2002**, 190, 171-175.

216. S. Gardelis, J. S. Rimmer, P. Dawson, and B. Hamilton, R. A. Kubiak, T. E. Whall, and E. H. C. Parker, *Appl. Phys. Lett.* **1991**, 59, 2118-2120.

217. S. Gardelis, A.G. Nassiopoulou, M. Mahdouani, R. Bourguiga, and S. Jaziri, *Physica E*, **2009**, 41, 986-989.

218. A. Sa'ar, Y. Reichman, M. Dovrat, D. Krapf, J. Jedrzejewsky, and I. Balberg, *Nano Lett.* **2005**, 5, 2443-2447.

219. S. Gardelis, I. Tsiaoussis, N. Frangis, A.G. Nassiopoulou, *Nanotechnology* **2007**, 18, 115705-1-5.

220. X.W. Du, Y. Jina, N.Q. Zhao, Y.S. Fu, and S.A. Kulinich, *Appl. Surf. Sci.* **2008**, 254, 2479-2482.

221. H. Y. Zheng, J. C. Chai, Y. C. Lam, and H. Zhu, *Surf. Rev. and Lett.* **2005**, 12, 351-354.

222. Y. Zhao, D. Li. W. Sang, D. Yang, and M. Jiang, *J. Mater. Sci.* **2007**, 42, 8496-8500.

223. D. F. Timokhov and F. P. Timokhov, *Semiconductors,* **2009**, 43, 88–91.

224. V. P. Bondarenko, V. E. Borisenko, A. M. Dorofeev, I. N. Germanenko and S. V. Gaponenko, *J. Appl. Phys.* **1994**, 75, 2727-2729.

225. A. Bsiesy, J. C. Vial, F. Gaspard, R. Herino, M. Ligeon, F. Miller, R. Romestain, A.

Wasiela, A. Halimaoui, and G. Bomchil, *Surf. Sci.* **1991**, 254, 195-200.

226. S M. Prokes, J. Glembocki, V. M. Bermudez, R. Kaplan, L. E. Friedersdorf, and P. C. Searson, *Phys. Rev. B* **1992**, 45, 13788-13794.

227. A. N. Ilham, H. A. Rafaie, S. Abdullah, and M. Rusop, CP1136, *Nanoscience and Nanotechnology, International Conference on Nanoscience and Nanotechnology*, (NANO-Sci-Tech **2008**), edited by M. Rusop and T. Soga, p830-834.

228. D. J. Blackwood and Y. Zhuang, *Surf. Rev. Lett.* **2001**, 8, 429-433.

229. C. Fang, H. Föll, and J. Carstensen, *J. Electroanal. Chem.* **2006**, 589, 259-288

230. H. C. Choi, and J. M. Buriak, *Chem. Commun.* **2000**, 1669-1670.

231. D. Sun, A. E. Riley, A. J. Cadby, E. K. Richman, S. D. Korlann, and S. H. Tolbert, *Nature* **2006**, 441, 1126-1130.

232. E. G. Rojas, H. Plagwitz, B. Terheiden, J. Hensen, C. Baur, G. L. Roche, G. F. X. Strobl, and R. Brendela, *J. Electrochem. Soc.* **2009,** 156, D310-D313.

233. C. Fang, H. Föll, and S. Langa, *Phys. Stat. Sol. (a)* **2007**, 5, 1292-1296.

234. G. Kartopu, A. V. Sapelkin, V. A. Karavanskii, U. Serincan, and R. Turan, *J. Appl. Phys.* **2008**, 103, 113518-1-7.

235. R. Memming, and G. Neumann, *J. Electroanal. Chem.* **1969**, 21, 295-305.

236. H. Gerischer, A. Mauerer, W. Windt, *Surf. Sci.* **1966**, 4, 431-439.

237. S. Bayliss, Q. Zhang and P. Harris, *Appl. Surf. Sci.*, **1996**, 102, 390-394.

238. J. Carstensen, M. Christophersen, and H. Föll, *Mat. Sci. Eng. B* **2000,** 69-70, 23-28.

239. D. R. Turner, *J. Electrochem. Soc.* **1958**, 105, 402-408.

240. V. P. Ulin, and S. G. Konnikov, *Semiconductors,* **2007**, 41, 832-844.

241. S-F. Chuang, S. D. Collins, and R. L. Smith, *Appl. Phys. Lett.* **1989**, 55, 675-677.

242. M. Rauscher, and H. Spohn, *Phys. Rev. E* **2001**, 64, 031604-031613.

243. A. Valance, *Phys. Rev. B* **1997**, 55, 9706-9715.

244. J. Carstensen, R. Prange, G.S. Popkirov, and H. Föll *Appl. Phys. A* **1998**, 67, 459-467.

245. J. Rappich, H. Jungblut, M. Aggour, and H.J. Lewerenz, *J. Electrochem. Soc.* **1994**, 141, L99-L102.

246. J. Wloka, D.J. Lockwood, and P. Schmuki, *Chem. Phys. Lett.* **2005**, 414, 47-50.

247. I. Vrublevsky, A. Jagminas, J. Schreckenbach, and W.A. Goedel, *Solid State Sci.* **2008**, 10, 1605-1611.

248. R. L. Smith and S. D. Collins, *J. Appl. Phys.* **1992**, 71, R1-R2.

249. S. Langa, J. Carstensen, I. M. Tiginyanu, M. Christophersen, and H. Foll, *Electrochem. Solid-State Lett.* **2001**, 4, G50-G52.

250. C. Kriegel, A. Arrechi, K. Kit, D. J. McClements, and J. Weiss, *Crit. Rev. Food. Sci. Nutr.* **2008**, 48, 775-797.

251. D. Li, and Y. Xia, *Adv. Mater.* **2004**, 16, 1151-1170.

252. J. Wu, *Fabrication and Optical Properties of Erbium doped Group IV Nanowires and Their Corresponding Oxides*, *Dissertation*, **2007**, 157, Texas Christian University.

253. B. Ding, M. Wang, J. Yu, and G. Sun. *Sensors*, **2009**, 9, 1609-1624.

254. W. Sigmund, J. Yuh, H. Park, V. Maneeratana, G. Pyrgiotakis, A. Daga, J. Taylor, and J. C.Nino, *J. Am. Chem. Soc.* **2006**, 89, 395-407.

255. S. V. Fridrikh, J. H. Yu, M. P. Brenner, and G. C. Rutledge, *Phys. Rev. Lett.* **2003**, 144502-144505.

256. A. Polman, *Physica B* **2001**, 300, 78-90.

257. P. G. Kik, and A. Polman, *MRS Bull.* **1998**, 23, 48-54.258. V. B. Voronkov, V. G. Golubev, A. V. Medvedev, A. B. Pevtsov, N. A. Feoktistov, N. I. Gorshkov, and D. N. Suglobov, *Phys. Solid State* **1998**, 40, 1433-1436.

259. A. Polman, and F. van Veggel, *J. Opt. Soc. Am. B* **2004**, 21, 871-892.

260. A. J. Kenyon, *Semicond. Sci. Technol.* **2005**, *20*, R65-R84.

261. A.J. Kenyon, *Progress in Quantum Electronics* **2002**, 26, 225-284.

262. R. Pérez-Casero, A. Gutiérrez-Llorente, O. Pons-Y-Moll, W. Seiler, R. M. Defourneau, D. Defourneau, E. Millon, J. Perrière, P. Goldner and B. Viana, *J. App. Phys.* **2005**, 97, 054905-1-2.

263. N. Mais, J. P. Reithmaier, A. Forchel, M. Kohls, L. Spanhel, and G. Mu□ller, *App.Phys. Lett.* **1999**, 75, 2005-2007.

264. T. M. Williams, D. Hunter, A. K. Pradhan, and I. V. Kityk, *Appl. Phys. Lett.* **2006**, 89, 043116-043118.

265. J. H. Chen, D. Pang, H. M. Cheong, P. Wickboldt, and W. Paul, *Appl. Phys. Lett.* **1995**, 67, 2182-2184.

266. M. Ardyanian, H. Rinnert, and M. Vergnat, *J. Appl. Phys.* **2007**, 102, 106103-1-4.

267. J. S. Jensen, T. P. L. Pedersen, J. Chevallier, B. B. Nielsen, and A. N. Larsen, *Nanotechnology* **2006**, 17, 2621-2624.

268. J. St. John, J. L. Coffer, Y. Rho, P. Diehl, R. Pinizzotto, T. Culp, and K. Bray, *Chem. Mater,* **1997**, 9, 3176-3180.

269. J. St. John, J. L. Coffer, Y. Chen, and R. Pinizzotto, *J. Am. Chem. Soc.* **1999**, 121, 1888-1892.

270. J. Ji, and J. L. Coffer, *J. Phys. Chem.* **2002**, 106, 3860-3863.

271. Z. Wang, and J. L. Coffer, *Nano Lett*, **2002**, 2, 1303-1305.

272. J. Wu, and J. L. Coffer, *Chem. Mater*. **2007**, 19, 6266-6276.

273 J. Wu, and J. L. Coffer, *J. Phys. Chem. C.* **2007**, 111, 16088-16091.

274. A. K. Pradhan, L. Douglas, H. Mustafa, R. Mundle, D. Hunter, and C. E. Bonner, *Appl. Phys. Lett.* **2007**, 90, 072108-072110.

275. K. Takahei, A. Taguchi, Y. Horikoshi, and J. Nakata, *J. Appl. Phys.* **1994**, 76, 4332-4339.

276. M-Y. Tsai, C-Y. Yu, C-C. Wang, and T-P. Perng, *Crystal Growth & Design* **2008**, 8, 2264-2269.

277. C. L. Heng and T. G. Finstad, P. Storås, Y. J. Li, A. E. Gunnæs, and O. Nilsen, *Appl. Phys. Lett.* **2004**, 85, 4475-4477.

278. K. Zhong, J. Xia, H. H. Li, C. L. Liang, P. Liu, and Y. X. Tong, *J. Phys. Chem. C* **2009**, 113, 15514-15523.

279. Y. Ding, X. Y. Kong, and Z. L. Wang, *J. Appl. Phys.* **2004**, 95, 306-310.

280. C. Yan, and P. S. Lee, *J. Phys. Chem. C* **2009**, 113, 14135-14139.

281. K. Z. Baba-Kishi, *J. Mater. Sci.* **2002**, 37, 1715-1746.

282. B.D. Cullity and S.R. Stock, *Elements of X-Ray Diffraction*, 3rd Ed., Prentice-Hall Inc. **2001**, p167-171.

283. Z. Liu, X. Jing, and L. Wang, *J. Electrochem. Soc.* **2007**, 154, H500-H506.

284. G. Anoop, K. M. Krishna, K. R. Kumar, and M. K. Jayaraj, *J. Electrochem. Soc.* **2008**, 155, J270-J273.

285. D. T. Emerson, J. R. Shealy, *Appl. Phys. Lett.* **1996**, 69, 2584-2586.

286. Z. T. Kang, B. K. Wagner, J. Parrish, D. Schiff, C. J. Summers, *Nanotechnology* **2007**, 18, 415709-1-5.

287. S. L. Sewell, R. D. Rutledge and D. W. Wright, *Dalton Trans.* **2008**, 29, 3857-3865.

288. J. Sato, H. Kobayashi, K. Ikarashi, N. Saito, H. Nishiyama, and Y. Inoue, *J. Phys. Chem. B* **2004**, 108, 4369-4375.

289. H. Y. Kim, P. Viswanathamurthi, N. Bhattarai, and D. R. Lee, *Rev. Adv. Mater. Sci.* **2003**, 5, 220-223.

290. T. Schmidt, G. Müller, L. Spanhel, K. Kerkel, and A. Forchel, *Chem. Mater.* **1998**, 10, 65-71.

291. A. M. Fischer, S. Srinivasan, R. Garcia, F. A. Ponce, S. E. Guaño, B. C. Di Lello, F. J. Moura, I. G. Solórzano, *Appl. Phys. Lett.* **2007**, 91, 121905-1-3.

292. M. Bitenc, P. Podbrsc□e□k, Z. C. Orel, M. A. Cleveland, J. A. Paramo, R. M.

Peters,

and Y. M. Strzhemechny, *Crystal Growth & Design* **2009**, 9, 997-1001.

293. W. P. Gillina and R. J. Curry, *Appl. Phys. Lett*. **1999**, 74, 798-799.

294. F. Song, G. Zhang, M. Shang, H. Tan, J.Yang, and F. Meng, *Appl. Phys. Lett.* **2001**, 79, 1748-1750.

295. S. H. Dalal, D. L. Baptista, K. B. K. Teo, R. G. Lacerda, D. A. Jefferson and W. I. Milne, *Nanotechnology* **2006**, 17**,** 4811-4818.

296. L. C. Kimerling, *Appl. Surf. Sci.* **2000**, 159-60, 8-13.

297. J. Wu, J. L. Coffer, Y. Wang and R. Schulze *J. Phys. Chem. C* **2009**, 113, 12-16.

298. H. Liang, R. G. Gordon, *J. Mater. Sci.* **2007**, 42, 6388-6399.

299. H. Y. Xu, Y. C. Liu, J. G. Ma, Y. M. Luo, Y. M. Lu, D. Z. Shen, J. Y. Zhang, X. W. Fan, and R. Mu, *J. Phys.: Condens. Matter* **2004**,16, 5143-5150.

300. S. Ilican, Y. Caglar, M. Caglar, F. Yakuphanoglu, *Appl. Surf. Sci.* **2008**, 255, 2353-2359.

301. R. J. Hong, X. Jiang, G. Heide, B. Szyszka, V. Sittinger, and W. Werner, *J. Cryst. Growth* **2003**, 249, 3/4, 461-469**.**

302. S. H. Jo, D. Banerjee, and Z. F. Ren, *Appl. Phys. Lett.* **2004**, 85, 8, 1407-1409.

303. C. Ye, X. Fang, Y. Hao, X. Teng, and L. Zhang, *J. Phys. Chem. B* **2005**, 42 19758-19765.

304. J. Coffer, S. Dunkle, J. Wu, A. Loni, and L. Canham, *5th International Conference - Porous Semiconductor Science and Technology*, **2006**, Extended

Abstract, O3-03.

305. A. I. Hochbaum, D. Gargas, Y. J. Hwang, and P. D. Yang, *NanoLett.* **2009**, 9, 3550-3554.

306. Y. Qu, L. Liao, Y. Li, H. Zhang, Y. Huang, and X. Duan, *NanoLett.* **2009**, 9, 4539-4543.

307. Y. F. Mei, Z. M. Li, R. M. Chu, Z. K. Tang, G. G. Siu, R. K. Y. Fu, P. K. Chu, W-W. Wu, and K-W. Cheah, *Appl. Phys. Lett.* **2005**, 86, 021111-1-3

308. Y. Su, X. Liang, S. Li, Y. Chen, Q. Zhou, S. Yin, X. Meng and M. Kong, *Mater. Lett.* **2008**, 62, 1010-1013.

309. P. L. Pernas, A. Martin-Rodero, and F. Flores, *Phys. Rev. B* **1990**, 41, 8553-8556.

310. M. Büttiker, *Phys. Rev. B* **1989**, 40, 3409-3412.

VITA

Xuezhen Huang was born in Nanjing, Jiangsu, China on October 27 1972. He is the first child of Guifang Huang and Zaiwen Liu. He received a bachelor degree of chemical engineering from Nanjing University of Technology (NJUT) in 1992, and then worked as a chemical engineer and technology director in Nanjing Sili Chemical Co. Ltd. for 6 years. He went back to NJUT again in 1999 and obtained a master degree of chemical engineering in 2002. He worked as a technology support of fluorine-contained polymer (FEP, PPVDF) in Shanghai New Materials Co. Ltd., before he enrolled in Texas Christian University to pursue his doctorate in inorganic/materials under the direction of Prof. Jeffery L. Coffer in the spring of 2005.

He is married to Xiaocong Wang of Yixian, China. They have one child.

ABSTRACT

FABRICATION AND OPTICAL PROPERTIES OF (I) ERBIUM-DOPED NANOWIRES CONTAINING GERMANIUM AND/OR ZINC OXIDE AND (II) POROUS GERMANIUM NANOWIRES

by

Xuezhen Huang, Ph. D., 2010
Department of Chemistry
Texas Christian University

Dissertation Advisor: Jeffery L. Coffer,
Professor of Chemistry

Nanomaterials have attracted great attention in the past two decades due to their superior mechanical, thermal, chemical, electrical and optical properties entirely different from bulk materials, which lead to numerous potential applications in nanodevices and nanoelectronics, such as FETs, LEDs, single electron memory devices, spin polarized electronics, quantum computing, sensors, photonic crystals/devices, solar cells etc.

Based on the previous work on Er-doped GeNWs, a core-shell nanostructure was built by introducing Zn/ZnO shell onto Er-doped GeNWs. It was found that Zn sources and corresponding surface modification processes (CVD and PVD) have important impact on Er^{3+} PL and ZnO UV/visible PL due to Zn_2GeO_4 formation, which were confirmed by HRTEM and XRD measurements. In another work, Ge and Er were used to modify the surface of ZnO tetrapods. Both strong ZnO visible PL and Er^{3+} PL were observed; considerable enhancement of Er^{3+} PL was made possible by Ge deposition as a sensitizer layer. The Zn_2GeO_4 phase observed could either separate from the ZnO phase or mix

uniformly with the ZnO phase. As a control system, Er/GeO_x/ZnO nanofibers were fabricated by electrospinning of selected sol-gel precursor solutions. These types of nanofibers exhibited strong Er^{3+} near IR PL at 1.54 μm after annealing to remove the polymer template. XRD spectra indicate that the Er/Ge/Zn mixture likely forms a disordered phase, especially with high Er^{3+} concentrations, which contributes to the strong Er^{3+} PL with the reduction of Er-Er interactions.

In another work, the fabrication of F-doped ZnO nanowires was investigated on different substrates with or without carrier gas (Ar). ZnO UV/visible PL spectra indicate that F-doping diminished the intensity of defect light emission at ~2.4 eV. Furthermore, ZnO/F-doped ZnO core-shell NWs were fabricated either by PVD or CVD processes; the PVD method provides better crystalline shell structures after annealing.

The last work describes the fabrication of porous Ge nanowires by the anodization of Ge nanowires (grown on Si substrates) using ethanolic HCl as an electrolyte. An initial cathodic Cu electrodeposition step is found to provide useful kinetic control of the pore morphology and to stabilize the nanowires attached to the Si surface. A systematic evaluation of the role of electrolyte composition, current/voltage density, and its duration on the resultant Ge NW morphology and structure have been carried out. Preliminary photoluminescence (PL) measurements suggest strong emission in the visible region. The electrochemical anodization mechanism is discussed involving the periodic localization of pores and a varying potential distribution of free electrons along 1D GeNWs.